UNIVERSIDAD AUTÓNOMA DE MADRID

DEPARTAMENTO DE BIOQUÍMICA

Tesis Doctoral

Nuevas herramientas para el análisis de interacciones y adquisición automatizada inteligente en microscopia óptica

Diego Megias

Madrid, 2015

UNIVERSIDAD AUTÓNOMA DE MADRID

DEPARTAMENTO DE BIOQUÍMICA

FACULTAD DE MEDICINA

Tesis Doctoral

Nuevas herramientas para el análisis de interacciones y adquisición automatizada inteligente en microscopia óptica

Doctorando: Diego Megias, licenciado en Biología por la Universidad Autónoma de Madrid.

Director de Tesis Dra. Maria C. Montoya

Madrid, 2015

MINISTERIO
DE ECONOMÍA
Y COMPETITIVIDAD

Instituto
de Salud
Carlos III

cnic

Dra. María C. Montoya, Jefa de la Unidad de Celómica del Centro de Investigaciones Cardiovasculares (CNIC)

CERTIFICA:

Que Diego Megías ha realizado el presente trabajo: "Nuevas herramientas para el análisis de interacciones y adquisición automatizada inteligente en microscopía óptica" que a mi juicio reúne plenamente todos los requisitos necesarios para optar al **grado de Doctor**, a cuyo efecto será presentado en la Universidad Autónoma de Madrid. El trabajo se ha realizado bajo mi dirección, autorizando su presentación ante el tribunal correspondiente.

Y para que conste se extiende el presente certificado

Madrid, a 23 de Noviembre de 2015

VºBº del Director de la Tesis
Dra. Maria C. Montoya

Fundación Centro Nacional de Investigaciones Cardiovasculares Carlos III
C/ Melchor Fernández Almagro, 3 28029 Madrid
Telf. 00 34 91-4531200 Fax: 00 34 91-4531245 www.cnic.es

AGRADECIMIENTOS

En primer lugar darle las gracias a María Montoya, que me dio la oportunidad de trabajar en el CNIO con ella descubrí otra forma de entender la microscopía y siempre me ha apoyado para que realizara esta tesis. Guardo algunos recuerdos muy buenos de los tiempos en que trabajamos juntos.

También agradecer a Javi y Raquel que me descubrieron la vida del estudiante pre-doctoral, con vosotros pasé muy buenos ratos en el micro discutiendo de todo y nada. A Arancha que me acogió cuando llegué al CNIO y estuvo conmigo durante años. Especialmente quería agradecer su apoyo y simpatía a Ángel que me ayudo mucho y siempre trajo la sonrisa y las ganas al laboratorio.

Después de muchos años en el centro ha habido gente que realmente ha sido determinante en mi trabajo y que he llegado a considerar amigo, con todo lo que ello significa, es el caso de José Rivera, con él he colaborado durante muchos años, me ha enseñado y me ha acompañado no tengo palabras para agradecerle todo su cariño y amistad.

A Lola, que me pica y me ayuda para hacerlo mejor todos los días, a Fernando por toda la ayuda que me ha dado, y a Giovi por su sonrisa y apoyo.

De más atrás me vienen caras que me enseñaron y ayudaron no solo en lo laboral sino también en lo personal, de mi paso por la UAM me acuerdo mucho de Paco, Cova y Juan Carlos Rodriguez que me metió en esta aventura de la microscopía confocal. Del IIB Agustín, Pignatelli, Olmeda y Ester, chinita eres lo más grande.

Agradecer a Ximo y Manu su trabajo conmigo en estos últimos años haciendo más fácil lo difícil.

Los últimos agradecimientos son para mi familia, a mis padres que me lo han dado todo. A Luz que es mi vida y a Bruno y Darío por cambiarme esa vida y darme otra mucho mejor.

I. RESUMEN / SUMMARY

RESUMEN

La comunidad científica necesita de nuevas tecnologías y métodos que permitan profundizar en el entendimiento de los distintos procesos biológicos.

En esta tesis presentamos nuevos abordajes en microscopía óptica que permiten resolver algunas de las limitaciones existentes en este campo.

Por una parte, presentamos el desarrollo de un nuevo método denominado λFRET que posibilita medir la interacción entre moléculas utilizando el fenómeno de transferencia de energía de la fluorescencia por resonancia, que permite resolver muchas de las limitaciones de los métodos existentes, haciendo este tipo de estudios más fiables y sensibles cuando se compara con algunos de los métodos más usados. Este nuevo método ha sido validado en estudios de interacción entre las moléculas CD44 y MT1-MMP, demostrando su utilidad en el campo.

Aun así, el mayor inconveniente de dicho tipo de ensayos y en general de las adquisiciones de imagen complejas es el gran consumo de tiempo y recursos. Las opciones disponibles de automatización son aún muy básicas y poco eficientes. Por ejemplo, las técnicas de *screening* convencional (o adquisición aleatoria automatizada) necesitan de muestras homogéneas y con una localización estandarizada que muchas veces resulta imposible de conseguir en biología, ya sea por la baja frecuencia del evento de estudio como por su heterogeneidad.

En este trabajo presentamos también el desarrollo y validación de una nueva técnica de "*screening inteligente*" denominado iMSRC (*Intelligent Matrix Screening Remote Control*) que posibilita realizar de forma fácil e intuitiva la adquisición de imágenes dirigida por análisis de imagen automatizada en microscopios de fluorescencia estándar y en microscopios confocales. Esta nueva herramienta permite la realización de estudios de microscopía óptica basados en la localización de eventos de baja frecuencia en una muestra y otros ensayos complejos, que antes eran prácticamente inviables.

SUMMARY

The scientific community needs new technologies and methods which may allow us to study biological processes in depth.

In this Ph.D. Thesis we present new approaches in optical microscopy which that allow solving some of the current limitations in this field.

On the one hand, we present here the development of a new method named λFRET which allows the measurement of molecular interactions by using the fluorescence resonance energy transfer phenomenon. This novel method overcomes most of the limitations from previously existing methods. The measurements with this new method proved to be more reliable and sensitive than most common ones based in optical microscopy.

Furthermore, we have validated this method in the study of the interaction between CD44 and MT1MMP.

The main problem of this kind of assays and of complex image acquisition in microscopy in general is that they require long acquisition time and resources.

The currently available options for automation are still very simple and poorly efficient. For example conventional *screening* approaches (random automated acquisition of images) require homogenous samples and the location of the events of interest must be predefined. This is often difficult to achieve in most common assays characterized by biological heterogeneity or when trying to quantify rare events.

To overcome these limitations we have developed and validated the iMSRC (intelligent matrix *screening* remote control), a new platform for running intelligent *screening*s (automated acquisition driven by image analysis) in a user friendly manner, and compatible with conventional and confocal microscopes. This new approach allow performing microscopy studies based on the detection of low frequency events in a sample and other complex assays that were almost impossible before.

ÍNDICE

INDICE

II. INTRODUCCIÓN

Prácticamente todo proceso biológico es consecuencia de las relaciones que se establecen entre los distintos componentes que forman parte del mismo. A nivel celular, el que una serie de moléculas interaccionen entre si de una manera u otra, determina procesos de enorme relevancia fisiopatológica, tales como la migración, proliferación o muerte celular.

Como piezas de un reloj, todos estos componentes celulares están finamente ajustados y gobiernan complejas rutas de señalización que afectan a su vez a otras. El estudio de cómo se organizan entre sí, así como los mecanismos que las dirigen, proporciona una información tremendamente valiosa desde el punto de vista de la investigación básica y nos ayuda a entender mejor dichos procesos, pero también resulta indispensable para la localización de dianas terapéuticas que nos permitan corregir mediante su activación o inhibición procesos que como resultado de una desregulación desencadenan distintas patologías, tales como el desarrollo de tumores.

1. TÉCNICAS DE DETECCIÓN Y ANALISIS DE INTERACCIONES MOLECULARES.

La investigación de la interacción molecular entre los distintos componentes en una respuesta biológica resulta fundamental para comprender su regulación y actividad. Desafortunadamente, el conocimiento del conjunto de interacciones entre moléculas biológicas (o interactoma celular) es aún incompleto, y dada su complejidad requiere un abordaje igualmente complejo. Esto incluye el uso de técnicas de detección indirectas de biología molecular, como la **co-inmunoprecipitación** (Figura 1) (Lee, Ryu et al. 2013), la **presentación de fagos** (phage display) (Gramatikoff, Georgiev et al. 1994), de genética molecular, como el **ensayo de doble hibrido** (James, Halladay et al. 1996), ensayos más recientes como el **marcado de proximidad *in vivo*** en los que se da la expresión de forma ectópica de una proteína de interés unida ya sea a una biotin-ligasa (BioID) (Roux, Kim et al. 2012) o a una enzima con actividad peroxidasa (método APEX) (Rhee, Zou et al. 2013). Una vez activada, la biotina se conjuga rápidamente y de forma covalente a residuos de Lisinas cercanas (en el caso del BioID) o de Tirosinas (en el caso del APEX). Esta

reacción facilita el enriquecimiento de potenciales candidatos a la interacción con un ensayo de derribo (pull-down) por Streptavidina para su posterior identificación en espectrometría de masas. ((Larance and Lamond 2015)), también existen métodos de **correlación de perfiles proteicos** (PCP - Protein correlation profiling). En esta técnica se usan tanto la cromatografía o la centrifugación en gradiente de densidad para separar los complejos proteicos en su forma nativa de acuerdo con su tamaño, densidad, forma o carga. Los extractos celulares se aíslan y fraccionan de forma que posteriormente son procesados de forma independiente por cromatografía liquida seguida de espectrometría de masas para así identificar las proteínas que los constituyen (Kirkwood, Ahmad et al. 2013),(Havugimana, Hart et al. 2012) o, por otro lado métodos de detección in situ basados en la biología celular.

Cada una de estas opciones tecnológicas presentan ventajas e inconvenientes, y normalmente el análisis de una interacción concreta requiere de la combinación de varias de ellas.

Figura 1. Ensayo de co-inmunoprecipitación

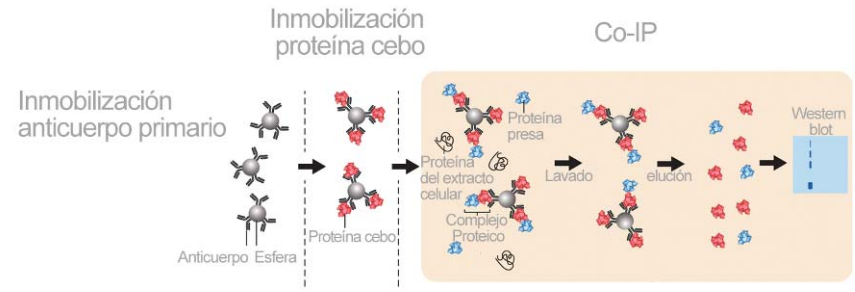

Adaptado de: Real-time single-molecule coimmunoprecipitation of weak protein-protein interactions
Hong-Won Lee, Ji Young Ryu, Janghyun Yoo, Byungsan Choi, Kipom Kim & Tae-Young Yoon

El mayor inconveniente de las técnicas indirectas es el de ser ensayos que se realizan fuera del entorno natural de las células. Por ejemplo, en el caso de la co-inmunoprecipitación se parte de extractos celulares, en los cuales se pueden producir contactos de forma artificial entre moléculas que en el contexto de una célula funcional, por el mero hecho de encontrarse en orgánulos diferentes, pudieran no ser posibles. Otra posible fuente de error es el hecho de que se revele una interacción indirecta, es decir, que no sea con la

proteína directamente ligada a la de estudio, sino con una tercera que esté unida a ambas formando un complejo, llevando a conclusiones equivocadas.

A su vez, uno de los mayores inconvenientes para el estudio de dichas interacciones es el hecho en sí de que son dependientes de las circunstancias espacio-temporales, esto es, se producen en sitios determinados de la célula y en momentos muy concretos. Este hecho suele hacer difícil su detección, dado que, dependiendo del caso concreto, puede ocurrir que solo un pequeño porcentaje del total de las moléculas implicadas estén interaccionando en un momento determinado, de forma que su detección es si cabe aún más compleja.

Es por todo lo mencionado anteriormente, que se hace vital el empleo de métodos directos de detección de dichas interacciones que puedan validar o complementar los ensayos realizados por métodos indirectos.

2. DETECCIÓN DE INTERACCIONES *IN SITU* BASADAS EN IMAGEN

Un paso fundamental en la investigación de la interacción entre dos biomoléculas sería demostrar que comparten ubicación al menos en ciertas regiones de la célula. Esto se puede demostrar mediante técnicas de microscopía óptica e inmuno-marcaje, o acoplamiento de las moléculas de interés a proteínas fluorescentes utilizando técnicas de biología molecular. Así, mediante el uso de se puede saber si las proteínas reveladas por dichos anticuerpos o por sus proteínas fluorescentes acopladas comparten ubicación o no en el contexto celular. Si bien este primer acercamiento nos puede dar una idea aproximada de que esa interacción puede ser posible, al ver coincidencia o no de dichos marcajes, el principal problema de este abordaje es la limitación en términos de resolución que sufre la microscopía óptica.

2.1 Limitaciones de la luz para el estudio de interacciones moleculares

El límite de resolución, o dicho de otra manera, la distancia mínima a la que aún es posible resolver dos objetos muy cercanos entre sí, está limitado por la difracción de la luz. La difracción entendida como una perturbación en la propagación de una onda, y según el principio de Huygens (Huygens 1690), se

genera por ejemplo cuando una onda impacta en un objeto o pasa por una ranura con un tamaño similar a su longitud de onda. De igual forma, cuando la luz pasa por la apertura circular de las lentes del microscopio se produce un efecto de difracción, haciendo que la luz no se enfoque en un punto determinado, sino que produzca una imagen en forma de anillos, denominados discos de Airy (Figura 2).

Figura 2. Creación de los discos de Airy.

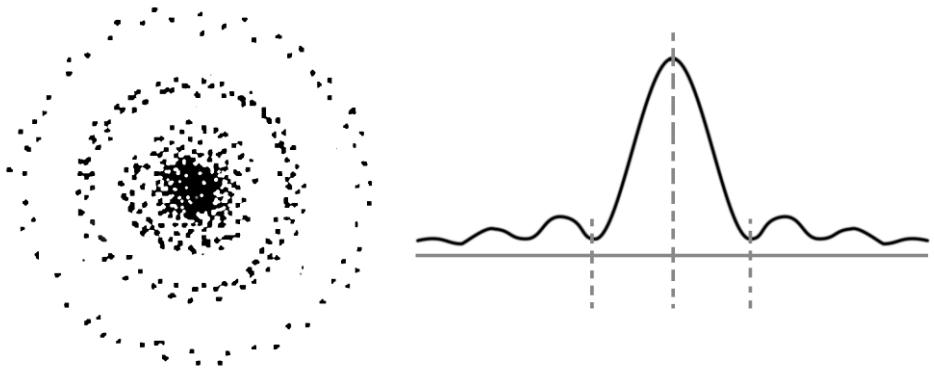

De esta forma, la resolución máxima en un microscopio óptico viene determinada por la apertura angular de las lentes del sistema. La apertura numérica viene derivada de la angular, y básicamente describe el rango de posibles ángulos en los que un sistema puede aceptar o emitir luz. La resolución óptica se puede calcular siguiendo la fórmula descrita por Ernst Abbe en 1873 (Abbe 1873) $d = \frac{\lambda}{2n \sin\theta}$ (teniendo en cuenta que la apertura numérica (N.A.) es : $\mathbf{NA} = \eta \sin\theta$).

Por tanto, la resolución está afectada por la longitud de onda de la luz, y por la apertura numérica del objetivo, que a su vez varía por el índice de refracción (η) del medio en el que se propaga dicha luz.

En la práctica, la apertura numérica máxima de un objetivo de inmersión en aceite está alrededor de 1,45, y la longitud de onda más corta visible se encuentra en torno a los 400 nanómetros (nm.), de forma que obtenemos una resolución máxima para un microscopio óptico de unos 250 nm.

Esto implica que, cuando observamos una muestra marcada en un microscopio óptico, si dos objetos están a una distancia entre sí inferior a ese límite de

resolución, y por tanto si sus discos de Airy no están suficientemente separados, estos objetos serán percibidos como un solo objeto en vez de dos (Figura 3).

Figura 3. Resolución de dos objetos

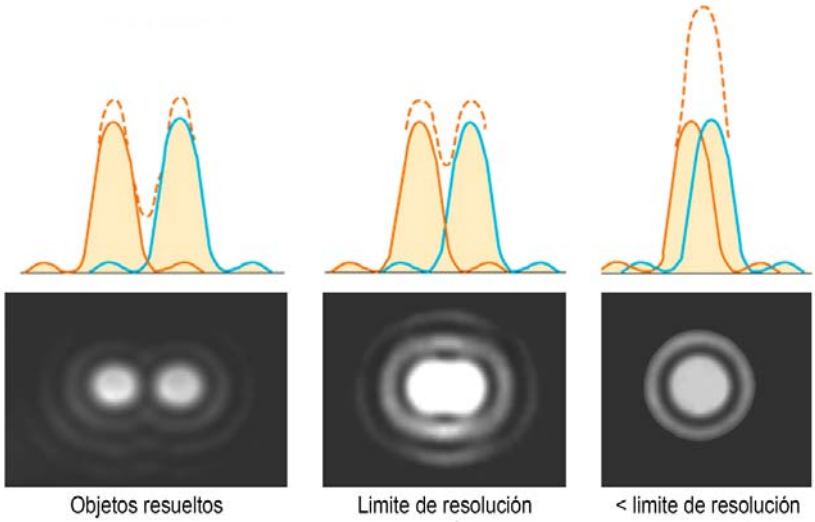

Las implicaciones de este hecho en el estudio de las interacciones moleculares son obvias si consideramos que cuando observamos dos posibles candidatos a interaccionar y los vemos juntos en la imagen, nos será totalmente imposible saber si están a menos de 250 nm. de distancia. Entendiendo que normalmente las interacciones moleculares se producen a una distancia inferior a los 10 nm, resulta que de una imagen de microscopía óptica en la que dos objetos co-localizan no se puede deducir inequívocamente que estos interaccionen entre sí, y solo se puede considerar como un indicio de que dicha interacción es posible dentro del contexto sub-celular (Figura 4).

Figura 4. Escala de medidas

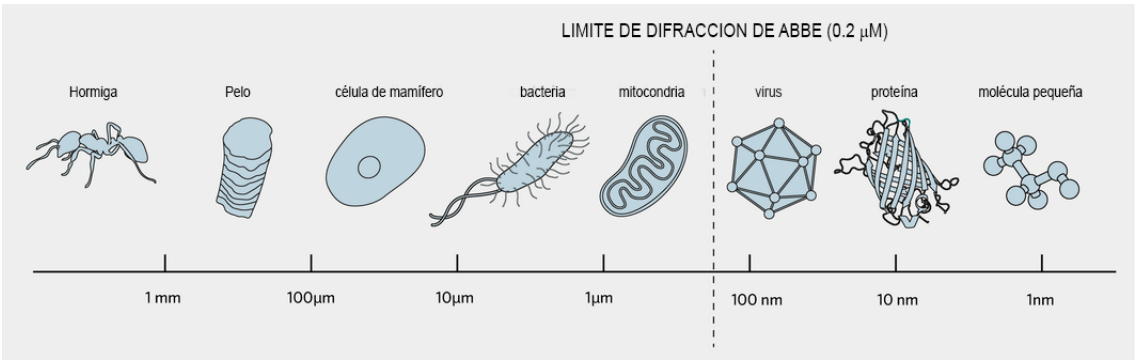

Recientemente han aparecido nuevas tecnologías que consiguen superar la barrera de la difracción de la luz. Dichas tecnologías se engloban dentro de las técnicas de súper-resolución tales como; el STED (stimulated emission depletion), el STORM (stochastic optical reconstruction microscopy) o el SSIM (saturated structured illumination microscopy) (Huang, Bates et al. 2009). Dichas técnicas nos permiten alcanzar una resolución en la microscopía óptica antes solo posible mediante la microscopía electrónica. La importancia de este cambio es capital en la forma de entender la microscopía, y ha sido reconocida con el premio Nobel de Química de 2014 a sus creadores Eric Betzig, Stefan W. Hell y William E. Moerner. Estos métodos no evitan la difracción de la luz, sino que básicamente consiguen eludir las limitaciones que derivan de ella, al recoger la luz de forma que consiguen que los fotones provenientes de la fluorescencia de la muestra no lleguen todos a la vez al detector, sino de forma que se pueda distinguir su punto de origen y así evitar el efecto de distorsión de la imagen provocado por la difracción de la luz.

Estos equipos a nivel comercial consiguen resoluciones por debajo de los 50 nm. según el método empleado, y en caso de equipos experimentales se consiguen resoluciones cercanas a los 10 nm. Sin embargo, en ensayos de co-localización también revelan aspectos que hasta ahora no eran relevantes, tales como el índice de marcaje de una proteína, es decir, qué porción de la proteína que estamos observando está marcada. Considerando que la mayor parte de los marcajes se realizan mediante el uso de anticuerpos y que estos reconocen regiones especificas de las proteínas, cabe la posibilidad de que dos moléculas unidas no co-localicen al ser observadas por súper-resolución. En cualquier caso sí que permiten medir la distancia entre ellas con mayor precisión, y realizar estudios mucho más fiables y detallados sobre las posibles asociaciones entre moléculas, que los obtenidos mediante las técnicas de co-localización llevadas a cabo con microscopios ópticos convencionales.

El equipamiento necesario para llevar a cabo las técnicas de súper-resolución es difícil que esté disponible en la mayoría de los laboratorios que realizan estudios de biología celular. Esto hace que la mayoría de estudios de interacciones moleculares estén sujetos a las limitaciones inherentes al empleo

de la luz en la microscopía lo que obliga al desarrollo de otros abordajes que, a pesar de estar sujetos a los límites de resolución de microscopía óptica convencional, permitan visualizar la interacción entre moléculas *in situ*. Con este propósito se han desarrollado diversos abordajes.

Uno de ellos es el método denominado P-Lisa (Soderberg, Gullberg et al. 2006) en el cual se emplean oligonucleótidos unidos a anticuerpos que reconocen las dos proteínas objeto de estudio. Si dichas sondas se acercan a distancia de interacción, entonces gracias a la incorporación en la reacción de un oligonucleótido conector se forma una estructura circular que puede ser amplificada usando una de las sondas como iniciador o primer. El producto de esa amplificación, denominada RCA (*rolling circle amplification*) es detectado con oligonucleótidos marcados con fluorescencia, complementarios a una región específica del producto de la amplificación (Figura 5).

Figura 5. Experimento de interacción por P-Lisa

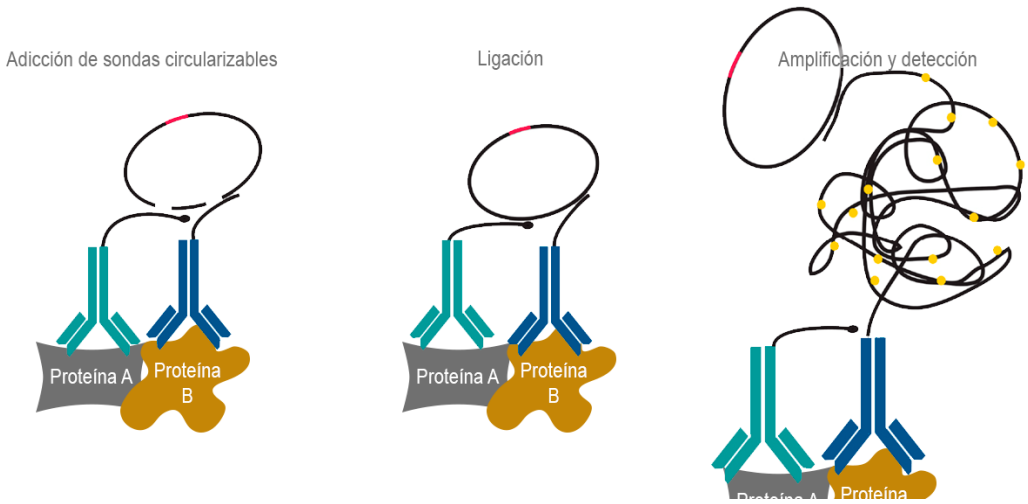

El mayor inconveniente de este método es que solo es visible el resultado de la amplificación, y no las sondas marcadas con oligonucleótidos, lo cual hace compleja su interpretación y el descartar los posibles falsos positivos.

Otro método para la observación de interacciones en microscopía es mediante el uso de fragmentos complementarios de proteínas fluorescentes denominado complementación bi-molecular fluorescente (*Bimolecular fluorescence complementation* o BiFC) (Kerppola 2006), (Magliery, Wilson et al. 2005) ,(Kerppola 2006). En este caso se unen dichos fragmentos a las proteínas que

se quieren analizar. Si la interacción se produce, los fragmentos de proteína fluorescente se re-asocian generando una proteína fluorescente funcional la cual emitirá la señal de fluorescencia detectable por microscopía. Las limitaciones de este sistema estriban en que una vez se ha producido, la asociación de ambos fragmentos es estable, por lo que no permite observar interacciones en tiempo real, y al retener a las proteínas unidas puede interferir en la dinámica de las mismas (Figura 6).

Figura 6. Experimento de interacción por BiFC

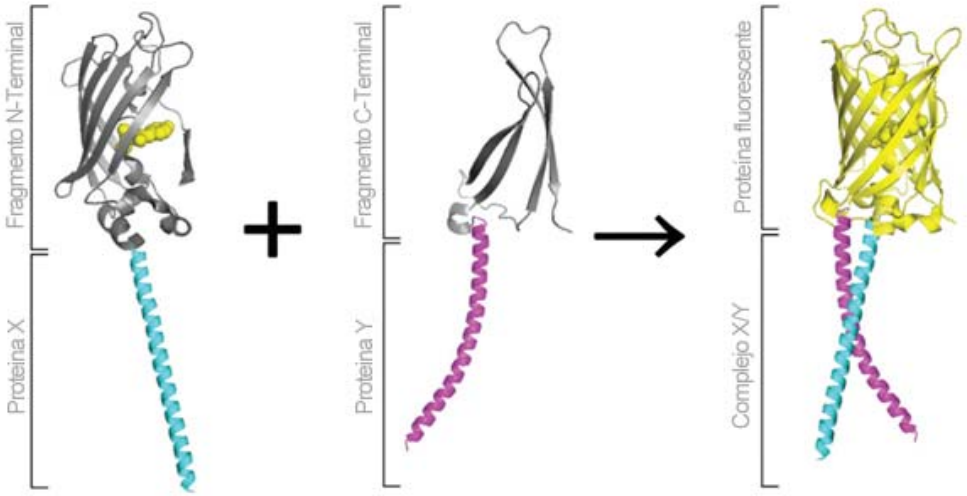

Adaptada de: Kodama, Y. and C. D. Hu "Bimolecular fluorescence complementation (BiFC): a 5-year update and future perspectives." Biotechniques 53(5): 285-98.

Otra alternativa, y por otro lado la más utilizada, aprovecha los cambios físicos y la transferencia de energía que se producen entre dos moléculas fluorescentes compatibles cuando se encuentran a una distancia menor a 10 nm. resolviendo la interacción entre moléculas. Esta metodología es el sujeto de estudio en este trabajo de tesis.

3. LA TRANSFERENCIA DE ENERGÍA DE LA FLUORESCENCIA POR RESONANCIA, EL FENÓMENO DEL FRET.

Una de las formas más comunes para el marcaje de macromoléculas y estructuras celulares en biología es el empleo de agentes fluorescentes, moléculas capaces de absorber fotones de luz que producen una transición energética en sus electrones, los cuales se desplazan a orbitales más energéticos. La molécula cargada de energía resulta inestable, y es la vuelta de

los electrones a su estado basal la que provoca la liberación de un fotón de luz, como se representa por medio del diagrama de Jablonski (Figura 7).

Figura 7. Diagrama de Jablonski simplificado

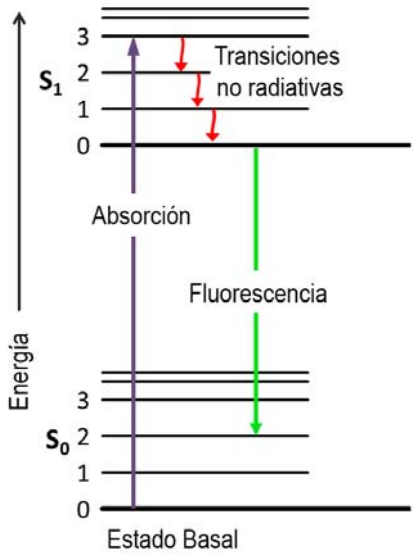

Durante este proceso se produce una cierta pérdida de energía, que se traduce en que la longitud de onda (λex) de excitación de la molécula sea siempre menor (más energética) que la de emisión (λem). Las longitudes de onda que provocan estas transiciones son características de cada molécula fluorescente (fluoróforos) y según la probabilidad con la que ocurren, conforman el espectro de excitación y de emisión de la misma.

En 1948 Theodor Föster (Förster 1948) describió cómo dos fluoróforos eran capaces, cuando se encontraban suficientemente cerca (menos de 10 nm.), y siempre y cuando cumplieran ciertos criterios de compatibilidad, de transferir energía entre ellos provocando que dicha energía de excitación puediera ser transferida desde una molécula a otra lo suficientemente cercana.

Este principio ha servido de base para el desarrollo de la tecnología denominada FRET (*fluorescence resonance energy transfer*) o transferencia de energía de la fluorescencia por resonancia, proceso mediante el cual un fluoróforo excitado (donador) transfiere su energía a otra molécula fluorescente próxima con capacidad para absorberla (aceptor) (Figura 8).

Figura 8 Diagrama de transferencia de energía por FRET

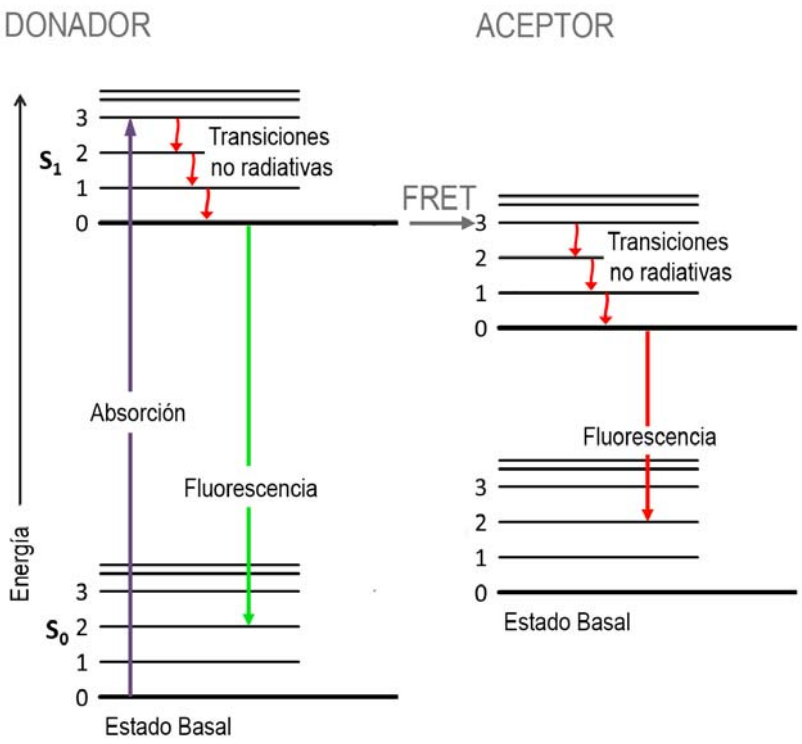

Para que se produzca el fenómeno FRET se requiere que se den una serie de circunstancias;

1. La más importante para su aplicación en el estudio de las interacciones, es que este fenómeno es dependiente de la proximidad de ambas moléculas, cuya distancia debe ser inferior a 10 nm. La relación entre la distancia y la eficiencia en la transferencia de energía, que mide la fracción de fotones absorbidos por el donador y que son transferidos al aceptor, viene determinada por la ecuación $E = \frac{1}{1+(r/R_0)^6}$ donde, E es la eficiencia de la transferencia de energía y R_0 la distancia en que dicha eficiencia es del 50%.

Como se puede observar, la eficiencia depende de forma extrema de la distancia r, por tanto pequeñas variaciones en la distancia afectan mucho a la medida de eficiencia, lo cual hace del FRET un método muy sensible en la medida de dichas distancias (Figura 9).

Figura 9 Requisitos para la transferencia de energía por FRET

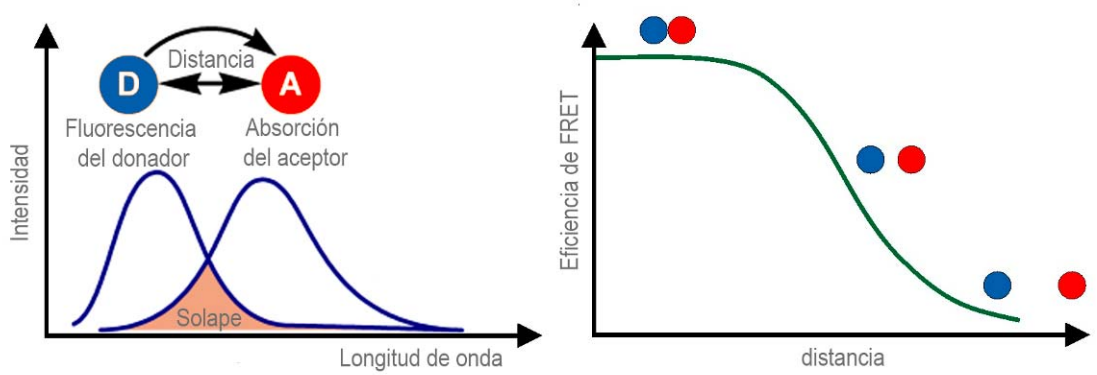

Dicho requerimiento para que se produzca FRET hace que esta técnica sea considerada única para analizar de forma cuantitativa las interacciones moleculares con resolución espacial y temporal (Förster 1948), (Jares-Erijman and Jovin 2006). El análisis del proceso FRET mediante la captura de imágenes de microscopía permite determinar la localización de las interacciones moleculares en el espacio (localización sub-celular o tisular) con resolución temporal, tanto para observar la formación como la interrupción de complejos moleculares (Wouters, Verveer et al. 2001), (Zhang, Campbell et al. 2002).

2. Otro requerimiento importante para que se produzca FRET se basa en la compatibilidad de las características espectrales de los fluorocromos utilizados. Esto es que las moléculas fluorescentes implicadas tengan espectros de excitación/emisión, esto es que el espectro de emisión de la molécula donadora debe solapar lo más posible con el de excitación del aceptor con el fin de que se produzca la transferencia de energía (Figura 9).

Los ensayos de FRET se basan por tanto generalmente en la presencia de dos especies fluorescentes; el donador y el aceptor. Cuando se excita el donador, en caso de que no haya transferencia de energía, este emitirá fluorescencia con su longitud de onda (λ) característica de emisión. Sin embargo, en presencia del aceptor, cuando ocurre el FRET, la energía emitida por el donador en estado excitado pasa a ser transferida al aceptor, el cual comienza a emitir con su λ característica. De esta manera, fruto de este proceso de FRET se producen varios cambios en los fluoróforos: la intensidad de la emisión de la fluorescencia

del donador disminuye, aparece una la emisión de la fluorescencia nueva correspondiente a las longitudes de onda características del espectro de emisión del aceptor, y la vida media del donador excitado se reduce.

La complejidad en el uso de esta tecnología genera con frecuencia artefactos y errores en la medida cuya corrección es crucial para su correcta interpretación. En esta Introducción hacemos un repaso de las herramientas existentes para el estudio de las interacciones moleculares por FRET. Finalmente como proyecto de Tesis Doctoral aportar un nuevo método de análisis y medida de este fenómeno. Así mismo se presentan ejemplos prácticos que demuestran que la tecnología desarrollada brinda a la comunidad científica nuevas herramientas para poder llevar a cabo ventajas significativas frente a otros métodos establecidos para el estudio de interacciones moleculares basados en microscopía óptica.

4. METODOS DE OBSERVACIÓN Y CUANTIFICACIÓN DEL FRET EN MICROSCOPÍA

Los diversos métodos existentes para medir el fenómeno de FRET se basan en la cuantificación de los cambios en la detección de la emisión de fluorescencia descritos en la sección anterior, y requieren diversos sistemas instrumentales; pudiendo utilizarse tanto microscopios de fluorescencia tradicionales como microscopios confocales por láser, o sistemas más costosos y altamente especializados, que son capaces de medir el tiempo en que la molécula se encuentra en estado excitado antes de emitir el fotón, o vida media de la fluorescencia (FLIM).

Entre los métodos de microscopía basados en la medida de las variaciones en intensidad de la fluorescencia se incluyen los siguientes:

4.1 Foto-blanqueado del aceptor

Es posiblemente, y debido a su simplicidad, el método más comúnmente usado para analizar el FRET en células fijadas.

En dicho método se realiza una primera captura de los marcajes de estudio y posteriormente se realiza un foto-blanqueado del aceptor mediante la irradiación

por láser con la longitud de onda especifica de excitación del aceptor de un área concreta de la célula donde se quiere interrogar si existe o no interacción. De producirse dicha interacción, la molécula donadora, ahora libre del aceptor previamente blanqueado, es capaz de recuperar su emisión original y por tanto de la diferencia entre la intensidad en las imágenes previas y posteriores al foto-blanqueado se puede inferir no solo si hay interacción o no sino también la si dicha interacción es más o menos estrecha (Figura 10)

Figura 10. Método de foto-blanqueado del aceptor

Mediante este método se puede demostrar no solo la interacción entre dos proteínas, sino también su localización sub-celular. Un buen ejemplo es el trabajo dedicado al estudio de la interacción entre Podoplanina y Ezrina (Martin-Villar, Megias et al. 2006), donde se llega incluso a identificar los residuos esenciales para la interacción de entre dichas proteínas.

El mayor inconveniente de este método es que es destructivo (dado que utiliza altas dosis de radiación para el blanqueado) y además requiere de una perfecta estabilidad entre la imagen previa y posterior al foto-blanqueado para su comparación. Por lo tanto no es una técnica aplicable a los estudios en células vivas. Además se han reportado efectos de foto-conversión de algunas moléculas fluorescentes, fruto del paso de irradiación, que podrían afectar a su medida (Kirber, Chen et al. 2007).

4.2 Emisión sensibilizada

Se utiliza habitualmente para estudiar el FRET intra-molecular sobre células vivas, ya sea en microscopios convencionales o en microscopios confocales.

En este método se capturan una serie de tres imágenes;1) La emisión dl donador excitado con su longitud de onda específica, 2) La emisión del aceptor excitada por la misma longitud de onda del donador, y 3) La emisión del aceptor excitada por su longitud de onda especifica. De esta forma, en la primera imagen obtenemos la intensidad del donador que viene disminuida por la interacción con el aceptor y en la tercera la imagen de aceptor sin estar alterado por el fenómeno del FRET, siendo en la segunda en la que podremos ver la emisión del aceptor sensibilizada por el donador, es decir proveniente de FRET. Por tanto.

En una situación ideal simplemente esa imagen nos daría idea de la eficiencia en la transferencia de energía, el problema radica en que esa imagen del aceptor está contaminada por dos aportes extras de señal. Por un lado la necesaria compatibilidad de espectros implica mucha cercanía entre la excitación del donador y la absorción del aceptor, lo cual genera que a la emisión del aceptor producida por la transferencia de energía haya que sumarle la producida por la excitación del donador. A esta contaminación se la denomina excitación cruzada.

A este problema, y derivado de la misma situación de cercanía de los espectros, hay que añadirle la proporción de señal del donador que puede llegar al canal de adquisición del aceptor, y que también debe sustraerse de la segunda imagen. Para realizar esas correcciones se emplean dos muestras separadas control en las que solo se marcan el donador o el aceptor por separado. En dichas muestras, y con la misma configuración de adquisición que se va a aplicar a la muestra problema, se miden los efectos de excitación cruzada, es decir la proporción de aceptor excitada por la longitud de onda del donador, y el cruce de emisión del donador sobre el área de detección del aceptor. Así se encuentran los índices de cruce de señal que deberán aplicarse sobre la adquisición de la muestra problema (Figura 11).

Figura 11 Método de emisión sensibilizada del aceptor

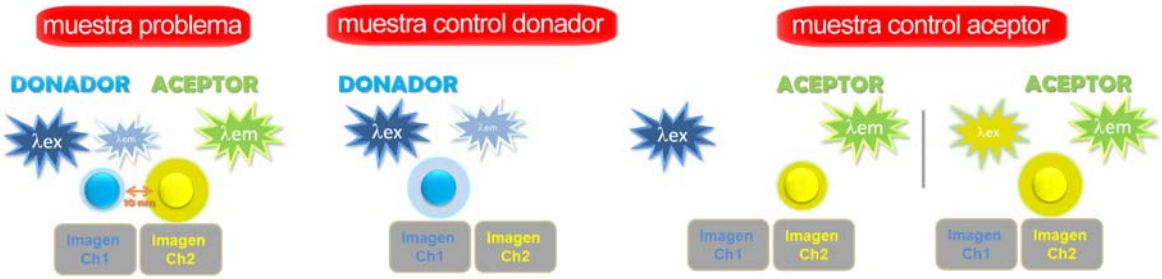

El cálculo de la eficiencia de la transferencia de energía se realiza aplicando la siguiente fórmula en cada píxel de la imagen, dando como resultado una imagen de eficiencia de FRET corregida.

$$E_A(i) = \frac{F^{DA}(i) - F^{D}(i)\cdot R_D - F^{A}(i)\cdot R_E}{F^{A}(i)}$$

Donde,

$E_A(i)$ =Eficiencia de FRET.

$F^{DA}(i)$=Emisión sensibilizada (FRET).

$F^{D}(i)$ =Emisión del donador con su excitación propia.

$F^{A}(i)$ = Emisión del aceptor con su excitación propia.

R_D = Ratio de intensidad de la emisión del donador en los canales de captura del aceptor y donador (índice del cruce de canal) en muestra control donador.

R_E = Ratio de intensidad de la emisión del aceptor al ser excitado por las longitudes de onda específicas de donador y de aceptor secuencialmente (índice de excitación cruzada) en muestra control aceptor.

Sin embargo, este método tiene también ciertas limitaciones intrínsecas; en concreto, la emisión sensibilizada sufre de una gran variabilidad en las medidas dada su fuerte dependencia de los controles externos a la muestra y a los cambios de expresión de las distintas proteínas que se producen a lo largo de la vida de la célula. Diversos autores han tratado de corregir estos cambios en la estequiometría entre donador y aceptor (Xia and Liu 2001), (van Rheenen, Langeslag et al. 2004), pero estas correcciones añaden complejidad al cálculo y no evitan un cierto grado de incertidumbre en la medida.

Una variante de este método es el **estudio ratiométrico** de las intensidades, en el cual simplemente se miden las variaciones de señal que se producen en una población doblemente marcada, excitada por la longitud de onda del donador. De esta manera se registran los cambios que se producen en la emisión del donador y del aceptor debidos a su interacción, esto es, cuando se produce la interacción el primero disminuirá la señal y el segundo la aumentará, y viceversa. Haciendo una división entre ambas imágenes obtendremos una nueva imagen resultante cuyos píxeles representan cuándo y dónde se produce dicha interacción. Este método obvia las contaminaciones de excitación cruzada y cruce de canal por considerarse porcentualmente fijas, de forma que solo es posible cuando la estequiometría de ambas moléculas es fija. El único ejemplo de esta situación sería el del empleo de biosensores (Aoki, Komatsu et al. 2011), (Kardash, Bandemer et al. 2011) basados en una misma secuencia de nucleótidos que codifican para ambos fluoróforos donador y aceptor dando lugar a una única molécula que incluye ambos fluoróforos, generalmente dichos fluoróforos están separados o bien incluyen en sus extremos secuencias específicas reactivas a los cambios de actividad en las células. Mediante el uso de biosensores e imagen ratiométrica se pueden estudiar por ejemplo eventos de proteólisis, ondas de calcio, cambios de fosforilación y niveles de glucosa (Zhang, Campbell et al. 2002) (Figura 12).

Figura 12. Tipos de biosensores

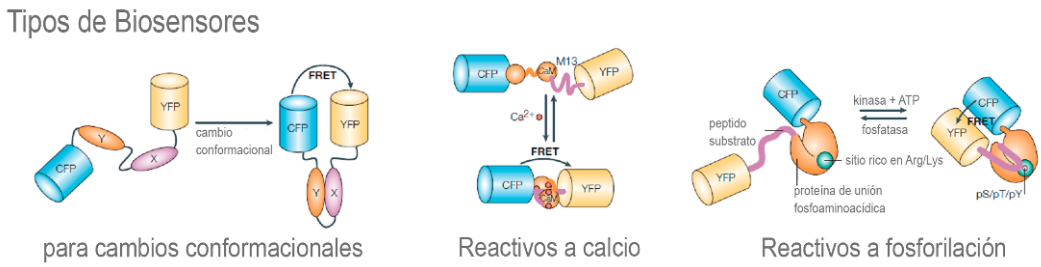

Adaptada de : J. Zhang, R. E. Campbell, A. Y. Ting, R. Y. Tsien, Nat. Rev. Mol. Cell Biol., 2002, 3, 906-918

4.3 Método por FLIM

El último método bien establecido para la observación del fenómeno de FRET implica la medida de la vida media del donador o **FLIM** (*fluorescence life-time imaging*), la cual disminuye cuando se produce la transferencia de energía.

Gracias al empleo de un láser pulsante y de una dotación de hardware específica que sincroniza el pulso de excitación con la detección de la fluorescencia, se puede calcular dicha vida media en una imagen y por tanto ver en que regiones es menor, proporcionando un registro de los puntos de interacción. Como ejemplo, este método ha sido utilizado para el estudio de la interacción entre la proteína Podoplanina y CD44 (Martin-Villar, Fernandez-Munoz et al.) y Sección de Apéndice. El mayor problema de este abordaje es la disponibilidad del equipamiento adecuado, así como la interpretación de los resultados, que puede requerir personal muy especializado debido a su elevada complejidad.

En base a todas estas dificultades, se puede decir que aún carecemos de un método definitivo en microscopía que utilice un procedimiento de corrección para el análisis cuantitativo de FRET que sea simple, robusto y aplicable a células vivas, utilizando sistemas convencionales de microscopía.

Estas son las razones por las que nos propusimos como objetivo de esta Tesis el desarrollar un método de análisis del FRET que solventara estos problemas y que fuera lo suficientemente sensible como para detectar las interacciones fisiológicas, con frecuencia débiles, que son típicas de los estudios de biología celular tanto en células vivas como fijadas.

4.4 Estudio de las interacciones moleculares por microscopia espectral.

En microscopía óptica la obtención del espectro de emisión de una muestra se produce gracias a la adquisición de imágenes de fluorescencia a diferentes longitudes de onda, el análisis posterior de todas esas imágenes será el que nos genere ese espectro.

Esta herramienta de adquisición espectral actualmente se encuentra implementada en la mayoría de los microscopios confocales por láser disponibles (Lerner and Zucker 2004), (Zimmermann, Rietdorf et al. 2003) y nos proporciona una capacidad única para analizar cambios de la intensidad de los fluoróforos, tales como los que ocurren en ensayos de FRET con el donador y el aceptor. En trabajos anteriores se han realizado diferentes acercamientos a la cuantificación del FRET por imagen espectral, basados en algoritmos de

separación de los fluoróforos. Estos métodos ((Zimmermann, Rietdorf et al. 2002) ,(Raicu, Jansma et al. 2005) ,(Chen, Mauldin et al. 2007),) usan el tiempo de vida media del fluoróforo (Raicu, Jansma et al. 2005) , (Neher and Neher 2004) o medidas del foto-blanqueado del aceptor en el procedimiento de calibración (Gu, Di et al. 2004), (Raicu, Jansma et al. 2005), (Zimmermann, Rietdorf et al. 2002) o se basan en las correcciones adicionales normalizadas de intensidad (Chen, Mauldin et al. 2007). También se han desarrollado otros interesantes métodos basados en la separación espectral con microscopía multifotón (Wallrabe and Periasamy 2005) o en sistemas de espectrofluorimetría (Thaler, Koushik et al. 2005), (Wlodarczyk, Woehler et al. 2008). Sin embargo, ningún método descrito hasta ahora puede medir FRET basándose solamente en la proyección de imagen espectral por microscopía confocal convencional.

En este trabajo de tesis, desarrollamos un nuevo método para el análisis del FRET basado enteramente en la adquisición espectral de la imagen por microscopía confocal por láser, al que denominamos como “lambda FRET” (λFRET) (Megias, Marrero et al. 2009) y a su vez evaluamos su funcionamiento por medio de muestras estándar de FRET, demostrando que este método resulta más sensible y reproducible que otros métodos más comunes como el foto-blanqueado del aceptor y la emisión sensibilizada.

5. ADQUISICIÓN AUTOMATIZADA DE IMAGEN

Uno de los mayores problemas en todos los ensayos basados en FRET descritos hasta la fecha radica en la limitada reproducibilidad y la alta dependencia de las condiciones de expresión o marcaje de los agentes fluorescentes. Todo ello hace que estos experimentos sean complejos y laboriosos, a la vez que costosos, y su fiabilidad depende en gran medida de la disponibilidad de repetidas capturas del mismo par de FRET bajo estudio, lo cual puede no ser siempre fácil cuando se trata de eventos poco frecuentes en la muestra analizada. Una posible solución a este problema es la adquisición automatizada de las muestras marcadas.

Para hacer este tipo de captura hay dos posibles abordajes. Por un lado estaría la adquisición de forma aleatoria de las mismas, o *screening* convencional. Este

tipo de captura se realiza de forma que no existe ninguna preselección de las áreas de adquisición, dándonos como resultado una ingente cantidad de imágenes que posteriormente deben ser analizadas y cuantificadas. Esta forma de adquisición es muy adecuada cuando las muestras resultan homogéneas en composición, o cuando la región de interés es abundante en la misma. Su mayor inconveniente estriba en ser muy poco eficiente, ya que requiere que por azar se adquieran las células adecuadas para el ensayo, con un posterior filtrado de todas aquellas que no sean válidas para el mismo. Este proceso es lento, y en caso de que las células adecuadas sean escasas en la muestra, no suele ser eficiente.

5.1 Adquisición automatizada dirigida por análisis de imagen

La alternativa a la adquisición automatizada de imágenes (*screening*) convencional que desarrollamos como parte del trabajo de la presente tesis se basa en la generación una herramienta de adquisición automatizada dirigida de forma inteligente mediante análisis de imagen, la cual nos permite la captura de forma selectiva exclusivamente de las regiones de interés, con el fin de alcanzar un mayor rendimiento de los equipos de microscopía y un ahorro considerable de tiempo, y esfuerzo evitando la necesidad de contar con una estructura tan compleja en cuanto a almacenamiento y procesado posterior de las imágenes que se requeriría en modo convencional de adquisición automatizada. En ese sentido se han desarrollado otras soluciones plataformas de adquisición automatizada dirigida o "*Screening inteligente"* que permiten lanzar capturas complejas de forma automática sobre regiones de interés de la muestra. (Conrad, Wunsche et al. 2011), (de Chaumont, Dallongeville et al. 2012), (Henriksson, Hench et al. 2013) En este tipo de captura la elección de las regiones de adquisición dentro de una muestra queda en manos de un proceso de automático de análisis de imagen, y se resume en tres pasos (Figura 13):

1. Se realiza una captura rápida de la muestra en la que se obtienen imágenes con la información mínima requerida para la identificación de las regiones o células de interés.

2. Estas imágenes son automáticamente analizadas mediante un software específico, identificando las regiones candidatas para su adquisición a mayor resolución.

3. De forma completamente automática el microscopio se reconfigura en todos los parámetros necesarios para una adquisición compleja de imágenes, y recorre todas las regiones o células localizadas en el segundo paso.

Figura 13 Proceso de adquisición automatizada inteligente de imágenes

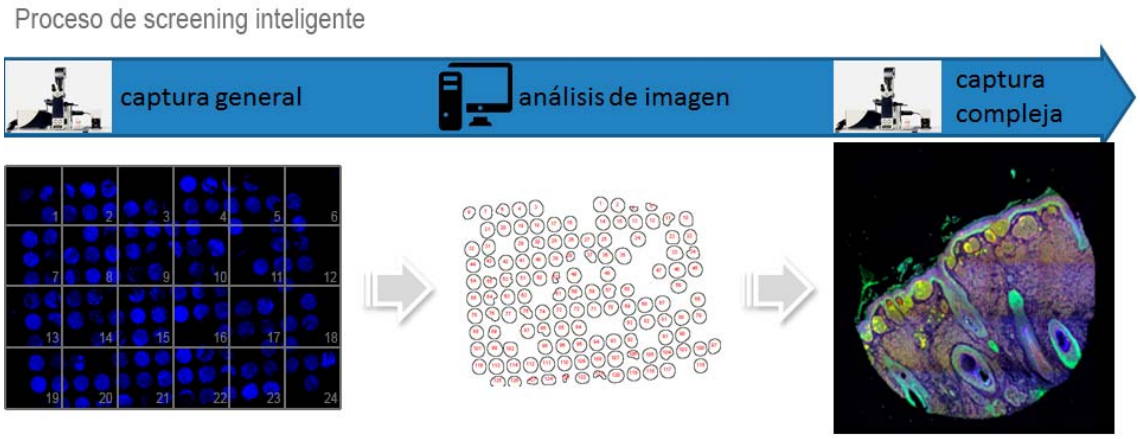

En concreto, este tipo de abordaje podrá ayudar en el ensayo de FRET a realizar de forma automatizada el número de medidas necesarias para lograr una cuantificación robusta, y solo adquirirá imágenes de las células que reúnan la relación adecuada en la expresión de los marcadores y con una morfología o fenotipo adecuada, con el consiguiente ahorro en tiempo y recursos, posibilitando ensayos en microscopía que antes eran imposibles debido a su elevada complejidad.

III. OBJETIVOS

El Objetivo de esta Tesis Doctoral es el de desarrollar nuevas herramientas en microscopía óptica de interés para la comunidad científica que permitan optimizar la realización de experimentos que implican la detección de interacciones entre macromoléculas y su co-localización en la célula. Con este propósito, se plantean los siguientes objetivos específicos:

1. Desarrollar una nueva metodología para analizar las interacciones moleculares cuantificando la transferencia de energía por resonancia (FRET) de una forma más robusta e informativa, basada en la medida de la fluorescencia a lo largo de todo el espectro de emisión de la muestra. Dicho método deberá ser de aplicación tanto en células fijadas como en células vivas, y con una menor dependencia de la estequiometría entre las moléculas donadora y aceptora que otros métodos convencionales.

2. Validación del método utilizando ejemplos de interacción real. El nuevo método debe ser sensible a diferentes distancias de interacción, aportando ventajas en cuanto a los métodos establecidos. Se incluirá el desarrollo de construcciones genéticas caracterizadas para distintas eficiencias de transferencia de energía que permitirán la comparación entre diferentes métodos de medida, adicionalmente se presentarán ejemplos prácticos de uso de otras aproximaciones al estudio de FRET para su comparación.

3. Con el fin de poder automatizar procesos complejos de captura como son los requeridos para los ensayos de FRET, pero con aplicación en otras áreas de estudio, se investigará el desarrollo de nuevas plataformas de adquisición automatizada de imagen basadas en el concepto del "*Screening inteligente*". Este nuevo entorno de trabajo deberá ser fácil en uso e instalación y compatible con microscopía de fluorescencia y confocal, y ser de utilidad tanto para muestras en tejido como para cultivos celulares como para muestras fijadas y vivas. Se aportarán ejemplos prácticos que demuestren la utilidad de esta nueva herramienta.

IV. MATERIALES, MÉTODOS Y RESULTADOS

4.1 SORTING NEXIN 6 INTERACTS WITH BREAST CANCER METASTASIS SUPPRESSOR-1 AND PROMOTES TRANSCRIPTIONAL REPRESSION

José Rivera, Diego Megías, Jerónimo Bravo

Este es un ejemplo de un trabajo en el que se muestra cómo se pueden combinar distintos métodos de análisis para el estudio de la interacción entre proteínas, en este caso *Sorting Nexin 6* (SNX6) y *Breast Cancer Metastasis Supressor 1* (BRMS). Por un lado se han utilizado métodos indirectos *in vitro,* mediante ensayos de doble híbrido en levaduras, estos estudios han sido validados y localizados en células tumorales utilizando métodos directos de estudio de interacción basados en FRET en concreto empleando la técnica de foto-blanqueado del aceptor.

De esta forma se reporta en este trabajo una interacción, previamente desconocida, entre dichas proteínas así como su ubicación en núcleo y citoplasma, y cómo determinados dominios de SNX6 no son fundamentales para la interacción en el citosol. Adicionalmente, se estudiaron los dominios mínimos de la proteína BRMS necesarios para su interacción con SNX6, y cómo la sobre-expresión de SNX6 es capaz de disminuir de forma dosis-dependiente la activación de la transcripción, en la que BRMS juega un papel clave. Estos hallazgos proponen un posible papel de la interacción entre SNX6 y BRMS en la interferencia de la actividad en el núcleo de esta última.

En este trabajo he participado de forma activa en la planificación y diseño de los experimentos que requerían el uso del microscopio óptico, en concreto los ensayos de co-localización y FRET por foto-blanqueado del aceptor, incluyendo la adquisición, análisis de imagen, cuantificación, interpretación y presentación de los datos.

ARTICLE
Journal of Cellular Biochemistry 111:1464–1472 (2010)

Journal of Cellular Biochemistry

Sorting Nexin 6 Interacts With Breast Cancer Metastasis Suppressor-1 and Promotes Transcriptional Repression

José Rivera,[1*] Diego Megías,[2] and Jerónimo Bravo[3*]

[1] *Centro Nacional de Investigaciones Cardiovasculares Carlos III, C/Melchor Fernández Almagro 3, E-28029 Madrid, Spain*

[2] *Confocal Microscopy Unit, Centro Nacional de Investigaciones Oncológicas, C/Melchor Fernández Almagro 3, E-28029 Madrid, Spain*

[3] *Instituto de Biomedicina de Valencia (IBV-CSIC), Jaime Roig 11, 46010 Valencia, Spain*

ABSTRACT

Sorting nexin 6 (SNX6), a predominantly cytoplasmic protein involved in intracellular trafficking of membrane receptors, was identified as a TGF-β family interactor. However, apart from being a component of the Retromer, little is known about SNX6 cellular functions. Pim-1-dependent SNX6 nuclear translocation has been reported suggesting a putative nuclear role for SNX6. Here, we describe a previously non-reported association of SNX6 with breast cancer metastasis suppressor 1 (BRMS1) protein detected by a yeast two-hybrid screening. The interaction can be reconstituted in vitro and further FRET analysis confirmed the novel interaction. Additionally, we identified their coiled-coil domains as the minimal binding motives required for interaction. Since BRMS1 has been shown to repress transcription, we sought the ability of SNX6 to interfere with this nuclear activity. Using a standard gene reporter assay, we observed that SNX6 increases BRMS1-dependent transcriptional repression. Moreover, over-expression of SNX6 was capable of diminishing trans-activation in a dose-dependent manner. J. Cell. Biochem. 111: 1464–1472, 2010.

KEY WORDS: PROTEIN–PROTEIN INTERACTION; YEAST TWO-HYBRID ASSAY; BINDING DOMAIN; FRET; BRMS1; SNX6

Sorting nexins (SNXs) are a family of cytoplasmic proteins involved in intracellular trafficking of membrane receptors and characterized by the presence of a Phox-homology domain (PX) which binds phosphoinositides [Worby and Dixon, 2002] and several proteins [Ishibashi et al., 2001; Parks et al., 2001; Vollert and Uetz, 2004] upstream of a coiled-coil domain [Parks et al., 2001]. Later, the adjacent C-terminal region of PX was defined as a BAR (Bin/Amphiphysin/Rvs) domain [Habermann, 2004]. SNX6 which was identified as an interactor of the TGF-β family of receptor serine–threonine kinases [Parks et al., 2001], is part of the Retromer complex mediating retrograde transport of trans-membrane cargo from endosomes to the trans-Golgi. Moreover, over-expression of SNX6 interferes TGF-β signaling [Parks et al., 2001], a receptor largely involved in metastasis.

Interaction with Pim-1 oncogene phosphorylates SNX6 leading to its nuclear translocation [Ishibashi et al., 2001]. However, the precise functions of SNX6 within the nuclear compartment have not been reported.

Breast cancer metastasis suppressor 1 (BRMS1), a member of a growing metastasis suppressors family, significantly reduce breast [Seraj et al., 2000] and melanoma [Shevde et al., 2002] metastasis without affecting primary tumor growth. Mechanism of action includes restoration of cell–cell communication [Saunders et al., 2001], phosphoinositides signaling reduction [DeWald et al., 2005], and gene repression [Meehan et al., 2004; Cicek et al., 2005; Rivera et al., 2007b; Yang et al., 2008].

In a search for proteins binding to BRMS1, we identify SNX6, as a novel BRMS1 binding partner. GST pull-down experiments and

Additional supporting information may be found in the online version of this article.

Grant sponsor: MCyT; Grant number: SAF2006-10269; Grant sponsor: MICINN; Grant number: SAF2008-04048-E SAF2009-10667; Grant sponsor: CSIC; Grant number: 200820I020; Grant sponsor: Fundación-Mutua-Madrileña; Grant sponsor: Conselleria de Sanitat, Generalitat valenciana; Grant number: AP-001/10.

*Correspondence to: Dr. José Rivera, Centro Nacional de Investigaciones Cardiovasculares Carlos III, C/Melchor Fernández Almagro 3, E-28029 Madrid, Spain. E-mail: jrivera@cnic.es

*Correspondence to: Jerónimo Bravo, Instituto de Biomedicina de Valencia (IBV-CSIC), Jaime Roig 11, 46010 Valencia, Spain. E-mail: jbravo@ibv.csic.es

Received 22 April 2010; Accepted 30 August 2010 • DOI 10.1002/jcb.22874 • © 2010 Wiley-Liss, Inc.

Published online 9 September 2010 in Wiley Online Library (wileyonlinelibrary.com).

fluorescence resonance energy transfer (FRET) analysis validated this interaction both in vitro and in vivo. We studied the interaction in more detail and found that the minimal segment of SNX6 sufficient for BRMS1 binding consists of amino acids 300–406, a segment predicted to form a coiled-coil. BRMS1 sequence contains two predicted coiled-coil (CC) motifs and we show that exclusively the N-terminal CC1, recently crystallized [Spinola-Amilibia et al., 2008], is implicated in the interaction. In addition, our data suggest that combined over-expression of the newly detected interactors further enhances transcriptional repression in a luciferase reporter assay. Furthermore, the interaction could indicate a potential mechanism by which BRMS1 might regulate intracellular membrane receptor trafficking of TGF-β receptor family members and thus affecting TGF-β signaling pathway which has largely been involved in metastasis.

MATERIALS AND METHODS

CELL CULTURE AND TRANSIENT TRANSFECTION EXPERIMENTS

HeLa, U2OS, T47D, and HEK293T cells were cultured in DMEM containing 10% foetal bovine serum, 2 mM glutamine and 1% penicillin/streptomycin. Melanoma cells were maintained as described [Rivera et al., 2007b]. Transfections were performed using Lipofectamine2000 (Invitrogen) following manufacturer's instructions.

PLASMIDS

Human BRMS1 cDNA [Rivera et al., 2007b] was used as a template for PCR and inserted into pAS2.1 (Clontech) to generate pAS2.1-BRMS1 bait vector. Deletion mutants were also created containing: the first putative BRMS1 coiled-coil domain (pAS2.1/CC1; residues 1–88); a BRMS1-CC1 deletion mutant (pAS2.1/ΔCC1; 89–246); a construct lacking both putative CCs domains (pAS2.1/ΔCCs; 181–246); and a construct spanning both CCs (pAS2.1/CCs; residues 1–180). Subcloning into pET-28 (Novagen), pCMV-HA, and pEYFP-N1 (Clontech) create pET28-BRMS1, pCMV-HA-BRMS1, and pEYFP-N1-BRMS1 vectors. Entire SNX6 sequence was cloned into pGEX-6-P2 (GE-Healthcare), pECFP-N1, pACT2, and pCMV-Tag2 (Stratagene) rendering pGEX-6-P2/SNX6, pECFP-N1-SNX6, pACT2/SNX6, and pCMV-Tag2-SNX6 plasmids. Deletion mutants of SNX6 for yeast system were also created: pACT2/PX (residues 1–180); pACT2/BAR (300–406); and pACT2/CC (181–406). Detailed information of specific primers and restriction sites are available upon request.

YEAST TWO-HYBRID

A human mammary gland cDNA-library (Clontech) was screened with pAS2.1-BRMS1 vector as described [Rivera et al., 2007a]. For sub-mapping interactions, constructs encoding distinct portions of SNX6 and BRMS1 were cloned into pACT2 and pAS2.1 vectors, respectively. Sequential transformations by lithium acetate into AH109 yeast strain [James et al., 1996] produced moderate–fast growing colonies on high-stringency selection media lacking adenine, tryptophan, leucine, and histidine after 5–7 days according to the Matchmaker protocol (Clontech). Grown colonies were subjected to a colony-lift filter assay for β-galactosidase activity. Inserts were identified by DNA sequencing. Chemicals were from Sigma–Aldrich (St. Louis, MO) unless specified.

GLUTATHIONE *S*-TRANSFERASE PULL-DOWN

GST, GST-SNX6, and 6xHis-BRMS1 proteins were expressed in *Escherichia coli* BL21 (DE3) cells and proteins were expressed as described [Rivera et al., 2007a]. Purifications of GST or GST-SNX6 were performed using Glutathione Sepharose4B (GE-Healthcare) beads according to the manufacturer's protocols. Equal amounts of GST-fusion proteins, assessed by Coomasie blue staining, were incubated with bacterial lysate containing over-expressed His6-BRMS1 protein in 50 mM HEPES, pH 7.5, 50 mM NaCl, 0.1% NP-40 with proteases inhibitors (Roche) binding buffer. After overnight incubation at 4°C glutathione sepharose beads were collected by centrifugation and extensively washed with binding buffer. Proteins were eluted in 2× SDS buffer fractionated onto 12% SDS–PAGE and then subjected to Western blot analysis. Nitrocellulose membranes were probed with anti-6xHis antibody (Clontech), before ECL detection (GE-Healthcare).

CONFOCAL MICROSCOPY AND FLUORESCENCE RESONANCE ENERGY TRANSFER (FRET) ANALYSIS

Cells grown on glass cover-slips were transfected for 48 h, then fixed for 15 min with 4% paraformaldehyde, permeabilized with 0.5% Triton X-100 for 30 min and blocked in TNB buffer (100 mM Tris–HCl; 150 mM NaCl, and 0.5% Blocking reagent (Boehringer)) for 1 h at room temperature. Next, cover-slips were sequentially incubated with α-HA (BAbCO; HA.11) and α-SNX6 (Santa Cruz; K-18) antibodies before incubation with secondary antibodies Alexa-Fluor488 and Cy3-coupled, respectively (Jackson Laboratories, West Grove, PA). Images were collected on a Leica-TCS-SP5 laser scanning confocal microscope equipped with a HCX PL APO 63x immersion oil objective (1.4NA). SNX6-ECFP and BRMS1-YFP co-transfected cells were examined for FRET efficiency ($FRET_{eff}$) [Sekar and Periasamy, 2003] by acceptor photobleaching method [Gu et al., 2004]. Energy transfer was detected as an increase in donor fluorescence (ECFP) after photobleaching of the acceptor molecules (EYFP). Images were background-corrected and $FRET_{eff}$ calculated as: $FRET_{eff} = (D_{post} - D_{pre})/D_{post}$; for all $D_{post} > D_{pre}$, where D_{pre} and D_{post} are donor intensities before and after photobleaching, respectively. Polyclonal anti-HDAC2 antibody was from Abcam (ab7029).

LUCIFERASE REPORTER ASSAY

Trans-activation activity assays were performed similarly to previous reports [Meehan et al., 2004; Hurst et al., 2008]. Briefly, HEK293 and T47D cells were plated in 24-well plates and allowed to attach. After 24 h cells were co-transfected, using Lipofectamine2000 in Opti-MEM medium, with various combinations of the following plasmids: pCMV-HA/BRMS1 (200 ng), pCMV-Tag2/SNX6 (100; 200 or 250 ng) and pGL-G5 luciferase reporter plasmid, containing five GAL4 binding sites upstream to the E1B promoter driving the expression of Firefly luciferase [Zurcher et al., 1996]. Assays were conducted in triplicate wells and total DNA amounts were uniformly adjusted with pcDNA3 vector to 0.5 μg/well. After transfection of 48 h, cells were lysed, and 20 μl of cell lysate were

used to measure trans-activation activity, using the Dual-Luciferase Reporter system (Promega), in a Glomax luminometer. To allow the normalization of Firefly luciferase readings based on transfection efficiencies, a co-reporter vector expressing Renilla luciferase (pRLSV40) was used as a transfection control at a ratio of 1:20 in the transfection mixture. Relative luciferase activities were calculated as the light units relative to the reporter plasmid controls and plotted. Data are expressed as percent luciferase activity relative to empty plasmid transfectants set as 100%.

RESULTS

IDENTIFICATION OF SNX6 AS A BRMS1-INTERACTING PROTEIN SECTION

Identification of new partners can provide useful information about protein functions. A human mammary gland cDNA library was screened by a yeast two-hybrid screen using a bait plasmid encompassing the entire human BRMS1-coding sequence that did not show trans-activation activity by itself upon over-expression and served as a negative control (Table I). The protein, which is 246 amino acids long, includes two predicted coiled-coil regions, which could account for protein–protein interactions (CC1 and CC2), and recently characterized localization signals, for nuclear export (NES) and nuclear localization (NLS1 and NLS2) (Fig. 1A) [Rivera et al., 2009].

Screening more than 10^6 yeast transformant colonies for activation of both the *His* and *LacZ* reporter genes yielded several positive clones that grew up on highly selective medium. Two independent clones expressed higher levels of β-galactosidase (β-gal) upon a lift-colony filter assay (Fig. 1B) compared to the remaining clones. After isolation and further plasmid purification of the selected clones, both inserts were different in size, but subsequent sequence analysis revealed that both encoded for human tumor necrosis factor receptor-associated factor 4 (TRAF4)-associated factor 2, also known as sorting nexin 6 (SNX6) [Parks et al., 2001]. One of them encoded the full-length mRNA and was therefore used in subsequent cloning experiments.

SNX6 is composed of a BAR domain at the carboxy-terminal end [Habermann, 2004] and a Phox-homology (PX) domain at its N-terminal end (Fig. 1A). Interestingly, the second one of the two identified clones encoded for a shorter form lacking the 180 N-terminal residues spanning the PX domain. This domain binds phosphoinositides and has been described also as a protein–protein interaction domain [Ishibashi et al., 2001; Parks et al., 2001; Vollert and Uetz, 2004]. Thus, our finding suggests that the PX domain of SNX6 is not involved in BRMS1–SNX6 interaction.

BRMS1 INTERACTS WITH SNX6 IN VITRO AND CO-LOCALIZE IN HUMAN CELLS

In order to validate the significance of this interaction and determine whether the interaction between SNX6 and BRMS1 was direct or involved additional (yeast) proteins, we tested binding in an in vitro assay system. Given that commercial antibodies against BRMS1 showed non-reproducible results in our hands for co-immunoprecipating endogenous proteins, we decided to perform more robust approaches over-expressing in a prokaryotic system both interacting proteins, as glutathione-*S*-transferase (GST) or histidine-tagged fusion proteins, respectively, in a prokaryotic system. GST pull-down experiments using GST/SNX6 fusion protein was mixed with over-expressed 6xHis/BRMS1 full-length protein. The GST-SNX6 fusion protein was purified from the mixture using Glutathione Sepharose4B beads and the pulled down proteins were tested for co-precipitation of the BRMS1 protein by Western blotting using an antibody raise against 6xhistidine-tag. As shown in Figure 1C (lane

TABLE I. Minimal Binding Domain Involved in the Interaction of SNX6 With BRMS1

	Gal4-AD (SNX6)	Gal4-BD (BRMS1)	SD/-T/-L/-H	β-Galactosidase assay
Control −ve	pACT2	FL	−	−
Control +ve	Ref 14	Ref 14	+ (+)	+++
	FL (1–406)	FL (1–246)	+ (+)	++
		CC1 (1–88)	+ (+)	+++
		ΔCC1 (89–246)	− (+)	−
		ΔCCs (181–246)	− (+)	−
		CCs (1–180)	+ (+)	+++
	CC (300–406)	FL (1–246)	+ (+)	+
		CC1 (1–88)	+ (+)	++
		ΔCC1 (89–246)	− (+)	−
		ΔCCs (181–246)	− (+)	−
		CCs (1–180)	+ (+)	++
	BAR (181–406)	FL (1–246)	+ (+)	+
		CC1 (1–88)	+ (+)	++
		ΔCC1 (89–246)	− (+)	−
		ΔCCs (181–246)	− (+)	−
		CCs (1–180)	+ (+)	++
	PX (1–180)	FL (1–246)	− (+)	−
		CC1 (1–88)	− (+)	−
		ΔCC1 (89–246)	− (+)	−
		ΔCCs (181–246)	− (+)	−
		CCs (1–180)	− (+)	−

Different domains of BRMS1 were fused to the Gal4-DNA-binding domain (Gal4-BD). SNX6 fragments were fused to the Gal4 transcription activation domain (Gal4-AD). Protein–protein interaction results in activation of reporter genes allowing yeast cells to grow in synthetic drop-out medium lacking, tryptophan, leucine, and histidine (SD/-T/-L/-H). The AH109 yeast cell co-transformed with: pACT2 empty vector and BRMS1; and a pair of interacting proteins previously reported [Rivera et al., 2007a] served as negative and positive controls, respectively. β-Galactosidase activity was evaluated by lift-colony filter assay. Growth of co-transformed yeast cells onto SD/-T/-L is shown in brackets. Numbers shown in brackets within the constructs columns represent the spanning residues according to the full-length protein as shown in Figure 3A,B. Intensity of the blue color is a measure for the interaction strength that was defined as: +++ strong, ++ moderate, + weak, and − not detectable.

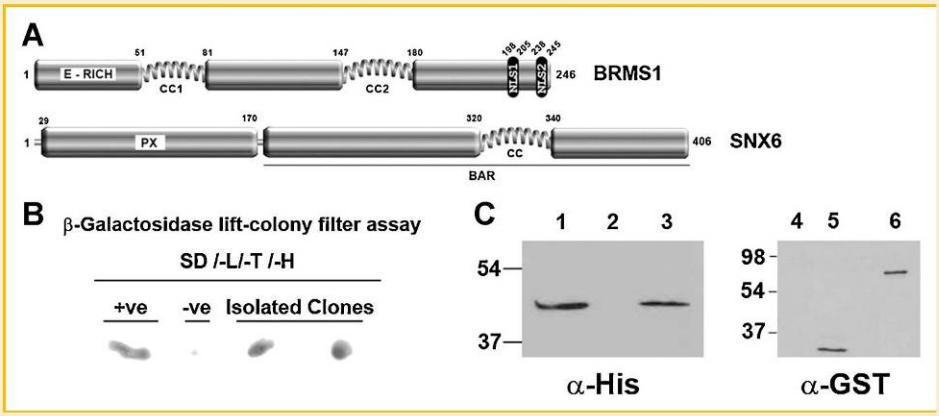

Fig. 1. In vitro association between SNX6 and BRMS1. A: Schematic representation of BRMS1 and SNX6 structures displaying boundaries of different domains: CC; coiled-coil, PX; Phox-homology. B: β-Galactosidase activity of grown co-transformant yeast colonies encoding SNX6 (isolated clones) after two-hybrid assay using BRMS1 bait vector to screen a human breast cDNA library. Positive (+ve) and negative (−ve) controls are also shown as described in the main text. C: GST or GST-SNX6 proteins were mixed with bacterial cell lysates containing 6xHis-tagged BRMS1 (see Materials and Methods Section) and pulled-down with Glutathione Sepharose4B beads. Co-immunoprecipitated proteins were eluted with 2× Laemli buffer, analyzed on 12% SDS-PAGE gels and blotted with specific antibodies raised against 6xHis (lanes 1–3) or GST (lanes 4–6) antibodies. BRMS1 was elicited as a pulled-down protein complex with a GST-SNX6 beads (lanes 3 and 6) but not in the control assays using GST alone (lanes 2 and 5). 6xHis-BRMS1 (lanes 1 and 4) containing samples were shown using α-His antibody but not detected with α-GST antibody. Protein markers are shown in kDa.

3), the full-length BRMS1-His tagged protein bound to GST-SNX6 in vitro. A single protein band was specifically recovered in the GST/SNX6 eluate (Fig. 1C, lane 3). This protein, running slower than the expected molecular mass (32.3 kDa), reacted with the anti-6xHis antibody on Western blots. Thus, we found that BRMS1 was specifically eluted from the sepharose beads containing GST/SNX6. GST protein used as a control in the assay instead of GST-SNX6, showed no co-precipitation of BRMS1 protein (Fig. 1C, lane 2), indicating that the observed binding is specific for SNX6. The presence of GST and GST/SNX6 was specifically confirmed in the same assay using anti-GST antibody (Fig. 1C, lanes 5 and 6). Thus, we conclude that SNX6 and BRMS1 bind each other in vitro and interact in vivo in a yeast assay.

The reported subcellular localization of SNX6 is mainly cytoplasmic [Parks et al., 2001; Worby and Dixon, 2002] although nuclear localization has also been shown [Ishibashi et al., 2001]. However, BRMS1 is mostly nuclear although it has also been detected in the cytosol [Rivera et al., 2007b; Stafford et al., 2008]. We reasoned that SNX6 and BRMS1 have to exhibit at least partial co-localization if their interaction is physiologically relevant. Therefore, we performed a co-localization analysis. Since we could not reliably detect endogenous BRMS1 protein by commercially available antibodies, we assessed the subcellular localization of HA-tagged BRMS1 transiently over-expressed in human cells followed by indirect immunofluorescence detection. We observed a predominantly nuclear localization pattern of the recombinant BRMS1 proteins upon transient transfection (Fig. 2A,B), in agreement with previous reports [Ishibashi et al., 2001; Worby and Dixon, 2002; Rivera et al., 2007b; Stafford et al., 2008]. As observed in transfection experiments, endogenous (Fig. 2A) and over-expressed SNX6 (Fig. 2B) partly co-localized with differently tagged BRMS1. This co-localization was detected more intensively in the nuclei (Fig. 2A cytofluorogram) of different human cell types (Fig. 2A,B and Supplementary Figs. S1 and S2).

DIRECT SNX6–BRMS1 PROTEINS INTERACTION DETECTED BY FRET

To complement co-localization studies and further examine the SNX6–BRMS1 interaction, we performed a FRET analysis. To achieve this goal, full-length BRSM1 and SNX6 proteins were tagged to the N-terminus of enhanced versions of yellow (EYFP) and cyan (ECFP) fluorescence proteins, respectively. Both constructs were co-transfected into human cells and FRET efficiency ($FRET_{eff}$) was measured by acceptor photobleaching method as previously reported [Gu et al., 2004]. This method calculates $FRET_{eff}$ as increments in the emission of the ECFP donor after photobleaching of the EYFP acceptor, which take place exclusively once both fluorophores are in close vicinity within a distance of a few nanometers and it is indicative of protein–protein interaction. Several plasmid pair-wise combinations were co-transfected into mammalian cells as negative controls, including among others co-transfection of pEYFP-N1-BRMS1 or pECFP-N1-SNX6 with a construct encoding for the full length of an unrelated molecule (pECFP-N1-p27 [Fuster et al., 2010] and pEYFP-N1-NMI [Rivera et al., unpublished data], respectively) as shown in Supplementary Figure S1. After photobleaching of randomly selected areas with the YFP-light, the ECFP channel increased considerably both in the nucleus and cytoplasm of co-transfected cells (Fig. 2B,C) while no increase was observed in cells co-transfected with the described unrelated molecules, even though some of them (p27-ECFP and BRMS1-EYFP) showed a perfect co-localization into the nuclear compartment (Supplementary Fig. S1). Moreover, the $FRET_{eff}$ values, measured and averaged from at least 10 cells along different experiments, consistently demonstrated, a higher $FRET_{eff}$ values within the nuclear compartment ($44 \pm 11.5\%$) compare to those observed for the cytosol ($27.5 \pm 7.5\%$). Interestingly, these differences showed statistical significance ($P < 0.05$), although we do not know the biological significance yet (Fig. 2C).

$FRET_{eff}$ was also measured by the alternative acceptor sensitized emission method (see Supplementary Materials and Methods). As

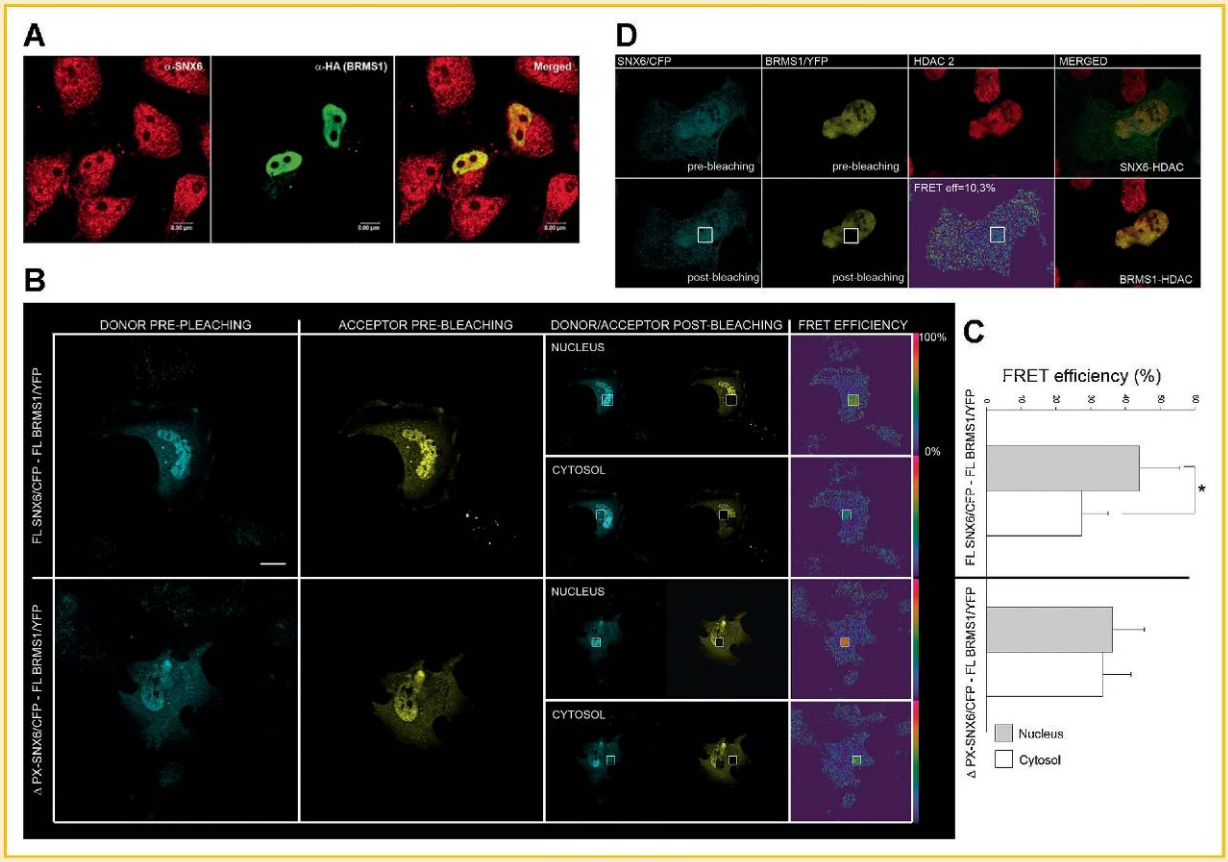

Fig. 2. Co-localization and FRET detection of SNX6–BRMS1 interaction. A: Partial co-localization of SNX6 and BRMS1. HeLa cells were stained using α-HA (green color, middle panel) and anti-SNX6 (red color, left panel). Right panel shows co-localization represented by a merge of adjacent spots populations overlapping red and green signals. Staining was analyzed by confocal microscopy and images show scanning of a single plane. B: Representative images of donor (ECFP) and acceptor (EYFP) fluorescence intensity before and after EYFP photobleaching. Images of co-transfected cells with full-length BRMS1 acceptor molecule and full-length SNX6 (top panels) or a PX-deletion mutants (bottom panels) donor molecule are shown. Scale bar, 20 μm. $FRET_{eff}$ (%) measured in randomly selected areas (white boxes) is shown at the right-hand panel as pseudo-colored images relatives to amplitude of $FRET_{eff}$ as shown in the scale bar. C: Averaged $FRET_{eff}$ (%) measured both in nuclei and cytosol of fixed melanoma cells ($n \geq 20$ cells for each experiment) as the increase of acceptor molecules following acceptor (BRMS1-EYFP) photobleaching. Note the significant reduction ($^{*}P < 0.05$) of $FRET_{eff}$ in cytosol compare to the nucleus in full-length transfected proteins. Error bars represent mean ± SEM from four different independent experiments carried out in duplicates. D: Representative images of co-transfected cells as described for subpanel (B), where endogenous HDAC-2 was detected by a polyclonal antibody. Pair-wise combinations of merged images are shown in the right-hand panel as stated.

shown in Supplementary Figure S2, cells co-transfected with constructs encoding ECFP-SNX6 and EYFP-BRMS1 fusion proteins confirmed the acceptor photobleaching $FRET_{eff}$ values reported above. Negative controls were also run in parallel (Supplementary Fig. S2).

Thus, FRET analysis confirms that interaction occurs, providing strong evidence for the association of SNX6 with BRMS1 in both cytoplasmic and nuclear compartments and thus corroborating the results of in vivo yeast two-hybrid, pull-down assays, and co-localization studies. Our findings suggest that SNX6 may play a role in the nucleus. Similarly, cytosolic presence of BRMS1 does not seem to be an artifact and might play a functional role in that compartment.

The PX motif was previously described as a binding site for diverse protein partners [Ishibashi et al., 2001; Xu et al., 2001; Worby and Dixon, 2002]. Since this motif is absent in one of the two fished out clones upon yeast screen, we hypothesized that this motif is not essential for the interaction. To test this hypothesis, we engineered and over-expressed a deletion mutant of SNX6 where the PX domain was not present (ECFP/ΔPX-SNX6). $FRET_{eff}$, measured by acceptor photobleaching, within the nucleus and cytoplasm showed values of 36.5 ± 7.5% and 33.6 ± 8%, respectively (Fig. 2C), which were indeed similar to those obtained upon co-transfection of full-length proteins, confirming that PX domain from SNX6 is dispensable for its interaction with BRMS1.

IDENTIFICATION OF MINIMAL DOMAINS INVOLVED IN BRMS1–SNX6 INTERACTION

In order to further map the regions of SNX6 and BRMS1 proteins that are relevant for its interaction, we created a series of truncated constructs (Fig. 3A,B) and perform yeast two-hybrid experiments. Engineered SNX6 constructs-domains were back-transformed into yeast together with the various BRMS1 constructs. After assessing self-activation inability for all the designed constructs (data not shown), all possible pair-wise combinations were tested for positive interactions by the activation of both reporter genes.

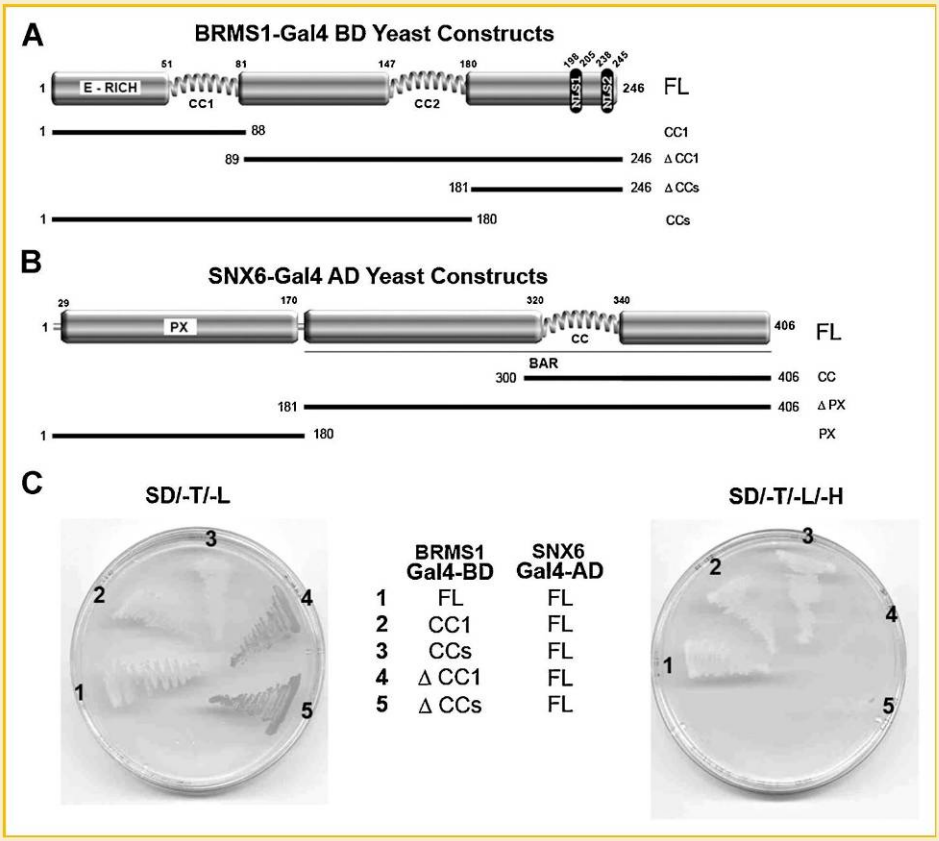

Fig. 3. Minimal domains responsible for SNX6–BRMS1 interaction. Diagram of BRMS1 (A) and SNX6 (B) deletion mutants are schematically depicted and referenced to the full-length protein sequences. C: Representative images of yeast cells co-transformed with a prey vector encoding the entire SNX6 and a combination of bait plasmids encoding the complete sequence of BRMS1 (1); 1–88 N-terminal residues containing the first putative coiled-coil domain (2), or both coiled-coil domains (3), or mutants lacking the first (4), or both coiled-coils (5). Co-transformed yeasts were grown on selective medium (SD-T-L) to assess co-transformation and further screened for a histidine reporter gene (SD-T-L-H).

We did not detect any binding of deletion mutant expressing solely the SNX6-PX domain (PX 1–180) with any of the BRMS1 constructs assayed, as judged by the inability of yeast cells to grow on deficient media (Table I). This result reinforces the hypothesis that the PX domain is dispensable for the interaction with BRMS1. Instead, SNX6 full-length construct strongly activated both reporter genes in yeast cells co-expressing all three constructs where the first 88 N-terminal residues of BRMS1 were present (FL, CC1, and CCs). A series of further truncated constructs mapped the minimal SNX6-binding site within BRMS1 protein to amino acids 1–88, containing the predicted coiled-coil domain (Fig. 3C and Table I), thus highlighting its crucial role. We therefore suggest that the N-terminal fragment of BRMS1, harboring a predicted coiled-coil domain, is necessary and sufficient for binding to SNX6.

Results in Table I show that a construct encompassing the entire BAR domain of SNX6 achieved interaction to the same extent that a shorter construct including a coiled-coil region, concluding that the C-terminal end of SNX6, shorter than the BAR domain, is necessary and sufficient for binding to BRMS1.

Of note is the observation that BRMS1-CC1 construct showed the strongest β-gal activity. This result suggests that a negative regulatory effect might exist in the context of full-length BRMS1 (e.g., the CC1 region might have been partially shielded in the presence of BRMS1 C-terminal end).

SNX6 AFFECTS TRANS-ACTIVATION AND CONTRIBUTES TO BRMS1-TRANSCRIPTIONAL REPRESSION

The results shown above indicate that BRMS1 interacts with SNX6 both in the nucleus and the cytoplasm. It has previously been reported that BRMS1 affects transcriptional repression by its interaction with different components of the mSin3–HDAC complex [Meehan et al., 2004]. We sought to investigate a possible functional relationship between BRMS1 and SNX6 by testing whether SNX6 might play a role in the modulation of transcriptional repression. To address this hypothesis, we carried out a conventional trans-activation assay as previously described [Meehan et al., 2004]. We performed a standard luciferase reporter assay in human cells transfected with a construct (pGL-G5) containing five binding sites of Gal4 promoter [Zurcher et al., 1996]. Proliferating HEK 293T cells exhibited a basal reporter activity that we set as 100% activity (Fig. 4A,B). As expected, trans-activation activity was specifically repressed to 65% upon the transient expression of BRMS1 (Fig. 4A). Importantly, co-expression of BRMS1 and SNX6 exhibited an additive effect on transcriptional repression reducing reporter

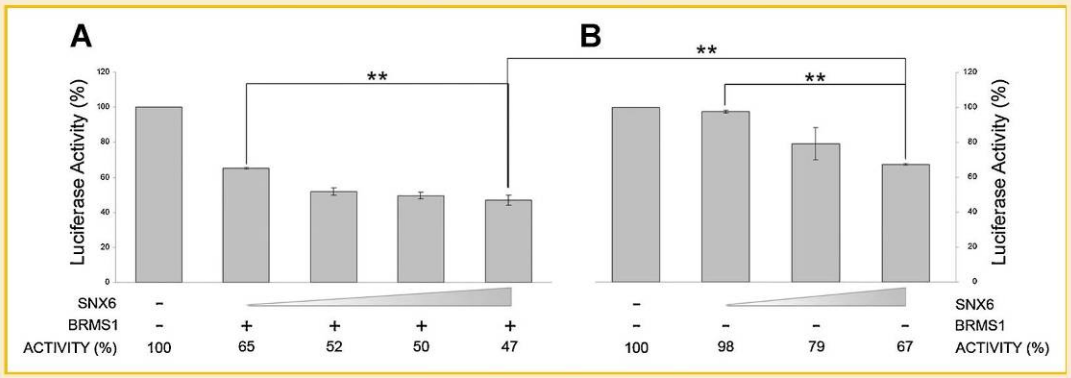

Fig. 4. Modulation of BRMS1-dependent trans-activation by SNX6. T47D transiently transfected cells with 100 ng of pGL-G5 luciferase reporter construct alone (lane 1) or in combination with HA-BRMS1 (0.20 μg) (lanes 5–8) were assayed in a dual-luciferase reporter system. Increasing amounts (0.1; 0.2; or 0.25 μg) of Flag-SNX6 expression plasmids were used as indicated. Equal amounts of plasmid DNA (0.5 μg/well) was accomplished with pcDNA3 vector. Cells in 24-well plates were lysed in 100 μl of passive lysis buffer 48 h post-transfection and 20 μl were used for the assay. Luciferase activity was normalized to Renilla measurements to take into account transfection efficiency variations. Data from five independent experiments assayed in triplicate are presented as the mean percentage ± SD compared to relative luciferase activity of cells transfected only with pcDNA3 vector (lane 1) considered as 100% activity. Symbol * represents statistical significance with $P < 0.05$.

activity up to more than twofold in an SNX6-dose dependent manner (Fig. 4A). The combination of BRMS1 expression with increasing amounts of SNX6 constructs displayed a statistically significant ($P < 0.001$) increase in transcriptional repression capability as compared to that exerted by BRMS1 when transfected alone (Fig. 4A). Moreover, transient expression of increasing amounts of SNX6 transfected plasmid also reduced luciferase reporter activity almost as effectively as BRMS1 when the highest SNX6 plasmid dose was used (Fig. 4B). Interestingly, the latter result suggests that SNX6 might play a role in transcriptional repression, although, no trans-activation domain has been reported for this protein. Whether this effect can be mediated by SNX6 on its own or by acting as a co-repressor is not known yet and should be further analyzed.

Similar and consistent repression of a reporter luciferase activity was also achieved when a different human T47D breast cell line was used (data not shown), suggesting that the observed effect on transcriptional repression might not be cell specific but a general mechanism.

Altogether, these combined results hypothesize a conceivable mechanism by which SNX6 and BRMS1 could modulate gene expression in mammalian cells.

DISCUSSION

In this study, we demonstrate that SNX6 and BRMS1 interact in vivo in a yeast two-hybrid system. Some previously reported BRMS1-interacting proteins were also fished out in our assay (data not shown), assessing the consistency for the performance of our screening.

This interaction can be reconstituted in vitro indicating that no additional yeast proteins are involved. GST pull-down assays demonstrated that an over-expressed construct encompassing the entire sequence of BRMS1 precipitated SNX6, validating yeast results and suggesting direct binding. The protein–protein interaction was further confirmed by FRET analysis. As shown in Figure 2 and Supplementary Figures S1 and S2, mammalian cells over-expressing ECFP-SNX6 and EYFP-BRMS1 showed specific and considerably high $FRET_{eff}$ values, demonstrating that SNX6–BRMS1 interaction occurs in vivo. The identification of this novel interaction of BRMS1 with a bona fide cytosolic protein is in agreement with recent reports demonstrating the nucleo-cytoplasmic shuttling capacity of BRMS1 and its cytosolic presence [Stafford et al., 2008; Rivera et al., 2009].

Moreover, the interaction of BRMS1 with SNX6 reported in this work opens up the possibility of a cytosolic role for this suppressor of breast cancer metastasis.

A previous report, using oligonucleotide microarrays coupled to a robust platform of informatic analysis, has shown that in response to BRMS1 re-expression the signature of diverse secretory/trafficking pathway-genes changed significantly. Interestingly, SNX1 and SNX5, two other members of the sorting nexin family, were repressed upon BRMS1 re-expression [Champine et al., 2007].

A common feature of the SNX family is its PX domain. SNX6 contains a predicted coiled-coil region C-terminal to the PX domain. Whereas homo- and heteromeric interactions with other members of the family involve both PX and coiled-coil domains, the majority of the interactions with membrane receptors, as well as with the oncogene Pim-1, take place by the PX motif [Ishibashi et al., 2001; Xu et al., 2001; Worby and Dixon, 2002]. Interestingly, one of the two cDNAs pulled out in our yeast two-hybrid screen lacked this motif, suggesting that, unlike most of the interactions reported for SNX6, the PX domain is dispensable for its interaction with BRMS1. This fact was confirmed in human cells by FRET analysis where protein–protein interaction efficiency, in cells transfected with a PX deletion mutant (ΔPX-SNX6/ECFP), was indistinguishable from cells over-expressing full-length SNX6. In addition, we have precisely mapped the regions mediating the interaction to the predicted coiled-coil motif of SNX6 and the CC1-BRMS1 located at the N-terminal end.

It is worth to mention that we have observed that SNX6 and BRMS1 interact both in the cytoplasm and the nucleus. Despite the

fact that no functional activity had been reported for SNX6 in the nucleus, it has been shown that Pim-1-mediated phosphorylation of SNX6 leads to its translocation from cytoplasm to the nucleus [Ishibashi et al., 2001]. Moreover, several PX domain-containing proteins interact with nuclear proteins [Vollert and Uetz, 2004] relating lipids with nuclear functions [Shi and Gozani, 2005]. BRMS1 has largely been restricted to the cell nucleus [Samant et al., 2000] where it acts as a transcriptional co-repressor by interacting with diverse components within the large mSin3–HDAC complex or in a smaller complex with HDAC1 [Meehan et al., 2004].

We therefore sought to address whether the novel SNX6–BRMS1 interaction co-localize with the HDAC complex. Despite the fact that FRET protein–protein interaction could not be detected between SNX6-ECFP and the endogenous HDAC2, likely due to the large size of the specific antibody anti-HDAC used, co-localization studies by confocal microscopy showed that BRMS1–SNX6 complex (Fig. 2B,C) co-localizes with the endogenous HDAC complex upon transient expression (Fig. 2D). These results raise the hypothesis of BRMS1–SNX6 playing a role in transcription. Furthermore, using a well-established luciferase reporter assay, we show that over-expression of SNX6 in human cells is capable of modulating the transcriptional machinery revealing a previously non-described function for SNX6 within the nuclear compartment and confirming that our findings might be of physiological relevance.

The absence of a trans-activation domain within the SNX6 sequence suggests that it might act as a transcriptional co-factor. In fact, a previous report, using a similar reporter assay, clearly indicated that SNX6 interferes with TGF-β signaling in a dose-dependent manner, although the assay did not provide a direct measure for any single component of the pathway but the ability of TGF-β to induce gene expression, concluding that the increasing amounts of SNX6 modified the TGF-β receptors. Importantly, although the significance of the BRMS1–SNX6 interaction is still not fully understood, the co-expression, in different human cell types, of BRMS1 and SNX6 in a gene reporter assay enhanced the transcriptional repression exerted by BRMS1, as judged by the reduction of luciferase trans-activation (Fig. 4). The transcriptional blockade achieved after co-expression although modest, it was consistently observed along five different experiments performed in triplicate and found statistically significant. Further studies are needed to evaluate the biological significance of the observed transcriptional repression.

We show that SNX6 affects transcriptional repression. This observation might be in agreement with previous data since SNX6 was first identified as a Smad1 protein partner [Kim et al., 2000] and later on reported to interact to a different extent with several members of the TGF-β family of serine–threonine kinase receptors interfering with TGF-β signaling [Parks et al., 2001]. Interestingly, TGF-β signaling have been largely associated to metastasis [Padua and Massague, 2009].

Moreover, it has recently been reported that the interaction of SNX6 with GIT1 enhances degradation of the epidermal growth factor receptor (EGFR) and alters EGFR signaling [Cavet et al., 2008]. EGFR has long been associated to carcinogenesis and it has been proposed that EGFR contributes to intravasation and metastasis [Xue et al., 2006]. The fact that SNX6 directly affects two signaling pathways involved in metastasis provides an interesting functional relationship to our reported molecular interaction between SNX6 and BRMS1.

BRMS1 was first identified as a largely down-regulated gene in highly metastatic breast carcinoma and melanoma cells. Reintroduction of BRMS1 in both human and mouse-derived cells correlated with reduced metastatic potential in in vivo metastasis assays [Samant et al., 2000, 2002; Shevde et al., 2002]. Interestingly, the aggressiveness of the highly metastatic C8161 melanoma cells and MDA-MB-231 and Hs 578T breast carcinoma cell lines has been recently correlated [Topczewska et al., 2006] with the over-expression of a secreted Nodal protein, which is precisely a ligand of the Activin and TGF-β family of receptors which interact with SNX6.

In summary, our study provides evidences of a novel interaction between the intracellular trafficking protein SNX6 and the breast cancer metastasis suppressor BRMS1, which is mediated by their respective coiled-coils motives. Furthermore, our results supply for the first time evidences that SNX6 might play a novel role as a modulator of the transcriptional repression machinery. Whether SNX6 is a component of the previously described BRMS1–HDAC complex or constitutes a novel level of transcription regulation is still unknown and should be the focus of further studies.

ACKNOWLEDGMENTS

This study was supported by Grant SAF2006-10269 from the MCyT, Grants SAF2008-04048-E, SAF2009-10667 from MICINN, Grant 200820I020 from CSIC, Fundación-Mutua-Madrileña and Grant AP001/10 from Conselleria de Sanitat, Generalitat Valenciana.

REFERENCES

Cavet ME, Pang J, Yin G, Berk BC. 2008. An epidermal growth factor (EGF)-dependent interaction between GIT1 and sorting nexin 6 promotes degradation of the EGF receptor. FASEB J 22(10):3607–3616.

Champine PJ, Michaelson J, Weimer BC, Welch DR, DeWald DB. 2007. Microarray analysis reveals potential mechanisms of BRMS1-mediated metastasis suppression. Clin Exp Metastasis 24(7):551–565.

Cicek M, Fukuyama R, Welch DR, Sizemore N, Casey G. 2005. Breast cancer metastasis suppressor 1 inhibits gene expression by targeting nuclear factor-kappaB activity. Cancer Res 65(9):3586–3595.

DeWald DB, Torabinejad J, Samant RS, Johnston D, Erin N, Shope JC, Xie Y, Welch DR. 2005. Metastasis suppression by breast cancer metastasis suppressor 1 involves reduction of phosphoinositide signaling in MDA-MB-435 breast carcinoma cells. Cancer Res 65(3):713–717.

Fuster JJ, Gonzalez JM, Edo MD, Viana R, Boya P, Cervera J, Verges M, Rivera J, Andres V. Tumor suppressor p27Kip1 undergoes endolysosomal degradation through its interaction with sorting nexin 6. FASEB J 24:2998–3009.

Gu Y, Di WL, Kelsell DP, Zicha D. 2004. Quantitative fluorescence resonance energy transfer (FRET) measurement with acceptor photobleaching and spectral unmixing. J Microsc 215(Pt 2):162–173.

Habermann B. 2004. The BAR-domain family of proteins: A case of bending and binding? EMBO Rep 5(3):250–255.

Hurst DR, Xie Y, Vaidya KS, Mehta A, Moore BP, Accavitti-Loper MA, Samant RS, Saxena R, Silveira AC, Welch DR. 2008. Alterations of BRMS1–

ARID4A interaction modify gene expression but still suppress metastasis in human breast cancer cells. J Biol Chem 283(12):7438–7444.

Ishibashi Y, Maita H, Yano M, Koike N, Tamai K, Ariga H, Iguchi-Ariga SM. 2001. Pim-1 translocates sorting nexin 6/TRAF4-associated factor 2 from cytoplasm to nucleus. FEBS Lett 506(1):33–38.

James P, Halladay J, Craig EA. 1996. Genomic libraries and a host strain designed for highly efficient two-hybrid selection in yeast. Genetics 144(4): 1425–1436.

Kim RH, Wang D, Tsang M, Martin J, Huff C, de Caestecker MP, Parks WT, Meng X, Lechleider RJ, Wang T, Roberts AB. 2000. A novel smad nuclear interacting protein, SNIP1, suppresses p300-dependent TGF-beta signal transduction. Genes Dev 14(13):1605–1616.

Meehan WJ, Samant RS, Hopper JE, Carrozza MJ, Shevde LA, Workman JL, Eckert KA, Verderame MF, Welch DR. 2004. Breast cancer metastasis suppressor 1 (BRMS1) forms complexes with retinoblastoma-binding protein 1 (RBP1) and the mSin3 histone deacetylase complex and represses transcription. J Biol Chem 279(2):1562–1569.

Padua D, Massague J. 2009. Roles of TGF-beta in metastasis. Cell Res 19(1): 89–102.

Parks WT, Frank DB, Huff C, Renfrew Haft C, Martin J, Meng X, de Caestecker MP, McNally JG, Reddi A, Taylor SI, Roberts AB, Wang T, Lechleider RJ. 2001. Sorting nexin 6, a novel SNX, interacts with the transforming growth factor-beta family of receptor serine–threonine kinases. J Biol Chem 276(22): 19332–19339.

Rivera J, Abrams C, Hernaez B, Alcazar A, Escribano JM, Dixon L, Alonso C. 2007a. The MyD116 African swine fever virus homologue interacts with the catalytic subunit of protein phosphatase 1 and activates its phosphatase activity. J Virol 81(6):2923–2929.

Rivera J, Megias D, Bravo J. 2007b. Proteomics-based strategy to delineate the molecular mechanisms of the metastasis suppressor gene BRMS1. J Proteome Res 6(10):4006–4018.

Rivera J, Megias D, Navas C, Bravo J. 2009. Identification of essential sequences for cellular localization in BRMS1 metastasis suppressor. PLoS ONE 4(7):e6433.

Samant RS, Seraj MJ, Saunders MM, Sakamaki TS, Shevde LA, Harms JF, Leonard TO, Goldberg SF, Budgeon L, Meehan WJ, Winter CR, Christensen ND, Verderame MF, Donahue HJ, Welch DR. 2000. Analysis of mechanisms underlying BRMS1 suppression of metastasis. Clin Exp Metastasis 18(8):683–693.

Samant RS, Debies MT, Shevde LA, Verderame MF, Welch DR. 2002. Identification and characterization of the murine ortholog (brms1) of breast-cancer metastasis suppressor 1 (BRMS1). Int J Cancer 97(1):15–20.

Saunders MM, Seraj MJ, Li Z, Zhou Z, Winter CR, Welch DR, Donahue HJ. 2001. Breast cancer metastatic potential correlates with a breakdown in homospecific and heterospecific gap junctional intercellular communication. Cancer Res 61(5):1765–1767.

Sekar RB, Periasamy A. 2003. Fluorescence resonance energy transfer (FRET) microscopy imaging of live cell protein localizations. J Cell Biol 160(5):629–633.

Seraj MJ, Samant RS, Verderame MF, Welch DR. 2000. Functional evidence for a novel human breast carcinoma metastasis suppressor, BRMS1, encoded at chromosome 11q13. Cancer Res 60(11):2764–2769.

Shevde LA, Samant RS, Goldberg SF, Sikaneta T, Alessandrini A, Donahue HJ, Mauger DT, Welch DR. 2002. Suppression of human melanoma metastasis by the metastasis suppressor gene, BRMS1. Exp Cell Res 273(2):229–239.

Shi X, Gozani O. 2005. The fellowships of the INGs. J Cell Biochem 96(6):1127–1136.

Spinola-Amilibia M, Rivera J, Bravo J. 2008. Crystallization and preliminary X-ray diffraction analysis of a breast cancer metastasis suppressor 1 predicted coiled-coil region. Acta Crystallogr F Struct Biol Cryst Commun 64(Pt 12):1156–1158.

Stafford LJ, Vaidya KS, Welch DR. 2008. Metastasis suppressors genes in cancer. Int J Biochem Cell Biol 40(5):874–891.

Topczewska JM, Postovit LM, Margaryan NV, Sam A, Hess AR, Wheaton WW, Nickoloff BJ, Topczewski J, Hendrix MJ. 2006. Embryonic and tumorigenic pathways converge via Nodal signaling: Role in melanoma aggressiveness. Nat Med 12(8):925–932.

Vollert CS, Uetz P. 2004. The phox homology (PX) domain protein interaction network in yeast. Mol Cell Proteomics 3(11):1053–1064.

Worby CA, Dixon JE. 2002. Sorting out the cellular functions of sorting nexins. Nat Rev Mol Cell Biol 3(12):919–931.

Xu Y, Seet LF, Hanson B, Hong W. 2001. The Phox homology (PX) domain, a new player in phosphoinositide signalling. Biochem J 360(Pt 3):513–530.

Xue C, Wyckoff J, Liang F, Sidani M, Violini S, Tsai KL, Zhang ZY, Sahai E, Condeelis J, Segall JE. 2006. Epidermal growth factor receptor overexpression results in increased tumor cell motility in vivo coordinately with enhanced intravasation and metastasis. Cancer Res 66(1):192–197.

Yang J, Zhang B, Lin Y, Yang Y, Liu X, Lu F. 2008. Breast cancer metastasis suppressor 1 inhibits SDF-1alpha-induced migration of non-small cell lung cancer by decreasing CXCR4 expression. Cancer Lett 269(1): 46–56.

Zurcher T, de la Luna S, Sanz-Ezquerro JJ, Nieto A, Ortin J. 1996. Mutational analysis of the influenza virus A/Victoria/3/75 PA protein: Studies of interaction with PB1 protein and identification of a dominant negative mutant. J Gen Virol 77(Pt 8):1745–1749.

4.2 NOVEL LAMBDA FRET SPECTRAL CONFOCAL MICROSCOPY IMAGING METHOD

Diego Megías, Raquel Marrero, Borja Martínez del Peso, María Ángel García, José-Javier Bravo-Cordero, Aránzazu García-Grande, Andrés Santos, and María C. Montoya

En este trabajo describimos un nuevo método, robusto, especifico y sensible aplicable al análisis de la transferencia de energía de la fluorescencia por resonancia (FRET) a partir de imágenes adquiridas en un microscopio confocal espectral láser. El proceso que engloba este método que llamamos lambda FRET (λFRET) analiza las imágenes de la muestra adquiridas a distintas longitudes de onda de forma que podemos estudiar su espectro de emisión, el cual posteriormente descomponemos en sus componentes de Donador y Aceptor de energía para calcular la eficiencia de FRET para cada píxel.

El método utiliza un novedoso procedimiento de pre-calibración para la corrección de las imágenes espectrales basado en la adquisición de imágenes de reflexión y de espectros referencia, el cual simplifica su aplicación y reduce la variabilidad. λFRET ha sido validado usando patrones de FRET estructuralmente caracterizados y específicamente diseñados para este propósito, con distancias y estequiometrias variables entre los fluoróforos.

El λFRET obtiene mejores resultados, en términos de especificidad, reproducibilidad, y sensibilidad a variaciones en distancia, que otros métodos bien establecidos, tales como el foto-blanqueado del aceptor y la emisión sensibilizada. Por otra parte, el análisis de λFRET no se ve afectado por fluorocromos con gran solapamiento espectral ni por la auto fluorescencia celular, mientras que los métodos mencionados anteriormente, resultan muy dependientes de dichos factores.

El método de λFRET ha demostrado ser aplicable tanto en muestras fijadas como en estudios de microscopía de célula viva.

En este trabajo he participado de forma fundamental en la planificación y diseño del método, incluyendo la generación por genética molecular de estándares de eficiencia de FRET fija, la preparación de muestras, su adquisición, el análisis de imagen e interpretación, además de en la creación de una aplicación informática que posibilita la realización los cálculos necesarios para el análisis.

Novel Lambda FRET Spectral Confocal Microscopy Imaging Method

DIEGO MEGÍAS,[1] RAQUEL MARRERO,[1] BORJA MARTÍNEZ DEL PESO,[2] MARÍA ÁNGEL GARCÍA,[1] JOSÉ-JAVIER BRAVO-CORDERO,[1] ARANZAZU GARCÍA-GRANDE,[1] ANDRÉS SANTOS,[2] AND MARÍA C. MONTOYA[1*]

[1]*Biotechnology Programme, Confocal Microscopy and Cytometry Unit, Centro Nacional de Investigaciones Oncológicas (CNIO), C/ Melchor Fernández Almagro 3, Madrid E-28029, Spain*

[2]*Department of Electronic Engineering, Biomedical Image Technology Lab, Universidad Politecnica de Madrid, ETSI Telecomunicacion, Madrid E-28040, Spain*

KEY WORDS FRET; spectral; microscopy; imaging; confocal; interaction

ABSTRACT We report a highly specific, sensitive, and robust method for analyzing fluorescence resonance energy transfer (FRET) based on spectral laser scanning confocal microscopy imaging. The lambda FRET (λFRET) algorithm comprises imaging of a FRET sample at multiple emission wavelengths rendering a FRET spectrum, which is separated into its donor and acceptor components to obtain a pixel-based calculation of FRET efficiency. The method uses a novel off-line precalibration procedure for spectral bleed-through correction based on the acquisition of reference reflection images, which simplifies the method and reduces variability. λFRET method was validated using structurally characterized FRET standards with variable linker lengths and stoichiometries designed for this purpose. λFRET performed better than other well-established methods, such as acceptor photobleaching and sensitized emission-based methods, in terms of specificity, reproducibility, and sensitivity to distance variations. Moreover, λFRET analysis was unaffected by high fluorochrome spectral overlap and cellular autofluorescence. The λFRET method demonstrated outstanding performance in intra- and intermolecular FRET analysis in both fixed and live cell imaging studies. *Microsc. Res. Tech. 72:1–11, 2009.*

INTRODUCTION

Fluorescence resonance energy transfer (FRET) is a process through which an excited fluorophore (donor) transfers its energy to a nearby light-absorbing molecule (acceptor). FRET is dependent on the proximity of both molecules, which must be within a range of 1–10 nm of each other, making this technique a unique tool to quantitatively analyze the molecular interactions with spatial and temporal resolution (Förster, 1965; Jares-Erijman and Jovin, 2003). Microscopy FRET imaging allows one to monitor the molecular interactions in space (i.e., localizing interactions within cells or tissues) and time (i.e., observing the formation and breakdown of molecular complexes within a live cell) (Wouters et al., 2001; Zhang et al., 2002).

FRET microscopy is usually based on the presence of two fluorescent species; donor and acceptor. When donor is excited it will either emit fluorescence with its characteristic emission wavelength (λ) (in case there is no transfer of energy) or (when FRET occurs), its excited energy will be transferred to the acceptor which will emit with its characteristic λ. Therefore, in the event of FRET the following changes will occur; donor fluorescence emission intensity decreases, fluorescence emission at wavelengths characteristic of the acceptor emission will appear, and the half life of excited donor is reduced. The various FRET measuring methods are based on the quantification of these changes and require different instrumental set ups; ranging from wide field or laser scanning confocal microscopes, to the costly and highly specialized fluorescence lifetime imaging (FLIM) systems. Intensity-based methods relying on measuring variations in fluorescence intensity include "acceptor photobleaching," which is the most commonly used method for analyzing FRET in fixed cells because of its simplicity, and "sensitized emission," which is extensively used to study intramolecular FRET in live cells by conventional wide field or confocal microscopy. However, these methods have intrinsic limitations; in particular, acceptor photobleaching is destructive and therefore not applicable to live cell studies, and sensitized emission-based methods are subject to variability because of their strong dependence on external controls, which introduce a high level of instability to the measure. Because of all these difficulties, a microscopy method that uses a simple and reliable correction procedure for analyzing quantitatively FRET, applicable to live cells is still missing. We therefore sought to develop a FRET analysis

Additional Supporting Information may be found in the online version of this article.

Abbreviations: CFP, cyan fluorescent protein; FLIM, fluorescence lifetime imaging; FRET, fluorescence resonance energy transfer; mRFP, monomeric red fluorescent protein; YFP, yellow fluorescent protein.

*Correspondence to: Maria C. Montoya, Confocal Microscopy and Cytometry Unit, Biotechnology Programme, Spanish National Cancer Research Center (CNIO), C/ Melchor Fernández Almagro 3, Madrid E-28029, Spain.
E-mail: mmontoya@cnio.es

Received 4 July 2008; accepted in revised form 25 July 2008

Contract grant sponsor: Fondo de Investigaciones Sanitarias; Contract grant number: FIS PI061839; Contract grant sponsor: Ministry of Science and Technology of Spain.

DOI 10.1002/jemt.20633

Published online 10 September 2008 in Wiley InterScience (www.interscience.wiley.com).

method that could overcome these problems and that could be sensitive enough to detect typically weak physiological interactions in live cell studies.

Spectral imaging comprises the acquisition of fluorescence images at multiple wavelengths, and is based on the capability of a microscope system to separate the light emitted from the excited sample into its spectral components and collect them separately. This tool has been implemented in most standard laser scanning confocal microscopes currently available (Lerner and Zucker, 2004; Zimmermann et al., 2003), and provides a unique capability for monitoring changes in the intensity of donors and acceptors, such as those that occur in FRET. Different approaches for measuring FRET using spectral imaging based on spectral unmixing algorithms have been reported. These methods (Chen et al., 2007; Gut et al., 2004; Neher and Neher, 2004; Raicu et al., 2005; Zimmermann et al., 2002), use lifetime (Neher and Neher, 2004; Raicu et al., 2005), or acceptor photobleaching measurements as calibration procedures (Gut et al., 2004; Raicu et al., 2005; Zimmermann et al., 2002). Chen and coworkers implemented an intensity normalized acceptor cross excitation correction (Chen et al., 2007). Other interesting methods based in spectral unmixing using multiphoton microscopy (Thaler et al., 2005) or spectrofluorometer systems (Wlodarczyk et al., 2008) have been developed. Here, we present a new method for the analysis of FRET based entirely on spectral image acquisition using laser scanning confocal microscopy. We evaluated the performance of lambda FRET (λFRET) using FRET standards, and found that this method is more sensitive and reproducible than acceptor photobleaching and sensitized emission-based methods. The method was applied to both fixed and live intra- and intermolecular FRET studies for the analysis of the in vivo interaction of CD44 and moesin in invasive tumor cells embedded in three-dimensional (3D) collagen matrices, further demonstrating the suitability of λFRET for monitoring molecular interactions in cell biology applications.

MATERIALS AND METHODS

FRET Microscopy and Image Analysis

Raw images for FRET analysis were collected with a Leica SP2 AOBS spectral confocal microscope equipped with a 63 × 1.4 NA oil objective (Leica Microsystems CMS, Mannheim, Germany) by using λ*D*488/λ*A*543 laser lines (for the pairs Alexa 488-Cy3 and GFP-mRFP), or λ*D*458/λ*A*514 laser lines (for the pair CFP-YFP and Cerulean-Venus). λ stacks are acquired by obtaining a λ series of fluorescence images by defining 30 (25-nm wide) detection windows over the range of 465–650 nm, although the number and width of detection windows is configurable depending on the signal strength and speed requirements. Accordingly, the time needed for the acquisition varies depending on the scan format, ranging from around 80–14 s for λ stacks of 30 or 18 fluorescence images respectively using a Leica SP2 microscope. In contrast sensitized emission raw image acquisition takes around 1 s. Standard reference spectra are obtained by exciting the donor and acceptor control samples with the donor excitation wavelengths. The donor excitation wavelength is used to obtain the acceptor reference spectra since it enables the acquisition of the complete λ stack ranging all the detection wavelengths. In λFRET analysis, a donor and acceptor excitation wavelengths are used to obtain one reflection and a λ stack of images. The reflected light intensity is measured from a reflection image obtained by configuring a detection window that matches the excitation wavelength. From each fluorescence image λ stack, intensities are plotted against the median wavelength value of each detection window to obtain the raw spectra (rawS), or reference spectra (refS), depending on whether the images are originated from the FRET or control samples respectively. RawS were analyzed as specified in the Results section. Theoretical derivation of λFRET corrections and efficiency calculation is detailed in Supporting Information Appendices 1 and 2. IDL software (ITT Visual Information Solutions, CO) was used to integrate computerized image analysis functions into a single λFRET algorithm that could be applied to sets of images and time-lapse image series to obtain FRET efficiency images. Processes performed by IDL include the complete λFRET measurement, including spectra interpolation, CAbs, $\frac{R_{\lambda D}}{R_{\lambda A}}$, and E calculations. Acceptor photobleaching and sensitized emission measurements were performed using the algorithm incorporated into the Leica SP2 confocal software (Wouters et al., 2001).

Spectrofluorometric Analysis of Cell Lysates

MDA-MB-231 pelleted cells were lysed with 50 μL of Triton 0.5%, 10 min on ice and centrifuged at 6,000 rpm 5 min. Supernatant was diluted in PBS at a density of 1×10^6 cells/mL. The emission spectrum of fluorescent proteins in the lysate was acquired with Quantamaster Spectrofotometer (Photon Technology International, Birmingham, NJ) and Felix32 software. CFP emission was traced from 460 to 560 nm with excitation at 430 nm and YFP was traced from 500 to 560 nm with excitation at 490 nm. The increment was 5 nm and the integration 1 s. Determination of FRET efficiencies was performed as described in Chen et al. (2005).

DNA Constructs

A YFP-17aa-CFP tandem construct was generated by amplifying CFP from the ECFP-N1 vector and subsequently cloning it into the EYFP-C1 vector (Clontech, Takara Bio, Shiga, Japan) using *Kpn*I and *Bam*HI. The YFP-8aa-CFP tandem was obtained by amplifying CFP from the ECFP-N1 vector using oligonucleotides introducing a GGTGG motif as a linker with *Bsp*EI-*Bam*HI sticky ends using the following synthetic oligonucleotides: forward, 5′-AGATCCG GAGGTACAGGTGGAGGTACCATGGTGAGCAAGGG C-3′; reverse: 5′-CGGGATCCTTACTTGTACAGCTCG TC-3′. The PCR product was cloned into the EYFP-C1 vector. The R16 domain of chicken α-spectrin was kindly provided by Dr. J. Clarke (University of Cambridge, UK) and the immunoglobulin domain of protein G DNA was kindly provided by Dr. F. Blanco (CNIO, Spain). The R16 and B1G domains were amplified without stop codons and cloned into the *Bsp*EI-*Kpn*I restricted YFP-17aa-CFP tandem to generate YFP-R16-CFP and YFP-B1G-CFP respectively. CFP-YFP-YFP and CFP-CFP-YFP fusion constructs were obtained by amplifying YFP and CFP from EYFP-N1 and ECFP-

N1 vectors respectively, and cloning them into YFP-17aa-CFP tandem with *XhoI-EcoRI* restriction sites. A caspase-sensitive FRET probe YFP-LEVD-CFP was generated by amplifying CFP from the ECFP-N1 vector using a forward oligonucleotide containing two caspase cleavage sites, 5′-AGATCCGGAGCACTGGAGGTCG ATGCCCTGGAGGTCGATGGTACCATGGTGAGCAAG GGCGAGGAG-3′ and cloning it into EYFP-C1 with *Bsp*EI-*Bam*HI. The C5V, C17V, and C32V constructs were provided by Dr. Vogel (National Institutes of Health, Bethesda, MD). The standard form of CD44 amplified from cDNA was provided by Dr. T Mizoi (Kumamoto University, Japan) and cloned into mRFP vector [provided by Dr. Tsien (University of California at San Diego] using *Kpn*I–*Sac*I restriction sites. The moesin-GFP construct was provided by Dr. Sánchez-Madrid (Hospital de la Princesa). All constructs were verified by DNA sequencing.

Cell Culture, Transfection, and Collagen Inclusion

Breast adenocarcinoma MDA-MB-231 cells were maintained in DMEM supplemented with 10% FBS. Cell transfection was performed using lipofectamine 2,000 (Invitrogen, Carlsbad, CA) according to the manufacturer's instructions. Twenty-four hours after transfection, cells were trypsinized and mixed with a readily prepared HA-Col I solution (2.4 mg/mL bovine Col I (Vitrogen, PAlo Alto, CA), 1 mg/mL HA (Sigma-Aldrich, St Louis, MO), 1 × RPMI, 19 mM Hepes, 0.19% sodium bicarbonate, 5% FBS, and allowed to polymerize for 2 h at 37°C (3D-Col I) or plated on cover slips either uncoated or coated with HA-Col I.

Immunofluorescence Experiments

FRET-positive controls were performed on MDA-MB-231 cells plated on HA-Col I-coated cover slips, fixed, and stained with HP2/9 mouse antihuman CD44 antibodies, kindly provided by Dr. Sánchez Madrid (Hospital de la Princesa, Spain). Cells were incubated with 5 μg/mL of goat antimouse Alexa 488 (Molecular Probes, Invitrogen) and then with 7.5 μg/mL of donkey antigoat Cy3 (Jackson Inmunoresearch, Westgrove, PA). The CD44-moesin interaction was studied in cells expressing moesin-GFP and CD44-mRFP fixed and stained with rabbit anti-Ezrin/Radixin/Moesin (90/3) and mouse anti-CD44 (HP2/9) antibodies revealed with secondary antirabbit Ab labeled with Alexa 488 (Molecular Probes, Invitrogen) and anti mouse Cy3 labeled Ab (Jackson, Amersham Biosciences, Uppsala, Sweden), respectively.

RESULTS

Rationale of the λFRET Method

A detailed procedure for λFRET data acquisition and analysis for Alexa 488 and Cy3 fluorophores is presented in Figures 1 and 2. Description of symbols can be found in Table 1. First, a series of images acquired at different detection wavelengths (λ stacks) were obtained from samples with only donor or acceptor species generating standard reference spectra (Fig. 2a). These are acquired once for every donor/acceptor pair as part of the precalibration procedure and apply for all subsequent FRET analysis using the same fluorophore combination. For FRET measurement two sets of the reflection image and λ stacks are acquired by exciting the double-labeled sample (FRET sample), with donor-specific (λ*D*, 488) and acceptor-specific (λ*A*, 543) excitation wavelengths and represent raw images (Fig. 2b). Following image background correction, fluorescence intensities are plotted against wavelength to obtain the rawS for every image pixel (Fig. 2b). The spectra datasets obtained with the donor excitation wavelength (raw FRET spectra; $\mathrm{rawS}^{DA}_{\lambda D}$) contain the FRET information, and the spectra acquired by exciting with acceptor specific light (raw direct acceptor spectra; $\mathrm{rawS}^{A}_{\lambda A}$) are used to estimate the cross-excitation contamination component.

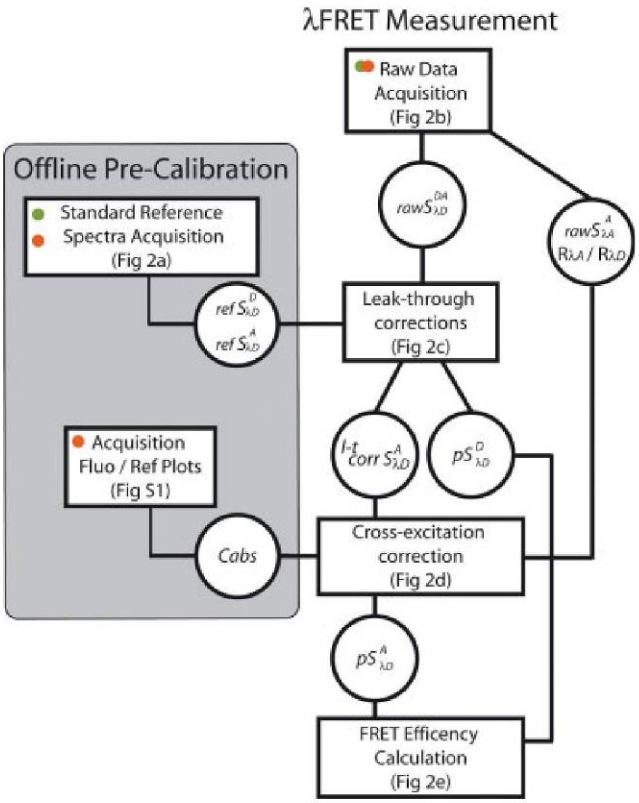

Fig. 1. Flowchart of the λFRET algorithm. Processes involving measurements on acceptor or donor control samples that can be obtained once for a given fluorochrome pair as an offline precalibration procedure are included in the gray box. FRET measurement steps for the processing of data originating from the FRET double labeled sample to calculate the FRET efficiency are shown. More detailed information about these processes can be found at the indicated figures. [Color figure can be viewed in the online issue, which is available at www.interscience.wiley.com.]

Separation of raw FRET spectrum ($\mathrm{rawS}^{DA}_{\lambda D}$) into its donor and acceptor components ($\mathrm{intS}^{A}_{\lambda D}$ and $\mathrm{intS}^{D}_{\lambda D}$ is based on an interpolation procedure that uses reference standard donor and acceptor spectra from single-labeled samples as detailed in Supporting Information Appendix 1 (Fig. 2ci). Leak-through corrections are then carried out by subtracting the fraction of acceptor interpolated emission peak ($\mathrm{intS}^{A}_{\lambda D}$) overlapping donor peak ($\mathrm{intS}^{D}_{\lambda D}$) and vice versa (Figs. 2cii and 2ciii) The leak-through corrected donor spectrum is termed pure donor spectra ($\mathrm{pS}^{D}_{\lambda D}$) because it does not require further

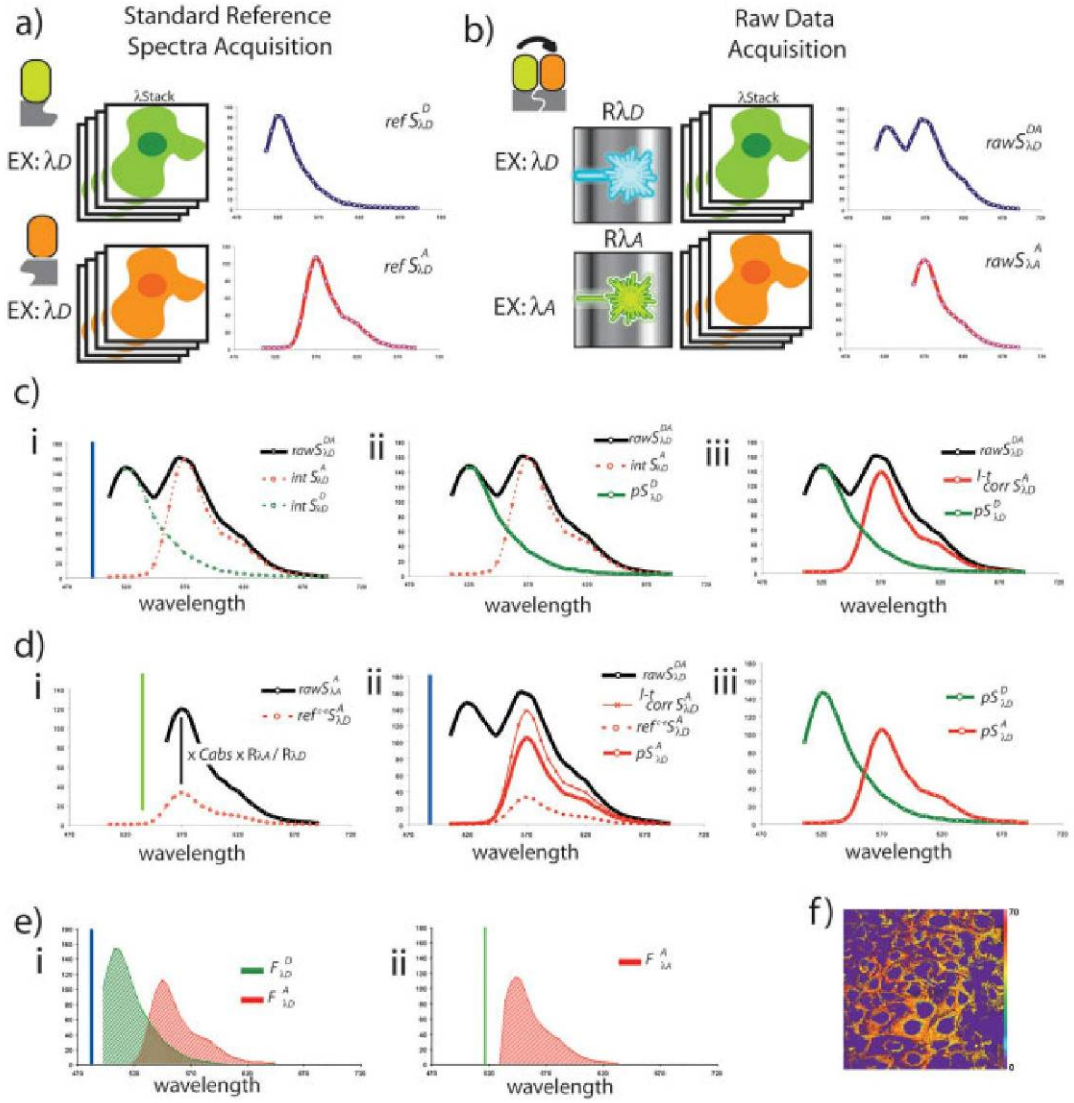

Fig. 2. λFRET data acquisition and analysis procedure. Fixed MDA-MB-231 cells were incubated with mouse anti-CD44 Ab, and then either with secondary goat antimouse Alexa 488, or antimouse Cy3 to obtain control samples (**a**) or with secondary goat antimouse Alexa 488 and with rabbit antigoat Cy3 obtaining the double labeled FRET sample (**b**). (a) λ stacks of 30 fluorescence images were obtained by exciting the control samples with 488 nm laser line (Ex:λ*D*) to render $refS^{A}_{\lambda D}$ and $refS^{D}_{\lambda D}$. (b) One reflection and a spectral series of 30 fluorescence images were obtained by exciting the double labeled sample with 488 nm (Ex:λ*D*) or 543 nm (Ex:λ*A*) laser lines. Representative raw FRET ($rawS^{DA}_{\lambda D}$) and raw direct acceptor emission spectra ($rawS^{A}_{\lambda A}$) are shown. (**c**) The raw FRET spectrum ($rawS^{DA}_{\lambda D}$, solid line) is decomposed into donor and acceptor raw emission peaks ($intS^{D}_{\lambda D}$ and $intS^{A}_{\lambda D}$, dashed lines) by interpolating standard donor and acceptor reference spectra (**i**). Leak-through correction subtracts the percentage of the spectral spillover of the acceptor into the donor (i) and vice versa (**ii**). Preliminary raw FRET spectrum ($rawS^{DA}_{\lambda D}$, solid line) and resultant donor ($pS^{D}_{\lambda D}$ thick solid line) and acceptor leak-through corrected spectra ($^{l\text{-}t}corrS^{A}_{\lambda D}$ thick solid line) are presented (iii). (**d**) The product of raw direct acceptor control spectra ($rawS^{A}_{\lambda A}$, dotted line), the predetermined absorbance constant (C_{Abs}), and reflection intensity ratio ($R_{\lambda D}/R_{\lambda A}$) render reference cross-excitation-corrected spectra ($ref^{c\text{-}e}\,S^{A}_{\lambda D}$, dotted line) i), which is subtracted from the acceptor leak-through-corrected spectra ($^{l\text{-}t}corrS^{A}_{\lambda D}$, thin solid line) to obtain the resultant fully corrected acceptor pure spectra ($pS^{A}_{\lambda D}$, thick solid line) ii). Resultant donor and acceptor pure spectra (thick solid lines) are presented iii). Raw FRET spectra ($rawS^{DA}_{\lambda D}$) is shown with clarity purposes in cii, ciii, and dii graphs. (**e**) Donor directly excited and acceptor sensitized fluorescence intensity values ($F^{D}_{\lambda D}$ and $F^{A}_{\lambda D}$) are calculated from the $pS^{D}_{\lambda D}$ and $pS^{A}_{\lambda D}$ spectral curve integrals (**i**) and acceptor directly excited fluorescence emission intensity value $F^{A}_{\lambda A}$ is calculated from $pS^{A}_{\lambda A}$ curve integral (**ii**). (**f**) The resultant λFRET efficiency image is shown.

corrections. In contrast, the leak-through corrected acceptor spectrum $^{l\text{-}t}corrS^{A}_{\lambda D}$ carries a cross-excitation contamination that needs to be corrected. The cross-excitation contamination component of the FRET spectrum is the amount of acceptor emission excited directly at the donor-specific wavelengths. We have developed a completely novel correction procedure based in imaging the double labeled sample to avoid the variability produced by introducing intensity measurements coming from control single labeled sample. The cross-excitation-correction procedure (Fig. 2d) is based on deriving a cross-excitation reference spectrum as the product of the direct acceptor raw spectrum, the ratio of reflection intensities at the donor and acceptor wavelengths ($R_{\lambda D}/R_{\lambda A}$), both obtained from the FRET double-labeled sample, and the

TABLE 1. Description of symbols

Code	Description	Originated in
$rawS^{DA}_{\lambda D}$	Raw FRET spectra of donor and acceptor emission excited at donor λ	FRET sample
$intS^{D}_{\lambda D}$	Interpolated donor raw emission spectra excited at donor λ	$rawS^{DA}_{\lambda A}$
$intS^{A}_{\lambda D}$	Interpolated acceptor raw emission spectra excited at donor λ	$rawS^{DA}_{\lambda A}$
$rawS^{A}_{\lambda A}$	Raw acceptor emission spectra directly excited at acceptor λ	FRET sample
$refS^{A}_{\lambda D}$	Reference acceptor emission spectra directly excited at donor λ	Control acceptor sample
$refS^{D}_{\lambda D}$	Reference donor emission spectra excited at donor λ	Control donor sample
$^{l-t}corrS^{A}_{\lambda D}$	Leak through corrected acceptor emission spectra excited at donor λ	$intS^{A}_{\lambda D}$
$ref^{c-e}\ S^{A}_{\lambda D}$	Reference acceptor cross excitation spectra	$rawS^{A}_{\lambda A}$
$pS^{D}_{\lambda D}$	Pure donor emission spectra excited at donor λ (leak-through corrected).	$intS^{D}_{\lambda D}$
$pS^{A}_{\lambda D}$	Pure acceptor emission spectra excited at donor λ (leak-through and cross excitation corrected).	$^{l-t}corrS^{A}_{\lambda D}$
$F^{D}_{\lambda D}$	Donor fluorescence intensity directly excited at donor λ	$pS^{D}_{\lambda D}$
$F^{A}_{\lambda D}$	Acceptor sensitized fluorescence intensity derived from energy transfer.	$pS^{A}_{\lambda D}$
$F^{A}_{\lambda A}$	Acceptor fluorescence intensity directly excited at acceptor λ	$rawS^{A}_{\lambda A}$

Capital Letter: S, spectra; L, incident light intensity; I, raw fluorescence intensity; F, corrected fluorescence intensity; Abs, light absorption; C, constant; R, reflected light intensity; E, FRET efficiency; Q, quantum yield. Super index: *D*, emission at donor wavelength range; *A*, emission at acceptor wavelength range. Sub index: λ*D*, donor-specific excitation wavelength; λ*A*, acceptor-specific excitation wavelength. Prefix: ref^{c-e}, reference for cross-excitation; ref, reference from control sample; $^{l-t}$corr, data corrected for leak-through; raw, raw data; int, interpolated values; p, pure, fully corrected. [Color figure can be viewed in the online issue, which is available at www.interscience.wiley.com.]

acceptor absorbance constant (C_{Abs}) (Fig. 2d) using the following equation:

$$ref^{c-e}S^{A}_{\lambda D} = \frac{R_{\lambda D}}{R_{\lambda A}} \cdot C_{\mathrm{abs}} \cdot rawS^{A}_{\lambda A}$$

(derived in Supp. Info. Appendix 1)

C_{Abs} is calculated by the software once for every donor–acceptor fluorochromes on an acceptor only sample as part of the precalibration procedure and used for cross-excitation correction of subsequent FRET studies. This value correlates linearly the acceptor absorption coefficients at the donor and acceptor laser lines. C_{Abs} calculation is computed as the relationship between the slopes of the fluorescence reflection plots excited at the donor and acceptor wavelengths (Supp. Info., Fig. S1) following:

$$C_{\mathrm{Abs}} = \frac{I^{A}_{\lambda D} \cdot R_{\lambda A}}{I^{A}_{\lambda A} \cdot R_{\lambda D}} \quad \text{(derived in Supp. Info. Appendix 1)}$$

By applying C_{Abs} and ($R_{\lambda D}/R_{\lambda A}$) correction factors, the acceptor emission spectra directly excited at the donor specific wavelength ($ref^{c-e}S^{A}_{\lambda D}$) can be deduced from the raw acceptor spectrum obtained from exciting the FRET sample at the acceptor wavelength ($rawS^{A}_{\lambda A}$) (Fig. 2di), then subtracted from the leak-through corrected acceptor spectrum ($^{l-t}corrS^{A}_{\lambda D}$) to obtain an acceptor pure spectrum ($pS^{A}_{\lambda D}$), (leak-through and cross-excitation corrected) (Fig. 2dii). Both donor and acceptor pure spectra ($pS^{D}_{\lambda D}$ and $pS^{A}_{\lambda D}$) are used for FRET efficiency calculations (Fig. 2diii). The corrected fluorescence intensities from direct excitation of donor $F^{D}_{\lambda D}$, and sensitized acceptor emission $F^{A}_{\lambda D}$ are obtained from pure spectra curve integrals (Fig. 2ei) and used for λFRET efficiency computation following equation:

$$E = \frac{F^{A}_{\lambda D} \cdot Q^{D}/Q^{A}}{F^{D}_{\lambda D} + F^{A}_{\lambda D} \cdot Q^{D}/Q^{A}}$$

(derived in Supp. Info. Appendix 2)

The acceptor direct fluorescence emission intensity calculated as the ($rawS^{A}_{\lambda A}$) curve integral (Fig. 2eii) is used for donor/acceptor ratio calculations (Supp. Info. Appendix 3). The λFRET software developed in-house automatically implements the analysis algorithm that determines E in a pixel-based manner to obtain a FRET efficiency image (Fig. 2f). Systematic and propagation errors in λFRET efficiency calculation were analyzed as detailed in Supporting Information Appendix 4. In a typical experimental analysis, the calculated maximum error value for each spectrum ($\Delta pS^{A}_{\lambda D} = \Delta pS^{D}_{\lambda D}$) was = 5,17 (Supp. Info. Fig. S2). The standard error (SE) propagation was 0.003 for a measured λFRET efficiency value of 0.35.

In summary, λFRET comprises spectral imaging of a FRET sample, and results in a pixel-based composite FRET spectrum which is separated into its donor and acceptor components, and is corrected for leak-through and acceptor cross-excitation using a novel, off-line precalibration procedure. Fully corrected donor and acceptor spectra, termed pure spectra, are used for the pixel-based calculation of λFRET efficiency, which renders an efficiency image.

Validation of λFRET Method Using Tandem Yellow Fluorescent Protein-Cyan Fluorescent Protein Constructs Generated as FRET Standards

To validate the λFRET method, a number of yellow fluorescent protein (YFP)-cyan fluorescent protein (CFP) fusion constructs with variable linker length and stoichiometry were genetically engineered. Tandem YFP-CFP fusions connected through scaffolds differing in length were designed to test λFRET accuracy. R16 domain of chicken brain α-spectrin (R16), and the immunoglobulin binding domain of streptococcal protein G (B1G) for both of which the 3D structures have been solved (Gronenborn et al., 1991; Pascual et al., 1997) (PDB accession numbers 1AJ3 and 1GB1) were used as linkers. According to their rigid structure and with their predicted length of 41 and 25 Å, R16 and B1G standards were expected to render medium and low FRET efficiencies, respectively. We also designed two fusion constructs incorporating short synthetic

flexible peptide linkers of 8 and 17 amino acids (named Ln8aa and Ln17aa, respectively), which were predicted to allow the closest proximity of fluorescent proteins and therefore optimal FRET efficiency. A caspase-sensitive probe, LEVD, consisting on two caspase cleavage sites inserted as a spacer into YFP-CFP fusion construct served as a negative control with fixed stoichiometry when cells where subjected to caspase activating campthotecin (Cpt) apoptotic stimuli. A schematic representation of the different constructs is shown in Figure 3a. To test the λFRET method, we analyzed MDA-MB-231 cells expressing each of these standards, or CFP and YFP coexpressed separately, which served as a negative control of unknown stoichiometry. Raw FRET spectra obtained from Ln17aa, B1G, and R16 constructs by spectral confocal imaging showed marked qualitative differences (Fig. 3b), that translated into significant differences in the λFRET efficiency images (Fig. 3c). Ln8aa and Ln17aa displayed equivalent results (not shown). As expected, the flexible peptide linker (Ln17aa) displayed the highest FRET efficiency value, and B1G or R16 domains displayed lower, but significant, efficiencies according to the length of the linker placed between the fluorescent proteins. These experiments validated λFRET as a method to calculate FRET efficiency that is specific and sensitive to distance variations.

λFRET Performance Evaluation

FRET standards developed herein were used to compare the performance of λFRET with other, well-established FRET-measuring methods based on confocal microscopy. The FRET efficiency values were obtained using λFRET, sensitized emission and acceptor photobleaching methods, as detailed in Supporting information Appendix 2. Analysis was performed in parallel in MDA-MB231 cells expressing either the Ln17aa, B1G, R16, or LEVD fusion constructs treated or not with Cpt, or CFP+YFP expressed separately (Fig. 4a). The λFRET results were consistent with those obtained with acceptor photobleaching method (Fig. 4a). Sensitized emission values resulted more unstable especially at low transfer efficiencies (R16) and negative control (CFP+YFP) (Supp. Info., Fig. S3). Fold induction calculation of the ratio of FRET efficiency obtained for the different FRET standards compared with the negative control (cells expressing LEVD treated with Cpt) represents an evaluation of the capability of the different methods of resolving molecular distances is shown in Supp. Info., Fig. S3). These results showed that, although other methods resolved the different distances of the tandem fusions, λFRET was more sensitive to distance variations (Fig. 3a and Supp. Info., Fig. S3). To further evaluate FRET accuracy, we expressed C5V, C17V, and C32V FRET standards that have been previously characterized (Koushik et al., 2006). The λFRET results obtained with these standards were in good agreement with the reported FRET efficiency values generated by averaging the results of E-FRET, FLIM, and sRET methods (Fig. 4b). These results further validate λFRET method and show clearly its advantage resolving molecular distances.

Intermolecular FRET studies are highly dependent on donor and acceptor concentrations. In order to test applicability of the λFRET method for intermolecular FRET of stoichiometry differing from 1:1, we generated CFP-CFP-YFP and CFP-YFP-YFP fusion constructs (Fig. 4c). λFRET resultant pure fluorescence emission intensities were used to calculate donor acceptor stoichiometry from these constructs following the equation;

$$[D]/[A] = \frac{(F^{A}_{\lambda D}/G) + F^{D}_{\lambda D}}{F^{A}_{\lambda A} \cdot R_{\lambda D}/R_{\lambda A} \cdot k}$$

(derived in Supp. Info. Appendix 3)

This equation is derived as a variation of the method described by Chen et al. (2006). Where G is a proportionality constant that represents the ratio of sensitized acceptor emission to the quenched donor emission and can be determining by analyzing two standard encoding donor acceptor fusion FPs differing widely in FRET efficiency. k is the ratio of donor to acceptor fluorescence for equimolar concentrations in the absence of FRET and can be calculated once the G factor is determined using a 1:1 donor–acceptor fusion construct. As detailed in Supporting Information Appendix 3, $[D]/[A]$, G, and k calculation based in λFRET resultant $F^{A}_{\lambda D}$ and $F^{A}_{\lambda A}$ values was generated from Ln17aa and R16aa standard analysis. The mean, $[D]/[A]$ ratios measured from cells expressing CFP-YFP fusion construct were 1.03 ± 0.12, whereas those obtained for the CFP-CFP-YFP and CFP-YFP-YFP were 2.13 ± 0.5 and 0.56 ± 0.16 respectively, very close to the expected values of 1, 2, and 0.5. Then, we analyzed FRET efficiencies by λFRET, sensitized emission, acceptor photobleaching, and spectrofluorometric methods. λFRET, acceptor photobleaching, and spectrofluorometric methods were proven to be quite stable to changes in the concentration of donor and acceptor (Fig. 4d). λFRET efficiency calculation was almost unaffected by addition of CFP, although it was slightly raised by the extra copy of YFP, most probably due to an increased availability of acceptor, rather than to the variation in the concentration. Accordingly, both acceptor photobleaching and spectrofluorometric methods, which are independent of donor/acceptor concentration, also resulted in an increase in efficiency of CFP-YFP-YFP standards compared with Ln17aa tandem (Fig. 4d), demonstrating it is due to an increase in energy transfer ruling out the possibility of a concentration-dependent error. The sensitized emission method underestimated efficiency at any given variation of stoichiometry (Supp. Info. Fig. S3). To demonstrate advantage of λFRET analyzing donor acceptor pairs with high spectral overlap, we constructed a CFP-Ln17aa-GFP fusion which rendered 32% efficiency, equivalent to its CFP-Ln17aa-YFP counterpart. Sensitized emission clearly underestimated efficiency of CFP-GFP and acceptor photobleaching was found useless for this fluorophore pair since bleaching of acceptor also produced donor fluorescence decay (Fig. 5a). Although autofluorescence can represent a problem with FRET determination, it should not affect the λFRET method, since the pixels that cannot be fitted to a reference spectrum are removed from the subsequent FRET calculation. This was formally demonstrated by analyzing cells expressing Ln17aa tandem bearing highly autofluorescent intracellular spots which did not affect the FRET measurement (Fig. 5b). This analysis demonstrates clearly the robustness of the λFRET method under conditions

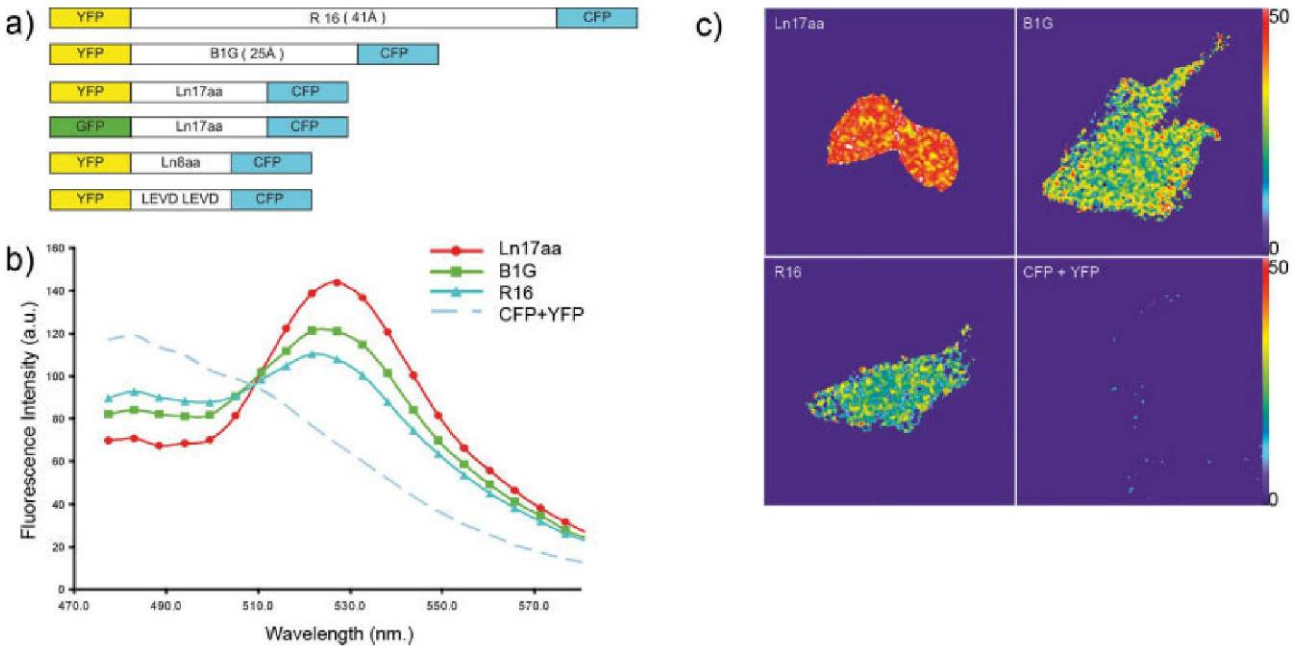

Fig. 3. Validation of the λFRET method with FRET standards. (**a**) Schematic representation of tandem YFP-CFP fusions (R16, B1G, Ln17aa, Ln8aa, and LEVD), and a spectral variant of tandem Ln17aa (GFP-Ln17aa-CFP). (**b**) MDA-MB231 cells were transfected with tandem YFP-CFP constructs (Ln17aa, B1G, and R16) or with YFP and CFP expression vectors (YFP+CFP) used as a negative control. Raw FRET spectra were obtained by spectral confocal imaging upon excitation at 458 nm. (**c**) Representative FRET efficiency pseudocolored images resulting from λFRET analysis of these constructs are shown.

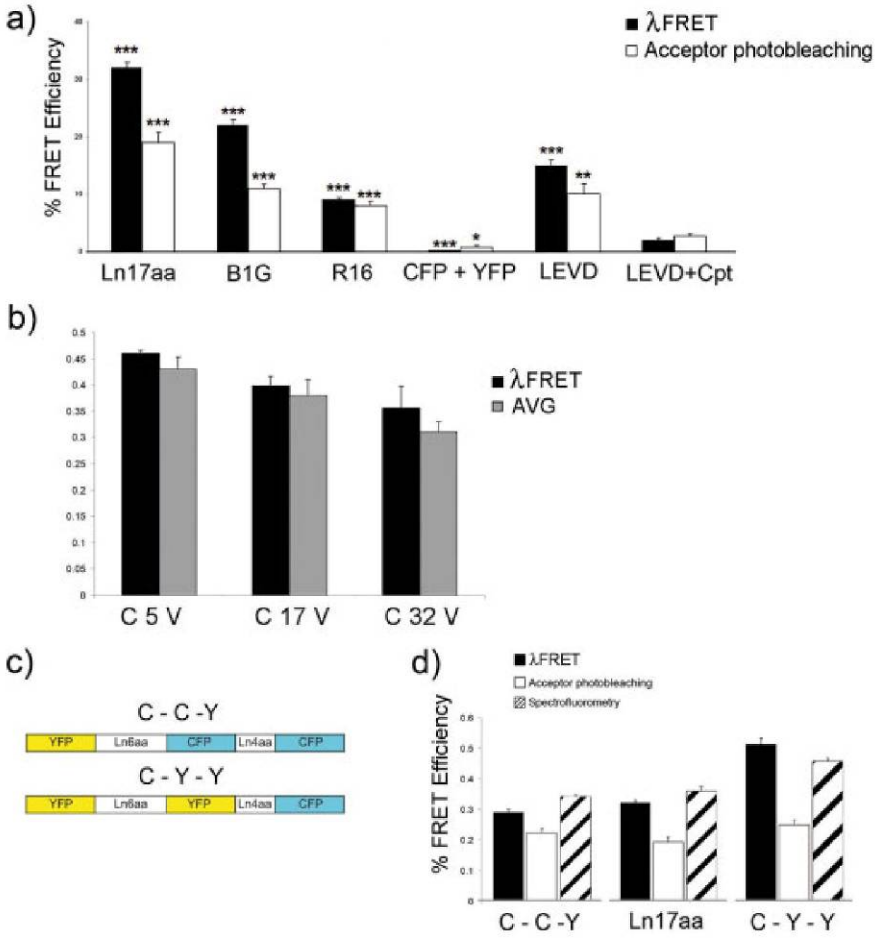

Fig. 4. λFRET comparative evaluation. (**a**) MDA-MB-231 cells were transfected with FRET standards (Ln17aa, B1G, and R16), LEVD, CFP-CFP-YFP, CFP-YFP-YFP, or CFP + YFP. Cells treated or not with 20 μM Cpt for 24 h were analyzed in parallel using λFRET (solid bars), acceptor photobleaching (open bars), or spectrofluorometric methods (dashed bars). The significance of differences between the FRET standard fusion constructs and control (LEVD + Cpt) values was evaluated using Student's *t*-test; $P < 0.05$ was considered significant ($^{*}P < 0.05$, $^{**}P < 0.01$, $^{***}P < 0.001$). (**b**) MDA-MB-231 cells were transfected with FRET standards C5V, C17V, and C32V. FRET efficiency was quantified using λFRET (solid bars) and compared with the average of FRET measurements described for these standards in Koushik et al. (2006) (gray bars). (**c**) Schematic representation of constructs with variable stoichiometry, YFP-CFP-CFP (Y-C-C) and YFP-YFP-CFP (Y-Y-C). (**d**) MDA-MB-231 cells transfected with Y-C-C, Y-Y-C, and Ln17aa were analyzed in parallel using λFRET (solid bars), acceptor photobleaching (open bars), or spectrofluorometric methods (dashed bars). (a–d) Bar diagrams represent FRET efficiency quantification calculated from 75 cells of five independent experiments, expressed as the mean ± SE.

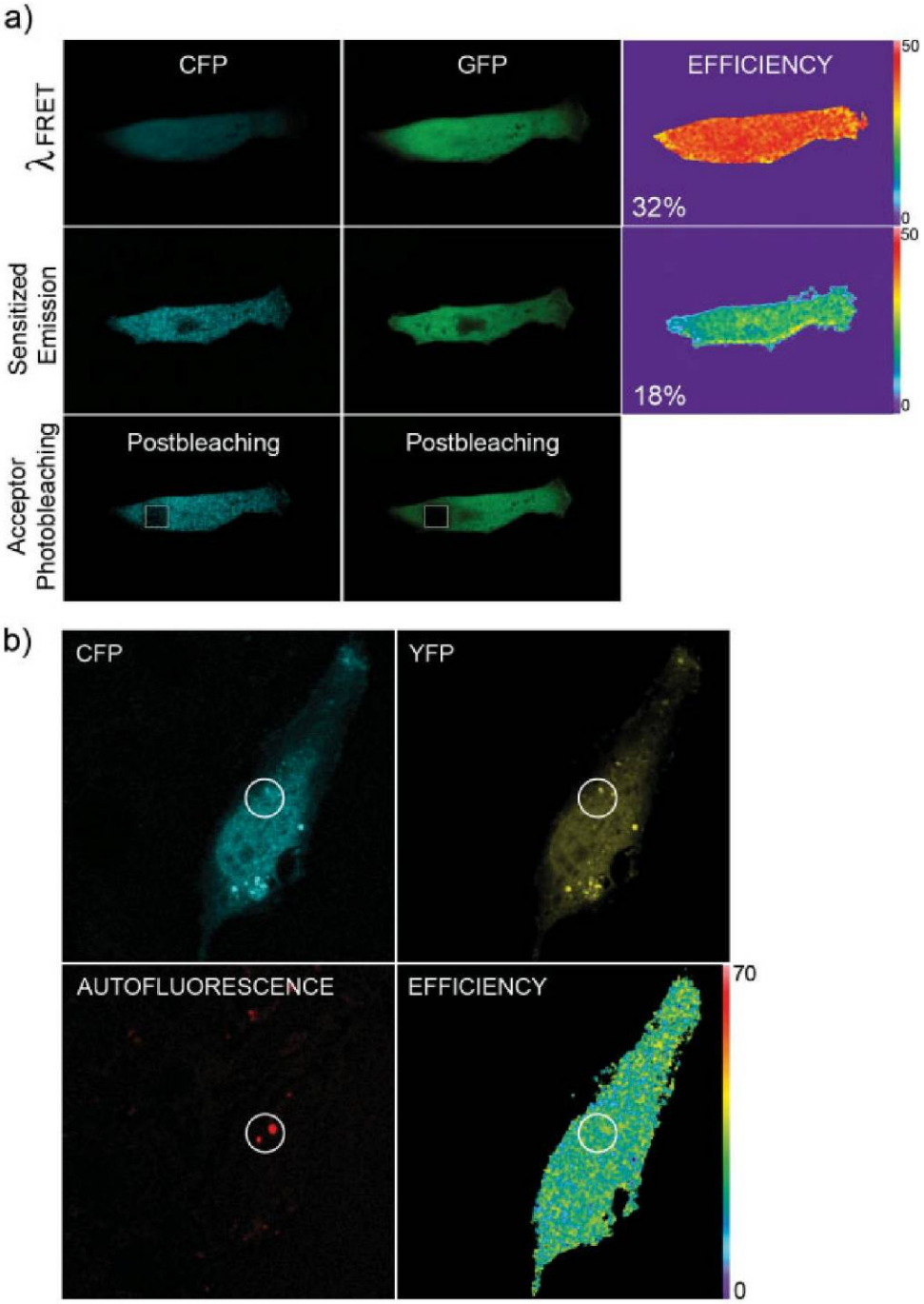

Fig. 5. Fluorochrome spectral overlap and autofluorescence does not affect λFRET efficiency measurement. (**a**) MDA-MB-231 cells expressing CFP-Ln17aa-GFP were analyzed. CFP, GFP, and efficiency images obtained using λFRET, sensitized emission, and acceptor photobleaching methods are shown. Measured FRET efficiency values are indicated. MDA-MB-231 cells expressing CFP-Ln17aa-YFP FRET standard were analyzed by λFRET. Expression of CFP (blue), YFP (yellow), autofluorescent granules (red), and FRET efficiency pseudocoloured image are shown. Circle highlights localization of autofluorescent granules.

of donor/acceptor stoichiometry differing from 1:1, high fluorochrome spectral overlap and cellular autofluorescence. Altogether, these results show that the performance was better for λFRET than for acceptor photobleaching and sensitized emission methods.

Application of λFRET to Fixed and Live Cell Intermolecular FRET Imaging

Interaction of CD44 and moesin has been previously studied using conventional biochemical approaches and by FRET studies monitored by FLIM microscopy (Legg et al., 2002; Yonemura et al., 1998), and therefore is a good candidate to test performance of λFRET for studying typically weak physiological molecular interactions. With this aim we analyzed breast carcinoma MDA-MB-231 cells expressing, moesin-GFP and CD44-monomeric red fluorescent protein (mRFP), or CD44-GFP and caveolin-mRFP used as a negative control. As expected, both acceptor photobleaching and λFRET methods rendered positive FRET efficiency values for CD44–moesin but not for CD44–caveolin analysis (Fig. 6a). To demonstrate applicability of λFRET for monitoring dynamic interactions in live cell studies, we

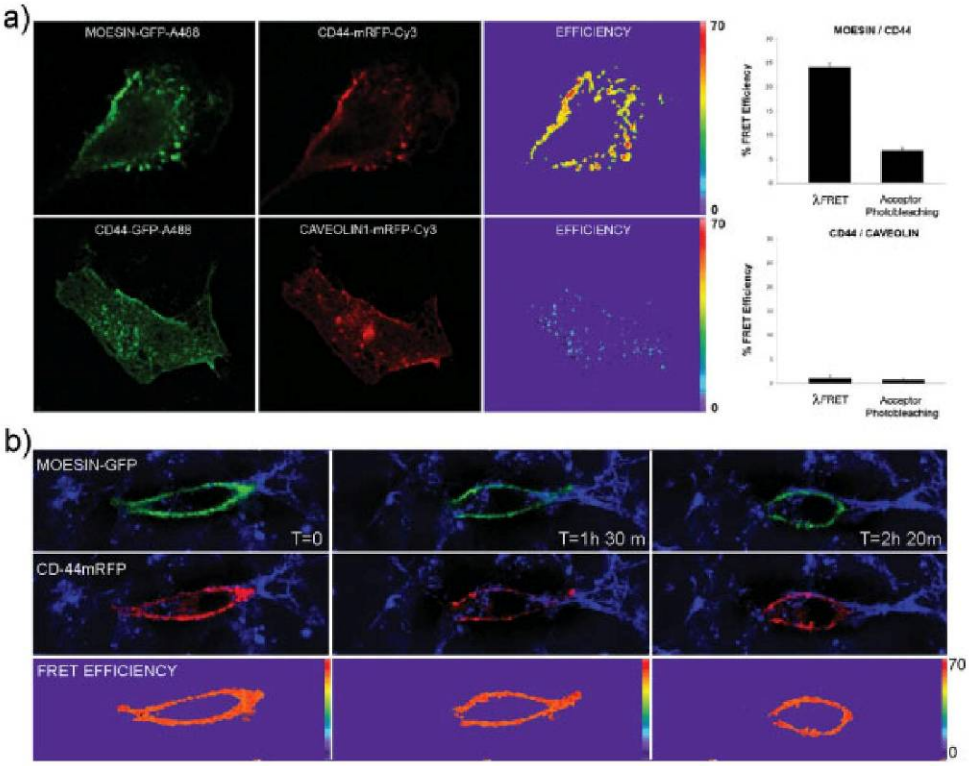

Fig. 6. λFRET study of CD44–moesin interaction in fixed and live cell studies of tumor cell invasion. (**a**) MDA-MB-231 cells were cotransfected with moesin-GFP and CD44-mRFP, or CD44-GFP and caveolin-mRFP, and plated on HA-Col I coated cover slips. Cells were fixed and stained with anti-CD44, anti-ERM, or anticaveolin antibodies revealed with secondary antibodies labeled with Alexa 488 or Cy3. Representative donor (green) and acceptor (red) fluorescence and pseudocolored FRET efficiency images are shown. Bar diagrams represent mean FRET efficiency values calculated using λFRET or acceptor photobleaching methods from 12 cells in three independent experiments. (**b**) MDA-MB-231 cells cotransfected with CD44-mRFP and moesin-GFP were embedded in 3D collagen matrices. Representative GFP (green) and mRFP (red) fluorescence, overlaid on the reflection image showing collagen fibers (blue) and pseudocolored λFRET efficiency images depicted from the video sequence at the times indicated are shown.

imaged MDA-MB-231 cells migrating into 3D collagen type-I matrices. A series of λFRET efficiency images depict the sequence of steps of tumor cell invasion where the interaction of CD44 and moesin at the cell surface was detected (Fig. 6b). Although most CD44 and moesin accumulated at the cell poles, this was not translated into higher FRET values at these areas. Regardless of the variations in fluorescence intensity of donor (moesin) and acceptor (CD44), FRET values remained constant during the migratory process, further demonstrating that FRET calculation is independent of the donor/acceptor concentration (Fig. 6b). Together, these studies demonstrate that λFRET is a suitable method for studying intermolecular interactions in both fixed and live cell imaging experiments.

DISCUSSION

Because of limitation of methods for monitoring FRET in living cells using standard, commercially available confocal microscopes, we sought to develop a procedure based on spectral analysis, to take advantage of its unique capability to detect complex changes associated with FRET. The method needed to be sensitive and nondestructive to be able to detect the typically weak physiological interactions in live cell studies. We herein describe the new λFRET method, which we validated with structurally characterized FRET standards of variable lengths that were designed and constructed for this purpose demonstrating λFRET outstanding performance compared with other well-established FRET methods.

Spectral imaging based linear unmixing algorithms are very useful for quantifying individual fluorophores from a combined emission spectra but fail when FRET is occurring because it takes into account spectral bleed-through contaminations but not for acceptor cross-excitation derived artifacts (Thaler et al., 2005). Different approaches for measuring FRET using spectral imaging based unmixing algorithms have been reported (Gut et al., 2004; Neher and Neher, 2004; Raicu et al., 2005; Thaler et al., 2005; Zimmermann et al., 2002). To overcome these linear unmixing limitations, these spectral methods introduce lifetime (Neher and Neher, 2004; Raicu et al., 2005) or acceptor photobleaching measurements (Gut et al., 2004; Raicu et al., 2005; Zimmermann et al., 2002) to the FRET calculations. Thaler and coworkers have implemented sRET, that uses a spectral unmixing formula which incorporates the emission by the donor and acceptor as result of direct excitation as well as emission from the acceptor resulting from FRET that is solved to obtain donor and acceptor concentrations as well as FRET efficiency values (Thaler et al., 2005). The relative contri-

bution of each fluorochrome and an excitation wavelength-dependent constant k are determined from spectral datasets coming from samples with only donor or acceptor at equal concentrations excited at two different wavelengths. Similarly to sRET, another spectral FRET method, lux-FRET, is also based on spectral unmixing two wavelength excitation measurements (Wlodarczyk et al., 2008) and uses four calibration spectra from donor and acceptor samples imaged at two excitation wavelengths. Interestingly, lux-FRET calculations take into consideration the contributions of unpaired donor and acceptor fluorophores and the influence of incomplete labeling of the interacting partners. The recently described spectral psFRET method (Chen et al., 2007) utilizes an spectral unmixing approach to calculate FRET efficiency based in confocal microscopy. psFRET removes acceptor cross-excitation at donor wavelengths using an algorithm that matches fluorescence intensity levels of control cells that express acceptor alone, to the sample that express both donor and acceptor fluorochromes.

Unlike any other previously described FRET measuring method, λFRET introduces a novel correction procedure based on the use of reflection images to normalize for different radiation light intensities. In addition, the λFRET method decomposes the FRET spectra into its donor and acceptor components using an interpolation procedure different from linear unmixing. This interpolation procedure has the disadvantage of being more susceptible to a reduction in the number of spectral detection windows compared to linear unmixing. However, the strength of our interpolation procedure is that it enables us to eliminate the pixels that cannot be fitted to the reference spectra for subsequent FRET calculation making this method independent of autofluorescence (Fig. 5b) or other sources of unspecific FRET distortions. In addition, it enables us to separate highly overlapping spectra, as was demonstrated here for the CFP GFP pair (Fig. 5a). Although we use a high number of overlapping detection windows in our λ stacks, the accuracy of λFRET efficiency calculations did not suffer from reducing the spectral channels to 18.

The two widely used methods of FRET quantification by confocal microscopy imaging are acceptor photobleaching and sensitized emission. Acceptor photobleaching is a simple, reproducible and concentration independent method that has a number of limitations, mainly because it is destructive and therefore unsuitable for live cell experiments, and because it gives information only about the bleached area. The FRET efficiency results were in good agreement with those obtained with acceptor photobleaching method, although the latter tended to give lower efficiency values. Taking into account that FRET efficiency is an instrument- and methodology-independent parameter, the values measured using these two methods should be equivalent. The differences in the absolute values observed herein are consistent with other studies which have reported that the acceptor photobleaching method renders an underestimation of the FRET efficiency which is reated to incomplete acceptor photobleaching and undesired donor photobleaching caused errors (Berney and Danuser, 2003; Karpova et al., 2003; Raicu et al., 2005).

Sensitized emission based methods are popular for live FRET imaging in laboratories that don't have access to FLIM microscopy. However, our sensitized emission results were unstable and not consistent at low transfer efficiencies (R16) and in the negative (CFP + YFP) control with unknown stoichiometry. This is most probably due to the use of confocal imaging, which raises a number of complications that do not apply to wide field imaging, like the use of two independent detectors and excitation laser lines. Some correction schemes for these errors have been developed (van Rheenen et al., 2004), although they were not accounted for in this work because we used the SP2 Leica confocal software which does not correct them. This may be the main cause of the herein registered inconsistencies. The λFRET method is not subject to these errors since it uses only one detector and the ratio of reflection intensities corrects for differences of incident light power coming from the use of different excitation laser lines. Another source of problems inherent to this method is the underlying assumption that the amount of leak through is independent of the absolute intensity of the fluorophores and can be calibrated off-line in samples containing only donor or acceptor at arbitrary concentrations. Confocal systems based in photomultiplier (PMTs) which have a limited linear range of detection, are more likely to render inconsistencies resulting from assuming a linear dependence of the spectral bleed-through component on the fluorescence intensity. Others have implemented interesting correction procedures to avoid instability problems of the sensitized emission method coming from this source (van Rheenen et al., 2004; Elangovan et al., 2003). However, these errors should, in principle not affect the λFRET method since the spectral leak-through corrections are not based in absolute intensities, or determining the contribution of fluorophore as in spectral unmixing, but is based in spectral curve interpolation. Additionally, λFRET inherently takes into account exclusively the values coming from the PMTs linear range of detection and therefore should avoid errors coming from this source.

λFRET is similar to sensitized emission based methods since both rely on the measurement of acceptor fluorescence emission due to energy transfer, although λFRET has a number of advantages. (1) Because it is based not on absolute fluorescence intensities, but on the analysis of spectral curve integrals, this method should be more robust to photobleaching induced by repeated analysis of the sample in live cell experiments. λFRET also avoids the variability resulting from the nonlinear relation between the leak-through and absolute fluorescence intensities. (2) λFRET monitors simultaneous changes in donor and acceptor fluorescence and is therefore more reliable. The measurements should in principle be less susceptible to artifacts caused by nonspecific quenchers such as formaldehide fixation, which has been shown to quench Cerulean and Venus FPs differentially and affect donor acceptor ratios dramatically (Chen et al., 2006). (3) Imaging of control single-labeled samples for spectral bleed-through corrections can be performed once for any given fluorochrome pair and microscope setup as a precalibration procedure, and used for subsequent FRET measurements. This avoids additional causes of

variability in the efficiency calculation because of inconsistencies in donor and acceptor concentrations between the control and the double-labeled sample. (4) Although detector PMT settings (gain and offset) must be kept constant, the normalization of excitation light intensity inherent to the λFRET method permits free tuning of the excitation light intensity, allowing a good signal-to-noise ratio imaging that avoids saturation effects. In addition, the normalization for the excitation light intensity corrects for variability because of laser instability in live cell studies. (5) Its ability to unmix spectrally overlapping signals, as demonstrated by the analysis of CFP-GFP tandem, allows high flexibility in the choice of FRET probes. Our comparison of methods using FRET standards tested in parallel demonstrated superior specificity, sensitivity, and stability of λFRET than both acceptor photobleaching and sensitized emission. (6) λFRET can be used to measure donor acceptor ratios. Moreover, λFRET was found to be quite stable at different donor/acceptor concentrations and independent of fluorochrome spectral overlap and autofluorescence. The main drawback of λFRET is that spectral imaging is time consuming and therefore not suitable for analyzing rapid live cell processes. However, commercially available spectral confocal instruments can work at an extremely high scan speed, and spectral acquisitions can be acquired simultaneously with an array of detectors working in parallel, so time is not a practical limitation. There are still some advantages of FLIM over λFRET, since the fluorescence lifetime is absolutely insensitive to variations in concentration and excitation intensity and no spectral bleed-through correction is needed, factors that relatively limit intensity based steady state measurements. However FLIM has some drawbacks since it requires expensive equipment and skilled manipulation and due to its sensitivity to environmental changes (Wallrabe and Periasamy, 2005).

In summary, the new λFRET method was useful for different combinations of donor–acceptor pairs (Alexa 488-Cy3, CFP-YFP, Cerulean-Venus, CFP-GFP and GFP-mRFP), intramolecular FRET of stoichiometric (1:1) donor–acceptor concentrations, and intermolecular FRET of unknown stoichiometry. More importantly, λFRET was successfully applied to analyzing CD44-moesin interaction in fixed and live cells during tumor cell invasion, demonstrating its outstanding capabilities.

ACKNOWLEDGMENTS

The authors thank Dr. F Blanco for help with design of FRET standards, F Camas, Dr. JF Poyatos, Dr. R Diaz, and Dr. J. Rivera for their helpful advice, and A Piera and Dr. J Llopis for their advice and critical reading of the manuscript. Dr. Mizoi, Dr. Sánchez-Madrid, Dr. Blanco, Dr. Clarke, and Dr. Tsien are acknowledged for providing us with reagents.

REFERENCES

Berney C, Danuser G. 2003. FRET or no FRET: A quantitative comparison. Biophys J 84:3992–4010.

Chen H, Cohen DM, Choudhury DM, Kioka N, Craig SW. 2005. Spatial distribution and functional significance of activated vinculin in living cells. J Cell Biol 169:459–470.

Chen Y, Mauldin JP, Day RN, Periasamy A. 2007. Characterization of spectral FRET imaging microscopy for monitoring nuclear protein interactions. J Microsc 228:139–152.

Chen H, Puhl HL, Koushik SV, Vogel SS, Ikeda SR. 2006. Measurement of FRET efficiency and ratio of donor to acceptor concentration in living cells. Biophys J 95:L39–L41.

Elangovan M, Wallrabe H, Chen Y, Day RN, Barroso M, Periasamy A. 2003. Characterization of one- and two-photon excitation fluorescence resonance energy transfer microscopy. Methods 29:58–73.

Förster T. 1965. Delocalized excitation and excitation transfer. In: Sinanoglu O, editor. Modern quantum chemistry, Vol. 3. New York: Academic Press Inc., pp 93–137.

Gronenborn AM, Filpula DR, Essig NZ, Achari A, Whitlow M, Wingfield PT, Clore GM. 1991. A novel, highly stable fold of the immunoglobulin binding domain of streptococcal protein G. Science 253:657–661.

Gu Y, Di WL, Kelsell DP, Zicha D. 2004. Quantitative fluorescence resonance energy transfer (FRET) measurement with acceptor photobleaching and spectral unmixing. J Microsc 215:162–173.

Jares-Erijman EA, Jovin TM. 2003. FRET imaging. Nat Biotechnol 21:1387–1395.

Karpova TS, Baumann CT, He L, Wu X, Grammer A, Lipsky P, Hager GL, McNally JG. 2003. Fluorescence resonance energy transfer from cyan to yellow fluorescent protein detected by acceptor photobleaching using confocal microscopy and a single laser. J Microsc 209:56–70.

Koushik SV, Chen H, Thaler C, Puhl HL, III, Vogel SS. 2006. Cerulean, venus, and venusY67C FRET reference standards. Biophys J 91:L99–L101.

Legg JW, Lewis CA, Parsons M, Ng T, Isacke CM. 2002. A novel PKC-regulated mechanism controls CD44 ezrin association and directional cell motility. Nat Cell Biol 4:399–407.

Lerner JM, Zucker RM. 2004. Calibration and validation of confocal spectral imaging systems. Cytometry A 62:8–34.

Neher RA, Neher E. 2004. Applying spectral fingerprinting to the analysis of FRET images. Microsc Res Tech 64:185–195.

Pascual J, Pfuhl M, Walther D, Saraste M, Nilges M. 1997. Solution structure of the spectrin repeat: A left-handed antiparallel triple-helical coiled-coil. J Mol Biol 273:740–751.

Raicu V, Jansma DB, Miller RJ, Friesen JD. 2005. Protein interaction quantified in vivo by spectrally resolved fluorescence resonance energy transfer. Biochem J 385:265–277.

Thaler C, Koushik SV, Blank PS, Vogel SS. 2005. Quantitative multiphoton spectral imaging and its use for measuring resonance energy transfer. Biophys J 89:2736–2749.

van Rheenen J, Langeslag M, Jalink K. 2004. Correcting confocal acquisition to optimize imaging of fluorescence resonance energy transfer by sensitized emission. Biophys J 86:2517–2529.

Wallrabe H, Periasamy A. 2005. Imaging protein molecules using FRET and FLIM microscopy. Curr Opin Biotechnol 16:19–27.

Wlodarczyk J, Woehler A, Kobe F, Ponimaskin E, Zeug A, Neher E. 2008. Analysis of FRET signals in the presence of free donors and acceptors. Biophys J 94:986–1000.

Wouters FS, Verveer PJ, Bastiaens PI. 2001. Imaging biochemistry inside cells. Trends Cell Biol 11:203–211.

Yonemura S, Hirao M, Doi Y, Takahashi N, Kondo T, Tsukita S. 1998. Ezrin/radixin/moesin (ERM) proteins bind to a positively charged amino acid cluster in the juxta-membrane cytoplasmic domain of CD44. CD43, and ICAM-2. J Cell Biol 140:885–895.

Zhang J, Campbell RE, Ting AY, Tsien RY. 2002. Creating new fluorescent probes for cell biology. Nat Rev Mol Cell Biol 3:906–918.

Zimmermann T, Rietdorf J, Pepperkok R. 2003. Spectral imaging and its applications in live cell microscopy. FEBS Lett 546:87–92.

Zimmermann T, Rietdorf J, Girod A, Georget V, Pepperkok R. 2002. Spectral imaging and linear un-mixing enables improved FRET efficiency with a novel GFP2-YFP FRET pair. FEBS Lett 531:245–249.

4.3 POLARIZED MT1-MMP-CD44 INTERACTION AND CD44 CLEAVAGE DURING CELL RETRACTION REVEAL AN ESSENTIAL ROLE FOR MT1-MMP IN CD44-MEDIATED INVASION

Raquel Marrero-Diaz, José J. Bravo-Cordero, Diego Megías, María A. García, Rubén A. Bartolomé, Joaquin Teixido, and María C. Montoya

En este trabajo se hace uso de herramientas avanzadas de microscopía óptica aplicadas al estudio de la relación entre la molécula de adhesión CD44 y la metaloproteinasa MT1-MMP, y como se coordinan en células tumorales promoviendo la invasión celular en matrices tridimensionales de colágeno.

En concreto gracias al empleo del método λFRET, se revela la interacción preferencial entre ambas proteínas en la zona posterior de las células en migración, tanto en muestras fijadas como en células vivas, siendo esta una prueba de concepto de la aplicabilidad del método.

A su vez se presenta un novedoso biosensor fluorescente de CD44 en el que se puede seguir como esta molécula trans-membrana es procesada por su porción extracelular de forma diferencial en la región posterior de las células tumorales durante ensayos de invasión.

En este trabajo he participado en la planificación y diseño de los experimentos, ayudando en la preparación de muestras, su adquisición, análisis de imagen e interpretación y presentación de las mismas, en concreto en los ensayos de FRET y los ensayos que requirieron del uso del microscopio confocal en los que se observó la interacción con MT1-MMP y la adquisición del sensor de procesamiento de CD44.

Cell Motility and the Cytoskeleton 66: 48–61 (2009)

Polarized MT1-MMP-CD44 Interaction and CD44 Cleavage During Cell Retraction Reveal an Essential Role for MT1-MMP in CD44-Mediated Invasion

Raquel Marrero-Diaz,[1] Jose J. Bravo-Cordero,[1] Diego Megías,[1] Maria A. García,[1] Ruben A. Bartolomé,[2] Joaquin Teixido,[2] and María C. Montoya[1]*

[1]*Confocal Microscopy and Cytometry Unit, Biotechnology Programme, Centro Nacional de Investigaciones Oncológicas (CNIO), Madrid, Spain*
[2]*Department of Cellular and Molecular Physiopathology, Centro de Investigaciones Biológicas, Consejo Superior de Investigaciones Científicas, Madrid, Spain*

The adhesion molecule CD44 and the membrane-type matrix metalloproteinase MT1-MMP act coordinately in tumor cells to promote cell invasion through a yet unclear mechanism. We are interested in studying the interplay between CD44 and MT1-MMP in carcinoma cells embedded in HA containing three-dimensional collagen I matrices (3D HA-Col I) by time-lapse confocal microscopy imaging. Here we report the in vivo interaction between CD44 and MT1-MMP, revealed by fluorescence resonance energy transfer (FRET) microscopy. MT1-MMP interacts with CD44 preferentially at the trailing edge of the invading tumor cells during rear retraction and on membrane fragments released during the invasion process. A fluorescent biosensor designed to monitor the proteolytic processing of CD44 by live cell imaging demonstrates that cleavage of the CD44 extracellular domain is enriched in the retracting rear ends of invasive tumor cells. Invasion assays showed that MT1-MMP mediates CD44-dependent tumor-cell invasion, whereas CD44 is not essential for MT1-MMP-mediated invasion of 3D HA-Col I matrices. Together, our results support a role for MT1-MMP in cell retraction during CD44-mediated cell invasion. Cell Motil. Cytoskeleton 66: 48–61, 2009.

Key words: matrix metalloproteinases; MT1-MMP; migration; CD44; tumour; invasion

INTRODUCTION

Migration is a process with complex spatial and temporal regulation and it plays a prominent role in the pathophysiology of tumor cell invasion and metastasis. Cell invasion relies on a highly polarized cell morphology and involves a series of important events, including (i) cell adhesion to the extracellular matrix (ECM) and actin polymerization, leading to membrane protrusion of the leading edge; (ii) degradation of extracellular components by metalloproteinases at the leading edge to release matrix steric resistance, allowing the advancing front of the cell to move forward [Wolf et al., 2007]; and (iii) detachment of the trailing edge, which involves mecha-

Additional Supporting Information may be found in the online version of this article.

Contract grant sponsor: Fondo de Investigaciones Sanitarias (FIS), Contract grant numbers: PI061839; Contract grant sponsors: Ministry of Science and Technology of Spain (MCYT), Fundación Canaria Dr. Manuel Morales.

*Correspondence to: Maria C. Montoya, Confocal Microscopy and Cytometry Unit, Biotechnology Programme, Spanish Nacional Cancer Research Center (CNIO), C/ Melchor Fernández Almagro 3. Madrid E-28029, Spain. E-mail: mmontoya@cnio.es

Received 29 May 2008; Revised 3 October 2008; Accepted 15 October 2008

Published online 20 November 2008 in Wiley InterScience (www.interscience.wiley.com).
DOI: 10.1002/cm.20325

nisms such as the disassembly of adhesion structures and the proteolytic cleavage and internalization of adhesion receptors [Friedl and Wolf, 2003]. Proteolytic cleavage is a key mechanism underlying the functional regulation of a number of membrane adhesion receptors. Shedding is particularly active in invasive cancer cells, where cell-surface components, including CD44 and MT1-MMP, are continually released into the extracellular medium [Friedl et al., 1997; Taraboletti et al., 2002; Nagano and Saya, 2004; Bravo-Cordero et al., 2007]. CD44 is a cell adhesion molecule for hyaluronan (HA), collagen, laminin, and fibronectin, and plays an important role in the migratory, invasive, and metastatic behavior of cancer cells [Marhaba and Zoller, 2004]. CD44 binds to the ezrin/radixin/moesin (ERM) proteins [Tsukita et al., 1994; Legg et al., 2002], which act as linkers to the actin cytoskeleton and to membrane type I matrix metalloproteinase (MT1-MMP), which proteolytically cleaves its extracellular domain stimulating cell motility [Kajita et al., 2001].

MT1-MMP is a critical factor in the invasion machinery of tumor cells and is involved in both matrix degradation and the processing of cell-surface receptors. Given its potential degradative activity, MT1-MMP expression at the cell surface is tightly regulated by intracellular vesicle trafficking [Itoh and Seiki, 2006]. MT1-MMP localization to the invasive front allows localized proteolysis of the extracellular matrix, which is a key to its invasion-promoting activity [Nakahara et al., 1997; Lehti et al., 2000; Mori et al., 2002]. Previous studies have showed that the delivery of MT1-MMP to the invasive front is regulated through its association with CD44 [Kajita et al., 2001; Mori et al., 2002; Suenaga et al., 2005]. CD44 would provide a link of MT1-MMP to the actin cytoskeleton through its interaction with ERMs thereby acting as a platform on which MT1-MMP produces matrix degradation [Itoh and Seiki, 2006]. We uncovered an alternative pathway that accounts for the recruitment of MT1-MMP to invasive structures in 3D Col I invading tumor cells, namely the Rab8-mediated intracellular exocytic traffic [Bravo-Cordero et al., 2007]. Although the localization of MT1-MMP to the leading edge has been extensively studied, its role in other membrane localizations has not been addressed.

Here, we investigate the in vivo interaction between CD44 and MT1-MMP using fluorescence resonance energy transfer (FRET) technology. A novel reporter was designed for imaging the proteolytic processing of CD44 by live cell microscopy. We show that the MT1-MMP interaction with CD44 and the MT1-MMP-mediated proteolytic processing of CD44 occurs preferentially at the retracting cell rear and that MT1-MMP is essential for CD44-mediated cell invasion.

MATERIALS AND METHODS

Cell Culture, Transfection, RNA Interference, and Collagen Inclusion

Breast adenocarcinoma MDA-MB-231 cells, human fibrosarcoma HT-1080 cells, and human melanoma BLM cells were maintained in Dulbecco's modified Eagle's medium (DMEM) supplemented with 10% fetal bovine serum (FBS) and 1% Penicillin/Streptomycin. The cells were transfected using Lipofectamine 2000 (Invitrogen, Carlsbad, CA) according to manufacturer's instructions. Twenty-four hours after transfection, the cells were trypsinized and mixed with newly prepared HA-Col I solution (2.4 mg/mL bovine Col I [Vitrogen, Palo Alto, CA], 1 mg/mL HA [Sigma-Aldrich, St Louis, MO], 1 × RPMI, 19 mM Hepes [Gibco, Invitrogen, Carlsbad, CA], 0.19% sodium bicarbonate [Sigma-Aldrich], 5% FBS), which was then allowed to polymerize for 2 h at 37°C (3D HA-Col I), plated onto prepolymerized 3D HA-Col I, or onto uncoated coverslips.

Small interfering RNA (siRNA) duplexes to human MT1-MMP and a control siRNA were designed [Bartolome et al., 2006], and purchased from Ambion (Austin, TX). MDA-MB-231 cells were transfected with siRNAs (20 μM) using X-tremeGene siRNA transfection reagent (Roche Diagnostics, Panzberg, Germany) according to the manufacturer's instructions. After 24 h, cells were transfected with Orange-CD44-GFP construct. 48 h after transfection of siRNAs, cells were either embeded in 3D HA-Col I and analyzed using confocal microscopy imaging to quantitate CD44 shedding or lysed and subjected to western blot analysis for biochemical studies.

Reagents and Antibodies

The reagents used included phorbol myristate acetate (PMA), ionomycin (IO) (Sigma-Aldrich), and GM6001, an MMP inhibitor (Chemicon, Millipore, Billerica, MA). Antibodies used included mouse anti-human CD44 antibody (HP2/9) and rabbit anti-human-ERM antibody (90/3), kindly provided by Dr. F. Sánchez Madrid, Hospital de la Princesa, and Lem-2/15 mouse anti-MT1-MMP antibody [Galvez et al., 2002]. Rabbit anti-caveolin-1 antibody was provided by Dr. M.A. del Pozo, Centro Nacional de Investigaciones Cardiovasculares. Rabbit anti-GFP antibody (Abcam, Cambridge, UK) and mouse anti-tubulin DM1a were from Sigma-Aldrich.

Cloning DNA Constructs

The cDNA of the standard form CD44 was PCR amplified from the CD44 pRc/CMV vector provided by Dr. T Mizoi, using the oligonucleotide primers (forward) 5′-GGAGCTCATGGACAAGTTTTGGTG-3′ and (reverse) 5′- ATGAAGATTGGGGTGTTGGTACCG-3′,

and was cloned into the ECFP-N1 and EGFP-N1 vectors (Clontech, Takara Bio, Otsu, Shiga, Japan) at the *Kpn*I/*Sac*I restriction sites. The CD44-mRFP construct was obtained by subcloning mRFP into the EGFP-N1 restriction sites to generate CD44-GFP. The CD44 shedding reporter was generated by amplifying the cDNA of mOrange fluorescent protein using the oligonucleotide primers (forward) 5′-CCATCGATATGGTGAGCAAGGG CGAG-3′ and (reverse) 5′-CCATCGATCTTGTACAG CTCGTCCATG-3′, from the pRSET-B-mOrange vector (Invitrogen), and inserted into the CD44 pRc/CMV vector at the *Cla*I restriction site to generate mOrange-CD44. mOrange-CD44 cDNA was amplified and inserted into the EGFP-N1 vector at the *Kpn*I/*Sac*I restriction sites, generating Orange-CD44-GFP. Tandem GFP-Orange was generated by amplifying the cDNA of mOrange fluorescent protein using the oligonucleotide primers (forward) 5′-GGGGTACCATGGTGAGCAA GGGC-3′ and (reverse) 5′- CGGGATCCTTACTTGTA CAGCTCGTC-3′ and was then inserted into the EGFP-N1 vector at the *Kpn*I/*Bam*HI restriction sites. The MT1-MMP-YFP, CFP, GFP, and mRFP constructs have been described elsewhere [Bravo-Cordero et al., 2007]. Full-length moesin-GFP, Cav-1-mRFP, and VSV-G-YFP were kindly provided by Dr. F. Sánchez Madrid, Dr. M.A. del Pozo, and Dr. R. Pepperkok, respectively. All constructs were verified by DNA sequencing.

Immunofluorescence and Microscopy

For fixed-cell FRET analysis, MDA-MB-231 cells expressing CD44-GFP and MT1-MMP-mRFP were plated on prepolymerized 3D HA-Col I, fixed, and stained with either mouse anti-human-CD44 antibody (HP2/9) and anti-MT1-MMP antibody (Lem-2/15) previously conjugated with Alexa 488 and Cy3 using protein monoclonal antibody labeling kits from Invitrogen and Jackson ImmunoResearch (Amersham Biosciences, Uppsala, Sweden), respectively. Control cells expressing CD44-mRFP/moesin-GFP and CD44-GFP/Cav-1-mRFP were stained with rabbit anti-ERM (90/3), mouse anti-CD44 (HP2/9), and rabbit anti-caveolin-1 antibodies, and visualized with secondary antibodies labeled with Alexa 488 and Cy3. MDA-MB-231 cells expressing Orange-CD44-GFP were plated on coverslips, fixed, and stained with mouse anti-human-CD44 antibody (HP2/9) and visualized with secondary antibody labeled with Alexa 633. Images were collected with Leica SP2 and SP5 spectral confocal microscopes using 63× objective lenses (Leica, Mannheim, Germany).

λFRET Microscopy and Image Analysis

λFRET analysis was performed as previously described [Megías et al., in press]. In brief, λFRET measurements were based on spectral imaging of a sample containing both donor (Alexa 488-CFP-GFP) and acceptor (Cy3-YFP-mRFP) species, which were excited using λD488/λA543 laser lines (for the pairs Alexa 488/Cy3 and GFP/mRFP) or λD458/λA514 laser lines (for the pair CFP/YFP). For each excitation wavelength, we obtained one reflection image and a λ series of fluorescence images by defining detection windows of 25 nm in width, ranging from 465 to 650 nm. Raw fluorescence images were first corrected for background. Fluorescence intensity was then plotted for each pixel in the spectral data set of the images against the median wavelength value for each emission window to form the raw fluorescence spectra. The raw FRET spectra were then processed to obtain pure spectra by applying leak-through and cross-excitation corrections. The FRET efficiency calculation based on pure spectra analysis generated a pixel-based calculation of FRET efficiency. IDL software (ITT Visual Information Solutions, Boulder, CO) was used to integrate the computerized image analysis functions into a single ''custom-made'' algorithm that could be applied to sets of images and a time-lapse image series to obtain FRET efficiency images.

Quantification of CD44 Shedding Using Confocal Microscopy Imaging

MDA-MB-231 cells expressing tandem GFP-Orange or Orange-CD44-GFP were preincubated or not with the MMP inhibitor GM6001 (10 μM) for 24 h, plated on coverslips, and treated with PMA (10 or 20 ng/mL) or ionomycin (50 nM) for 2 h at 37°C. The cells were plated on coverslips either uncoated or coated with HA or 3D HA-Col I in the presence or absence of Lem-2/15 anti-MT1-MMP antibody (10 μg/mL). To control for the differences in quantum yields of GFP and Orange fluorescence, we used cells expressing the tandem GFP-Orange construct to define image acquisition settings in which the intensities of GFP and Orange were equivalent. The quantitative evaluation of CD44 proteolytic processing was measured as the GFP/Orange ratio fluorescence intensities obtained from microscopic images of invasive cells expressing Orange-CD44-GFP, using the GFP-Orange construct in a ratio (1:1) as the control. GFP/Orange ratio images were obtained with MetaMorph Offline Premier software (Molecular Devices Corporation, Downingtown, PA). The ratio image was built using the *4 Ratios with 64 Intensities* option, which has four distinct hues, each with 64 intensities visible in its contrast/threshold slider. The ratio images were pseudo-colored, ranging from 0 to 2.5, from 0 to 4, or from 0 to 8, where red and blue represent high and low ratio values, respectively. Finally, we used a low-pass fil-

ter of 3 pixels (width) × 3 pixels (height) to obtain the resultant ratio images.

Western Blot Analysis

HT-1080 cells stably expressing Orange-CD44-GFP or MDA-MB-231 cells transiently transfected with MT1-MMP or control siRNA and Orange-CD44-GFP for 48 h were preincubated or not with the MMP inhibitor GM6001 (10 μM) for 24 h and treated or not with 20 ng/mL PMA, a CD44-cleavage-stimulating agent, for an additional 2 h at 37°C. Cell lysates were isolated with lysis buffer (50 mM Tris [pH 7.4], 150 mM NaCl, 1 mM EDTA, 1% Triton, 2 mM $MgCl_2$) supplemented with protease inhibitors. Protein concentrations were determined using the Bio-Rad DC Protein assay kit. Cell lysates were separated by SDS-PAGE and transferred to a nitrocellulose membrane under semi-dry conditions. The membrane was then blocked with 5% nonfat milk in PBS-Tween 0.2% and incubated with polyclonal anti-GFP antibody (1/1000; Abcam), and monoclonal anti-tubulin DM1a antibody (1/10,000; Sigma). Alexa-Fluor-680-conjugated secondary antibodies were used to visualize and quantify the proteins with the Odyssey Infrared Imaging System (Li-COR, Biosciences, Lincoln, NE).

Cell Invasion Assays

Invasion assays of MDA-MB-231 and BLM cells transfected with the different constructs were performed in HA-3D-Col-I-coated 8 μm pore transwell chambers (Corning, Costar, New York, NY). Twenty-four hours after transfection, the cells were seeded at 5×10^4 cells/well in serum-free medium in the presence of 10 μg/mL blocking antibodies: anti-CD44 (HP2/9), anti-MT1-MMP (Lem-2/15), control isotype IgG1 or MMP inhibitor GM6001 (10 μM). The cells were allowed to transmigrate to 10% FBS medium for 48 h and were imaged by confocal microscopy. Invasion was quantified by the image analysis of GFP- or GFP-Orange-expressing cells counted at the top and bottom of the chamber using Imaris software (Bitplane AG, Zurich, Switzerland). The bars represent the percentage of invasive cells relative to the total number of fluorescent cells.

Statistical Analysis

All numerical values reported represent means ± S.E. The statistical significance of differences between the experimental and control values was evaluated using Student's t test. $P < 0.05$ was taken as the limit of statistical significance ($*P < 0.05$; $**P < 0.01$; $***/^{+++}P < 0.001$).

RESULTS

Polarized Interaction Between MT1-MMP and CD44 During Tumor Cell Invasion

CD44 and MT1-MMP function in a coordinated manner to promote cell invasion, although the precise mechanism behind this interplay is as yet unclear [Kajita et al., 2001; Mori et al., 2002; Vivinus-Nebot et al., 2004]. To study the regulation of CD44 and MT1-MMP during the invasion process, we first expressed cyan fluorescent protein tagged CD44 (CD44-CFP) and yellow fluorescent protein tagged MT1-MMP (MT1-MMP-YFP) in breast carcinoma MDA-MB-231 cells and embedded them in three-dimensional (3D) hyaluronan (HA)-collagen 1 (Col I) matrices. The cells typically acquired a bipolar morphology, displaying a front or leading edge (LE) that determines the direction of movement and a rear or trailing edge (TE) that eventually retracts. Monitoring the molecular dynamics by live cell confocal imaging showed clear colocalization of CD44 and MT1-MMP during cell exploratory contacts with the ECM. Most interestingly, these studies revealed enrichment of both CD44 and MT1-MMP at the trailing edge of the cell preceding and during the detachment of the rear of the cell during migration (Fig. 1 and Supporting Video 1). Colocalization analysis at different membrane localizations is shown (Supporting Fig. 1). Although standard biochemical approaches have previously demonstrated that MT1-MMP forms a complex with CD44 via its hemopexin domain [Mori et al., 2002], there is still no in vivo evidence of the CD44-MT1-MMP interaction. To address this issue, we performed FRET studies, which allowed us to demonstrate this in vivo molecular interaction and analyze its sub-cellular localization. First, fixed MDA-MB-231 cells expressing either CD44-GFP, and monomeric red fluorescent protein tagged MT1-MMP (MT1-MMP-mRFP), moesin-GFP and CD44-mRFP, or CD44-GFP and caveolin-1 (Cav-1)-mRFP were analyzed using two different FRET analysis methods, namely, λFRET and acceptor photobleaching. We used a recently developed λFRET method [Megías et al., In press], because it is highly sensitive and reproducible, and unlike acceptor photobleaching method, it is applicable to live cell studies. CD44-Cav-1 produced negative FRET results, whereas CD44-moesin produced positive FRET results in cells plated on coverslips coated with Col I and HA (Fig. 2a). Although homogeneous FRET efficiency values were recorded for the CD44-moesin interaction, the CD44-MT1-MMP pair displayed a heterogeneous distribution of FRET efficiency values across the cell surface. For quantitative purposes, the two poles of the cells were classified as leading or trailing edges. Front/rear polarity was established by the direction of cell movement in live cell experiments or by

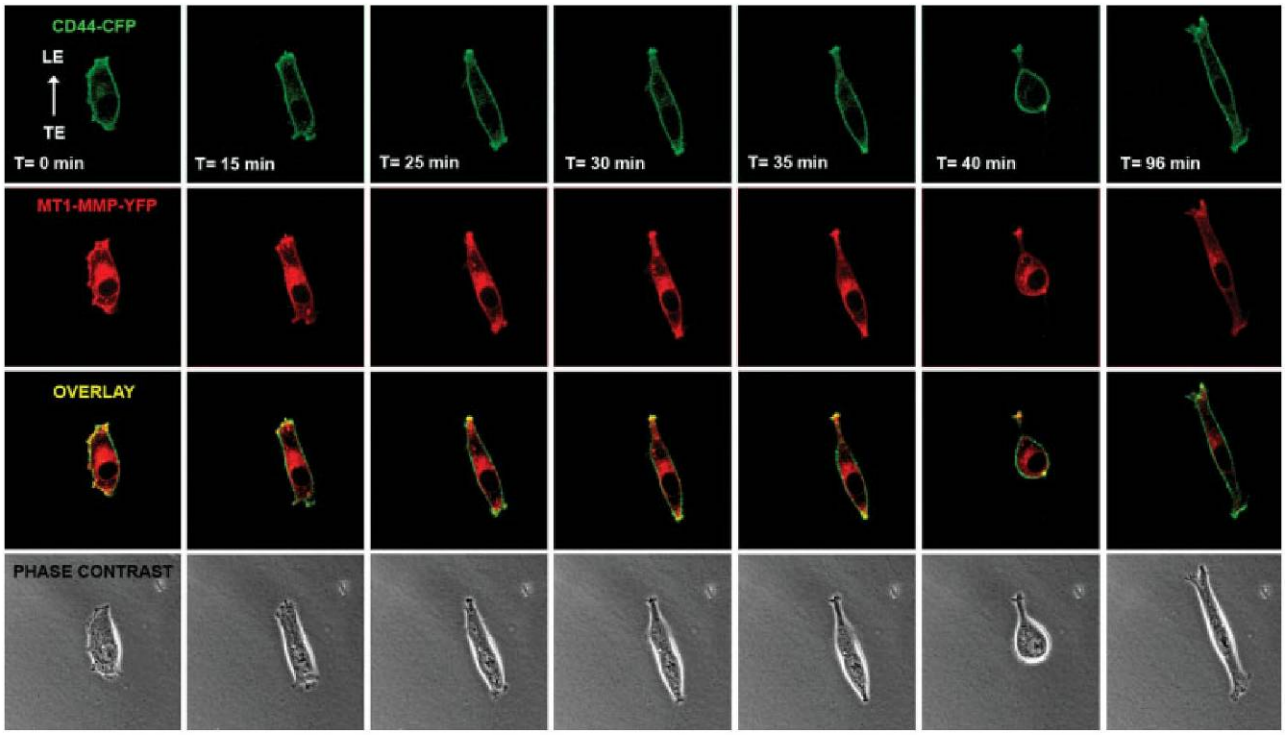

Fig. 1. Dynamics of CD44 and MT1-MMP localization in invading carcinoma cells. Breast carcinoma MDA-MB-231 cells were cotransfected with CD44-CFP and MT1-MMP-YFP, embedded in HA-3D Col I matrices, and analyzed by live cell confocal microscopy imaging. Representative CFP (green) and YFP (red) fluorescence images, their superimposition, and a transmitted light image showing collagen fibers (gray) obtained at the times indicated are shown. Position of the leading (LE) and trailing edges (TE) is indicated. The arrow indicates the direction of movement.

localizing the track of the membrane fragments deposited behind the migrating cell in fixed cell experiments. Membrane fragments that remain attached to the matrix after the retraction of the cell rear, in the process termed ripping (RIP), were also analyzed. CD44-MT1-MMP FRET efficiency values were significantly higher in the ripping and cell trailing edge compared with that in the leading front, where FRET analysis rendered low efficiency values (Fig. 2a). This interaction was also studied in human fibrosarcoma HT1080 cells. Exogenously expressed CD44-CFP and MT1-MMP-YFP, also displayed significant differences in FRET results measured at different membrane sub-domains (Fig. 2b).

To study the spatial and temporal regulation of this interaction, we performed FRET studies on live MDA-MB-231 cells expressing CD44-CFP and MT1-MMP-YFP. Consistent positive FRET efficiency values were recorded during the process of rear retraction in cells invading HA-3D Col I, confirming that the MT1-MMP-CD44 interaction takes place mainly at the trailing edges of migrating cells (Fig. 3a). As a control, we studied cells expressing CD44-mRFP and moesin-GFP. Although most CD44 and moesin accumulated at the cell poles, this was not traduced into higher FRET efficiency values in these areas, which remained constant during the migratory process regardless of their dynamic redistribution (Fig. 3b). These results together demonstrate that, ''in vivo,'' the CD44-MT1-MMP interaction is enriched at the rear of the cell and in the membrane fragments released into the extracellular medium by invasive cells.

MT1-MMP-Dependent Proteolytic Cleavage of the CD44 Extracellular Domain is Enriched at the Retracting Trailing Edges of Invading Tumor Cells

Because MMP inhibitors abolish CD44 processing and cell migration on HA, matrix metalloproteinase-dependent CD44 cleavage must play a critical role in tumor cell migration [Okamoto et al., 1999b; Kajita et al., 2001; Mori et al., 2002]. The polarized MT1-MMP-CD44 interaction reported here could be related to CD44 proteolytic processing at the cell rear. To directly address this issue, we generated a chimeric construct of CD44 tagged with both Orange and GFP fluorescent proteins at the N-terminal extracellular and C-terminal cytoplasmic domains, respectively (Figs. 4a and 4b). A GFP-Orange tandem was generated as a reference construct. GFP and Orange fluorescence images obtained with a

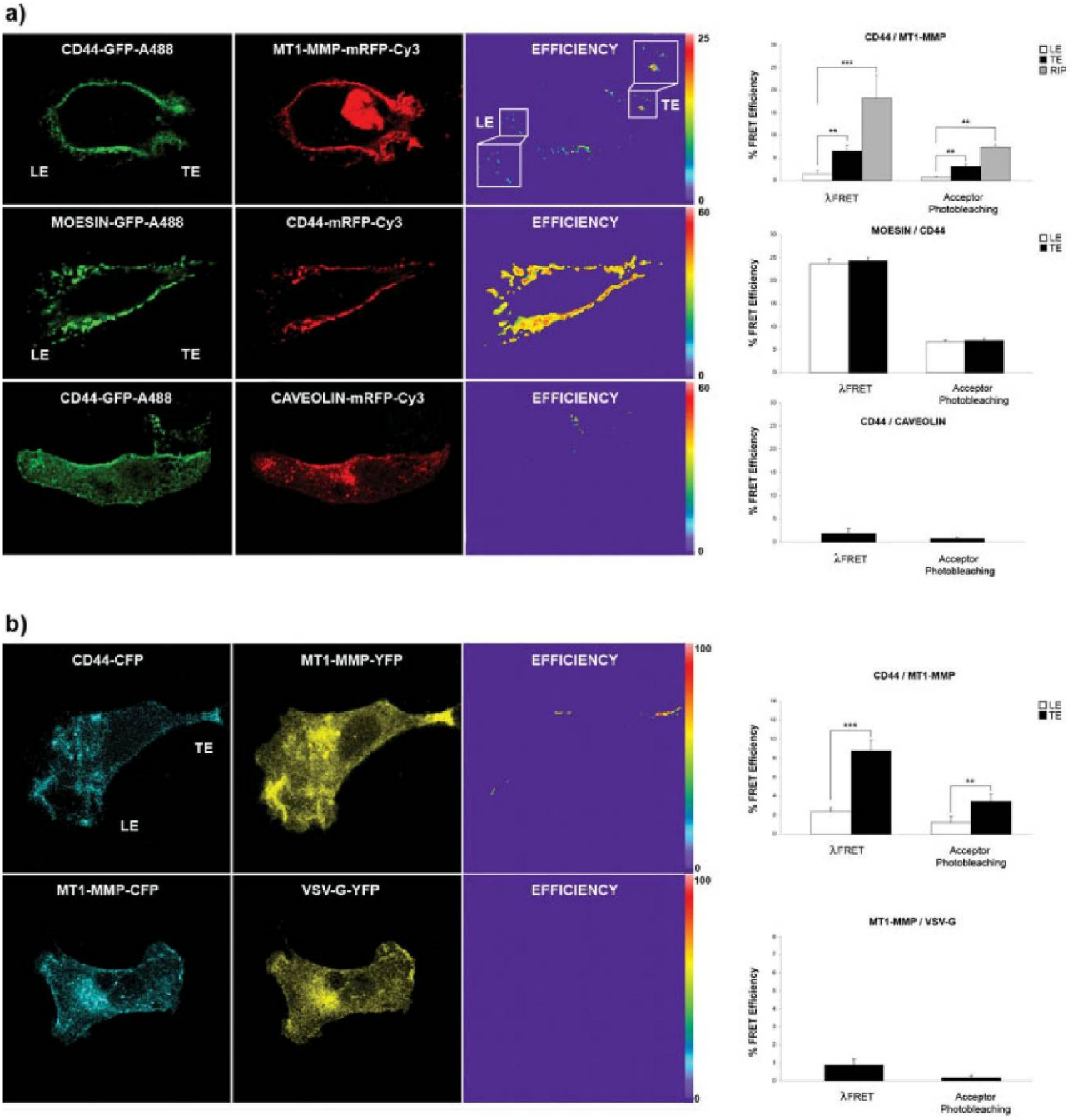

Fig. 2. Sub-cellular localization of the CD44-MT1-MMP interaction at the trailing edge of the cell. (**a**) Breast carcinoma MDA-MB-231 cells cotransfected with CD44-GFP and MT1-MMP-mRFP, moesin-GFP and CD44-mRFP, or CD44-GFP and Cav-1-mRFP, were plated on HA-Col-I-coated coverslips. The cells were fixed and stained with anti-CD44, anti-MT1-MMP, anti-moesin, or anti-caveolin antibodies labeled with Alexa 488 and Cy3. Representative donor (green) and acceptor (red) fluorescence and pseudo-colored FRET efficiency images are shown. Bar diagrams represent FRET values calculated at the leading and trailing edges (LE and TE, respectively) and ripping (RIP), using λFRET or acceptor photobleaching methods. (**b**) Human fibrosarcoma HT-1080 cells were transfected with either CD44-CFP and MT1-MMP-YFP or MT1-MMP-CFP and vesicular stomatitis virus G protein (VSV-G)-YFP. Representative CFP (cyan) and YFP (yellow) fluorescence and λFRET efficiency pseudo-colored images are shown. Bar diagrams represent the FRET efficiency values calculated using the λFRET or acceptor photobleaching methods at the indicated subcellular locations from 12 cells in three independent experiments.

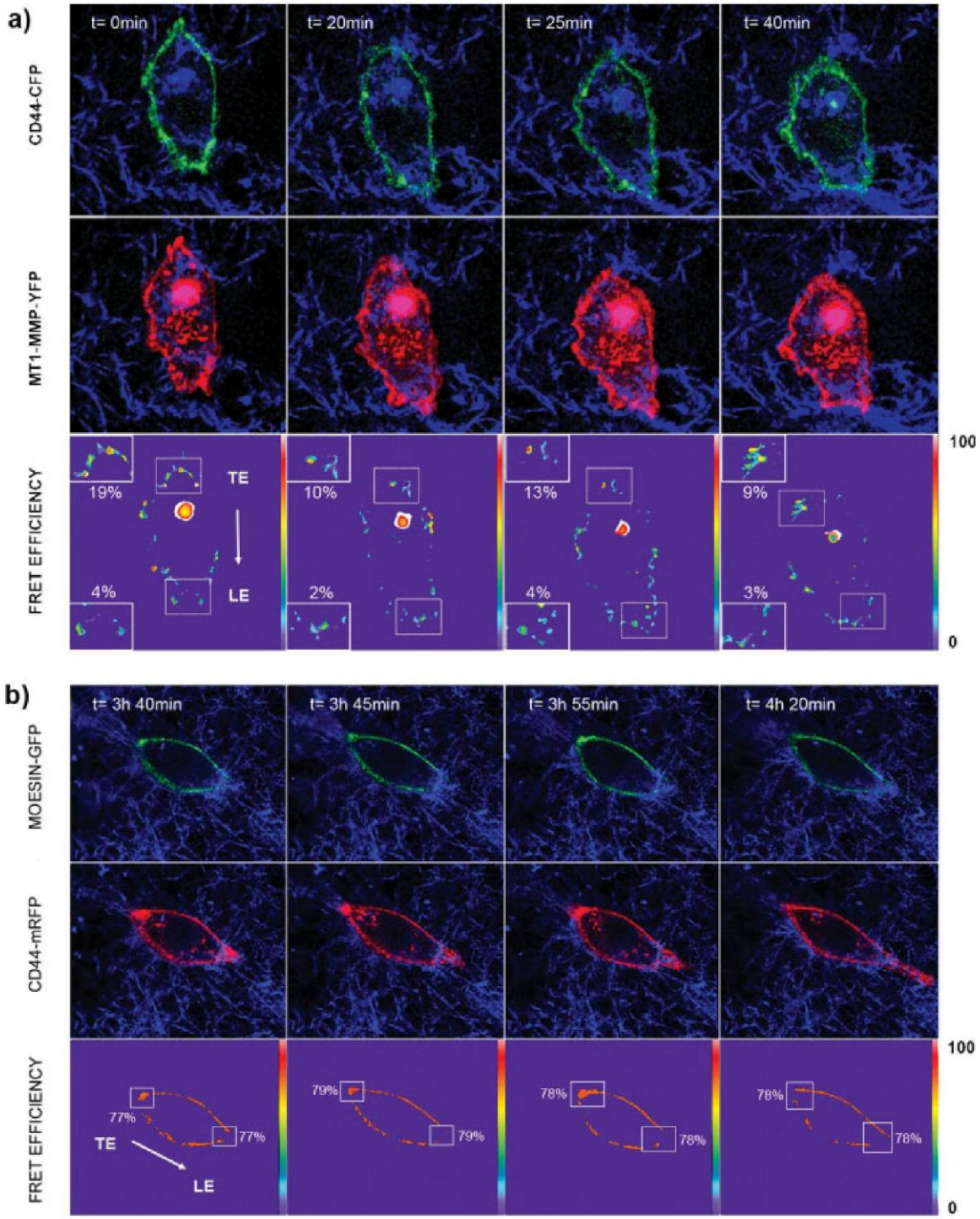

Fig. 3. Dynamic assessment of CD44-MT1-MMP and CD44-moesin interactions in live cell studies of tumor cell invasion. MDA-MB-231 cells were cotransfected with (**a**) CD44-CFP and MT1-MMP-YFP or (**b**) CD44-mRFP and moesin-GFP, and embedded in HA-3D Col I matrices. Representative CFP or GFP (green) and YFP or mRFP (red) fluorescence images superimposed on a reflection image showing collagen fibers (blue) obtained at the times indicated are shown. The arrow indicates the direction of movement. Pseudo-colored λFRET efficiency images include details of the trailing and leading edges (TE and LE) in the upper and lower insets, respectively. The FRET efficiency values calculated in these areas are indicated.

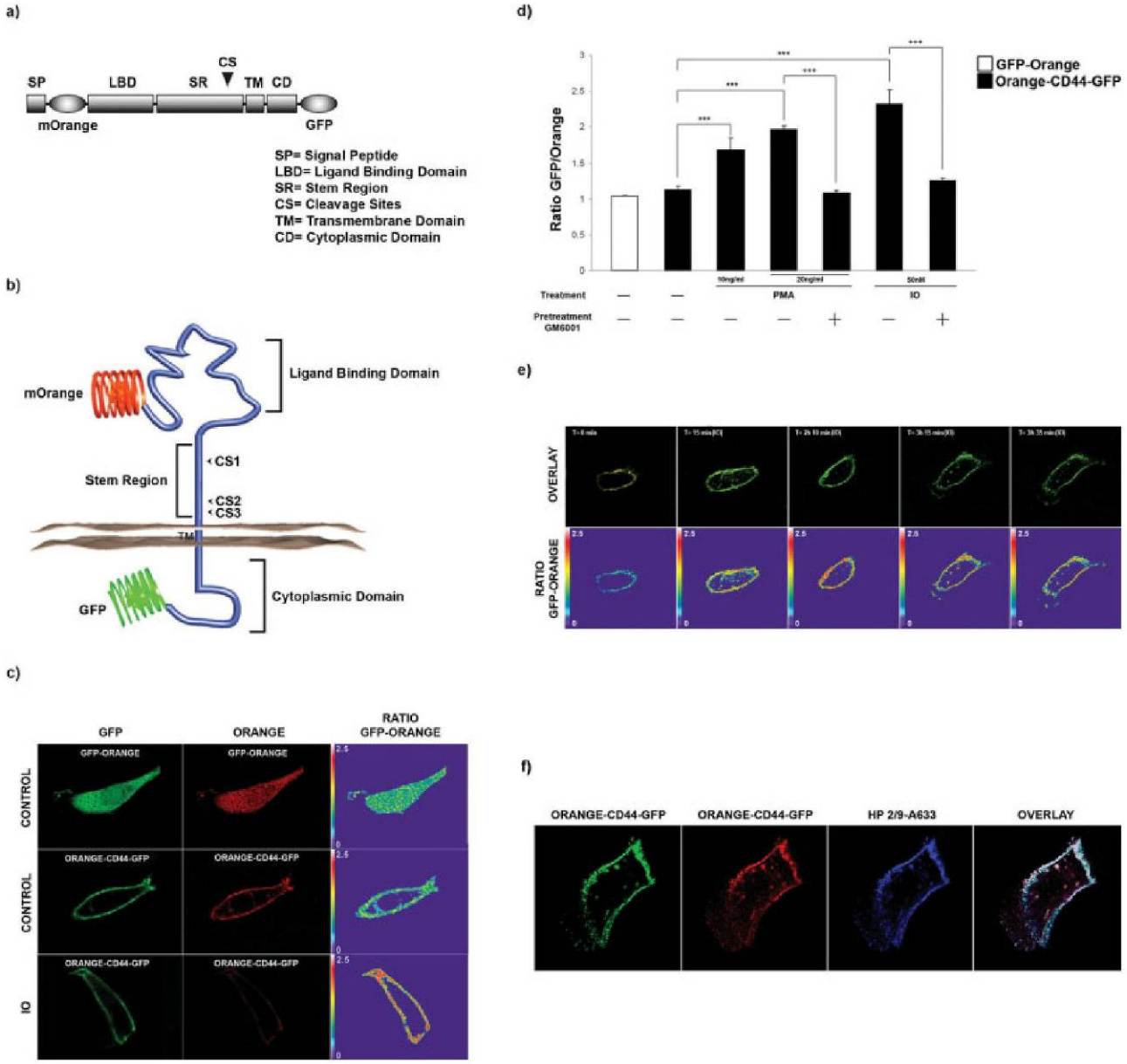

Fig. 4. Design and evaluation of the Orange-CD44-GFP shedding reporter. Schematic representation of the coding sequence (**a**) and structure (**b**) of the Orange-CD44-GFP shedding reporter. (**c**–**f**) MDA-MB-231 cells expressing tandem GFP-Orange or Orange-CD44-GFP were either (c, e) treated with or without IO (50 nM) for 2 h, or (d) pretreated with or without the MMP inhibitor GM6001 (10 μM) for 24 h and incubated with PMA (10 and 20 ng/mL) or IO (50 nM) for an additional 2 h. The cells were either fixed and analyzed by confocal microscopy imaging (c,d) or analyzed by live confocal microscopy imaging (e). (c) Representative GFP and Orange fluorescence images and the resulting GFP/Orange ratio image obtained under confocal microscopy are shown. (d) Bars represent quantification of the GFP/Orange ratio from microscopic images corresponding to 25 cells in three independent experiments. (e) Representative GFP and Orange fluorescence superimposed images and GFP/Orange ratio pseudo-colored images were obtained at the times indicated. (f) MDA-MB-231 cells expressing Orange-CD44-GFP were fixed and stained with anti-CD44 (HP2/9) primary monoclonal antibody and Alexa-633-conjugated anti-mouse secondary antibody. Fluorescence images show Orange (red), GFP (green), or Alexa 633 (blue) fluorescence and their superimposition.

confocal microscope from cells expressing the Orange-CD44-GFP or GFP-Orange construct were used to produce a GFP-Orange ratio image (Fig. 4c). This image represents the relationship between the intracellular and extracellular domains of CD44 within the cell, and is used to quantitatively estimate CD44 cleavage (such as that produced by ionomycin (IO) treatment [Okamoto et al., 1999a]) with sub-cellular resolution (Fig. 4c). The

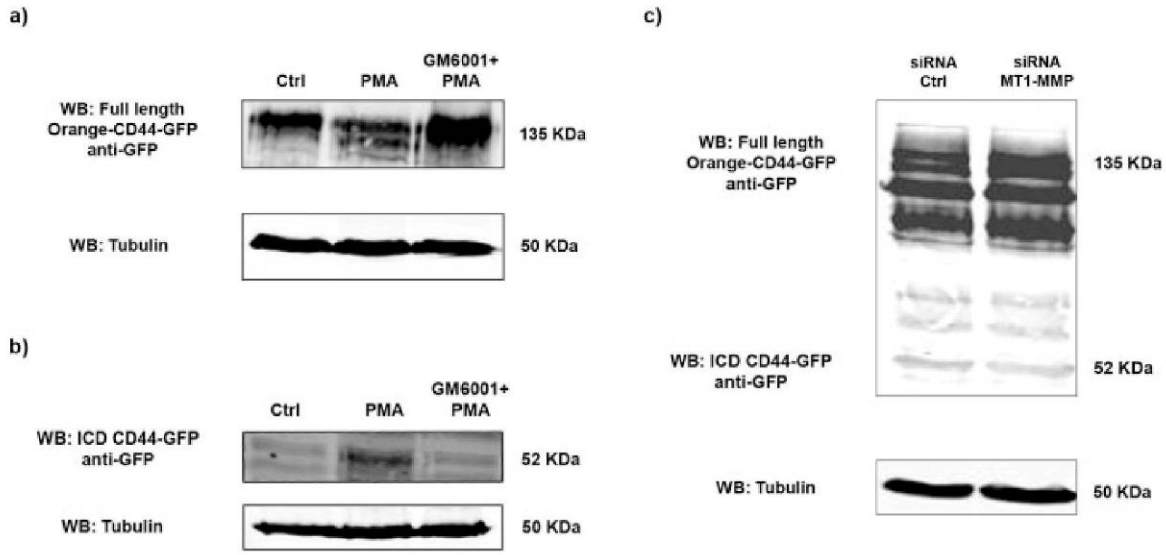

Fig. 5. Biochemical characterization of the Orange-CD44-GFP shedding reporter. (**a**, **b**) HT-1080 cells stably expressing Orange-CD44-GFP were pretreated or not with GM6001 (10 μM) for 24 h and then incubated with PMA (20 ng/mL) for additional 2h. (**c**) MDA-MB-231 cells were transfected with control or MT1-MMP siRNA and Orange-CD44-GFP. Forty-eight hours after, cell lysates were isolated and analyzed by western blotting using polyclonal anti-GFP, or anti-tubulin primary antibody, and Alexa-Fluor-680-conjugated secondary antibodies.

GFP-Orange relationship estimated from the microscopic fluorescence ratio image was quantitatively determined as described in the Materials and Methods section. Analysis of cells treated with the stimulating agents phorbol myristate acetate (PMA) and IO, which have been shown to induce CD44-cleavage, [Okamoto et al., 1999a] in the presence or absence of the MMP inhibitor GM6001, demonstrated that the reporter was subject to proteolytic processing (Fig. 4d). Monitoring the kinetics of IO induced CD44 cleavage further validated its use as a shedding reporter in live cell microscopy studies (Fig. 4e). We further tested this construct by immunolocalizing the Orange (red) and GFP (green) signals with anti-CD44 antibody staining (blue), which confirmed the overlap of the fluorescence signals and that the CD44 membrane localization pattern was not altered (Fig. 4f). Colocalization analysis is shown (Supporting Fig. 2). Moreover, expression of the Orange-CD44-GFP reporter induced an increase of 39.6% in cell invasion which was inhibited by GM6001 protease inhibitor (Supporting Fig. 3), thus revealing it retains some functional properties of the CD44 molecule. Biochemical studies were carried out to further evaluate the CD44 shedding reporter. PMA treatment induced a reduction in the 135 kD band corresponding to full length Orange-CD44-GFP reporter (Fig. 5a). The 52 kD intracellular CD44-GFP domain was detected in the cell lysates (Fig. 5b). Cleavage was inhibited by pretreating the cells with the MMP inhibitor GM6001 (Figs. 5a and 5b), or by transfecting cells with MT1-MMP siRNA (Fig. 5c) which induced an increased 135 kD full length Orange-CD44-GFP band and the reduction of 52 kD intracellular CD44-GFP band.

MDA-MB-231 cells expressing the shedding reporter were plated on coverslips coated or not with HA, or HA-3D Col I matrices, to determine the effect of the extracellular microenvironment on CD44 cleavage ''in vivo''. These studies showed that HA-3D Col I induced CD44 release globally at the cell surface, which was greater than that induced on HA-coated surfaces. Importantly, the shedding of the Orange-CD44-GFP reporter expressed in cells plated on HA-3D Col I was completely abolished by function-blocking antibodies directed against MT1-MMP [Galvez et al., 2002] (Figs. 6a and 6c). To further clarify this point we analyzed cells transfected with MT1-MMP siRNA, which showed impaired CD44 cleavage in HA-Col I surfaces (Figs. 6b and 6d). Together, these results demonstrate that MT1-MMP is responsible for CD44 cleavage in our invasion model. We then monitored the dynamics of CD44 release and its localization in different plasma membrane sub-domains by analyzing the sequences of the GFP/Orange ratio images of live cells invading HA-3D Col I (Figs. 7a and 7b). This analysis revealed that CD44 shedding occurs preferentially at the retracting trailing edge during cell migration. These results support a role for the CD44-MT1-MMP interaction and subsequent CD44 processing in cell trailing-edge detachment, possibly by the MT1-MMP-mediated release of CD44-dependent

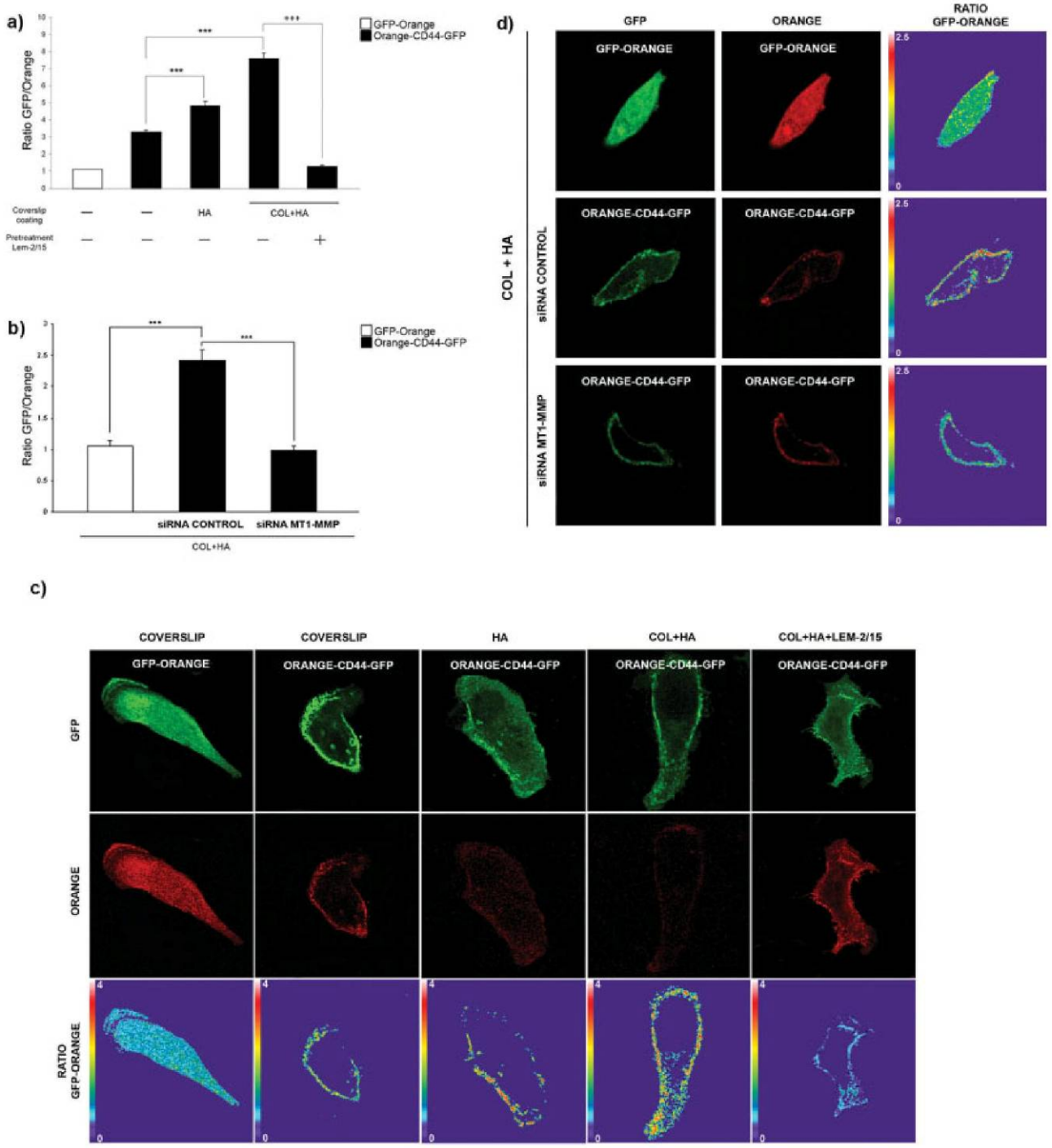

Fig. 6. MT1-MMP-dependent proteolytic processing of CD44 extracellular domain is induced in 3D HA-Col I matrices. MDA-MB-231 cells were transfected with the tandem GFP-Orange or Orange-CD44-GFP constructs. (**a**, **c**) Cells incubated with or without function-blocking anti-MT1-MMP (Lem-2/15) monoclonal antibody (10 μg/mL) were plated on coverslips coated or not with HA-3D Col I or HA, and were then fixed and analyzed by confocal microscopy imaging. (**b**, **d**) Cells were transfected with a control or MT1-MMP specific siRNA and plated on HA-3D Col I coated coverslips (a, b) The GFP/Orange ratio was quantified from 25 cells in three independent experiments and is represented in the bar diagrams. (c,d) Images show GFP and Orange fluorescence (green and red, respectively) and the GFP/Orange ratio (pseudo-colored).

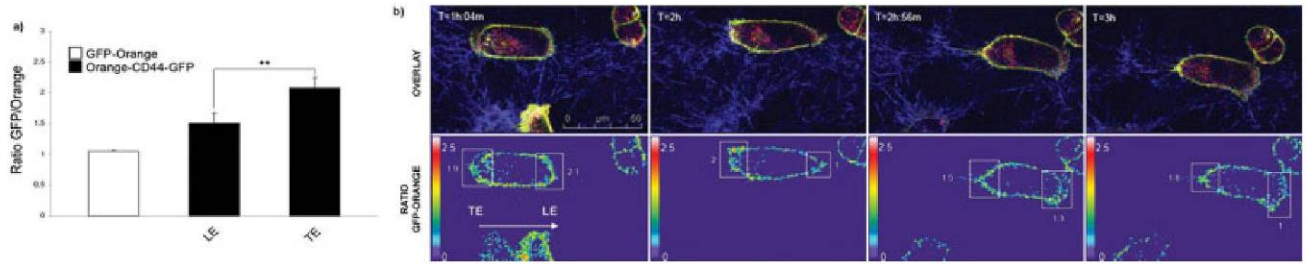

Fig. 7. Proteolytic cleavage of CD44 by MT1-MMP occurs preferentially at the trailing edge during tumor cell invasion. Cells expressing Orange-CD44-GFP were embedded in 3D HA-Col I matrices and analyzed by live confocal imaging. (**a**) Bars represent the GFP/Orange ratio values calculated at leading (LE) or trailing edges (TE) from 25 cells in three independent experiments. (**b**) Representative GFP-Orange fluorescence images superimposed on a reflection image showing collagen fibers (blue) and the GFP/Orange ratio pseudo-colored images were obtained at the times indicated. The GFP/Orange ratio pseudo-colored images include details of the trailing and leading edges, and the GFP/Orange ratio values calculated in these areas are indicated. The arrow indicates the direction of movement.

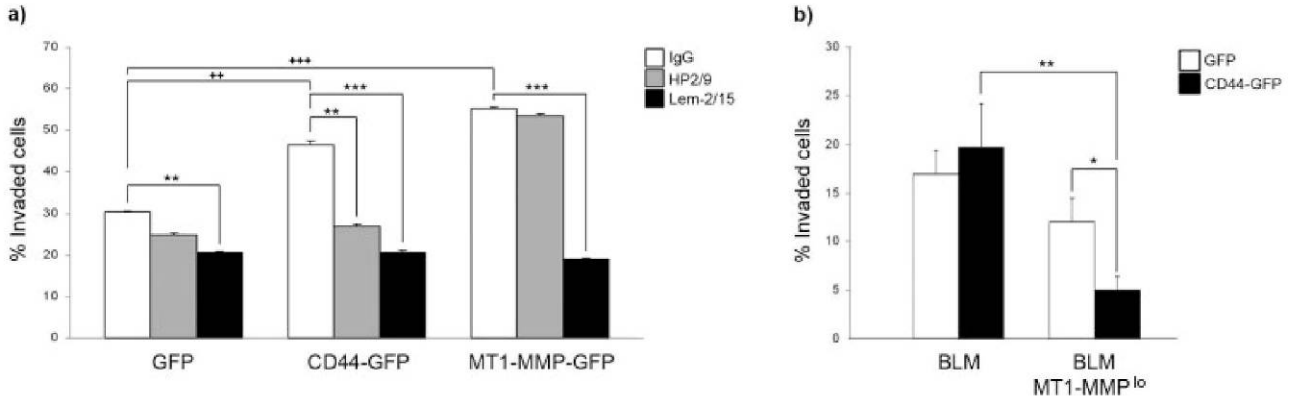

Fig. 8. CD44- and MT1-MMP-dependence of tumor cell invasion of HA-3D Col matrices. MDA-MB-231 (**a**) or BLM (**b**) cells were transfected with GFP, CD44-GFP, or MT1-MMP-GFP and then allowed to migrate for 48 h on transwell filters coated with 3D HA-Col I to 10% fetal bovine serum (FBS)-containing medium in the presence of isotype control IgG, function-blocking anti-CD44 antibody (HP2/9), or anti-MT1-MMP (Lem-2/15) antibody (10 μg/mL). Bars represent the percentages of invading GFP-expressing cells quantified in four different fields for each of the seven independent experiments performed.

cell-matrix bonds, which would in turn promote cell movement.

MT1-MMP-Dependence of CD44-Mediated Tumor Cell Invasion on Collagen Matrices

Our previous results allowed us to hypothesize that MT1-MMP is required for CD44-mediated invasion by promoting the proteolytic cleavage of CD44 at the trailing edge of the cell during retraction. The interdependence of CD44 and MT1-MMP in their invasion-promoting activities was investigated by performing transwell invasion assays of MDA-MB-231 cells over-expressing CD44 and MT1-MMP in the presence or absence of function-blocking antibodies directed against these molecules. Our results show that CD44 over-expression induced a significant increase in invasion and function blocking antibodies against CD44 [Lara-Pezzi et al., 2001] inhibited this effect (Fig. 8a). Blocking MT1-MMP function diminished both MT1-MMP- and CD44-mediated invasion, whereas blocking CD44 function did not affect the invasion induced by MT1-MMP (Fig. 8a). These results indicate that CD44-dependent invasion requires MT1-MMP functionality, whereas CD44 is not essential for MT1-MMP-mediated invasion. Melanoma BLM cells presented a decreased invasive capacity when the MT1-MMP gene was silenced (MT1-MMP^{lo}). It is important to note that the expression of CD44-GFP induced a 16% increase in cell invasion compared with that induced by GFP in cells with intact MT1-MMP activity. On the contrary, in the absence of this protease, MT1-MMP^{lo} BLM cells, CD44-GFP expression produced a 74% inhibition of cell invasion compared to control GFP expressing (Fig. 8b). In summary, an excess of CD44 surface molecules promoted invasion under physiological conditions, whereas it impaired the invasive capacity of cells in which MT1-MMP had been inacti-

vated. Thus, CD44 involvement in cell invasion depends on its levels of expression at the cell surface and the activity of MT1-MMP in our invasion model.

DISCUSSION

This study addresses, for the first time, the in vivo CD44-MT1-MMP interaction and CD44 shedding using live cell confocal microscopy. Three dimensional collagen matrices used in our study mimic the ''in vivo'' environment encountered in tissues surrounding tumours, which are more fibrous than normal tissues because of the increased deposition of fibrillar collagen and HA being associated with higher Col I fibre density and HA expression levels [Toole et al., 1979; Zhang et al., 1995; Wang et al., 2002]. It therefore represents an ideal model in which to study tumour cell invasion in vitro. We used state of the art technology to perform this study; namely the new λFRET method, which has been validated with structurally characterized FRET standards of variable lengths demonstrating its outstanding performance compared with well-established FRET methods in terms of sensitivity [Megías et al., In press]. We used λFRET to study the in vivo interaction of CD44 with its partners because its weakness requires a highly sensitive FRET analysis method, and because it enabled us to monitor FRET in live cells. The FRET efficiency values obtained for CD44-MT1-MMP interaction were low, and were restricted to certain areas of the cell perimeter. Due to these facts, we performed extensive quantifications using two different FRET analysis methods, which showed that, although faint, the results were highly consistent thus demonstrating the physiological relevance of the results presented herein.

The importance of CD44 shedding in the pathogenesis of human tumors has been highlighted by several reports that show in situ the CD44 cleavage product enriched in human tumor tissues compared with that in the surrounding normal tissues [Okamoto et al., 2002; Nakamura et al., 2004]. We developed a technologically innovative tool for the study of CD44 shedding which proved to be very useful for monitoring the sub-cellular localization of the proteolitic processing of CD44, a matter that could not be explored with the techniques available up to date. This technology should prove to be useful in the future for the study of a number of membrane molecules, which are subjected to ecto-domain shedding as a mechanism underlying their functional regulation being key for physiopathologically relevant processes [Nagano and Saya, 2004; Garton et al., 2006].

The CD44-MT1-MMP interaction is here shown to be finely regulated at the cell surface during the invasion process, with preferential localization at the retracting trailing edge, where CD44 proteolytic cleavage was also shown to be enriched. CD44 proteolytic processing in this 3D Col I was shown to be MT1-MMP dependent, since it was abolished by function blocking antibodies and siRNA silencing of this molecule. In our cell invasion model, an increase in the levels of surface CD44 promoted cell invasion when activity of MT1-MMP was intact, whereas it had the opposite effect in the absence of MT1-MMP. These results may be explained by the the fact than an increased expression of CD44 provides new adhesive contacts that firmly attach the cells to the substrate and must be released by the MT1-MMP-mediated cleavage of the extracellular domain to allow cell motility. We propose a role of MT1-MMP-dependent CD44 proteolytic processing in releasing cell contacts to the ECM at the trailing edge of the cell allowing rear detachment required for the forward movement of the cell during invasion. Thus, CD44 can exert a pro-, anti-invasive or have no effect on the invasive ability of tumour cells in a manner, that is, dependent on its levels of expression at the cell surface and the activity of MT1-MMP. This may help to explain contradictory conclusions regarding the correlation between CD44 expression and the migratory and invasive ability of tumour cell lines, the metastatic capacity of cancer cells and cancer disease prognosis [Driessens et al., 1995; Maaser et al., 1999; Naor et al., 2002; Weber et al., 2002].

It has been shown that CD44 is responsible for MT1-MMP delivery to the leading edges of migrating cells [Mori et al., 2002]. This does not seem to be the case in our invasion model, because a blocking anti-CD44 antibody did not affect MT1-MMP-mediated invasiveness. However, we cannot rule out this possibility because the MT1-MMP-CD44 interaction was also detected at the leading edge in our studies The localization of CD44 and MT1-MMP molecules at the lamellipodia of migrating cells [Kajita et al., 2001; Mori et al., 2002] supports the prevailing hypothesis that proposes a role for CD44 as a platform for the presentation of MT1-MMP and other MMPs, such as MMP9 at the leading edge of the cell [Itoh and Seiki, 2006]. These studies addressed the protein domains involved in CD44-MT1-MMP interaction and developed deletion mutants to abolish the interaction, which inhibited CD44 shedding and perturbed cell migration [Kajita et al., 2001; Mori et al., 2002]. The data presented herein reveal novel functional implications of CD44-MT1-MMP interplay that are in accordance with the afore mentioned works. The extracellular context composition, probably the presence of fibrillar collagen, which was shown to promote CD44 shedding, is most likely responsible for the novel MT1-MMP-dependent regulation of CD44-mediated invasion described herein. Accordingly, previous studies have demonstrated the differential regulation of MT1-MMP depending on the composition of the extra-

cellular matrix, showing that Col I promotes MT1 activation, redistribution to specialized membrane microdomains and specific sub-cellular localization [Galvez et al., 2002; Annabi et al., 2004]. Moreover, our previous studies showed that MT1-MMP is relocalized to a different intracellular vesicle trafficking compartment when cells are embedded in 3D Col I matrices [Bravo-Cordero et al., 2007]. This study uncovered a Rab8-mediated exocytic traffic capable of delivering MT1-MMP to invasive structures which may represent a physiologically relevant pathway of MT1-MMP regulation during tumour cell invasion of collagen rich tissues, such as those surrounding tumours.

MT1-MMP is one of the most critical factors in the invasive machinery of tumor cells because its overexpression enhances the invasive capacity of cells and its silencing suppresses cell migration and invasion [Egeblad and Werb, 2002]. MT1-MMP pro-invasive activity is based on its ability to degrade ECM proteins and activate soluble MMPs, like pro-MMP2, and processing cytokines and surface receptors, including integrins and the CD44 adhesion molecule [Sato et al., 2005]. These processes have been ascribed to the leading edge of the cell. Moreover, our studies reveal a novel aspect of MT1-MMP pro-invasive activity by highlighting its role at the retracting cell rear during the invasion process. Our study provides a novel perspective for MT1-MMP-dependent functional regulation of CD44 which should prove to be very useful considering the importance of MT1-MMP in tumour cell invasion and angiogenesis, which makes this enzyme a key molecular target for cancer therapeutics.

ACKNOWLEDGMENTS

The authors thank Dr. A.G. Arroyo for critical reading of the manuscript, Drs. Mizoi, Sánchez-Madrid, del Pozo, and Tsien are acknowledged for providing us with reagents.

REFERENCES

Annabi B, Thibeault S, Moumdjian R, Beliveau R. 2004. Hyaluronan cell surface binding is induced by type I collagen and regulated by caveolae in glioma cells. J Biol Chem 279(21):21888–21896.

Bartolome RA, Molina-Ortiz I, Samaniego R, Sanchez-Mateos P, Bustelo XR, Teixido J. 2006. Activation of Vav/Rho GTPase signaling by CXCL12 controls membrane-type matrix metalloproteinase-dependent melanoma cell invasion. Cancer Res 66(1):248–258.

Bravo-Cordero JJ, Marrero-Diaz R, Megías D, Genís L, García-Grande A, García MA, Arroyo AG, Montoya MC. 2007. MT1-MMP pro-invasive activity is regulated by a novel Rab8-dependent exocytic pathway. EMBO J 26(6):1499–1510.

Driessens MH, Stroeken PJ, Rodriguez Erena NF, van der Valk MA, van Rijthoven EA, Roos E. 1995. Targeted disruption of CD44 in MDAY-D2 lymphosarcoma cells has no effect on subcutaneous growth or metastatic capacity. J Cell Biol 131(6 Part 2):1849–1855.

Egeblad M, Werb Z. 2002. New functions for the matrix metalloproteinases in cancer progression. Nat Rev Cancer 2(3):161–174.

Friedl P, Maaser K, Klein CE, Niggemann B, Krohne G, Zanker KS. 1997. Migration of highly aggressive MV3 melanoma cells in 3-dimensional collagen lattices results in local matrix reorganization and shedding of alpha2 and beta1 integrins and CD44. Cancer Res 57(10):2061–2070.

Friedl P, Wolf K. 2003. Tumour-cell invasion and migration: Diversity and escape mechanisms. Nat Rev Cancer 3(5):362–374.

Galvez BG, Matias-Roman S, Yanez-Mo M, Sanchez-Madrid F, Arroyo AG. 2002. ECM regulates MT1-MMP localization with beta1 or alphavbeta3 integrins at distinct cell compartments modulating its internalization and activity on human endothelial cells. J Cell Biol 159(3):509–521.

Garton KJ, Gough PJ, Raines EW. 2006. Emerging roles for ectodomain shedding in the regulation of inflammatory responses. J Leukoc Biol 79(6):1105–1116.

Itoh Y, Seiki M. 2006. MT1-MMP: A potent modifier of pericellular microenvironment. J Cell Physiol 206(1):1–8.

Kajita M, Itoh Y, Chiba T, Mori H, Okada A, Kinoh H, Seiki M. 2001. Membrane-type 1 matrix metalloproteinase cleaves CD44 and promotes cell migration. J Cell Biol 153(5):893–904.

Lara-Pezzi E, Serrador JM, Montoya MC, Zamora D, Yanez-Mo M, Carretero M, Furthmayr H, Sanchez-Madrid F, Lopez-Cabrera M. 2001. The hepatitis B virus X protein (HBx) induces a migratory phenotype in a CD44-dependent manner: Possible role of HBx in invasion and metastasis. Hepatology 33(5):1270–1281.

Legg JW, Lewis CA, Parsons M, Ng T, Isacke CM. 2002. A novel PKC-regulated mechanism controls CD44 ezrin association and directional cell motility. Nat Cell Biol 4(6):399–407.

Lehti K, Valtanen H, Wickstrom SA, Lohi J, Keski-Oja J. 2000. Regulation of membrane-type-1 matrix metalloproteinase activity by its cytoplasmic domain. J Biol Chem 275(20):15006–15013.

Maaser K, Wolf K, Klein CE, Niggemann B, Zanker KS, Brocker EB, Friedl P. 1999. Functional hierarchy of simultaneously expressed adhesion receptors: Integrin alpha2beta1 but not CD44 mediates MV3 melanoma cell migration and matrix reorganization within three-dimensional hyaluronan-containing collagen matrices. Mol Biol Cell 10(10):3067–3079.

Marhaba R, Zoller M. 2004. CD44 in cancer progression: Adhesion, migration and growth regulation. J Mol Histol 35(3):211–231.

Megías D, Marrero-Diaz R, Martínez del Peso B, Bravo-Cordero JJ, García MA, Santos A, Montoya MC. In press. Novel lambda FRET spectral confocal microscopy imaging method. Microsc Res Tech 10: in press..

Mori H, Tomari T, Koshikawa N, Kajita M, Itoh Y, Sato H, Tojo H, Yana I, Seiki M. 2002. CD44 directs membrane-type 1 matrix metalloproteinase to lamellipodia by associating with its hemopexin-like domain. EMBO J 21(15):3949–3959.

Nagano O, Saya H. 2004. Mechanism and biological significance of CD44 cleavage. Cancer Sci 95(12):930–935.

Nakahara H, Howard L, Thompson EW, Sato H, Seiki M, Yeh Y, Chen WT. 1997. Transmembrane/cytoplasmic domain-mediated membrane type 1-matrix metalloprotease docking to invadopodia is required for cell invasion. Proc Natl Acad Sci USA 94(15):7959–7964.

Nakamura H, Suenaga N, Taniwaki K, Matsuki H, Yonezawa K, Fujii M, Okada Y, Seiki M. 2004. Constitutive and induced CD44

shedding by ADAM-like proteases and membrane-type 1 matrix metalloproteinase. Cancer Res 64(3):876–882.

Naor D, Nedvetzki S, Golan I, Melnik L, Faitelson Y. 2002. CD44 in cancer. Crit Rev Clin Lab Sci 39(6):527–579.

Okamoto I, Kawano Y, Matsumoto M, Suga M, Kaibuchi K, Ando M, Saya H. 1999a. Regulated CD44 cleavage under the control of protein kinase C, calcium influx, and the Rho family of small G proteins. J Biol Chem 274(36):25525–25534.

Okamoto I, Kawano Y, Tsuiki H, Sasaki J, Nakao M, Matsumoto M, Suga M, Ando M, Nakajima M, Saya H. 1999b. CD44 cleavage induced by a membrane-associated metalloprotease plays a critical role in tumor cell migration. Oncogene 18(7):1435–1446.

Okamoto I, Tsuiki H, Kenyon LC, Godwin AK, Emlet DR, Holgado-Madruga M, Lanham IS, Joynes CJ, Vo KT, Guha A, Matsumoto M, Ushio Y, Saya H, Wong AJ. 2002. Proteolytic cleavage of the CD44 adhesion molecule in multiple human tumors. Am J Pathol 160(2):441–447.

Sato H, Takino T, Miyamori H. 2005. Roles of membrane-type matrix metalloproteinase-1 in tumor invasion and metastasis. Cancer Sci 96(4):212–217.

Suenaga N, Mori H, Itoh Y, Seiki M. 2005. CD44 binding through the hemopexin-like domain is critical for its shedding by membrane-type 1 matrix metalloproteinase. Oncogene 24(5):859–868.

Taraboletti G, D'Ascenzo S, Borsotti P, Giavazzi R, Pavan A, Dolo V. 2002. Shedding of the matrix metalloproteinases MMP-2, MMP-9, and MT1-MMP as membrane vesicle-associated components by endothelial cells. Am J Pathol 160(2):673–680.

Toole BP, Biswas C, Gross J. 1979. Hyaluronate and invasiveness of the rabbit V2 carcinoma. Proc Natl Acad Sci USA 76(12):6299–6303.

Tsukita S, Oishi K, Sato N, Sagara J, Kawai A. 1994. ERM family members as molecular linkers between the cell surface glycoprotein CD44 and actin-based cytoskeletons. J Cell Biol 126(2):391–401.

Vivinus-Nebot M, Rousselle P, Breittmayer JP, Cenciarini C, Berrih-Aknin S, Spong S, Nokelainen P, Cottrez F, Marinkovich MP, Bernard A. 2004. Mature human thymocytes migrate on laminin-5 with activation of metalloproteinase-14 and cleavage of CD44. J Immunol 172(3):1397–1406.

Wang W, Wyckoff JB, Frohlich VC, Oleynikov Y, Huttelmaier S, Zavadil J, Cermak L, Bottinger EP, Singer RH, White JG, Segall JE, Condeelis JS. 2002. Single cell behavior in metastatic primary mammary tumors correlated with gene expression patterns revealed by molecular profiling. Cancer Res 62(21):6278–6288.

Weber GF, Bronson RT, Ilagan J, Cantor H, Schmits R, Mak TW. 2002. Absence of the CD44 gene prevents sarcoma metastasis. Cancer Res 62(8):2281–2286.

Wolf K, Wu YI, Liu Y, Geiger J, Tam E, Overall C, Stack MS, Friedl P. 2007. Multi-step pericellular proteolysis controls the transition from individual to collective cancer cell invasion. Nat Cell Biol 9(8):893–904.

Zhang L, Underhill CB, Chen L. 1995. Hyaluronan on the surface of tumor cells is correlated with metastatic behavior. Cancer Res 55(2):428–433.

4.4 IMSRC: CONVERTING A STANDARD AUTOMATED MICROSCOPE INTO AN INTELLIGENT SCREENING PLATFORM

Ángel Carro, Manuel Pérez-Martínez, Joaquim Soriano, David G. Pisano y Diego Megías

La necesidad de nuevas herramientas aplicables a la automatización de adquisiciones complejas en microscopía ha sido una demanda recurrente de la comunidad científica, las pocas plataformas disponibles hasta la fecha tienen el gran inconveniente de ser extraordinariamente complejas y normalmente requieren de programadores avanzados para su uso e instalación. Con el ánimo de solucionar este problema en este trabajo presentamos y proponemos el uso de una nueva plataforma de software que permite por primera vez realizar abordajes de adquisición automatizada Inteligente de forma fácil y completamente compatible con microscopios ópticos convencionales y confocales de alta resolución.

Esta nueva plataforma denominada iMSRC (Intelligent Matrix Screening Remote Control) permite nuevas aplicaciones que no solo son útiles para la captura de muestras de FRET, sino también para la detección y cuantificación de eventos poco frecuentes y el *screening* de alta resolución en tejido. Esta nueva solución informática permite la adquisición de varios portas en paralelo, de placas multipocillo, y ensayos con células vivas.

Para asegurar la compatibilidad se hace uso de las ventajas de la aplicación de captura comercial y se pone en contacto su facilidad de uso con programas de análisis de imagen, todo el dentro del entorno del iMSRC que es el encargado de gestionar el intercambio entre microscopio y análisis.

En este trabajo he tenido un papel fundamental, habiendo participado desde la misma concepción de la idea así hasta la elaboración de todos los cálculos, el diseño, testado, corrección de errores y validación de su funcionamiento, tanto en microscopía confocal como de campo ancho. Además he coordinado el desarrollo de la aplicación informática que gestiona los cálculos. La relevancia en mi papel en este artículo viene avalada por el hecho de firmar como *corresponding author* del mismo.

SCIENTIFIC REPORTS

OPEN

iMSRC: converting a standard automated microscope into an intelligent screening platform

Received: 10 November 2014
Accepted: 14 April 2015
Published: 27 May 2015

Angel Carro[1,*], Manuel Perez-Martinez[2,*], Joaquim Soriano[2,*], David G. Pisano[1] & Diego Megias[2]

Microscopy in the context of biomedical research is demanding new tools to automatically detect and capture objects of interest. The few extant packages addressing this need, however, have enjoyed limited uptake due to complexity of use and installation. To overcome these drawbacks, we developed *iMSRC*, which combines ease of use and installation with high flexibility and enables applications such as rare event detection and high-resolution tissue sample screening, saving time and resources.

High automation capabilities applied to optical microscopy paved the way for converting microscopes into intelligent screening platforms, i.e. instruments able to automatically detect objects of interest based on an image analysis routine and capture them at high resolution. The use of this new strategy saves on acquisition time, optimizes resources (Fig. 1 and Fig. 2b and c and Supplementary Fig. S5) and enables advanced applications, such as rare event detection (e.g. circulating tumour cells (CTCs); Fig. 1 and Fig. 2c).

While there are a small number of open-source codes which might permit microscope automation (see, e.g. Icy[1], Endrov[2] or Micropilot[3]), these usually require advanced programming skills and are often hobbled by hardware compatibility issues (e.g. driver availability on the Micro-manager[4] platform), making their implementation difficult for core facilities and, more importantly, being complex to use and adapt.

On the other hand, microscope manufacturers' acquisition software is much easier to use and boasts optimized hardware compatibility. However, due to its very limited flexibility, its use in intelligent screening approaches is often unfeasible.

To overcome these limitations, we developed ***iMSRC*** (intelligent Matrix Screener Remote Control), a new open source software-based solution capable of implementing distinct intelligent screening applications through exploiting the simplicity of the microscope's native software (Supplementary Fig. S1).

iMSRC gathers all relevant information from acquisition files generated by proprietary software. Then, upon analyzing preliminary images ("First scan") through conventional image analysis platforms (e.g. ImageJ[5] or MATLAB) it creates new acquisition files containing ad hoc generated settings, managing the launch of a new capture sequence focused on objects of interest, meeting the specific requirements of any experimental design, and allowing for complex experimental set-up not otherwise possible (Fig. 1 and Supplementary Fig. S1). Symbiosis with proprietary software guarantees hardware compatibility (there is no need for installing new pieces of hardware or drivers, or programming new drivers), ease of use (there is no need to learn to use a new capturing environment) and avoids the need for complex hardware and software installation.

iMSRC-driven microscopy is user-friendly, fully compatible with both confocal and wide-field microscopes and accessible to any user, independently of their programming or microscopy skills.

[1]Bioinformatics unit, Structural Biology and Biocomputing Programme, Spanish National Cancer Research Centre (CNIO), Madrid, Spain. [2]Confocal Microscopy Unit, Biotechnology programme, CNIO, Madrid, Spain. *These authors contributed equally to this work. Correspondence and requests for materials should be addressed to D.M. (email: dmegias@cnio.es)

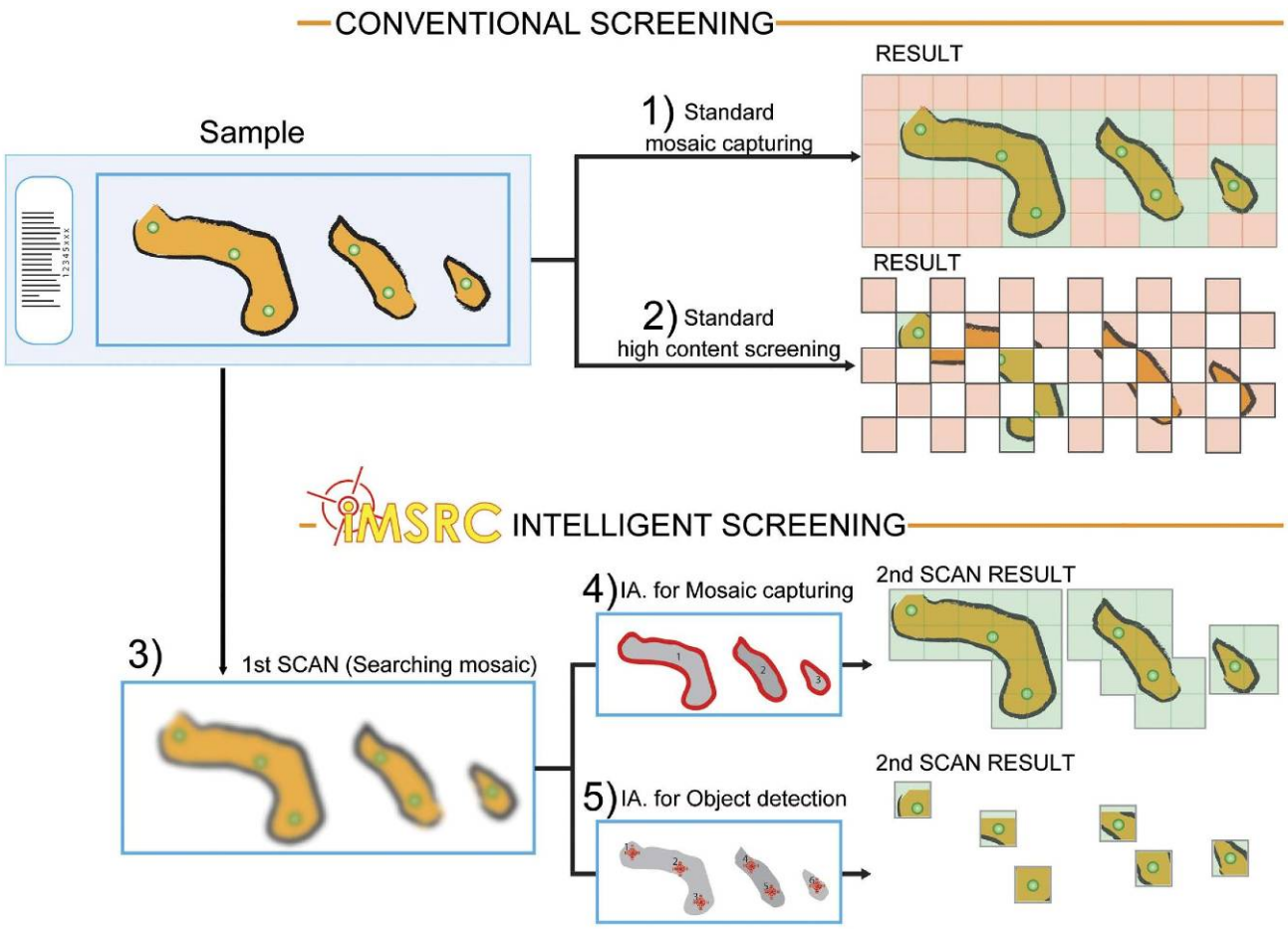

Figure 1. Standard mosaic capturing (1) and high content screening (2) compared to *IMSRC*'s intelligent screening applied to mosaic capturing (4) and object detection(5). ***iMSRC*** uses a three-step approach: capturing a searching mosaic through a first scan (3), extracting objects of interest's coordinates by using image analysis routines (4 and 5) and ,finally, using these coordinates for a second scan (4 and 5, right column images). ***iMSRC*** increases capturing efficiency by preventing non-informative-area capturing (light red insets on 1 and 2, right column images). Light green insets on right column images show final resolution, meaningful captured areas.

iMSRC has already proven its functionality and versatility in several research applications, including high-resolution Tissue Microarray confocal capture[6] (Fig. 2b), live, time-lapse, single stem cell detection in customized PDMS microchips[7,8], hippocampus dentate gyrus-specific cell-type detection in brain sections (Supplementary Fig. S6) and circulating tumour cell (CTCs) detection[9] (Fig. 2c). The identification and high-magnification mosaic capturing of specific regions within tissue sections, such as in the case of breast metastasis and GFP-expressing regions in different organs have also been successfully accomplished.

iMSRC can be deployed in any conventional Linux PC following a few simple installation steps, publishing the user graphical interface for software control as a web page, which is then fully accessible through the most common web browsers from any computer within the same network (Supplementary Fig. S1b). The addition of new microscopes to the structure is straightforward, rapid and can be performed within the same web page (Supplementary Fig. S2).

Although direct connection with a microscope workstation is also possible, network access offers the following advantages, which are particularly useful to core facilities and laboratories that share equipment: (i) a single ***iMSRC*** installation can be accessed by all instruments, managing intelligent screening in all of them, unifying access and simplifying use; (ii) access to all required utilities, including image analysis script routines and microscope choice dialog, is centralized, making management easier; (iii) to ensure safety, all software administration (including macro upload, see Supplementary Fig. S3, or a new microscope addition, see Supplementary Fig. S2) can be made accessible only to authorized staff using authentication. Besides the novelty of this approach, no additional software installation on the microscope computers is required, maintaining maximum performance.

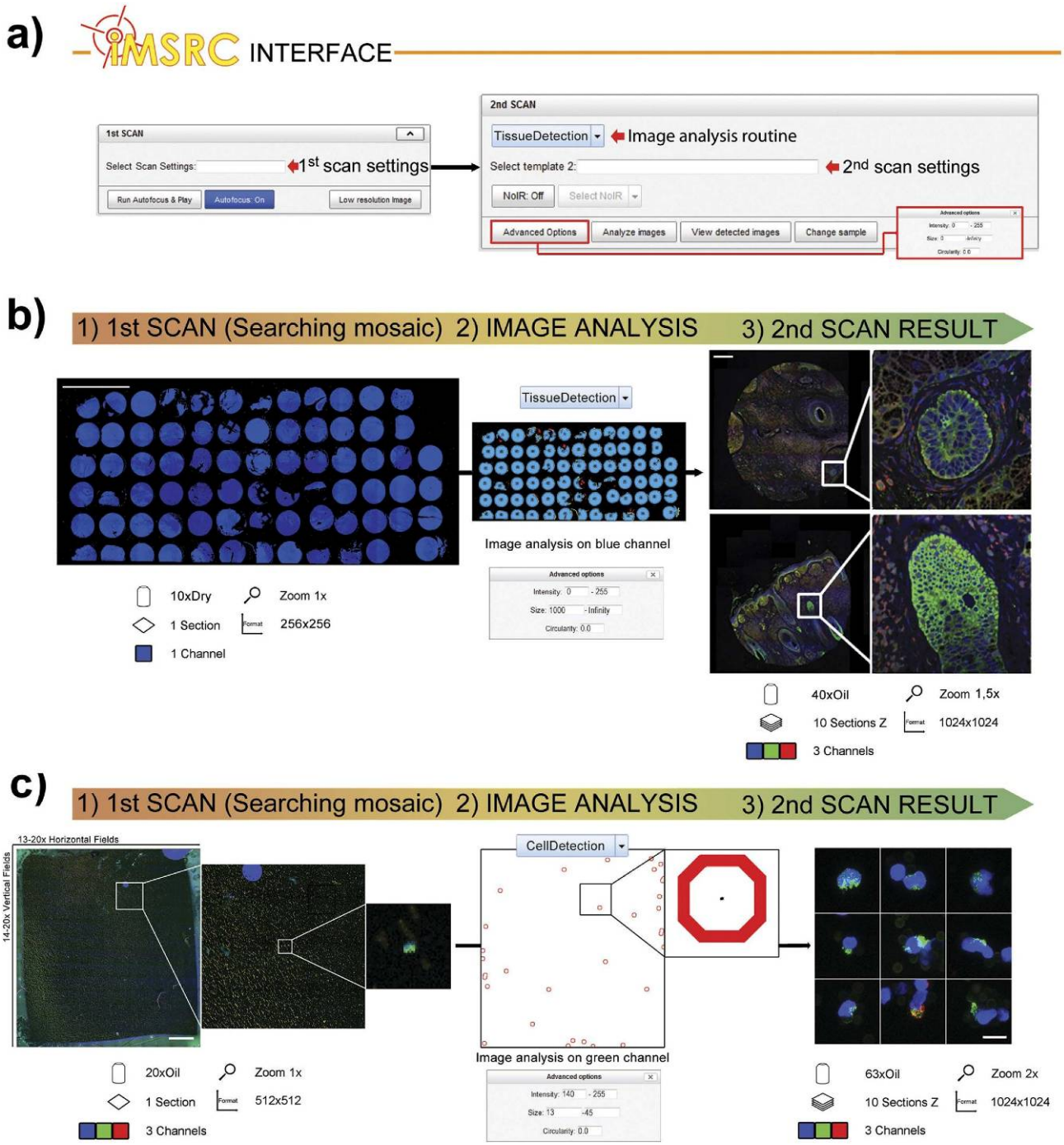

Figure 2. ***iMSRC*** **user's interface (a),** ***iMSRC*** **applied to mosaic capturing (b) and detection of rare events (c).** ***iMSRC*** allows the automatic capturing of complex experimental designs by choosing previously saved files on extendable menus, and tuning three simple image analysis parameters (**a**). Searching mosaic (b1 and c1), image-analysis-detected objects (b2 and c2) and final, merged-colour maximum projections (b3 and c3) are shown. Seventy-seven differently sized tissue pieces belonging to a Tissue Microarray were automatically captured overnight in (**b**). Circulating Tumour Cells (1:400) were automatically detected in (**c**). Insets show details. Text and icons show step specifics; see the Material and Methods section for further details. Scale bars (b1): 5 mm; (b3): 250 microns; (c1): 600 microns; and (c3): 12 microns.

iMSRC's full compatibility has been thoroughly assessed in different institutions and on a wide variety of systems and local network configurations.

iMSRC has been tested on Leica TCS-SP5 and TCS-SP8 laser scanning confocals and in Leica DMI6000B and DMI8 wide-field microscopes. The only requisite for iMSRC to work is that the

proprietary software running a microscope generates a comprehensive metadata file that can be edited and loaded again into such software. For this reason, compatibility with Nikon and Zeiss does not seem plausible to date; compatibility with any other microscopes (e.g. Olympus) is conditioned to the fact that the previous criteria are fulfilled.

How to use ***iMSRC***

Intelligent screenings with ***iMSRC*** are performed in three steps (Figs. 1,2 and Supplementary Fig. S6).

Step 1. First scan: capture of a searching mosaic, composed of juxtaposed images covering the entire sample. This is intended to have minimum resolution, with a large field of view in order to locate the events of interest at the maximum possible speed.

Step 2. Running an image analysis routine designed to locate the coordinates of the objects of interest previously defined in the searching mosaic

Step 3. Second scan: Final acquisition of identified objects using the parameter settings predefined to achieve the desired image properties (i.e. objective, zoom, Z-stack and time lapse). Importantly, the change of objective lenses between scans will be directly controlled by ***iMSRC***, which automatically applies predefined paracentricity correction (Supplementary Fig. S4).

iMSRC supports multiple sample acquisition and allows any format compatible with a particular microscope's frame adapters, such as microtiter plates and dishes, or up to five slides in parallel (Supplementary Fig. S6).

Parameters for both first and second scans are built up in the proprietary software and must be stored as two independent files in a local or remote shared folder (Supplementary Fig. S2).

iMSRC is equipped by default with a series of macros for tissue or cell detection which covers the vast majority of applications. If these are not sufficient to implement a particular object detection, a user with no programming skills but basic knowledge of image analysis could create his or her own image analysis routine and simply copy and paste one line of code in order to make it fully compatible with ***iMSRC*** (Supplementary Fig. S3).

New image analysis routines can be virtually, designed using any image analysis software, as long as the final result is a list of coordinates of detected objects. Additionally, objects of interest can also be manually selected from the searching mosaic image by the user, adding a further layer of useful flexibility to the whole system (Supplementary Fig. S6).

The ***iMSRC*** graphical interface is accessible through a web page where the user can easily choose among different options, allowing for loading the previously saved capture settings for both first and second scans on extendable menus and fine-tuning of all parameters necessary for objects detection (Fig. 2a and Supplementary Fig. S3).

Once all the settings have been defined, they can be saved as a template and reloaded, which simplifies further experiments.

When ***iMSRC*** is launched, objects smaller than a single field of view will be captured as an individual picture; bigger objects will be covered by high-resolution mosaics. In the case of the latter, the acquisition of non-informative regions (NoIR) in the vicinity of the objects of interest can be prevented by activating the "NoIR" option (Fig. 2a). When this additional feature is activated, a secondary analysis for just those objects identified in Step 2 will run, disabling irrelevant acquisition fields. This ensures the perfect fitting for irregular samples, saving valuable acquisition time and resources — something that is particularly relevant when capturing large, irregularly-shaped objects (Supplementary Fig. S5).

If a microscope is equipped with a communications port (i.e. the Computer Aided Microscope port [CAM] of Leica microscopes), ***iMSRC*** can automatically launch the whole process that directs information flow between the capturing and analysis software by means of a single click ("Play"; Supplementary Fig. S1). Importantly, even when this port is not available, each step can still be sequentially launched by the user. Manual workflow is also recommended when performing complex image analysis, which might require a revision of the identified areas prior to launching the final acquisition step.

Conclusions

We present ***iMSRC***, a tool based on a new approach that converts conventional automated microscopes into easy-to-use intelligent systems able to automatically localize and capture events of interest, making novel experimental designs affordable.

iMSRC's has already proved its applicability thorough its implementation in several papers publications and its spreading to different institutions. The combination of features offered by the iMSRC platform make it a valuable tool, which fills a wide gap in the field of bioimaging software usability, as identified in a recent publication[10].

IMSRC download and more details are available in http://***iMSRC***.bioinfo.cnio.es web page.

Materials and Methods

In all cases, images were acquired using a confocal TCS-SP5-WLL (AOBS) spectral microscope (Leica Mycrosystems, Wetzlar, Germany). Its acquisition software is LAS AF v2.6 (Leica).

Automated, multiple, size- and shape-heterogeneous, tissue microarray capturing (Fig. 2b). This is based on previously published work — check reference 7 for further details.

Several control and clinical tissues can be extracted, fixed, cut into small pieces and placed on the same slide for further staining. The result is called a Tissue Microarray (TMA), which is useful for minimizing sample variation and use of reagents.

Briefly, TMAs consisting of a mixture of healthy and cancerous tissue types and phases were obtained from mouse xenograft models, double immunostained for different pairs of primary antibodies, revealed with Alexa Fluor 488 and Alexa Fluor 555, and nucleus-counterstained with DAPI.

The resulting sample was analyzed under a microscope driven by ***iMSRC*** which was tuned to automatically detect and capture at high resolution every single region of tissue in the TMA.

The acquisition workflow is detailed in supplementary materials and methods.

Automated image analysis detection of rare circulating tumour cells (Fig. 2c). Circulating tumour cells (CTCs) spread to the blood from both primary and metastatic cancers, and are believed to play a role in the spread of the disease throughout the body[9].

A novel microfluidic device (The IsoFlux System, Fluxion Biosciences Inc, South San Francisco,CA) has recently been described and which enables the CTC enrichment of blood samples. These samples are usually further tested using an immunofluorescence assay based on detecting nucleated, cytokeratin (CK)-positive, CD45-negative cells.

Detailed protocols can be found in reference 9 and in Fluxion Biosciences Inc's CTC Enumeration and CTC Enrichment kits.

A typical analytical design for testing CTC recovery in this device begins with preparing samples with a defined number of CTCs, which is done by isolating a known number of positive CTCs and spiking them into blood from a healthy donor. The frequency of CTCs in these samples is generally less than 1 in 400 (0.25%), which justifies the need for automated cell detection.

Briefly, clinical blood samples were processed for CTC enrichment, subsequently spiked into healthy donor blood and dispensed on to a standard slide for imaging. Cell nuclei were then counterstained with Hoechst 33342 and double immunostained for CK (FITC directly conjugated fluorophore) and CD45 (indirectly labeled with a Cy3-conjugated antibody).

The resulting sample was analyzed under a microscope driven by ***iMSRC*** set to automatically detect and capture CTCs at high resolution.

The acquisition workflow is detailed in supplementary materials and methods.

References

1. de Chaumont, F. *et al.* Icy: an open bioimage informatics platform for extended reproducible research. *Nat. Methods* **9,** 690–696 (2012).
2. Henrikѕson, J. *et al.* Endrov: an integrated platform for image analysis. *Nat. Methods* **10,** 454–456 (2013).
3. Conrad, C. *et al.* Micropilot: automation of fluorescence microscopy-based imaging for systems biology. *Nat. Methods* **8,** 246 (2011).
4. Edelstein A., Amodaj N., Hoover K., Vale R., Stuurman N. Computer control of microscopes using μManager. *Curr. Protoc. Mol. Biol.* Chapter 14:Unit14.20 (2010).
5. Schneider, C. A., Rasband, W. S. & Eliceiri, K. W. NIH Image to ImageJ: 25 years of image analysis. *Nat. Methods* **9,** 671–675 (2012).
6. Alonso-Curbelo, D. *et al.* RAB7 controls melanoma progression by exploiting a lineage-specific wiring of the endolysosomal pathway. *Cancer Cell* **26,** 61–76 (2014).
7. Clausell-Tormos, J. *et al.* Nano-volume well array chip for large-scale propagation and high-resolution analysis of individual cancer stem cells. *J. Nanomed. Nanotechnol.* **5,** 191–198 (2014)
8. Miranda-Lorenzo, I. *et al.* Intracellular autofluorescence: a biomarker for epithelial cancer stem cells. *Nat. Methods* **11,** 1161–1169 (2014).
9. Harb, W. *et al.* Mutational Analysis of Circulating Tumor Cells Using a Novel Microfluidic Collection Device and qPCR Assay. *Transl. Oncol.* **6,** 528–538 (2013).
10. Carpenter, A. E., Kamentsky, L., & Eliceiri, K. W. A call for bioimaging software usability. *Nat. Methods* **9,** 666–670 (2012).

Acknowledgements

The authors would like to thank Dr. Rocio Ramos-Medina, from the Laboratory of Translational Oncology, Health Research Institute of Gregorio Marañón [IiSGM], Madrid, Spain, for her contribution on cell rare detection, Ms. Lola Martínez, and Drs Maria Luigia de Bonis and Ultan Philip Cronin for reviewing the manuscript, Juan Luis Monteagudo, Paco Porto and Frank Sieckmann for technical support and Drs. Direna Alonso and Jenifer Clausell for beta testing.

Author Contributions

D. conceived ***iMSRC***. A. developed ***iMSRC*** software and website. J. developed and tested the image analysis scripts. D. M. and J. designed the experiments, tested the system, analyzed data and wrote the main text of the manuscript. D. and D.G. supervised microscopy and software development, respectively. All authors reviewed the manuscript, prepared the figures and contributed to the website contents.

Additional Information

Supplementary information accompanies this paper at http://www.nature.com/srep

Competing financial interests: The authors declare no competing financial interests.

How to cite this article: Carro, A. *et al. iMSRC*: converting a standard automated microscope into an intelligent screening platform. *Sci. Rep.* **5**, 10502; doi: 10.1038/srep10502 (2015).

4.5 INTRACELLULAR AUTOFLUORESCENCE: A BIOMARKER FOR EPITHELIAL CANCER STEM CELLS.

Irene Miranda-Lorenzo, Jorge Dorado, Enza Lonardo, Sonia Alcala, Alicia G Serrano, Jenifer Clausell-Tormos, Michele Cioffi, Diego Megías, Sladjana Zagorac, Anamaria Balic, Manuel Hidalgo, Mert Erkan, Joerg Kleeff , Aldo Scarpa, Bruno Sainz Jr y Christopher Heeschen

Este trabajo representa una primera prueba de concepto de la utilidad de la metodología de *Screening inteligente* (iMSRC) presentada en este proyecto de tesis para la detección de eventos raros infrecuentes en microscopía. En este trabajo se describe un nuevo biomarcador válido para la localización de células madre cancerígenas epiteliales (CSCs, *cancer stem cells*) que se consideran fundamentales en el crecimiento del tumor y los procesos de metástasis. En concreto se encontró una acumulación de auto-fluorescencia subcelular característico de este tipo celular. Las células con dicho marcador mostraron resistencia a la quimioterapia y expresan genes asociados a la pluripotencia. Gracias a la caracterización espectral y a experimentos utilizando microscopía avanzada se pudo identificar el marcaje como una acumulación de riboflavina. Para ello se sembraron dichas células sobre un chip de 1400 nano-pocillos, y gracias a el empleo de la tecnología de *Screening inteligente* por IMSRC se pudieron localizar aquellos pocillos con una sola célula de partida, y posteriormente seguirlas in vivo durante 72 horas. Si bien se observó en estos ensayos que las células auto-fluorescentes eran capaces de dividirse produciendo una población mixta positiva y negativa para el biomarcador, ninguna de las células no fluorescentes seguidas generaron dicho marcaje auto-fluorescente durante el mismo periodo de tiempo, apuntando a la posibilidad de que, las células sin fenotipo de célula pluripotente tumoral son incapaces de recuperar dicha capacidad.

En este trabajo he participado de forma activa en la planificación de los experimentos que requerían el uso de microscopio óptico, en concreto los ensayos de localización y caracterización espectral de la auto-fluorescencia, aportando ideas y diseños experimentales además de colaborar en su adquisición, análisis de imagen, cuantificación, interpretación y presentación de los datos.

Intracellular autofluorescence: a biomarker for epithelial cancer stem cells

Irene Miranda-Lorenzo[1], Jorge Dorado[1], Enza Lonardo[1], Sonia Alcala[1], Alicia G Serrano[2], Jenifer Clausell-Tormos[1], Michele Cioffi[1], Diego Megias[3], Sladjana Zagorac[1], Anamaria Balic[1], Manuel Hidalgo[4], Mert Erkan[5], Joerg Kleeff[5], Aldo Scarpa[6], Bruno Sainz Jr[1] & Christopher Heeschen[1,7]

Cancer stem cells (CSCs) are thought to drive tumor growth, metastasis and chemoresistance. Although surface markers such as CD133 and CD44 have been successfully used to isolate CSCs, their expression is not exclusively linked to the CSC phenotype and is prone to environmental alteration. We identified cells with an autofluorescent subcellular compartment that exclusively showed CSC features across different human tumor types. Primary tumor–derived autofluorescent cells did not overlap with side-population (SP) cells, were enriched in sphere culture and during chemotherapy, strongly expressed pluripotency-associated genes, were highly metastatic and showed long-term *in vivo* tumorigenicity, even at the single-cell level. Autofluorescence was due to riboflavin accumulation in membrane-bounded cytoplasmic structures bearing ATP-dependent ABCG2 transporters. In summary, we identified and characterized an intrinsic autofluorescent phenotype in CSCs of diverse epithelial cancers and used this marker to isolate and characterize these cells.

The CSC model, which postulates a hierarchical tumor organization such that only a smaller subset of 'stem-like' cells is responsible for tumor promotion and cellular heterogeneity[1], provides a plausible explanation for therapeutic resistance and disease relapse following initial tumor regression[2]. CSCs are regularly identified by the use of surface markers, which have emerged as powerful tools for isolating distinct cell populations from freshly harvested primary tumors[3–6]. Nonetheless, these markers bear the caveats that not only can their expression levels change depending on environmental conditions (such as patient-derived xenografts (PDXs) and primary cell culture) and tissue digestion protocols, but their expression is neither exclusively nor reproducibly linked to a functional CSC phenotype across or even within similar tumor types[7]. Indeed, the use of different surface markers and isolation methodologies has created conflicting data in some settings, emphasizing our lack of sensitive methods to isolate these cells as well as our still immature knowledge of their role in cancer[8–11].

Thus, alternate detection and isolation methods based on CSC functional properties would avoid the use of artifact-prone surface markers and should also provide new insights into CSC biology. Toward this end we have identified an intrinsic autofluorescent phenotype in CSCs of diverse human solid tumors and used this marker as a novel and functionally relevant tool to both isolate and characterize these cells. Specifically, autofluorescent cells could be tracked and isolated, by flow cytometry, in tumors of pancreatic ductal adenocarcinoma (PDAC), colorectal carcinoma (CRC), hepatocellular carcinoma (HCC) and non-small-cell lung carcinoma (NSCLC). These cells demonstrated enhanced CSC features and phenotypes, such as exclusive long-term tumorigenicity and invasiveness *in vivo*. We determined that autofluorescence was a result of the accumulation of the fluorescent vitamin riboflavin in ABCG2-coated vesicles exclusively located within the cytoplasm of CSCs. This new autofluorescent marker can be easily used to isolate CSCs across numerous solid tumors and should allow for the eventual development of screening platforms aimed at identifying anticancer compounds that target CSCs.

RESULTS

Identification of new functional marker for CSCs

Although we have previously shown that different cell surface markers (for example, CD133) can be used to isolate CSCs from freshly resected PDAC tissue[12], we found that the expression levels of these markers could vary considerably on the basis of time to analysis and environmental changes, often resulting in variable and modest functional enrichment for CSCs (**Supplementary Fig. 1**). Moreover, although CSCs expressing combinations of surface markers (for example, CD133 and CD44) showed stronger enrichment than cells that lacked surface marker expression, these marker combinations still left behind large populations of cells expressing either one of the two markers, which were themselves only modestly and variably enriched in CSCs (**Supplementary Fig. 1c**). Interestingly, SP cells, which were previously shown to contain CSCs in some established cancer cell lines[13–15] but not in

[1]Stem Cells and Cancer Group, Molecular Pathology Programme, Spanish National Cancer Research Centre (CNIO), Madrid, Spain. [2]Melanoma Group, Molecular Pathology Programme, CNIO, Madrid, Spain. [3]Confocal Microscopy Unit, Biotechnology Programme, CNIO, Madrid, Spain. [4]Gastrointestinal Cancer Clinical Research Unit, Clinical Research Programme, CNIO, Madrid, Spain. [5]Chirurgische Klinik, Technische Universität München, Munich, Germany. [6]Università degli Studi di Verona, Centro Ricerca Applicata ARC-NET, Verona, Italy. [7]Centre for Stem Cells in Cancer & Ageing, Barts Cancer Institute, Queen Mary University of London, London, UK. Correspondence should be addressed to B.S. (bruno.sainz@uam.es) or C.H. (c.heeschen@qmul.ac.uk).

RECEIVED 16 DECEMBER 2013; ACCEPTED 30 JULY 2014; PUBLISHED ONLINE 28 SEPTEMBER 2014; DOI:10.1038/NMETH.3112

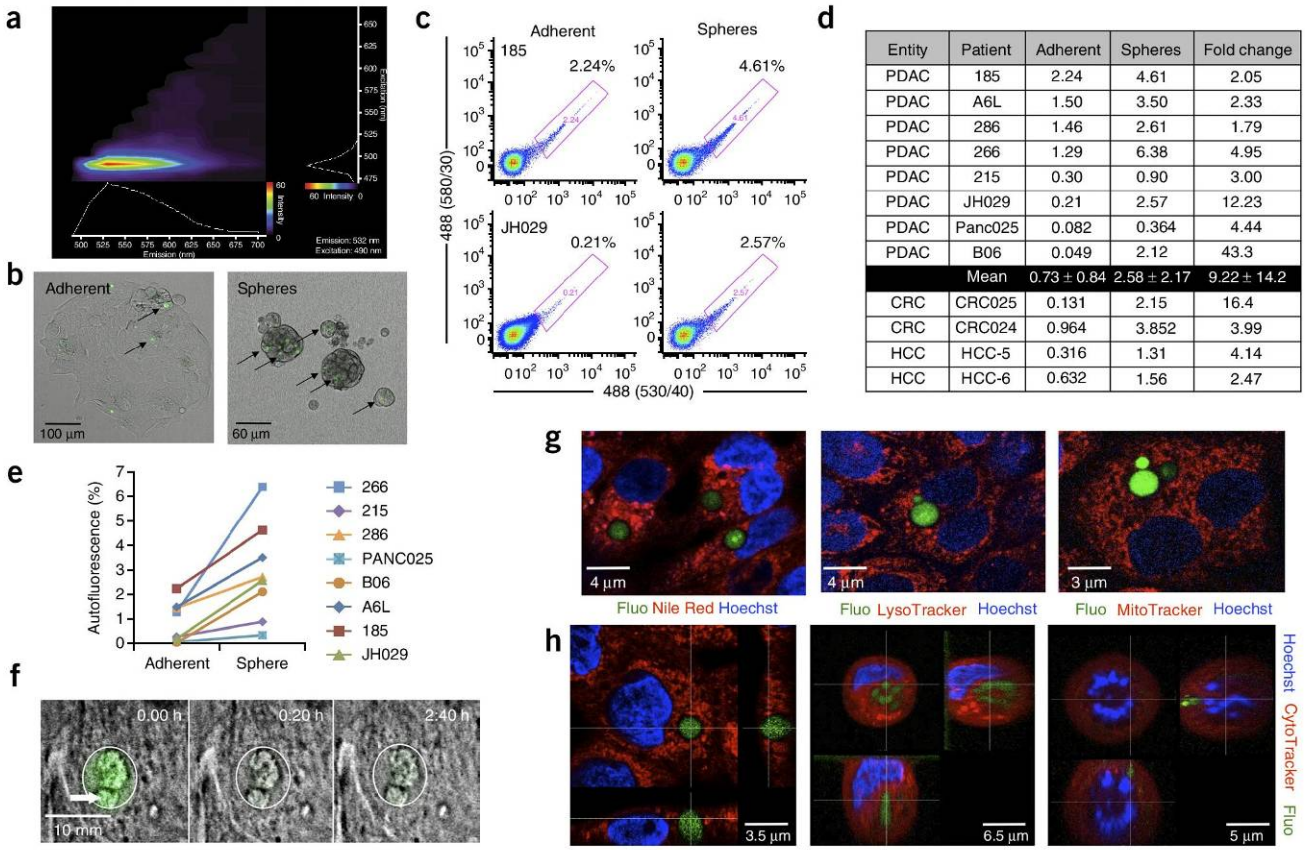

Entity	Patient	Adherent	Spheres	Fold change
PDAC	185	2.24	4.61	2.05
PDAC	A6L	1.50	3.50	2.33
PDAC	286	1.46	2.61	1.79
PDAC	266	1.29	6.38	4.95
PDAC	215	0.30	0.90	3.00
PDAC	JH029	0.21	2.57	12.23
PDAC	Panc025	0.082	0.364	4.44
PDAC	B06	0.049	2.12	43.3
	Mean	0.73 ± 0.84	2.58 ± 2.17	9.22 ± 14.2
CRC	CRC025	0.131	2.15	16.4
CRC	CRC024	0.964	3.852	3.99
HCC	HCC-5	0.316	1.31	4.14
HCC	HCC-6	0.632	1.56	2.47

Figure 1 | Identification of autofluorescent cancer stem cells. (**a**) Spectrum of autofluorescence in primary PDAC PDX-derived cancer cells. (**b**) Representative images of autofluorescent cells (arrows) in primary PDAC PDX-derived *in vitro* cultures grown as adherent cells or spheres ($n = 6$). (**c**) Flow cytometry analysis of autofluorescent content in adherent (left) and sphere cultures (right). Autofluorescent cells are excited with a 488-nm blue laser and best selected as the intersection with filters 530/40 and 580/30. (**d**) Percentage of autofluorescent cells in adherent and sphere cultures for different PDXs ($n = 12$). Fold change is between sphere and adherent percentages. (**e**) Autofluorescence across different PDAC PDX tumors ($n = 8$) cultured as adherent cells or spheres. (**f**) Fluorescence recovery after photobleaching in autofluorescent vesicles (time listed as hours:minutes). Arrow indicates bleached area. Circle highlights autofluorescent vesicle. (**g**) Confocal images of PDAC PDX-derived *in vitro* cultures showing the localization of the indicated markers (Nile red, lipid droplets; LysoTracker, lysosomes; MitoTracker, mitochondria; Hoechst, nuclear staining) relative to autofluorescence (green). (**h**) *z*-stack confocal images of CytoTracker-stained cells (red) illustrating the cytosolic localization of the autofluorescent (green) compartment.

others[16,17], did not efficiently enrich for CSCs in primary PDAC (**Supplementary Fig. 2a**). Similarly disappointing *in vivo* results were obtained for other markers such as aldehyde dehydrogenase (**Supplementary Fig. 2b**). In contrast, spheres were enriched in CSCs (**Supplementary Figs. 2b** and **3**), but sphere formation is not suitable for *ad hoc* identification of CSCs.

We sought to develop new methodologies, devoid of the aforementioned caveats, to efficiently identify CSCs from primary tumors. While searching for such markers, we noticed a small subpopulation of autofluorescent cells in freshly digested tumors from PDAC PDXs and in freshly digested primary patient tumors (PDAC-Tumor) that could be excited (excitation and emission maxima of 490 nm and 532 nm, respectively) with a standard blue laser (for example, 488 nm) (**Fig. 1a**,**b**) but not with yellow-green (for example, 561 nm) or red (for example, 640 nm) lasers (**Supplementary Fig. 4a**). These autofluorescent cells were also visible in PDAC PDX-derived adherent cultures, were strongly enriched for in spheres and showed an enhanced *in vivo* tumorigenic phenotype compared to non-autofluorescent cells or cells isolated via more traditional methods (**Supplementary Figs. 1c**, **2** and **3**).

Autofluorescence was previously reported for glioblastoma cells but turned out to be related to contamination with 293T cells stably expressing GFP[18]. To exclude such artifacts, we demonstrated that (i) the autofluorescence spectrum observed was distinct from that of GFP (**Supplementary Fig. 4b**), (ii) there was no evidence of *gfp* mRNA or GFP protein in our samples (**Supplementary Fig. 4c**), (iii) autofluorescent and non-autofluorescent cells could not be distinguished by size or granularity (**Supplementary Fig. 4d**), and (iv) autofluorescent and non-autofluorescent cells were genotypically identical to unsorted bulk cells as determined by TaqMan OpenArray technology (**Supplementary Fig. 5a**). We also showed that (v) autofluorescent cells were of epithelial origin (i.e., $EPCAM^+$) (**Supplementary Fig. 5b**), (vi) they could not be detected in the tumor stroma (**Supplementary Fig. 5c**), and (vii) autofluorescence was not a result of dying or apoptotic cells (**Supplementary Fig. 6**). In sum, autofluorescence was a cell-specific authentic feature present within the bulk tumor cell population.

We next analyzed the autofluorescent phenotype across a large panel of tumors and showed that autofluorescence could be tracked and reproducibly quantified by flow cytometry (**Fig. 1c**). We observed cells with this phenotype in a large panel of PDAC PDX-derived *in vitro* cultures, and these cells were consistently enriched in culture conditions promoting sphere growth[19]

(**Fig. 1d**,**e**). We also detected autofluorescent cells in PDX-derived cultures from other tumor types such as CRC, HCC and NSCLC (**Fig. 1d** and **Supplementary Fig. 7**). Interestingly, the autofluorescence signal was confined to one or more distinct vesicles but could be eliminated in all vesicles by localized laser-induced photobleaching (**Fig. 1f**), indicating that the source of the signal was diffusible and neither attached to any structure nor crystalline in nature, and that the apparently separate autofluorescent compartments present in some cells were interconnected. Moreover, autofluorescence did not colocalize with lipid droplets or lysosomes, nor was it mitochondria-restricted, as demonstrated by costaining with Nile red, LysoTracker or MitoTracker, respectively (**Fig. 1g**); rather, the autofluorescence was restricted to distinct membrane-bound cytoplasmic vesicles (**Fig. 1h**).

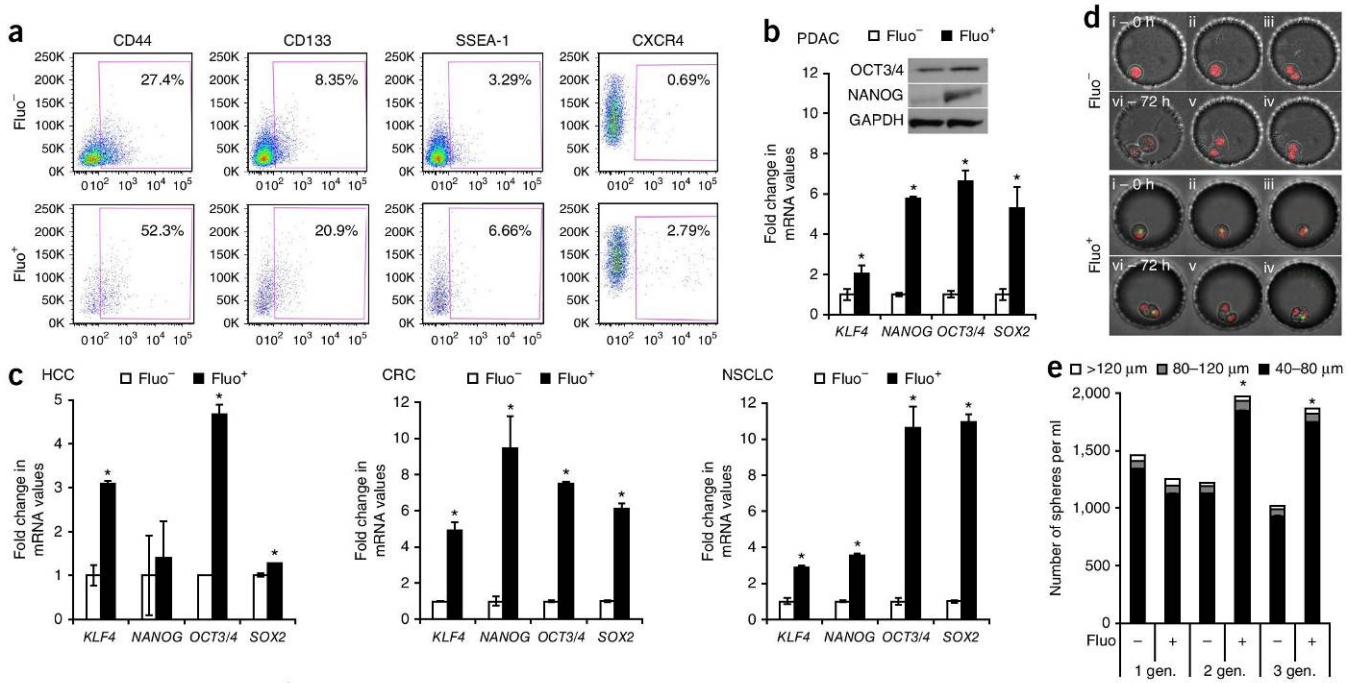

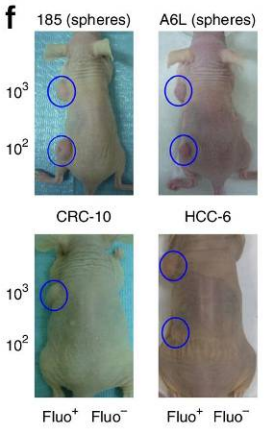

Tumor take after 3 months (# tumors/# injections)

No. of cells injected		10^4	10^3	10^2	1	Freq	*P* value
A6L	Fluo⁻		4/5	0/5		0.06%	0.0017
	Fluo⁺		5/5	4/5		1.6%	
185	Fluo⁻		2/5	0/5	0/21	0.014%	0.0007
	Fluo⁺		4/5	4/5	2/21	0.56%	
215	Fluo⁻	2/4	1/4	0/4		<0.001%	<0.0001
	Fluo⁺	3/4	3/4	2/4		0.16%	
CRC-10	Fluo⁻	3/4	0/4	0/4		<0.0001%	0.0025
	Fluo⁺	4/4	2/4	2/4		0.14%	
CRC-14	Fluo⁻	1/4	0/4			<0.0001%	0.067
	Fluo⁺	3/4	0/4			0.03%	
HCC-6	Fluo⁻	3/4	1/4	0/4		<0.0001%	<0.00001
	Fluo⁺	4/4	4/4	2/4		0.18%	
HCC-5	Fluo⁻	1/2	0/2	0/2		<0.0001%	0.00016
	Fluo⁺	1/2	2/2	1/2		0.02%	
NSCLC-005	Fluo⁻	0/2	0/2	0/2		<0.0001%	0.0043
	Fluo⁺	2/2	1/2	0/2		0.04%	

Average 80× enrichment (95% confidence interval 27–150)

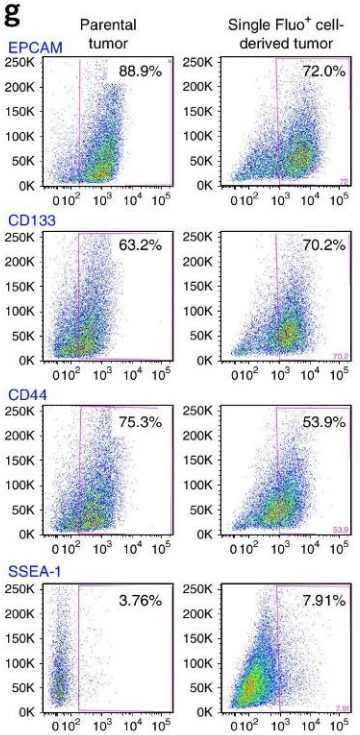

Figure 2 | *In vitro* and *in vivo* characterization of autofluorescent cells. (**a**) Representative flow cytometry analysis for the indicated markers in primary PDAC non-autofluorescent (Fluo⁻) and autofluorescent (Fluo⁺) cells. Plots shown are representative of three primary PDAC PDX-derived *in vitro* cultures each performed in duplicate. (**b**) RT-qPCR analysis of pluripotency-associated genes in sorted Fluo⁻ and Fluo⁺ PDAC cells. Data shown are normalized for β-actin expression and represent the average gene expression from different primary PDAC PDX-derived *in vitro* cultures and freshly digested PDAC patient derived tumors ($n = 6$). Inset, western blot for OCT3/4 (POU5F1) and NANOG FACS-sorted Fluo⁻ and Fluo⁺ cells. (**c**) RT-qPCR analysis of pluripotency-associated genes in sorted Fluo⁻ and Fluo⁺ of different primary PDX-derived *in vitro* cultures from HCC, CRC and NSCLC ($n = 2$, 4 and 2, respectively, each performed in duplicate). Data shown are normalized for β-actin expression and represent the relative ratio Fluo⁺ vs. Fluo⁻. (**d**) Single Fluo⁺ and Fluo⁻ pancreatic cancer cells were followed by time-lapse microscopy for 72 h. Roman numerals indicate the order of the pictures. (**e**) Representative sphere numbers and diameter (µm) for FACS-sorted Fluo⁻ and Fluo⁺ cells over three generations (gen.). Data are representative of different primary PDAC PDX-derived *in vitro* cultures ($n = 3$, each performed in duplicate). (**f**) Representative photos of mice subcutaneously injected with Fluo⁺ and Fluo⁻ cells (PDAC PDX) (left) and summary of *in vivo* tumorigenicity of subcutaneously injected FACS-sorted Fluo⁻ and Fluo⁺ cells from PDXs of pancreatic (185, A6L, 215), colorectal (CRC-10, CRC-14), liver (HCC-6, HCC-5) and lung (NSCLC-005) cancers (right). (**g**) Flow cytometry analysis of the indicated markers in parental and single-cell–derived 185 tumors. Error bars (**b**,**c**,**e**), s.d. (n = biological replicates). Statistical significance was assessed by Mann-Whitney test, $^*P < 0.05$.

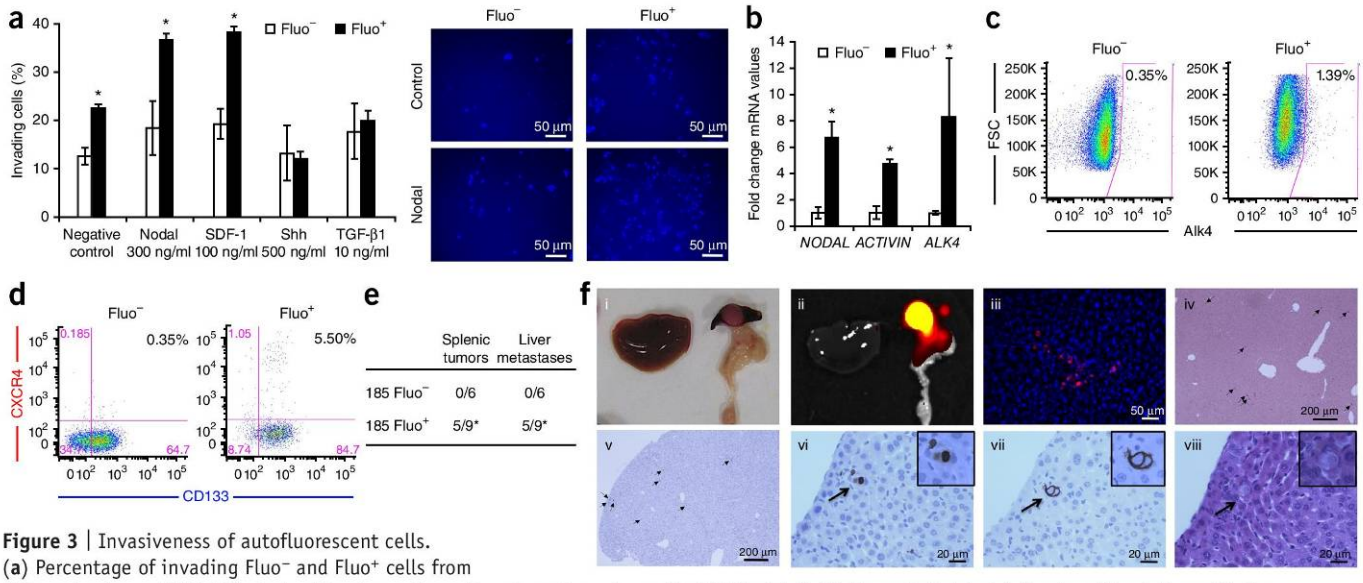

Figure 3 | Invasiveness of autofluorescent cells. (**a**) Percentage of invading Fluo⁻ and Fluo⁺ cells from different primary PDAC PDX-derived *in vitro* cultures ($n = 2$, each performed in triplicate) (left) through Matrigel following stimulation with the indicated factors. Representative images of invaded cells (right). (**b**) RT-qPCR analysis of *NODAL*, *ACTIVIN* (*INHBA*) and *ALK4* (*ACVR1*) in sorted Fluo⁻ and Fluo⁺ cells of primary PDAC PDX-derived *in vitro* cultures ($n = 3$). Data are normalized for β-actin expression and represent the relative ratio Fluo⁺ vs. Fluo⁻. (**c**) Flow cytometry analysis of ALK4 receptor expression in Fluo⁻ and Fluo⁺ cells. Plots shown are representative of different primary PDAC PDX-derived *in vitro* cultures ($n = 2$, each performed in duplicate). FSC, forward scatter. (**d**) Flow cytometry analysis of CXCR4 and CD133 expression on Fluo⁻ and Fluo⁺ cells. Plots shown are representative of different primary PDAC PDX-derived *in vitro* cultures ($n = 3$, each performed in duplicate). (**e**) Quantification of *in vivo* tumorigenicity and subsequent liver metastases for Fluo⁻ and Fluo⁺ cells. (**f**) Representative images of pancreatic cancer cell human metastases in mouse livers 4 months after intrasplenic injection of PDAC PDX (185) Fluo⁺ sorted cells. Panels show (i) mouse liver, spleen and pancreas; (ii) IVIS (*in vivo* imaging system) for mCherry⁺ cells in the spleen; (iii) *ex vivo* whole-tissue confocal image for mCherry⁺ cells in the liver; (iv) *in situ* hybridization using a human-specific Alu probe; (v) immunohistochemistry for DsRed; and (vi–viii) serial sections stained for DsRed, human cytokeratin19 and hematoxylin-eosin, respectively. Arrows indicate cells stained positive for indicated markers. Error bars (**a**,**b**), s.d. (n = biological replicates). Statistical significance was assessed by Mann-Whitney test, $^*P < 0.05$.

Autofluorescent cells display functional features of CSCs

We next determined whether these cells were phenotypically and functionally distinct from their non-autofluorescent counterparts. First, although CSC surface markers were variably overexpressed in autofluorescent cells, which is in line with the significantly ($P < 0.05$; P values calculated via Mann-Whitney test throughout) stronger enrichment for tumorigenic cells in the autofluorescent population (**Supplementary Fig. 3**), none of these markers was exclusively restricted to autofluorescent cells (**Fig. 2a**). Reverse-transcription quantitative PCR (RT-qPCR) analysis revealed that autofluorescent cells also significantly ($P < 0.05$) overexpressed pluripotency-associated genes at both the mRNA and protein level (**Fig. 2b**,**c** and **Supplementary Fig. 7a–c**). Last, using a customized nanowell chip, which allows one to microscopically follow single cells, we observed that over a period of 72 h, autofluorescent cells gave rise to both autofluorescent and non-autofluorescent cells; however, out of more than 400 single non-autofluorescent cells monitored, none gave rise to autofluorescent cells irrespective of whether they underwent cell division (**Fig. 2d** and **Supplementary Fig. 8a**). Thus, in contrast to earlier cell population–based studies[20], our data argue against the notion that non-CSCs are capable of replenishing CSCs.

Regarding self-renewal capacity, autofluorescent cells formed significantly ($P < 0.05$) more secondary and tertiary spheres *in vitro*, whereas non-autofluorescent cells appeared to lose this capacity during passaging (**Fig. 2e**). To more rigorously test this, we performed serial *in vivo* transplantation experiments and observed that tumors derived from non-autofluorescent cells disappeared during serial passaging, whereas autofluorescent cell-derived tumors maintained their intrinsically high self-renewal capacity (**Supplementary Fig. 8b**), demonstrating that long-term tumorigenic capacity was restricted to autofluorescent cells. Moreover, implantation of decreasing numbers of autofluorescent cells from PDX *in vitro* cultures from various sources (PDAC, HCC, CRC and NSCLC) revealed that autofluorescent cells were more tumorigenic (**Fig. 2f**). Notably, for tumor PDAC PDX 185, we simultaneously analyzed a large panel of putative CSC markers, which revealed that autofluorescence as a single marker more strongly enriched for CSCs than did any of the other tested single markers or combinations thereof (**Supplementary Figs. 1c**, **2** and **3**). In addition, whereas single non-autofluorescent cells never gave rise to tumors, single autofluorescent cells generated tumors that recapitulated the heterogeneous composition of the original tumors at the level of autofluorescence, expression of cell surface markers (**Fig. 2g**) and pluripotency-associated genes (**Supplementary Fig. 8c**). Finally, we sorted autofluorescent cells from several freshly digested PDX tumors as well as from primary tumors from patients and consistently found that these cells exhibited stem-like properties, including the expression of pluripotency-associated genes and significantly ($P < 0.05$) enhanced *in vivo* tumorigenicity without any *in vitro* culturing (**Supplementary Fig. 9a**,**b**).

Autofluorescent cells are highly invasive

Holding true to the CSC phenotype[21], *in vitro* invasion assays revealed an overall enhanced invasive capacity of autofluorescent cells (**Fig. 3a**). Chemoattraction of invading cells by the CXCR4

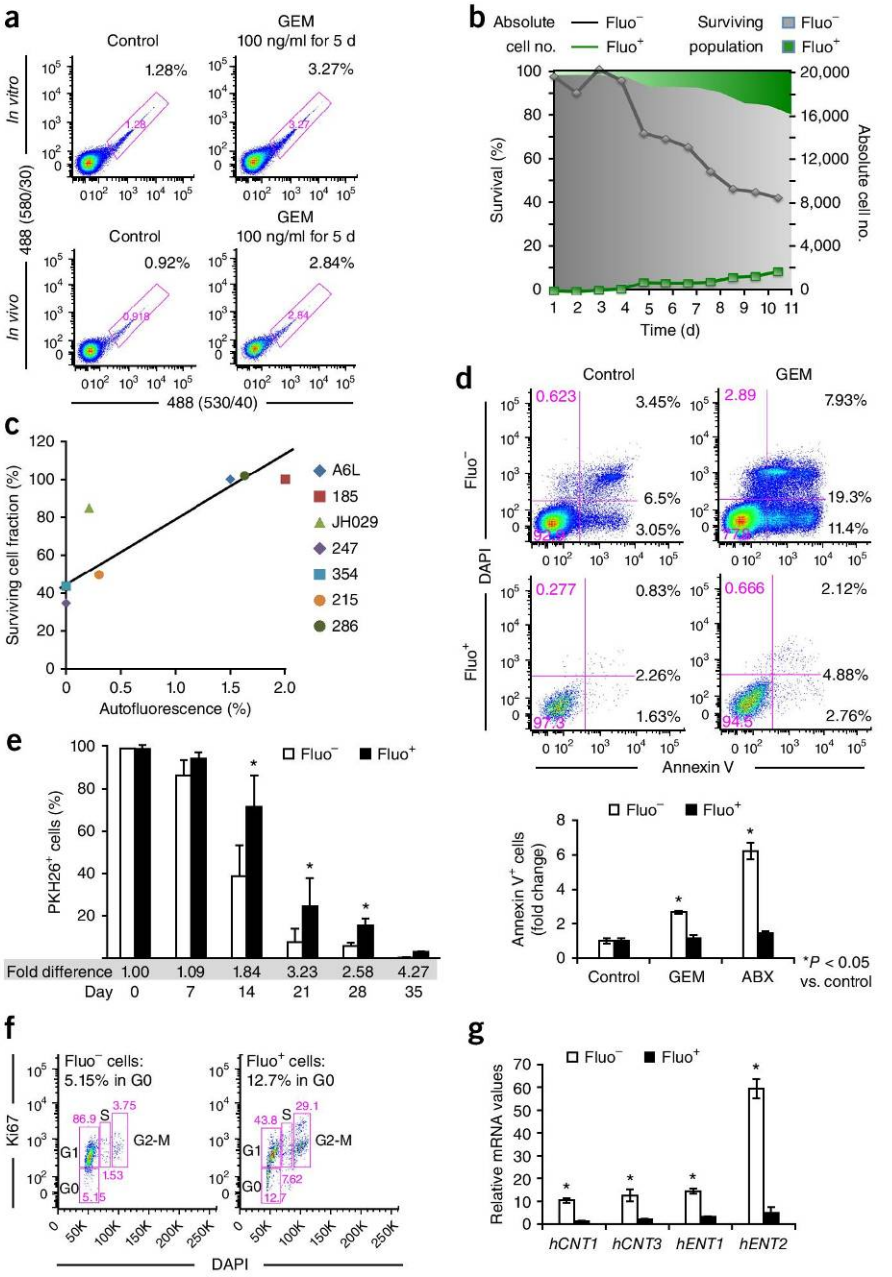

Figure 4 | Autofluorescent cells are resistant to chemotherapy. (**a**) Representative flow cytometry analysis of autofluorescence in control versus gemcitabine (GEM)-treated cells for different primary PDX-derived (PDAC, CRC) *in vitro* cultures (top, $n = 3,1$, respectively) and PDAC PDX tumors (bottom, $n = 3$) each performed in triplicate. (**b**) Chemoresistance of autofluorescent PDAC PDX-derived *in vitro* cultures (185) cells during 12 d of treatment with GEM. Areas indicate surviving cell fraction. Lines indicate absolute number of surviving cells. (**c**) Correlation between autofluorescence and chemoresistance for different primary PDAC PDX-derived *in vitro* cultures ($n = 7$) treated with GEM for 72 h. (**d**) Representative flow cytometry analysis of annexin V staining in GEM-treated cells for different PDAC PDX-derived *in vitro* cultures compared to control-treated cells (top), and quantification of the annexin V staining in GEM-treated and Abraxane (ABX)-treated cells ($n = 2$) each performed in triplicate (bottom). (**e**) Loss of PKH26 labeling in Fluo⁻ and Fluo⁺ cells during 5 weeks of culture. Data are representative of different primary PDAC PDX-derived *in vitro* cultures ($n = 2$, each performed in duplicate). (**f**) Representative flow cytometry analysis for Ki67 and DAPI for sorted Fluo⁻ and Fluo⁺ cells derived from a freshly digested PDAC PDX tumor ($n = 1$, performed in triplicate). (**g**) RT-qPCR analysis of human concentrative nucleoside transporter (hCNT) 1 and 3 and human equilibrative nucleoside transporter (hENT) 1 and 2 (*SLC28A1*, *SLC28A3*, *SLC29A1* and *SLC29A2*) in sorted Fluo⁻ and Fluo⁺ cells of different primary PDAC PDX-derived *in vitro* cultures. Data are normalized for β-actin expression and represent the relative ratio Fluo⁺ vs. Fluo⁻ ($n = 3$, each performed in triplicate). Error bars (**d**,**e**,**g**), s.d. (n = biological replicates). Statistical significance was assessed by Mann-Whitney test, $^*P < 0.05$.

ligand SDF-1 (ref. 22) and the ALK4 ligand Nodal[19] both resulted in enhanced invasion of these cells, whereas sonic hedgehog and TGF-β1 had no specific impact. Consistently, autofluorescent cells overexpressed ALK4 as well as its specific ligands Nodal and Activin (**Fig. 3b**), and they also harbored a subset of ALK4⁺ cells (**Fig. 3c**). Moreover, autofluorescent cells (Fluo⁺) also overexpressed CXCR4 (**Fig. 2a**), and these Fluo⁺CXCR4⁺ cells were additionally enriched in CD133, a subpopulation (CD133⁺CXCR4⁺) that we have previously shown to be metastatic CSCs[12] (**Fig. 3d**). Intrasplenic injections of cells expressing an H2B-mCherry reporter revealed exclusive tumor formation and subsequent cell dissemination to the liver (i.e., micrometastases) for autofluorescent cells only, as determined by RT-qPCR analysis of human *GAPDH* and mCherry-encoding mRNA expression in livers (**Fig. 3e** and data not shown). These data were further corroborated by *ex vivo* whole liver tissue confocal microscopy showing mCherry⁺ cells and immunohistochemistry demonstrating the presence of cells positive for human-specific ALU, huCK19 and DsRed (**Fig. 3f**).

Autofluorescent cells are highly chemoresistant

CSCs are believed to be highly chemoresistant. In line with this hypothesis, treatment with the cytotoxic drug gemcitabine resulted in the enrichment of autofluorescent cells *in vitro* and *in vivo* (**Fig. 4a**). Longer treatment with gemcitabine *in vitro* reduced the non-autofluorescent cell population to ~40% of the total starting population, whereas autofluorescent cells showed no reduction in absolute cell numbers but were rather relatively enriched (**Fig. 4b**). We expanded these findings to a representative panel of seven primary PDAC PDX tumors, in which overall chemoresistance *in vitro* correlated with autofluorescence content (**Fig. 4c**). Last, we observed *in vivo* that long-term gemcitabine-treated autofluorescent cells were tumorigenic, whereas their autofluorescent-negative counterparts were not (**Supplementary Fig. 9c**).

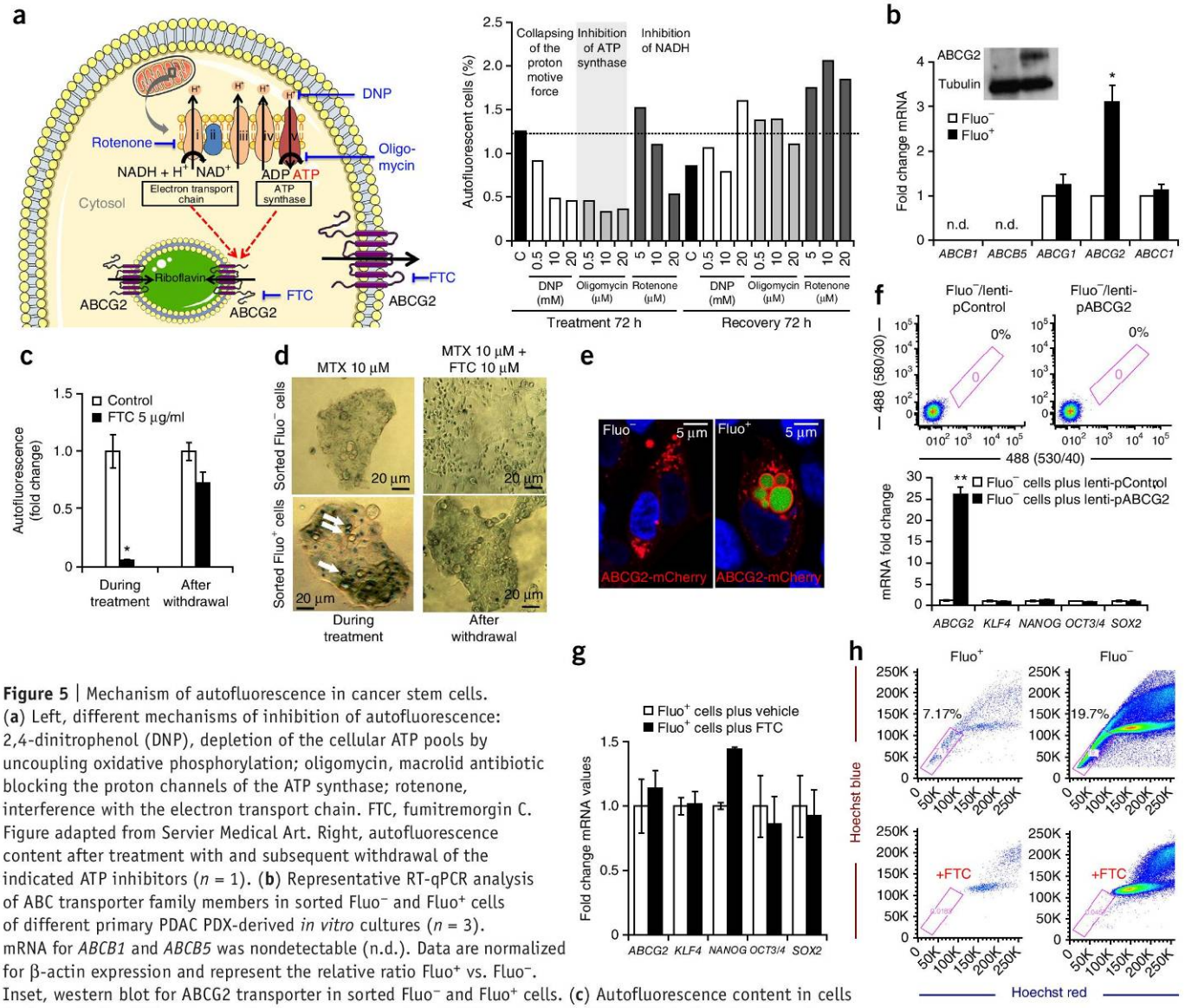

Figure 5 | Mechanism of autofluorescence in cancer stem cells. (**a**) Left, different mechanisms of inhibition of autofluorescence: 2,4-dinitrophenol (DNP), depletion of the cellular ATP pools by uncoupling oxidative phosphorylation; oligomycin, macrolid antibiotic blocking the proton channels of the ATP synthase; rotenone, interference with the electron transport chain. FTC, fumitremorgin C. Figure adapted from Servier Medical Art. Right, autofluorescence content after treatment with and subsequent withdrawal of the indicated ATP inhibitors ($n = 1$). (**b**) Representative RT-qPCR analysis of ABC transporter family members in sorted Fluo$^-$ and Fluo$^+$ cells of different primary PDAC PDX-derived *in vitro* cultures ($n = 3$). mRNA for *ABCB1* and *ABCB5* was nondetectable (n.d.). Data are normalized for β-actin expression and represent the relative ratio Fluo$^+$ vs. Fluo$^-$. Inset, western blot for ABCG2 transporter in sorted Fluo$^-$ and Fluo$^+$ cells. (**c**) Autofluorescence content in cells during and after FTC treatment. Data are representative of different primary PDAC PDX-derived *in vitro* cultures ($n = 3$, each performed in triplicate). (**d**) Representative images of mitoxantrone (MTX) accumulation in cytoplasmic vesicles of sorted Fluo$^-$ and Fluo$^+$ cells in the presence or absence of 10 μm FTC. (**e**) Representative confocal images of ABCG2-mCherry expression in Fluo$^-$ and Fluo$^+$ cells. (**f**) Top, flow cytometry analysis of autofluorescence content in different PDAC PDX-derived *in vitro* cultures ($n = 2$) sorted for Fluo$^-$ cells and subsequently infected with a control or *ABCG2*-overexpressing lentiviral vector. Bottom, RT-qPCR analysis of pluripotency-associated gene expression in sorted Fluo$^-$ control or ABCG2-overexpressing cells of different primary PDAC PDX-derived *in vitro* cultures ($n = 2$) each performed in duplicate. Data are normalized for β-actin expression and represent the relative ratio Fluo$^+$ vs. Fluo$^-$. (**g**) RT-qPCR analysis of pluripotency-associated gene expression in sorted Fluo$^+$ cells of different primary PDAC PDX-derived *in vitro* cultures ($n = 2$) treated with FTC, each performed in duplicate. Data are normalized for β-actin expression and represent the relative ratio Fluo$^+$ vs. Fluo$^-$. (**h**) Representative flow cytometry plots for side-population analysis in sorted Fluo$^-$ and Fluo$^+$ cells from different PDAC PDX-derived cultures ($n = 3$, each performed in duplicate). ABCG2 was specifically inhibited by FTC. Error bars (**b**,**c**,**f**,**g**), s.d. (n = biological replicates). Statistical significance was assessed by Mann-Whitney test, $^*P < 0.05$, $^{**}P < 0.01$.

Annexin V staining revealed that PDX-derived *in vitro*–cultured non-autofluorescent cells were more rapidly forced into apoptosis compared to autofluorescent cells (**Fig. 4d**). We investigated two possible reasons for their enhanced chemoresistance. First, we compared the *in vitro* cycling profile of autofluorescent and non-autofluorescent cells using the label-retaining dye PKH26 (ref. 23) and observed that autofluorescent cells had a significantly ($P < 0.05$) higher label-retaining and slow-cycling phenotype (**Fig. 4e**). The slow-cycling profile was confirmed *in vivo* as we found a marked enrichment in the G0 population in autofluorescent cells (12.7%) compared to the non-autofluorescent cells (5.15%) from freshly harvested tumors (**Fig. 4f**). Second, RT-qPCR analysis for the human concentrative nucleoside (hCNT) and equilibrative nucleoside (hENT) transporters, on which gemcitabine uptake depends[24], showed significantly ($P < 0.05$) lower expression in autofluorescent cells (**Fig. 4g**). Thus, the inherent chemoresistant nature of autofluorescent cells could be explained, in part, by their slow-cycling nature and the lack of expression of gemcitabine transporters.

Mechanism of autofluorescence

Because we noted that autofluorescent cells contained higher intracellular ATP levels (**Supplementary Fig. 10a**), and inhibition of ATP production by different means (oligomycin, rotenone and 2,4-dinitrophenol (DNP)) resulted in reproducible but reversible loss of autofluorescence (**Fig. 5a**), we reasoned that the subcellular autofluorescent compartment is driven by ATP-dependent transporters. Indeed, autofluorescent cells overexpressed ABCG2 at both the mRNA and protein level (**Fig. 5b**), whereas other ATP transporters were not differentially expressed.

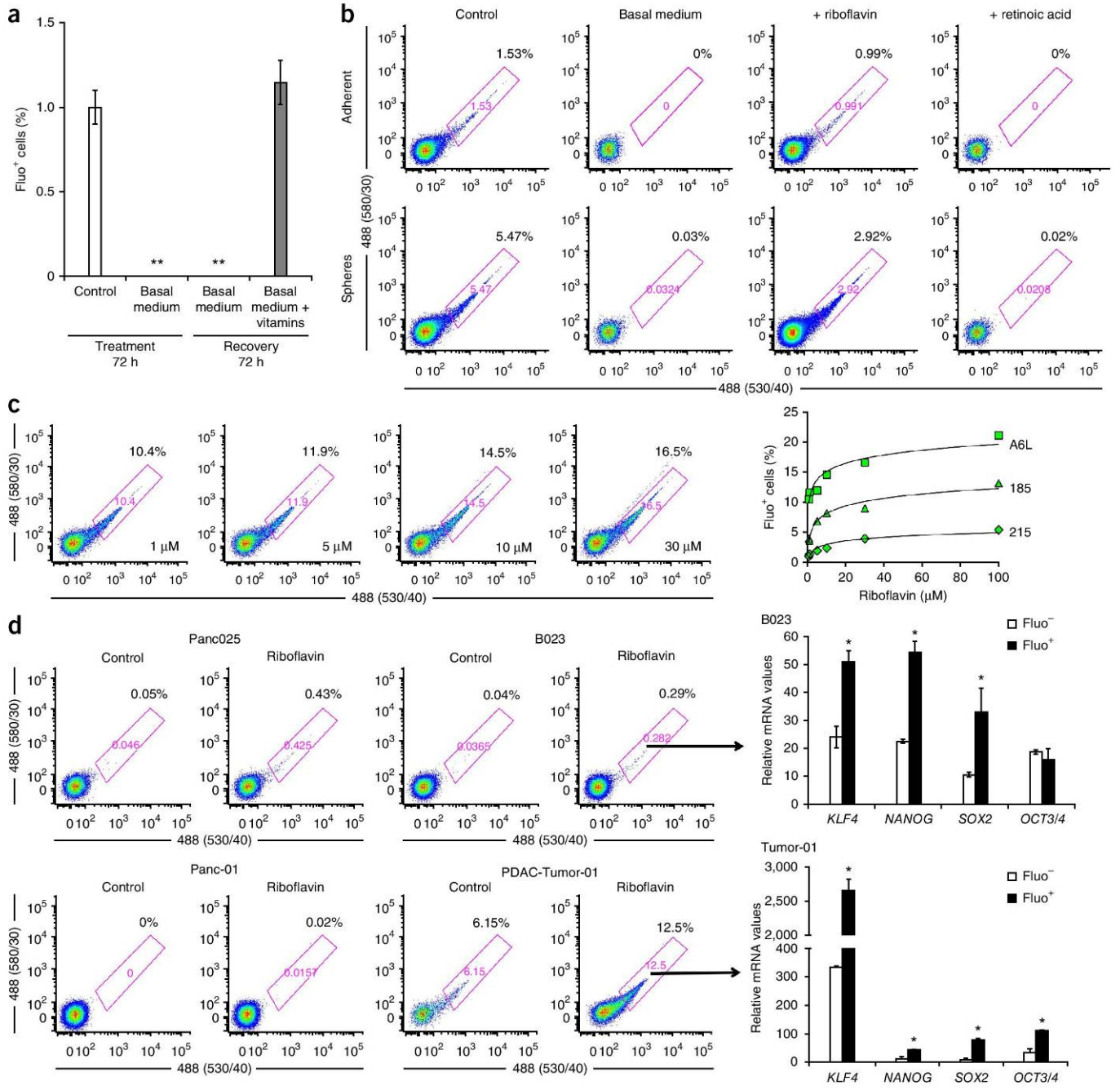

Figure 6 | Source of autofluorescence in cancer stem cells. (**a**) Percentage of autofluorescent cells in different primary PDAC PDX-derived *in vitro* cultures ($n = 3$, each performed in triplicate) in basal medium (without vitamins) or after recovery in basal medium or basal medium plus vitamin cocktail. (**b**) Representative flow cytometry analysis of autofluorescence recovery in adherent cells or spheres cultured in basal medium or basal medium supplemented with riboflavin or retinoic acid (each at 1 µM). Plots shown are representative of different primary PDAC PDX-derived *in vitro* cultures ($n = 3$, each performed in duplicate). (**c**) Representative flow cytometry plots of cells exposed to increasing concentrations of riboflavin (left), whose effects were quantified for different primary PDAC PDX-derived *in vitro* cultures (right) ($n = 3$). (**d**) Left, representative flow cytometry plots of primary PDAC PDX-derived *in vitro* cultures (Panc025 and B023), the Panc01 cell line and a freshly digested patient tumor (PDAC-Tumor-01), with and without riboflavin treatment (30 µM). Right, RT-qPCR analysis of pluripotency-associated gene expression in Fluo$^-$ and Fluo$^+$ cells from the indicated samples after exposure to 30 µM riboflavin, each performed in duplicate. Data are normalized for β-actin expression and represent the relative mRNA values of Fluo$^+$ and Fluo$^-$. Error bars (**a**,**d**), s.d. (n = biological replicates). Statistical significance was assessed by Mann-Whitney test, $^*P < 0.05$, $^{**}P < 0.01$.

Moreover, functionally inhibiting ABCG2 with fumitremorgin C (FTC)[25] reversibly eliminated autofluorescence (**Fig. 5c**), and the ABCG2-dependent fluorescent type II topoisomerase inhibitor mitoxantrone[26] colocalized with the autofluorescent compartment, suggesting expression of ABCG2 transporters in membranes of autofluorescent vesicles (**Fig. 5d**). The latter was confirmed by colocalization studies using a lentiviral vector expressing an ABCG2-mCherry fusion protein. ABCG2 transporters were expressed in the membrane of autofluorescent vesicles, whereas in non-autofluorescent cells, ABCG2 expression was detected throughout the cytoplasm and in the cell membrane (**Fig. 5e**). Notably, in non-autofluorescent cells, overexpression of *ABCG2* did not result in *de novo* generation of autofluorescent vesicles, nor did these cells acquire stem-like features such as the overexpression of pluripotency-associated genes (**Fig. 5f**). As these results suggested that ABCG2 activity was not responsible for the stem-like phenotypes of CSCs, we next functionally inhibited ABCG2 transporter activity with FTC in autofluorescent cells and did not observe any effect on the expression of pluripotency-associated genes or on their sphere-formation capacity (**Fig. 5g** and data not shown). Last, because overexpression of *ABCG2* is a defining feature of SP cells, we investigated the distribution of autofluorescent cells between SP and non-SP cells. Interestingly, autofluorescent cells were more prominent in the non-SP population, indicating that autofluorescent cells represent a distinct ABCG2-expressing subpopulation that is phenotypically different from SP cells (**Fig. 5h**), which is consistent with our earlier finding that SP-sorted cells were not enriched for CSCs (**Supplementary Fig. 2**).

Source of autofluorescence

Autophagy has been related to autofluorescence[27], but neither expression levels of the autophagy-related gene *ATG12* or autophagy related-protein LC3 nor inhibition or induction of autophagy supported this notion in our studies (**Supplementary Fig. 10b,c**). On the basis of these results and our observations that autofluorescent vesicles colocalized with ABCG2, we reasoned that a specific ABCG2-transported substrate may be responsible for autofluorescence. Culturing primary PDAC PDX-derived cells in basal medium (vitamin free) resulted in complete loss of autofluorescence within 72 h (**Fig. 6a**; medium composition in **Supplementary Table 1**), and although basal medium alone could not restore autofluorescence following FTC treatment, basal medium supplemented with a cocktail of essential vitamins could (**Fig. 6a**), suggesting that one or more vitamins were responsible for the autofluorescence. Using the spectroscopic profile of the autofluorescent CSC feature (excitation, 490 nm; emission, 532 nm (490/532 nm); **Fig. 1a**), we identified retinoic acid (330/500 nm) and riboflavin (450/520 nm) as the most likely candidates, as both have overlapping spectroscopic profiles. Interestingly, only riboflavin (vitamin B_2), which is a specific substrate for ABCG2 (ref. 28), was capable of restoring autofluorescence (**Fig. 6b** and **Supplementary Fig. 10d**). In addition, we found a strong association between the percentage of autofluorescence and riboflavin concentration in the medium, which plateaued at 30 μM (**Fig. 6c**). Notably, the enhanced number of autofluorescent cells was not related to nonspecific enrichment of non-CSCs, as riboflavin-enriched autofluorescent cells maintained high expression of pluripotency-associated genes and enhanced *in vivo* tumorigenicity (**Supplementary Fig. 11a**). By adding 30 μM riboflavin in the isolation medium, we further enhanced our ability to isolate otherwise dim autofluorescent cells from primary PDAC PDX-derived *in vitro* cultures (Panc025 and B023) and from freshly digested tumors, in which autofluorescence was difficult to detect with regular riboflavin concentrations (**Fig. 6d**). However, the addition of riboflavin to the isolation medium did not enable better identification of the autofluorescent CSC subpopulation in established cell lines such as Panc-1, which did not display autofluorescence under *in vitro* or *in vivo* conditions or following exposure to riboflavin (**Fig. 6d**, **Supplementary Fig. 11b** and data not shown). This result further corroborates the notion that higher riboflavin concentrations do not nonspecifically create autofluorescent cells and highlights the importance of working with early-passage primary cells for studying CSCs.

DISCUSSION

In this study, we identified a distinct autofluorescent population of self-renewing and highly tumorigenic CSCs with an inherent ability to concentrate the fluorescent vitamin riboflavin in ABCG2-coated intracellular vesicles. This feature allowed for the reliable identification and isolation of CSCs from the large pool of nontumorigenic cancer cells independent of the expression of CD133 or other surface markers and across numerous different tumor types (PDAC, HCC, NSCLC and CRC). These autofluorescent cells could be identified by flow cytometry, purified from primary cultures or freshly digested tumors by FACS without the need for fixation or antibody staining, and sensitivity could be further enhanced by the addition of riboflavin. Autofluorescent cells bore all defining CSC features: they overexpressed pluripotency-associated genes, harbored self-renewal capacity, were highly chemoresistant and metastatic and, most notably, demonstrated *in vivo* tumorigenicity. Autofluorescent cells also demonstrated exclusive long-term self-renewal capacity as shown by serial *in vivo* transplantation and tumorigenicity at the single-cell level.

After we excluded autophagy as a putative source of autofluorescence, we found ABCG2 to be overexpressed in autofluorescent cells. ABCG2 is strongly induced in the mammary gland during lactation[29,30] and responsible for pumping riboflavin (vitamin B_2) into milk[28]. ABCG2 also has broad substrate specificity for various drugs (for example, mitoxantrone), carcinogens and dietary toxins[28–31]. Using autofluorescent CSCs isolated from a variety of carcinomas, we found a marked concentration of riboflavin and mitoxantrone in intracellular vesicles, which was specifically mediated by ABCG2 transporters. The intracellular autofluorescent vesicles identified were coated in ABCG2 and could be depleted using the ABCG2 inhibitor FTC, confirming that the autofluorescent phenotype was indeed ABCG2 dependent. Apart from acting as a sink for ABCG2-dependent substrates, such as mitoxantrone and riboflavin, we did not, however, identify a CSC-specific advantage associated with the presence of autofluorescent phenotype. For example, elimination of the autofluorescent phenotype by functionally inhibiting ABCG2 with FTC did not affect CSC phenotypes such as the expression of pluripotency-associated genes or *in vivo* tumorigenicity. Likewise, overexpression of *ABCG2* in non-CSCs did not result in *de novo* formation of autofluorescent vesicles, nor did we observe an increase in CSC features in these cells. Thus, although we cannot definitively state

that autofluorescent vesicles are not biologically important for CSCs, our data do not support a functional role for the accumulation of riboflavin in these vesicles in the biology of CSCs.

Although more in-depth studies are still needed to determine the exact role of autofluorescent vesicles in CSC biology, our studies unequivocally demonstrate that, regardless of their function, autofluorescent vesicles can be used to track, isolate and purify CSCs from several epithelial cancers without the use of antibodies or extensive manipulation. Further exploiting autofluorescence may allow us to more accurately capture the dynamic complexity of CSCs as well as develop new CSC-specific therapies.

METHODS

Methods and any associated references are available in the online version of the paper.

Note: Any Supplementary Information and Source Data files are available in the online version of the paper.

ACKNOWLEDGMENTS

We thank A. González-Neira and L. Moreno from the CNIO Human Genotyping-CEGEN Unit for performing the TaqMan OpenArray SNAP analysis, and S.M. Trabulo and M. Tatari for their excellent *in vivo* technical assistance. The research was supported by the ERC Advanced Investigator Grant (Pa-CSC 233460), the European Community's Seventh Framework Programme (FP7/2007-2013) under grant agreement no. 256974 (EPC-TM-NET) and no. 602783 (CAM-PaC), the Associazione Italiana Ricerca Cancro (AIRC grant no. 12182 to A.S.), the Italian Cancer Genome Project Ministry of University and Research (FIRB RBAP10AHJB to A.S.), the FIMP-Italian Ministry of Health (CUP_J33G13000210001), the Subdirección General de Evaluación y Fomento de la Investigación, Fondo de Investigación Sanitaria (PS09/02129 & PI12/02643) and the Programa Nacional de Internacionalización de la I+D, Subprogramma: FCCI 2009 (PLE2009-0105; both Ministerio de Economía y Competitividad (es), Spain). M.C. was supported by the La Caixa Predoctoral Fellowship Program.

AUTHOR CONTRIBUTIONS

I.M.-L. acquired, analyzed and interpreted data as well as developed the study concept and drafted the manuscript; J.D. and A.B. performed the *in vivo* experiments; E.L., S.A., M.C., A.G.S. and S.Z. acquired and analyzed *in vitro* data; J.C.-T. designed the microchip-based single-cell assay; D.M. characterized the autofluorescence signal by confocal microscopy and developed the protocol for automated analysis of autofluorescence; M.H., M.E., J.K. and A.S. provided extensively characterized PDAC samples; B.S. and C.H. developed the study concept, obtained funding, interpreted the data and wrote the manuscript.

COMPETING FINANCIAL INTERESTS

The authors declare no competing financial interests.

1. Clarke, M.F. *et al.* Cancer stem cells—perspectives on current status and future directions: AACR Workshop on cancer stem cells. *Cancer Res.* **66**, 9339–9344 (2006).
2. Campbell, L.L. & Polyak, K. Breast tumor heterogeneity: cancer stem cells or clonal evolution? *Cell Cycle* **6**, 2332–2338 (2007).
3. Balic, A., Dorado, J., Alonso-Gómez, M. & Heeschen, C. Stem cells as the root of pancreatic ductal adenocarcinoma. *Exp. Cell Res.* **318**, 691–704 (2012).
4. Hermann, P.C., Bhaskar, S., Cioffi, M. & Heeschen, C. Cancer stem cells in solid tumors. *Semin. Cancer Biol.* **20**, 77–84 (2010).
5. Al-Hajj, M., Wicha, M.S., Benito-Hernandez, A., Morrison, S. & Clarke, M.F. Prospective identification of tumorigenic breast cancer cells. *Proc. Natl. Acad. Sci. USA* **100**, 3983–3988 (2003).
6. Gallmeier, E. *et al.* Inhibition of ataxia telangiectasia- and Rad3-related function abrogates the *in vitro* and *in vivo* tumorigenicity of human colon cancer cells through depletion of the $CD133^+$ tumor-initiating cell fraction. *Stem Cells* **29**, 418–429 (2011).
7. Wicha, M.S., Liu, S. & Dontu, G. Cancer stem cells: an old idea—a paradigm shift. *Cancer Res.* **66**, 1883–1890 (2006).
8. Beier, D. *et al.* $CD133^+$ and $CD133^-$ glioblastoma-derived cancer stem cells show differential growth characteristics and molecular profiles. *Cancer Res.* **67**, 4010–4015 (2007).
9. Joo, K.M. *et al.* Clinical and biological implications of CD133-positive and CD133-negative cells in glioblastomas. *Lab. Invest.* **88**, 808–815 (2008).
10. Ogden, A.T. *et al.* Identification of $A2B5^+CD133^-$ tumor-initiating cells in adult human gliomas. *Neurosurgery* **62**, 505–514 (2008).
11. Wang, J. *et al.* CD133 negative glioma cells form tumors in nude rats and give rise to CD133 positive cells. *Int. J. Cancer* **122**, 761–768 (2008).
12. Hermann, P.C. *et al.* Distinct populations of cancer stem cells determine tumor growth and metastatic activity in human pancreatic cancer. *Cell Stem Cell* **1**, 313–323 (2007).
13. Zhang, S.N., Huang, F.T., Huang, Y.J., Zhong, W. & Yu, Z. Characterization of a cancer stem cell-like side population derived from human pancreatic adenocarcinoma cells. *Tumori* **96**, 985–992 (2010).
14. Zhou, J. *et al.* Persistence of side population cells with high drug efflux capacity in pancreatic cancer. *World J. Gastroenterol.* **14**, 925–930 (2008).
15. Kabashima, A. *et al.* Side population of pancreatic cancer cells predominates in TGF-β-mediated epithelial to mesenchymal transition and invasion. *Int. J. Cancer* **124**, 2771–2779 (2009).
16. Broadley, K.W. *et al.* Side population is not necessary or sufficient for a cancer stem cell phenotype in glioblastoma multiforme. *Stem Cells* **29**, 452–461 (2011).
17. Burkert, J., Otto, W.R. & Wright, N.A. Side populations of gastrointestinal cancers are not enriched in stem cells. *J. Pathol.* **214**, 564–573 (2008).
18. Clément, V. *et al.* Retraction: Marker-independent identification of glioma-initiating cells. *Nat. Methods* **10**, 1035 (2013).
19. Lonardo, E. *et al.* Nodal/Activin signaling drives self-renewal and tumorigenicity of pancreatic cancer stem cells and provides a target for combined drug therapy. *Cell Stem Cell* **9**, 433–446 (2011).
20. Iliopoulos, D., Hirsch, H.A., Wang, G. & Struhl, K. Inducible formation of breast cancer stem cells and their dynamic equilibrium with non-stem cancer cells via IL6 secretion. *Proc. Natl. Acad. Sci. USA* **108**, 1397–1402 (2011).
21. Hermann, P.C. & Heeschen, C. Metastatic cancer stem cells—*quo vadis*? *Clin. Chem.* **59**, 1268–1269 (2013).
22. Hermann, P.C. *et al.* Multimodal treatment eliminates cancer stem cells and leads to long-term survival in primary human pancreatic cancer tissue xenografts. *PLoS ONE* **8**, e66371 (2013).
23. Cicalese, A. *et al.* The tumor suppressor p53 regulates polarity of self-renewing divisions in mammary stem cells. *Cell* **138**, 1083–1095 (2009).
24. Santini, D. *et al.* Prognostic role of human equilibrative transporter 1 (hENT1) in patients with resected gastric cancer. *J. Cell. Physiol.* **223**, 384–388 (2010).
25. Rabindran, S.K., Ross, D.D., Doyle, L.A., Yang, W. & Greenberger, L.M. Fumitremorgin C reverses multidrug resistance in cells transfected with the breast cancer resistance protein. *Cancer Res.* **60**, 47–50 (2000).
26. Bell, D.H. Characterization of the fluorescence of the antitumor agent, mitoxantrone. *Biochim. Biophys. Acta* **949**, 132–137 (1988).
27. White, E. Deconvoluting the context-dependent role for autophagy in cancer. *Nat. Rev. Cancer* **12**, 401–410 (2012).
28. van Herwaarden, A.E. *et al.* Multidrug transporter ABCG2/breast cancer resistance protein secretes riboflavin (vitamin B2) into milk. *Mol. Cell. Biol.* **27**, 1247–1253 (2007).
29. Jonker, J.W. *et al.* The breast cancer resistance protein protects against a major chlorophyll-derived dietary phototoxin and protoporphyria. *Proc. Natl. Acad. Sci. USA* **99**, 15649–15654 (2002).
30. van Herwaarden, A.E. & Schinkel, A.H. The function of breast cancer resistance protein in epithelial barriers, stem cells and milk secretion of drugs and xenotoxins. *Trends Pharmacol. Sci.* **27**, 10–16 (2006).
31. Ifergan, I., Goler-Baron, V. & Assaraf, Y.G. Riboflavin concentration within ABCG2-rich extracellular vesicles is a novel marker for multidrug resistance in malignant cells. *Biochem. Biophys. Res. Commun.* **380**, 5–10 (2009).

ONLINE METHODS

Primary human cancer cells. Human PDAC tumors as well as CRC, HCC and NSCLC tumors were obtained with written informed consent (PA 34_2012; Ethics Committee of the Instituto de Salud Carlos III; Madrid, Spain and Comunidad de Madrid, Spain (C.P. CNIO-CTC-11 - C.I. 11/103-E)), minced, mechanically digested (gentleMACS Dissociator; Miltenyi), enzymatically digested with collagenase (Stem Cell Technologies) and subsequently cultured *in vitro* as previously detailed[32]. PDAC patient-derived xenografts (PDAC PDXs) (185, A6L, 286, 266, 215, JH029, PANC025, B06, B023, 354, 247, CRC025, CRC024, HCC-5, HCC-6) were processed as previously described[32]. Within the paper, primary PDAC PDX-derived *in vitro* cultures are referred to by their patient number designation (for example: 185, A6L, etc.), freshly digested noncultured PDXs are referred to as 'PDAC PDX' and freshly digested noncultured primary patient tumors are referred to as 'PDAC-Tumor'. Primary cultures were tested for mycoplasma at least every 4 weeks (Gen-Probe-Mycoplasma Tissue Culture- NI Rapid Detection System MTC-NI).

Flow cytometry and cell sorting. Human PDAC tumors, as well as CRC, HCC and NSCLC cells or dissociated cells from primary sphere cultures were adjusted to a concentration of 10^6 cells/ml in Sorting buffer [1X PBS; 3% FBS (v/v); 3 mM EDTA (v/v)] before analysis or sorting with a FACS Canto II or FACS Influx instrument, respectively (BD). Autofluorescent cells were excited with a 488 nm blue laser and selected as the intersection with filters 530/40 and 580/30 as shown in **Figure 1c**. Some non-autofluorescent cells are lost during sorting due to the gate settings that maintain an appropriate distance between autofluorescent and non-autofluorescent cells. However, such settings are required to ensure high purity during sorting. To characterize autofluorescent cells, the following antibodies were used: anti-CD133/1-APC (Miltenyi Biotec); EpCAM-APC, CD44-APC, SSEA-1-APC, CXCR4-APC or appropriate isotype-matched control antibodies (all from BD) and anti-ALK4 (Cell Signaling Technology, Inc.). DAPI was used for exclusion of dead cells. Annexin V–APC (BD) staining was performed according to the manufacturer's instructions. Data were analyzed with FlowJo 9.2 software (Tree Star).

Protocol for acquiring and sorting autofluorescent cells. We used the following protocol to acquire and sort autofluorescent cells from tumors or cultured cells.

1. Mince the tumor into small pieces.
2. Mechanically digest with a gentleMACS Dissociator (Miltenyi).
3. Incubate with collagenase (Stem Cell Technologies) for 60 min at 37 °C and centrifuge for 5 min at 300*g*.
4. Resuspend cell pellets in 10 ml of RPMI (Invitrogen) supplemented with 10% FBS and 50 units/ml penicillin/streptomycin (referred to hereafter as 'complete medium').
5. Filter the suspension through a 70-µm strainer and centrifuge for 5 min at 300*g*.
6. Resuspend the cell pellet in 10 ml of RPMI complete media and add 30 µM Riboflavin (Sigma) to the suspension. (Note: hereafter is the starting point for cultured primary cells, including an optional addition of 30 µM of riboflavin to the medium.)
7. Incubate at least 2 h or overnight at 37 °C.
8. Centrifuge at 300*g* for 5 min and resuspend cell pellets in 1× PBS for acquisition or in sorting buffer (1× PBS containing 3% (v/v) FBS and 2 mM EDTA) for FACS.
9. Analyze or sort autofluorescent cells using standard flow cytometer equipment (here we used FACS Canto II flow cytometer and BD Influx cell sorter; both BD). Autofluorescent cells are excited with a 488-nm blue laser and best selected as the intersection with filters 530/40 and 580/30 (or similar filters), and a proper distance between gates for autofluorescent and non-autofluorescent cells is required to achieve high purity during sorting. Example cytometry plots including the gating strategy are shown in **Supplementary Figure 6a**.
10. If additional immunophenotyping is required, autofluorescence can be easily covisualized with fluorochromes excitable with a 640-nm red laser without the need for compensations. When combined with antibodies, conjugated PE or alike, autofluorescence can be covisualized with a 488-blue laser (compensations may be required) or using a 561-nm yellow-green laser without the need for compensation as autofluorescence is not excited with this laser.

Side population. Human primary PDAC cells at a concentration of 10^6 cells/ml were stained with Hoechst 33342 (5 µg/ml) at 37 °C for 2 h in the absence or presence of the ABCG2 transporter inhibitor fumitremorgin C (5 µg/ml; Sigma). Cells were washed and resuspended in cold 1× PBS. Propidium iodide (Sigma) was used to exclude dead cells. SP and non-SP cells were sorted using a FACS Influx sorter (BD).

Immunofluorescence. Primary pancreatic cancer cells and sphere-derived cells were seeded in 96-well culture dishes (Corning) and incubated at 37 °C for 24 h. For tracking the cytosol, mitochondria, lysosomes and lipid droplets, CytoTracker, MitoTracker, LysoTracker, and Nile red, respectively, were used at dilutions of 1:20,000 for 30 min at 37 °C (all from Invitrogen). Following two washes with 1× PBS, and 5 min incubation with Hoechst stain (5 µg/ml; Sigma), cells were analyzed using an SP5 confocal microscope (Leica).

Sphere formation assay. Spheres were generated by culturing ~2 × 10^4 human primary PDAC cells in suspension in serum-free DMEM/F12 supplemented with B27 (1:50, Invitrogen), 20 ng/ml bFGF and 50 units/ml pen/strep for a total of 7 d, allowing spheres to reach a size of >75 µm. For serial passaging, 7-d-old spheres were harvested using 40-µm cell strainers, dissociated into single cells and then recultured for 7 additional days as previously described[19].

RNA preparation and qRT-PCR. Total RNAs from human primary pancreatic cancer cells or livers of NSG mice were extracted with Trizol (Life Technologies) according to the manufacturer's instructions. 1 µg of total RNA was reverse transcribed with SuperScript II reverse transcriptase (Life Technologies) using random hexamers. Quantitative real-time PCR was performed with an Applied Biosystems 7500 real-time thermocycler (Applied Biosystems) using Fast SYBR Green (Qiagen) as per the

doi:10.1038/nmeth.3112

manufacturer's instructions. The list of primers used can be found in **Supplementary Table 2**.

Microchip-based single-cell analysis. The microchip pattern was designed with AutoCAD (Autodesk) and was manufactured using standard soft-lithography techniques[33]. This post-array is made of poly(dimethylsiloxane) and contains ~4,600 microwells of 80-μm diameter. The chip was bonded to a 24-well glass-bottom plate using a plasma oven before cell seeding (**Fig. 2d**). For semiautomated analysis of single cells seeded in microwells, we used a custom-developed software (CNIO MSRC). During a first low-resolution fast scan, settings for generating one image per well were established. After image acquisition, the software automatically localizes nanovolume wells containing single cells and records the presence or absence of autofluorescence and the respective well coordinates. Using this spatial information, the application interacts with the SP5 microscope (Leica) and loads high-resolution settings, scanning automatically just the areas of interest at customizable time intervals.

***In vivo* tumorigenicity and metastasis assays.** Human primary PDAC, CRC, HCC and NSCLC cells were sorted for autofluorescence as detailed below. For tumorigenicity assays, serial dilutions of single cells resuspended in Matrigel (BD Biosciences) were subcutaneously injected into 4- to 5-week-old female nude mice (Hsd:Athymic Nude-Foxn1^{nu}/Foxn1+; Harlan Laboratories) and tracked for 3 months for tumor formation because in previous experiments lasting 6 months, we did not observe any tumor formation, specifically with non-autofluorescent cells, after 3 months. For metastasis assays, 10^3 FACS-sorted autofluorescent and non-autofluorescent cells, with mCherry labeling directed by histone H2B type 2-E (HIST2H2BE), were resuspended in 1× PBS and intrasplenically injected into 4- to 5-week-old female NSG mice (NOD.Cg-Prkdcscid Il2rgtm1Wjl/SzJ; Charles River) as previously described[34]. All animal experiments were conducted in accordance with FELASA guidelines and approved protocols. Animal treatments were approved (Protocol PA 34_2012) by the Animal Experimental Ethics Committee of the Instituto de Salud Carlos III (Madrid, Spain).

PKH26 assay. Human primary PDAC cells were labeled with PKH26 red fluorescent cell membrane labeling dye (Sigma) according to the manufacturer's instructions. Every 7 d, cells were harvested and PKH26$^+$ cells were determined using a FACS Canto II (BD) for a total of 3 weeks.

Invasion and migration assays. Invasion assays were performed using modified Boyden chambers filled with Matrigel (BioCoat, BD Biosciences). Human primary pancreatic cancer cells were added to the Matrigel coated inserts, and 750 μl of serum-free medium supplemented with recombinant human Nodal (300 ng/ml), SDF-1 (100 ng/ml), Shh (100 ng/ml), or TGF-β (10 ng/ml) was added to the lower chamber. Cells were incubated for 22 h at 37 °C, and invaded cells were fixed in 4% PFA and stained with 4′,6-diamidino-2-phenylindole (DAPI). The ratio of cells in the lower chamber versus total seeded cells (as a percentage) was calculated. The data are presented as the mean of ten high-power fields (HPF).

Histology and immunohistochemistry. For histopathological analysis, FFPE blocks were serially sectioned (3 μm thick) and stained with hematoxylin and eosin (H&E). Additional serial sections were probed with antibodies against DsRed (Clontech), human cytokeratin 19α (Abcam), or *in situ* hybridization was performed using the Alu probe (Qbiogene). Following incubation with primary antibodies, samples were incubated with HRP-conjugated secondary antibodies (Dako), and positive cells were visualized using 3,3-diaminobenzidine tetrahydrochloride plus (DAB$^+$) as a chromogen.

Western blot analysis. Cells were harvested in RIPA buffer (Sigma) supplemented with a protease inhibitor cocktail (Roche Applied Science). 50 μg of protein were resolved by SDS-PAGE and transferred to PVDF membranes (Amersham Pharmacia). Membranes were sequentially blocked with 1× TBS containing 5% BSA (w/v), 1% chicken albumin (w/v) and 0.1% Tween 20 (v/v), incubated with a 1:1,000 dilution of antibodies against ABCG2 (ab24115; Abcam), NANOG (D73G4; Cell Signaling), OCT3/4 (H-134. Sc-9081; Santa Cruz Biotechnology), Tubulin (Sigma) or GAPDH (ab8245; Abcam) overnight at 4 °C, washed three times with 1× PBS containing 0.05% Tween 20 (v/v), incubated with horseradish peroxidase–conjugated goat anti-rat or goat anti-mouse antibody (Sigma), and washed again to remove unbound antibody. Bound antibody complexes were detected with SuperSignal chemiluminescent substrate (Amersham).

Lenti-mCherry-C1-huABCG2. The human ABCG2-mCherry lentiviral expression plasmid (pLVX-mCherry-C1-huABCG2) was cloned by PCR amplifying the human ABCG2 coding sequence (cds) from pOTB7-ABCG2 (CNIO, Genomics Unit collection) with primers 5′-GCC TCG AGC GTC TTC CAG TAA TGT CGA AG-3′ (sense) and 5′- GC GGA TCC AGA ATA TTT TTT AAG AAA TAA C-3′ (anti-sense). This PCR product was subcloned into pGEM-T Easy (Promega Biotech Ibérica S.L.) for sequence verification and then cloned as a XhoI/BamHI fragment into XhoI/BamHI-digested pLVX-mCherry-C1 (Clontech). The resulting construct contained the human ABCG2 cds ligated in frame to the C-terminal end of the mCherry reporter, so that an ABCG2-mCherry fusion protein was made.

Lentiviruses were produced as previously described[35]. Briefly, viruses were generated by cotransfection of the pLVX-mCherry-C1-huABCG2 lentivirus expression plasmid, packaging plasmid (Pax2) and envelope plasmid (pCDNA3.1-VSVG) into 293T producer cells. Supernatants were collected 48 h post transfection, filtered through a 0.45-μm-pore-size filter (BD Biosciences), concentrated by centrifugation for 1 h at 10,062*g*, divided into aliquots, frozen and subsequently titered by flow cytometry analysis of mCherry expression in 293T cells infected with increasing dilutions of virus. For infection of primary PDAC cells, autofluorescent-positive and autofluorescent-negative FACS-sorted cells were infected in suspension with Lenti-mCherry-C1-huABCG2 at a multiplicity of infection of ten infectious units per cell.

OpenArray genotyping assay. TaqMan OpenArray technology was used for medium-scale 64 SNPs genotyping array format. One array was performed and analyzed uniformly according to the manufacturer's standard protocol. HapMap and sample duplicates

were included in the array to serve as internal controls and to ensure reproducibility of the results. Genotype calling and sample clustering for OpenArray assays was performed in TaqMan Genotyper Software v1.3 (Applied Biosciences).

Statistical analyses. Results for continuous variables are presented as mean ± s.d. unless stated otherwise, and significance was determined using the Mann-Whitney test. Analyses were performed using SPSS 22.0. Normal distribution was tested before each statistical analysis was performed. Variance was equally distributed between groups. For statistical analysis of *in vivo* tumorigenicity, we used limiting dilution analysis (LDA; http://bioinf.wehi.edu.au/software/elda/). LDA is based on the Poisson single-hit model, which assumes that the number of biological active cells in each group varies according to a Poisson distribution, and a single biologically active cell is sufficient for inducing tumor formation[36,37]. Studies were designed to allow for the detection of differences of 50% as the minimum requirement. Considering the power for detecting such a difference to be 80%, s.d. 15% and two groups ($Fluo^+$ and $Fluo^-$) the appropriate sample size is $n = 3$. For the majority of experiments, the experimental group size contained 4 or more samples.

32. Mueller, M.T. *et al.* Combined targeted treatment to eliminate tumorigenic cancer stem cells in human pancreatic cancer. *Gastroenterology* **137**, 1102–1113 (2009).
33. Qin, D., Xia, Y. & Whitesides, G.M. Soft lithography for micro- and nanoscale patterning. *Nat. Protoc.* **5**, 491–502 (2010).
34. Sainz, B. Jr. *et al.* Identification of the Niemann-Pick C1-like 1 cholesterol absorption receptor as a new hepatitis C virus entry factor. *Nat. Med.* **18**, 281–285 (2012).
35. Sainz, B. Jr., Barretto, N. & Uprichard, S.L. Hepatitis C virus infection in phenotypically distinct Huh7 cell lines. *PLoS ONE* **4**, e6561 (2009).
36. Greenwood, M. & Yule, G.U. On the statistical interpretation of some bacteriological methods employed in water analysis. *J. Hyg. (Lond.)* **16**, 36–54 (1917).
37. Taswell, C. Limiting dilution assays for the determination of immunocompetent cell frequencies. I. Data analysis. *J. Immunol.* **126**, 1614–1619 (1981).

doi:10.1038/nmeth.3112

V.DISCUSIÓN

5.1 NUEVOS ABORDAJES PARA LA INVESTIGACIÓN DE INTERACCIONES MOLECULARES *IN SITU*

Este Proyecto de Tesis está centrado en el desarrollo de nuevas metodologías que permitan dotar a la comunidad científica de nuevas herramientas útiles para la realización de estudios de interacción entre moléculas así como para la automatización de adquisición de imagen compleja en microscopía.

En principio y con el ánimo de observar las interacciones moleculares por métodos directos de microscopía óptica hemos explorado los métodos disponibles haciendo hincapié en aquellos que nos permiten ver dichas interacciones en tiempo real.

En esta tesis describimos como los abordajes indirectos e *in situ* para el estudio de las interacciones moleculares pueden ser complementarios y permiten una mejor caracterización de dicha interacción. Este concepto queda perfectamente ilustrado en el primer artículo aportado en la sección de Resultados, en el que se describe como un ensayo *in vitro* de doble hibrido para localizar una posible interacción entre SNX6 y BRMS1 es perfectamente complementado y validado por un ensayo de FRET realizado por foto-blanqueado del aceptor. La combinación de ambos métodos confiere al estudio una mayor profundidad proporcionando indicios de la función de dicha interacción en base a su localización subcelular.

El foto-blanqueado del aceptor de hecho es uno de los métodos más comúnmente usados de cuantificación del FRET por imagen. El *foto-blanqueado* del aceptor es un método simple, reproducible e independiente de la concentración pero con un gran número de limitaciones, principalmente que es destructivo y por lo tanto inadecuado para realizar experimentos *in vivo*, y porque ofrece solamente información sobre el área blanqueada.

El otro método más comúnmente utilizado, el de la emisión sensibilizada si que posibilita la visualización y medida del FRET en células vivas. Sin embargo, los resultados obtenidos con este método en el trabajo en el que describimos el λFRET (Megias, Marrero et al. 2009) en el cual se comparan ambas

aproximaciones fueron inestables y poco reproducibles sobre todo en las construcciones reporteras de FRET con eficiencia de transferencia baja (R16) y con el control negativo consistente en las proteínas fluorescentes (CFP+YFP) expresadas de forma independiente con estequiometría desconocida. Además cuando se realiza empleando microscopía confocal, se incrementa el número de factores a tener en cuenta en comparación con la microscopía convencional de fluorescencia, tales como el uso de dos detectores independientes y de distintas líneas de láser para la excitación. Para la corrección de estos errores se han desarrollado algunos métodos (Xia and Liu 2001), (van Rheenen, Langeslag et al. 2004), que añaden cierta mejora pero no resuelven el problema.

El tipo de muestra en que esta medida de emisión sensibilizada resulta más fiable es cuando la estequiometria de ambas moléculas es fija. En este caso basta el cálculo del ratio entre la emisión sensibilizada del aceptor excitado por la longitud de onda del donador, y la emisión de dicho donador con la misma longitud de onda, para calcular un índice resultante. Dicho índice está directamente relacionado con la eficiencia de la transferencia de energía y se puede obtener en tiempo real. Este tipo de análisis está indicado para el análisis de biosensores que son construcciones proteicas fluorescentes que engloban al aceptor y al donador con una secuencia intermedia que reacciona frente a distintos estímulos aumentando o disminuyendo la eficiencia en la transferencia (Aoki, Komatsu et al. 2011).

Como ejemplo de este tipo de ensayos hemos añadido en la sección de Apéndice un trabajo centrado en el papel de AMPK y PFKFB3 como enzimas implicadas en el aumento de la glucolisis y la supervivencia de células sometidas a arresto mitótico (Domenech, Maestre et al. 2015) en el que he colaborado y donde se hace uso de este tipo de acercamiento aplicado a la medida de la absorción de glucosa.

Como solución a los problemas encontrados en los ensayos tradicionales de FRET, nos propusimos desarrollar un nuevo método de medida en el que, a diferencia de los más comúnmente utilizados, se tuviera en cuenta el espectro de emisión de las moléculas donadora y aceptora. Así hemos desarrollado un

procedimiento denominado λFRET basado en el análisis espectral de las muestras, que aprovecha la capacidad única de los espectros de fluorescencia para reflejar los complejos cambios asociados al FRET. El método demostró ser sensible y no destructivo al detectar las interacciones fisiológicas típicamente débiles en estudios de célula viva.

Tras describir los principios y el desarrollo del análisis de las imágenes asociado al uso del λFRET hemos comparado este abordaje con los métodos más comunes utilizando construcciones estándares de FRET estructuralmente caracterizadas con longitudes variables, diseñadas específicamente para este propósito. Estos experimentos demostraron el funcionamiento excepcional de λFRET comparado con otros métodos clásicos establecidos para la medida de FRET.

A diferencia de cualquier otro método previamente descrito de medida de FRET, λFRET introduce un novedoso procedimiento de corrección basado en el uso de las imágenes de la reflexión para normalizar las intensidades de distintas longitudes de onda. Además, el método del λFRET descompone los espectros del FRET en sus componentes puros de donador y de aceptor usando un procedimiento de interpolación distinto de la separación lineal. Dicho procedimiento de interpolación es más susceptible a la reducción de la anchura de la ventana de detección espectral comparado con la separación lineal, pero ofrece la ventaja de permitirnos eliminar los píxeles que no se ajusten a los espectros de referencia para el cálculo de FRET, lo cual hace que este método resulte independiente de la auto-fluorescencia. Además, este procedimiento nos permite separar espectros altamente solapantes, como se demuestra en dicho trabajo para el par de fluoróforos CFP-GFP. Aunque en este trabajo hemos utilizado un alto solapamiento en las ventanas de detección, la exactitud de los cálculos de la eficiencia de FRET no sufrió variaciones por la reducción de estos canales espectrales.

El método de λFRET no sufre de estos errores típicos en los ensayos de emisión sensibilizada puesto que utiliza solamente un detector y el cociente de las intensidades de la reflexión, corrigiendo las diferencias de la energía de la

luz incidente que viene del uso de diversas líneas de excitación de láser. Por otro lado, los sistemas confocales basados en PMTs (fotomultiplicadores) que tienen un rango de detección lineal limitado, son más sensibles a inconsistencias resultantes de la asunción de una relación lineal de la componente de cruce espectral con la intensidad de fluorescencia que es una de las fuentes de error del método de emisión sensibilizada. Si bien aún no hemos tenido la oportunidad de comprobarlo es muy probable que el uso de nuevos detectores híbridos (HyD) mejoren las medidas de intensidad debido a su mayor sensibilidad y rango dinámico. Otros autores han desarrollado interesantes procedimientos de corrección para evitar estos problemas de inestabilidad del método de *emisión sensibilizada* (van Rheenen, Langeslag et al. 2004), (Xia and Liu 2001). Sin embargo, estos errores en principio no afectan al método de λFRET, puesto que las correcciones de cruce espectral no se basan en intensidades absolutas, o en la determinación de la contribución del fluoróforo como en la separación espectral, sino que se basan en la interpolación espectral de la curva. Además, λFRET intrínsecamente considera exclusivamente los valores que vienen del rango lineal de la detección del PMT, y por lo tanto evita esta fuente de error. λFRET se ha demostrado útil para diversas combinaciones de pares donador-aceptor (Alexa 488-Cy3, CFP-YFP, Cerulean-Venus, CFP-GFP y GFP-mRFP), para analizar el FRET intra-molecular en concentraciones estequiometricas de donador-aceptor (de 1:1), y para el FRET inter-molecular de estequiometria variable. Tras su validación ha sido empleado con éxito al estudio de la interacción entre CD44-y moesina (Megias, Marrero et al. 2009) en el de CD44 y MT1MMP (Marrero-Diaz, Bravo-Cordero et al. 2009) en células fijadas y vivas durante la invasión de células tumorales indicando un posible papel de dichas interacciones durante la migración celular, y ha permitido demostrar sus excepcionales capacidades.

El método λFRET es en cierto modo similar a la *emisión sensibilizada* puesto que ambos analizan la medida de la emisión de la fluorescencia del aceptor debido a la transferencia de energía, aunque el λFRET tiene un gran número de ventajas.

(1) Al estar basado en el análisis de las integrales espectrales de la curva y no en intensidades absolutas de la fluorescencia, este método resulta ser más robusto que el *foto-blanqueado* en experimentos de célula viva. El λFRET también evita la variabilidad resultante de la relación no lineal entre el cruce de canal y las intensidades absolutas de la fluorescencia.

(2) El λFRET analiza cambios simultáneamente en la fluorescencia del donador y del aceptor y es por lo tanto más fiable. Las medidas son en principio menos susceptibles a los artefactos causados por agentes reductores de la fluorescencia no específicos tales como la fijación por formaldehído, que se ha demostrado que disminuye la fluorescencia de las proteínas fluorescentes Cerulean y Venus afectando enormemente la relación donador/aceptor (Chen, Puhl et al. 2006).

(3) La adquisición de imágenes de las muestras control con solo un marcaje para las correcciones espectrales del cruce de canal se pueden realizar una vez para cualquier par y microscopio dado y pueden ser usados para las siguientes medidas de FRET. Esto evita causas adicionales de variabilidad (que ocurren en la *emisión sensibilizada*) en el cálculo de la eficiencia debido a la baja similitud en concentraciones de donador y de aceptor entre el control y la muestra doblemente teñida.

(4) Aunque los ajustes del detector foto multiplicador (PMT) (ganancia y Offset) deben ser mantenidos constantes, la normalización de la intensidad de luz de la excitación inherente al método de λFRET permite ajustar libremente la intensidad de luz de la excitación, permitiendo obtener una buena relación señal-ruido evitando también los efectos de la saturación. Además, la normalización para la intensidad de luz de la excitación corrige para cualquier variabilidad producto de una inestabilidad del láser en estudios de células vivas.

(5) Su capacidad de distinguir señales con un alto solapamiento espectral, según lo demostrado por el análisis del tándem de CFP-GFP, permite mayor flexibilidad en la elección de las sondas de FRET. Nuestra comparación entre los métodos

usando estándares de FRET probó una especificidad, sensibilidad, y estabilidad superiores al comparar en paralelo el λFRET con el *foto-blanqueado* del aceptor y la *emisión sensibilizada*.

(6) El λFRET se puede utilizar para medir la relación entre donador y aceptor. Por otra parte, el λFRET demostró ser absolutamente estable frente a diversas concentraciones de donador/aceptor e independiente del solapamiento espectral y auto fluorescencia.

Previamente ya existían otros acercamientos a la medición de FRET igualmente basados en algoritmos de separación espectral (Elangovan, Wallrabe et al. 2003), (Gu, Di et al. 2004), (Jares-Erijman and Jovin 2006), (Karpova, Baumann et al. 2003), (Wallrabe and Periasamy 2005). En estos métodos, para evitar las limitaciones derivadas de la separación lineal de espectros, introducen en los cálculos de FRET el tiempo de vida media de la fluorescencia (Jares-Erijman and Jovin 2006), (Gu, Di et al. 2004) o lo combinan con medidas de *foto-blanqueado* del aceptor (Karpova, Baumann et al. 2003) (Jares-Erijman and Jovin 2006), (Gronenborn, Filpula et al. 1991). Entre dichos métodos de medida están el sRET (Wallrabe and Periasamy 2005), en el que se aplica una fórmula de separación espectral que incorpora la emisión del donador y el aceptor como resultado de la excitación directa, así como la emisión del aceptor, producto del FRET, que proporciona información sobre las concentraciones de donador y de aceptor, así como los valores de la eficiencia de FRET. Según este método, la contribución relativa de cada fluorocromo, así como una constante k dependiente de la longitud de onda de excitación, se determinan a partir de los datos espectrales procedentes de muestras en las que solo está presente el donador o el aceptor a las mismas concentraciones, que son excitados a diferentes longitudes de onda. Semejante al sRET, otro método espectral de FRET, el lux-FRET, también se basa en la separación espectral con dos medidas de la longitud de onda de excitación (Wlodarczyk, Woehler et al. 2008) y cuatro espectros de calibración del donador y de las muestras del aceptor adquiridos con dos longitudes de onda de excitación. Curiosamente, los cálculos del lux-FRET toman en consideración las contribuciones de los fluoróforos no unidos

tanto del donador como del aceptor y la influencia del marcaje incompleto de las moléculas que interactúan. El método espectral descrito por Chen y colaboradores denominado psFRET (Chen, Mauldin et al. 2007), utiliza un abordaje basado en la separación espectral para calcular la eficiencia de FRET basada en microscopía confocal. El psFRET elimina la excitación cruzada del aceptor por la longitud de onda del donador, usando un algoritmo que empareja los niveles de intensidad de la fluorescencia obtenidos a partir de las células control, que expresan solo el aceptor, con la muestra sujeto de evaluación, que expresa los fluorocromos del donador y del aceptor. A diferencia de los métodos descritos el de λFRET usa exclusivamente los datos provenientes de la adquisición espectral adquirida en un microscopio confocal de barrido por láser.

El último método con el que podemos comparar el λFRET es el FLIM, que se basa en la medición de la vida media de fluorescencia del fluoróforo donador de la pareja de FRET. Este método presenta como principal ventaja el que la vida media es absolutamente insensible a las variaciones en la concentración e intensidad de la excitación y no requiere ninguna corrección espectral. Sin embargo el FLIM presenta la desventaja de requerir un equipo costoso y el manejo muy especializado, dada su elevada sensibilidad a los cambios ambientales (Wallrabe and Periasamy 2005), En la sección de Apéndice se incluye un trabajo en el que se utiliza este método para el análisis de la asociación entre podoplanina y CD44 y su implicación en la migración celular, en el cual he colaborado (Martin-Villar, Fernandez-Munoz et al. 2010) .

La principal limitación de λFRET es que la adquisición de la imagen espectral consume más tiempo y por lo tanto no es conveniente para analizar procesos muy rápidos en células vivas. Sin embargo, los instrumentos confocales espectrales comercialmente disponibles pueden trabajar ya a una velocidad extremadamente alta, y las adquisiciones espectrales se pueden realizar simultáneamente con una batería de detectores que trabajan en paralelo, así que el tiempo no resulta una limitación práctica actualmente.

En la sección de apéndice de esta tesis se incluyen varios trabajos en los que he participado y donde se pueden apreciar las diferencias y campos de aplicación de algunos de los métodos de medida de FRET más frecuentes.

Los últimos avances en el desarrollo de nuevas proteínas y moléculas fluorescentes han aumentado la potencial utilidad del FRET, y muy probablemente el futuro de esta tecnología esté íntimamente relacionado con el desarrollo de nuevos fluoróforos que estén dotados de cada vez mayor foto-estabilidad, menor tamaño y más variantes en cuanto a sus capacidades de absorción y emisión (Selvin 2000), (Grunberg, Burnier et al. 2013).

Es muy probable que parte de la evolución en el estudio de las interacciones moleculares pase en el futuro por el uso de técnicas de super-resolución que realmente permitan observar de forma directa dichas interacciones. Si bien esta nueva forma de hacer microscopía está todavía en plena evolución, ya empiezan a aparecer estudios en los que se combinan con los métodos clásicos para observar la interacción entre moléculas (Liu, Xing et al. 2014) abriendo un campo excitante de posibilidades para el futuro.

5.2 AUTOMATIZACIÓN DE ENSAYOS POR MICROSCOPÍA ÓPTICA

A pesar de todos los avances realizados en el estudio de las interacciones moleculares por microscopía, un punto que aún queda por resolver en este tipo de capturas es su complejidad, tanto en cuanto a su proceso de adquisición, como en la selección de las células apropiadas para realizar los ensayos, lo cual hace necesario el uso de herramientas de automatización que aumenten el rendimiento y faciliten su adquisición.

Como ya hemos descrito, y como por otro lado es habitual en los estudios de biología experimental, es difícil conseguir datos fiables si no se repite la prueba en repetidas ocasiones de forma que se pueda cuantificar la reproducibilidad de un evento determinado. De esta forma, se hace cada día más necesario el uso

de la automatización en la adquisición de imágenes de microscopía. Hasta hace bien poco la única forma de realizar dicha automatización era mediante el muestreo al azar en distintas coordenadas de una preparación. Sin embargo recientemente, nuevos abordajes han permitido añadir un paso de selección automatizada de las regiones de interés en dicha muestra (*screening inteligente*).

El mayor problema de los abordajes de adquisición automatizada dirigida por análisis de imagen, si bien permiten ahorrar tiempo y recursos, es que no están disponibles en las aplicaciones de captura comerciales, que suelen ser muy rígidas en cuanto a su uso.

Actualmente, solo hay unas pocas herramientas de este tipo desarrolladas por laboratorios muy especializados, que normalmente requieren programadores e ingenieros capaces de realizar y usar dichas plataformas (Conrad, Wunsche et al. 2011), (de Chaumont, Dallongeville et al. 2012), (Henriksson, Hench et al. 2013). Las grandes limitaciones en cuanto a disponibilidad de las mismas ha sido la razón que nos animó a desarrollar una nueva plataforma que permitiera este tipo de ensayos en microscopios automatizados estándar. Buscando la plena compatibilidad con el equipamiento sin importar las características de las fuentes de iluminación, cámaras o filtros de fluorescencia con los que estén provistos y que además fuera extremadamente fácil tanto en uso como en instalación.

Dentro de este proyecto de tesis hemos desarrollado una nueva plataforma de *Screening inteligente* denominada iMSRC que reúne estos requisitos, y que además es compatible con plataformas de análisis de imagen de libre disposición, y que permite aplicaciones de localización de eventos raros. En el artículo en el que describimos este abordaje (Carro, Perez-Martinez et al. 2015) se utiliza como herramienta para la búsqueda de células tumorales circulantes. En este caso sobre una muestra de sangre de pacientes con cáncer se hace una primera adquisición rápida con baja resolución que se analiza para revelar cualquier objeto candidato a ser una célula tumoral para después ser validado

con una adquisición automática a alta resolución. De esta forma se pretende cuantificar la cantidad de este tipo de células como indicativo pronóstico del tratamiento al que se somete a dichos pacientes.

En este desarrollo tecnológico se ha primado la usabilidad de la plataforma permitiendo su uso con un navegador web estándar y haciendo una interfaz gráfica muy intuitiva que solo requiere del operador el conocimiento previo necesario para el uso convencional del microscopio.

Mediante su uso conseguimos la adquisición inteligente en todo tipo de muestras ya sea en células fijadas o vivas o en tejido e independientemente de su soporte dado que admite la adquisición de varios porta-objetos (hasta 5 en paralelo) o placas multipocillo, con plena compatibilidad con equipamiento del sistema y permitiendo el uso de rutinas de análisis de imagen de aplicaciones gratuitas tales como el “image J”.

Así se consigue combinar la potencia de captura de un equipo de microscopía de altas prestaciones con la identificación de objetos por análisis de imagen.

Una sola instalación de iMSRC es capaz de manejar por red varios microscopios a la vez, manteniendo una uniformidad en la estructura y además su gestión centralizada evita los problemas derivados de las posibles inconsistencias en las actualizaciones de los programas de análisis de imagen que controla.

Esta herramienta permite de forma accesible para los científicos con conocimientos básicos de microscopía realizar protocolos de adquisición complejos que no son posibles desde las aplicaciones informáticas comerciales disponibles y que aprovecha la simpleza de la navegación por web para su uso.

Ya existen diversos ejemplos del uso de esta solución informática. Uno de ellos en concreto es en la adquisición células madres tumorales vivas dispuestas sobre chips con más de 1400 nano-pocillos en los que el uso de iMSRC permitió localizar los nano-pocillos que contenían una sola célula de partida haciendo posible su seguimiento in vivo y la caracterización del tipo de división de dichas células. En dicho trabajo se realizó un gran esfuerzo en la caracterización de un

novedoso bio marcador de células madre tumorales con una gran parte basada en microscopía óptica en la que participé de forma muy activa. (Miranda-Lorenzo, Dorado et al. 2014). Otro area de aplicación del iMSRC es el de posibilitar el *screening* sobre muestras de tejido. En estas preparaciones la disposición de las muestras se realiza normalmente de forma manual y suelen tener formas y composición muy heterogénea lo cual empeora el rendimiento de un abordaje de *screening* convencional. Hemos demostrado la aplicabilidad del iMSRC en este tipo de muestras por ejemplo en la captura por confocal en alta resolución de muestras con TMAs (*Tissue Micro Arrays*) en los que se disponen cientos de muestras de secciones de tejidos, la gran calidad de la imagen y el ahorro en tiempo proporcionado por nuestra plataforma posibilita la cuantificación de los distintos marcadores a nivel sub-celular (Alonso-Curbelo, Riveiro-Falkenbach et al. 2014), en este trabajo además he aportado mis conocimientos tanto en el planteamiento como en la adquisición y análisis de los experimentos relacionados con microscopía. También hemos empleado el iMSRC en la cuantificación de neuronas en el giro dentado de cerebro (figura suplementaria en (Carro, Perez-Martinez et al. 2015).

Este novedoso abordaje viene a resolver una gran demanda de usabilidad en este tipo de tecnologías (Carpenter, Kamentsky et al. 2012) y tenemos como objetivo su difusión a otros laboratorios por lo que se ha realizado en código abierto y como muestra se ha lanzado en paralelo la web http://imsrc.bioinfo.cnio.es/. En la actualidad esta plataforma se ha distribuido ya a varios laboratorios de España y Europa.

VI. CONCLUSIONES

1. Se ha desarrollado un nuevo método de análisis de FRET (λFRET) para el análisis de interacciones moleculares que ofrece numerosas ventajas con respecto a los métodos convencionales.

2. Se han desarrollado construcciones genéticas caracterizadas con distintas eficiencias de FRET que han permitido la comparación entre métodos de forma cuantitativa.

3. El uso de dicho método a permitido demostrar la interacción entre CD44 y MT1-MMP, aportando indicios sobre su papel en la migración celular.

4. Se ha desarrollado una novedosa aproximación en la captura automatizada dirigida por análisis de imagen (iMSRC), y que proporciona con menos requerimientos y menor tiempo de captura información estadística fiable en muestras heterogéneas o eventos raros.

5. El uso de iMSRC ha permitido entre otras aplicaciones localizar en un *array* de nano-pocillos, aquellos en los que se disponía una única célula de partida con expresión de un biomarcador autofluorescente de células madre tumorales, a fin de seguirlas *in vivo* a lo largo del ciclo celular y observar su comportamiento.

VII. BIBLIOGRAFÍA

Abbe, E. (1873). "About a New Illumination Apparatus to the Microscope." Archive for Microscopic Anatomy **9**: 413-420.
Alonso-Curbelo, D., E. Riveiro-Falkenbach, et al. (2014). "RAB7 controls melanoma progression by exploiting a lineage-specific wiring of the endolysosomal pathway." Cancer Cell **26**(1): 61-76.
Aoki, K., N. Komatsu, et al. (2011). "Stable expression of FRET biosensors: a new light in cancer research." Cancer Sci **103**(4): 614-9.
Carpenter, A. E., L. Kamentsky, et al. (2012). "A call for bioimaging software usability." Nat Methods **9**(7): 666-70.
Carro, A., M. Perez-Martinez, et al. (2015). "iMSRC: converting a standard automated microscope into an intelligent screening platform." Sci Rep **5**: 10502.
Conrad, C., A. Wunsche, et al. (2011). "Micropilot: automation of fluorescence microscopy-based imaging for systems biology." Nat Methods **8**(3): 246-9.
Chen, H., H. L. Puhl, 3rd, et al. (2006). "Measurement of FRET efficiency and ratio of donor to acceptor concentration in living cells." Biophys J **91**(5): L39-41.
Chen, Y., J. P. Mauldin, et al. (2007). "Characterization of spectral FRET imaging microscopy for monitoring nuclear protein interactions." J Microsc **228**(Pt 2): 139-52.
de Chaumont, F., S. Dallongeville, et al. (2012). "Icy: an open bioimage informatics platform for extended reproducible research." Nat Methods **9**(7): 690-6.
Domenech, E., C. Maestre, et al. (2015). "AMPK and PFKFB3 mediate glycolysis and survival in response to mitophagy during mitotic arrest." Nat Cell Biol **17**(10): 1304-16.
Elangovan, M., H. Wallrabe, et al. (2003). "Characterization of one- and two-photon excitation fluorescence resonance energy transfer microscopy." Methods **29**(1): 58-73.
Förster, T. (1948). "Intermolecular energy migration and fluorescence." Annalen der Physik **437**.
Gramatikoff, K., O. Georgiev, et al. (1994). "Direct interaction rescue, a novel filamentous phage technique to study protein-protein interactions." Nucleic Acids Res **22**(25): 5761-2.
Gronenborn, A. M., D. R. Filpula, et al. (1991). "A novel, highly stable fold of the immunoglobulin binding domain of streptococcal protein G." Science **253**(5020): 657-61.
Grunberg, R., J. V. Burnier, et al. (2013). "Engineering of weak helper interactions for high-efficiency FRET probes." Nat Methods **10**(10): 1021-7.
Gu, Y., W. L. Di, et al. (2004). "Quantitative fluorescence resonance energy transfer (FRET) measurement with acceptor photobleaching and spectral unmixing." J Microsc **215**(Pt 2): 162-73.
Havugimana, P. C., G. T. Hart, et al. (2012). "A census of human soluble protein complexes." Cell **150**(5): 1068-81.
Henriksson, J., J. Hench, et al. (2013). "Endrov: an integrated platform for image analysis." Nat Methods **10**(6): 454-6.
Huang, B., M. Bates, et al. (2009). "Super-resolution fluorescence microscopy." Annu Rev Biochem **78**: 993-1016.
Huygens, C. (1690). "Traite de la lumiere." **1**.
James, P., J. Halladay, et al. (1996). "Genomic libraries and a host strain designed for highly efficient two-hybrid selection in yeast." Genetics **144**(4): 1425-36.
Jares-Erijman, E. A. and T. M. Jovin (2006). "Imaging molecular interactions in living cells by FRET microscopy." Curr Opin Chem Biol **10**(5): 409-16.
Kardash, E., J. Bandemer, et al. (2011). "Imaging protein activity in live embryos using fluorescence resonance energy transfer biosensors." Nat Protoc **6**(12): 1835-46.

Karpova, T. S., C. T. Baumann, et al. (2003). "Fluorescence resonance energy transfer from cyan to yellow fluorescent protein detected by acceptor photobleaching using confocal microscopy and a single laser." J Microsc **209**(Pt 1): 56-70.
Kerppola, T. K. (2006). "Complementary methods for studies of protein interactions in living cells." Nat Methods **3**(12): 969-71.
Kerppola, T. K. (2006). "Design and implementation of bimolecular fluorescence complementation (BiFC) assays for the visualization of protein interactions in living cells." Nat Protoc **1**(3): 1278-86.
Kirber, M. T., K. Chen, et al. (2007). "YFP photoconversion revisited: confirmation of the CFP-like species." Nat Methods **4**(10): 767-8.
Kirkwood, K. J., Y. Ahmad, et al. (2013). "Characterization of native protein complexes and protein isoform variation using size-fractionation-based quantitative proteomics." Mol Cell Proteomics **12**(12): 3851-73.
Larance, M. and A. I. Lamond (2015). "Multidimensional proteomics for cell biology." Nat Rev Mol Cell Biol **16**(5): 269-80.
Lee, H. W., J. Y. Ryu, et al. (2013). "Real-time single-molecule coimmunoprecipitation of weak protein-protein interactions." Nat Protoc **8**(10): 2045-60.
Lerner, J. M. and R. M. Zucker (2004). "Calibration and validation of confocal spectral imaging systems." Cytometry A **62**(1): 8-34.
Liu, Z., D. Xing, et al. (2014). "Super-resolution imaging and tracking of protein-protein interactions in sub-diffraction cellular space." Nat Commun **5**: 4443.
Magliery, T. J., C. G. Wilson, et al. (2005). "Detecting protein-protein interactions with a green fluorescent protein fragment reassembly trap: scope and mechanism." J Am Chem Soc **127**(1): 146-57.
Marrero-Diaz, R., J. J. Bravo-Cordero, et al. (2009). "Polarized MT1-MMP-CD44 interaction and CD44 cleavage during cell retraction reveal an essential role for MT1-MMP in CD44-mediated invasion." Cell Motil Cytoskeleton **66**(1): 48-61.
Martin-Villar, E., B. Fernandez-Munoz, et al. "Podoplanin associates with CD44 to promote directional cell migration." Mol Biol Cell **21**(24): 4387-99.
Martin-Villar, E., B. Fernandez-Munoz, et al. (2010). "Podoplanin associates with CD44 to promote directional cell migration." Mol Biol Cell **21**(24): 4387-99.
Martin-Villar, E., D. Megias, et al. (2006). "Podoplanin binds ERM proteins to activate RhoA and promote epithelial-mesenchymal transition." J Cell Sci **119**(Pt 21): 4541-53.
Megias, D., R. Marrero, et al. (2009). "Novel lambda FRET spectral confocal microscopy imaging method." Microsc Res Tech **72**(1): 1-11.
Miranda-Lorenzo, I., J. Dorado, et al. (2014). "Intracellular autofluorescence: a biomarker for epithelial cancer stem cells." Nat Methods **11**(11): 1161-9.
Neher, R. A. and E. Neher (2004). "Applying spectral fingerprinting to the analysis of FRET images." Microsc Res Tech **64**(2): 185-95.
Raicu, V., D. B. Jansma, et al. (2005). "Protein interaction quantified in vivo by spectrally resolved fluorescence resonance energy transfer." Biochem J **385**(Pt 1): 265-77.
Rhee, H. W., P. Zou, et al. (2013). "Proteomic mapping of mitochondria in living cells via spatially restricted enzymatic tagging." Science **339**(6125): 1328-31.
Roux, K. J., D. I. Kim, et al. (2012). "A promiscuous biotin ligase fusion protein identifies proximal and interacting proteins in mammalian cells." J Cell Biol **196**(6): 801-10.
Selvin, P. R. (2000). "The renaissance of fluorescence resonance energy transfer." Nat Struct Biol **7**(9): 730-4.
Soderberg, O., M. Gullberg, et al. (2006). "Direct observation of individual endogenous protein complexes in situ by proximity ligation." Nat Methods **3**(12): 995-1000.

Thaler, C., S. V. Koushik, et al. (2005). "Quantitative multiphoton spectral imaging and its use for measuring resonance energy transfer." Biophys J **89**(4): 2736-49.
van Rheenen, J., M. Langeslag, et al. (2004). "Correcting confocal acquisition to optimize imaging of fluorescence resonance energy transfer by sensitized emission." Biophys J **86**(4): 2517-29.
Wallrabe, H. and A. Periasamy (2005). "Imaging protein molecules using FRET and FLIM microscopy." Curr Opin Biotechnol **16**(1): 19-27.
Wlodarczyk, J., A. Woehler, et al. (2008). "Analysis of FRET signals in the presence of free donors and acceptors." Biophys J **94**(3): 986-1000.
Wouters, F. S., P. J. Verveer, et al. (2001). "Imaging biochemistry inside cells." Trends Cell Biol **11**(5): 203-11.
Xia, Z. and Y. Liu (2001). "Reliable and global measurement of fluorescence resonance energy transfer using fluorescence microscopes." Biophys J **81**(4): 2395-402.
Zhang, J., R. E. Campbell, et al. (2002). "Creating new fluorescent probes for cell biology." Nat Rev Mol Cell Biol **3**(12): 906-18.
Zimmermann, T., J. Rietdorf, et al. (2002). "Spectral imaging and linear un-mixing enables improved FRET efficiency with a novel GFP2-YFP FRET pair." FEBS Lett **531**(2): 245-9.
Zimmermann, T., J. Rietdorf, et al. (2003). "Spectral imaging and its applications in live cell microscopy." FEBS Lett **546**(1): 87-92.

VIII. APÉNDICE

Podoplanin binds ERM proteins to activate RhoA and promote epithelial-mesenchymal transition

Ester Mart n-Villar[1], Diego Meg as[2], Susanna Castel[3], Maria Marta Yurrita[1], Sen n Vilar [3,*] and Miguel Quintanilla[1,‡]

[1]Instituto de Investigaciones Biom dicas Alberto Sols, Consejo Superior de Investigaciones Cient ficas (CSIC)-Universidad Aut noma de Madrid (UAM), 28029 Madrid, Spain
[2]Centro Nacional de Investigaciones Oncol gicas, 28029 Madrid, Spain
[3]Departamento de Biolog a Celular, Universidad de Barcelona, 08028 Barcelona, Spain
*Author died on 4 December 2005 and this paper is published in his memory
‡Author for correspondence (e-mail: mquintanilla@iib.uam.es)

Accepted 9 August 2006
Journal of Cell Science 119, 4541-4553 Published by The Company of Biologists 2006
doi:10.1242/jcs.03218

Summary

Podoplanin is a small membrane mucin expressed in tumors associated with malignant progression. It is enriched at cell-surface protrusions where it colocalizes with members of the ERM (ezrin, radixin, moesin) protein family. Here, we found that human podoplanin directly interacts with ezrin (and moesin) in vitro and in vivo through a cluster of basic amino acids within its cytoplasmic tail, mainly through a juxtamembrane dipeptide RK. Podoplanin induced an epithelial-mesenchymal transition in MDCK cells linked to the activation of RhoA and increased cell migration and invasiveness. Fluorescence time-lapse video observations in migrating cells indicate that podoplanin might be involved in ruffling activity as well as in retractive processes. By using mutant podoplanin constructs fused to green fluorescent protein we show that association of the cytoplasmic tail with ERM proteins is required for upregulation of RhoA activity and epithelial-mesenchymal transition. Furthermore, expression of either a dominant-negative truncated variant of ezrin or a dominant-negative mutant form of RhoA blocked podoplanin-induced RhoA activation and epithelial-mesenchymal transition. These results provide a mechanistic basis to understand the role of podoplanin in cell migration or invasiveness.

Supplementary material available online at
http://jcs.biologists.org/cgi/content/full/119/21/4541/DC1

Key words: Podoplanin/PA2.26 antigen, Ezrin, RhoA, Epithelial-mesenchymal transition, Cell migration

Introduction

Epithelial to mesenchymal transition (EMT) represents a phenotypic conversion by which epithelial cells lose their polarity and cohesiveness and acquire migratory features characteristic of fibroblasts. EMTs are required for morphogenetic processes and tissue remodelling during development, but are also involved in pathological situations such as wound healing, inflammation and tumor invasion and metastasis (Bissell and Radisky, 2001; Thiery, 2002). A wide variety of biological agents from cytokines to transcription factors has been found to promote either cell scattering or EMT in cultured epithelial cells (Gotzmann et al., 2004). In a previous work, we reported that podoplanin, a small mucin-like transmembrane glycoprotein also known as PA2.26 antigen or T1α among other names, induced the conversion from an epithelial to a fibroblast-like morphology when ectopically expressed in keratinocytes (Scholl et al., 1999).

Podoplanin is expressed in a variety of normal cells and tissues, including mesothelia, certain types of epithelia, neuronal cells, osteocytes and endothelia of lymphatic capillaries (Rishi et al., 1995; Wetterwald et al., 1996; Williams et al., 1996; Scholl et al., 1999; Kotani et al., 2003; Schacht et al., 2005; Breiteneder-Geleff et al., 1997; Breiteneder-Geleff et al., 1999). Mice deficient for podoplanin die immediately after birth owing to respiratory failure caused by malformation of alveoli (Ramirez et al., 2003). The *podoplanin* null mice also show defects in the lymphatic pattern formation associated with congenital lymphedema, dilation of vessels and diminished lymphatic transport (Schacht et al., 2003). These data point to an important role for podoplanin in the development of the lung and lymphatic vascular system, but its precise biological function remains poorly understood.

Podoplanin expression is upregulated in different types of experimental and human tumors, including squamous cell carcinomas of the skin, lung, esophagus, cervix, larynx and oral cavity (Gandarillas et al., 1997; Mart n-Villar et al., 2005; Schacht et al., 2005; Kato et al., 2005; Wicki et al., 2006), colorectal adenocarcinomas (Kato et al., 2003), testicular germ cell tumors (Kato et al., 2004; Schacht et al., 2005) and mesotheliomas (Chu et al., 2005). In squamous cell carcinomas, podoplanin expression is frequently restricted to the invasive front (Mart n-Villar et al., 2005; Wicki et al., 2006), and in some tumors correlates with downregulation of the cell-cell adhesion protein E-cadherin (Mart n-Villar et al., 2005). Confocal and immunoelectron microscopy studies aimed at studying its subcellular localization revealed that podoplanin is concentrated at actin-rich microvilli and plasma membrane projections, where it colocalizes with members of the ERM (ezrin, radixin, moesin) protein family (Scholl et al., 1999; Mart n-Villar et al., 2005). ERM proteins link integral

membrane proteins to the cortical actin cytoskeleton and participate in signal transduction pathways that regulate cell motility and adhesion (Bretscher et al., 2002). The presence of podoplanin at cell-surface projections and the finding that ezrin and moesin, but not radixin, can be coimmunoprecipitated with podoplanin from cell lysates suggested that this glycoprotein is involved in motility processes (Scholl et al., 1999). Further studies showed a pro-migratory function for podoplanin, because its expression in immortalized or premalignant keratinocytes either stimulated cell scattering (Mart n-Villar et al., 2005) or promoted an EMT associated with increased invasive and metastatic features (Scholl et al., 1999; Scholl et al., 2000). In both cases, podoplanin stimulated the formation of plasma membrane extensions concomitantly with a major reorganization of the actin cytoskeleton and redistribution of ezrin to cell-surface protrusions (Scholl et al., 1999; Mart n-Villar et al., 2005). Taken together, these data suggested an involvement of podoplanin in cell migration and invasiveness during tumor progression. We reasoned that an important cue for this function should be its ability to reorganize the actin cytoskeleton through recruitment of ERM proteins.

In this article, we show that wild-type human podoplanin promotes a complete EMT in Madin-Darby canine kidney (MDCK) type-II epithelial cells, a well-characterized cellular model to analyze the molecular mechanisms of epithelial cell plasticity (Gotzmann et al., 2004). The key elements for podoplanin to promote this phenotypic conversion are its ability to interact with ERM proteins through a cluster of basic amino acids within its cytoplasmic tail and the regulation of RhoA GTPase activity.

Results

The binding of podoplanin to ERM proteins requires a juxtamembrane cluster of basic amino acids.

The 162 amino acid human podoplanin molecule contains an ectodomain (EC) with a high proportion of O-glycosylated S and T residues, a membrane-spanning domain (TM) and a short cytoplasmic tail (CT) of only nine amino acids (Fig. 1). The TM and CT domains are highly conserved across species (Zimmer et al., 1999; Mart n-Villar et al., 2005; Kaneko et al., 2006). Within the CT domain the only obvious functional motif is a cluster of basic amino acids (Fig. 1, bold) shared by transmembrane proteins of the microvillus that has been shown to be involved in direct binding to ERM proteins (Yonemura et al., 1998). However, although coimmunoprecipitation experiments suggested an association of podoplanin with ezrin and moesin (Scholl et al., 1999), no proof for a direct interaction of the podoplanin endodomain with these cytoskeletal linkers exists. To analyze whether podoplanin binds ERM proteins directly through this cluster of basic residues, we expressed the wild-type cytoplasmic tail of human podoplanin (PCT) as a fusion protein with glutathione-S-transferase (GST), and tested whether the substitution of positively charged residues (RK…R) by uncharged polar amino acids (see Fig. 1) affected the interaction of PCT with purified recombinant full-length ezrin and moesin or their N-terminal sequences (N-ERMAD domains). Although both controls (GST-Sepharose and uncoupled Sepharose) bound some ezrin and moesin, the interaction of these proteins with GST-PCT was clearly increased over the non-specific background (Fig. 2A). The same occurred with the CT of the cell-surface receptor CD44, used in this experiment as a positive control (Hirao et al., 1996; Legg and Isacke, 1998; Yonemura et al., 1998). Phosphatidylinositol 4,5-bisphosphate (PIP_2), a positive regulator of ERM binding to membrane proteins (Bretscher et al., 2002), enhanced the interaction of ezrin and moesin with the CTs of both podoplanin and CD44 (data not shown), as demonstrated previously for CD44 (Hirao et al., 1996). Mutation of one (PCT.N), two (PCTQN) or all three (PCTQN.N) basic amino acids highly decreased the binding of PCT to ezrin and moesin, although PCT.N (in which only the most C-terminal R159 was mutated) appeared to conserve some specific binding activity, particularly to moesin. These data indicate that the motif RK…R within the podoplanin endodomain is able to interact directly with ERM proteins in vitro.

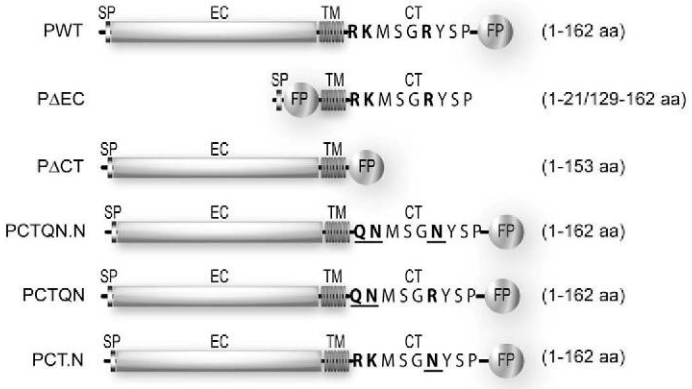

Fig. 1. Schematic representation of podoplanin fusion constructs used for transfection. Numbers indicate podoplanin amino acid sequences (Mart n-Villar et al., 2005) conserved in the construct. CT, cytoplasmic domain; EC, ectodomain; FP, fluorescent protein (EYFP or EGFP) used for the experiments specified in the text; SP, signal peptide; TM, transmembrane domain. Basic amino acids (bold) within the CT domain were substituted by uncharged polar residues (bold and underlined).

To ascertain whether this cluster of basic residues mediates the binding of podoplanin to ERM proteins in vivo, we engineered several constructs encoding wild-type or mutant podoplanin proteins fused to enhanced yellow fluorescent protein (EYFP). Mutant proteins were obtained that lacked the cytoplasmic tail (PΔCT) or in which the juxtamembrane cluster of basic amino acids was substituted by uncharged polar residues, as above (see Fig. 1). Wild-type podoplanin (PWT) and the mutant constructs fused to EYFP were cotransfected with enhanced cyan fluorescent protein (ECFP)-tagged ezrin in MDCK type-II cells and the interaction between ezrin and podoplanin proteins determined by fluorescence resonance energy transfer (FRET). In contrast to MDCK type-I cells, MDCK type-II cells do not express endogenous podoplanin (Zimmer et al., 1999) (our own results). FRET efficiency ($FRET_{eff}$) between EYFP-tagged podoplanin constructs and ECFP-tagged ezrin was monitored by acceptor photobleaching in different cells and cell regions (Fig. 2C-E). The mean $FRET_{eff}$ value for wild-type podoplanin was 27.1%, indicating that a substantial proportion of PWT is complexed with ezrin in vivo. $FRET_{eff}$ decreased to about 5.9% in cells expressing PCT.N, whereas $FRET_{eff}$ values fall to zero in cells expressing mutant PΔCT, PCTQN.N and PCTQN (Fig. 2B). These results

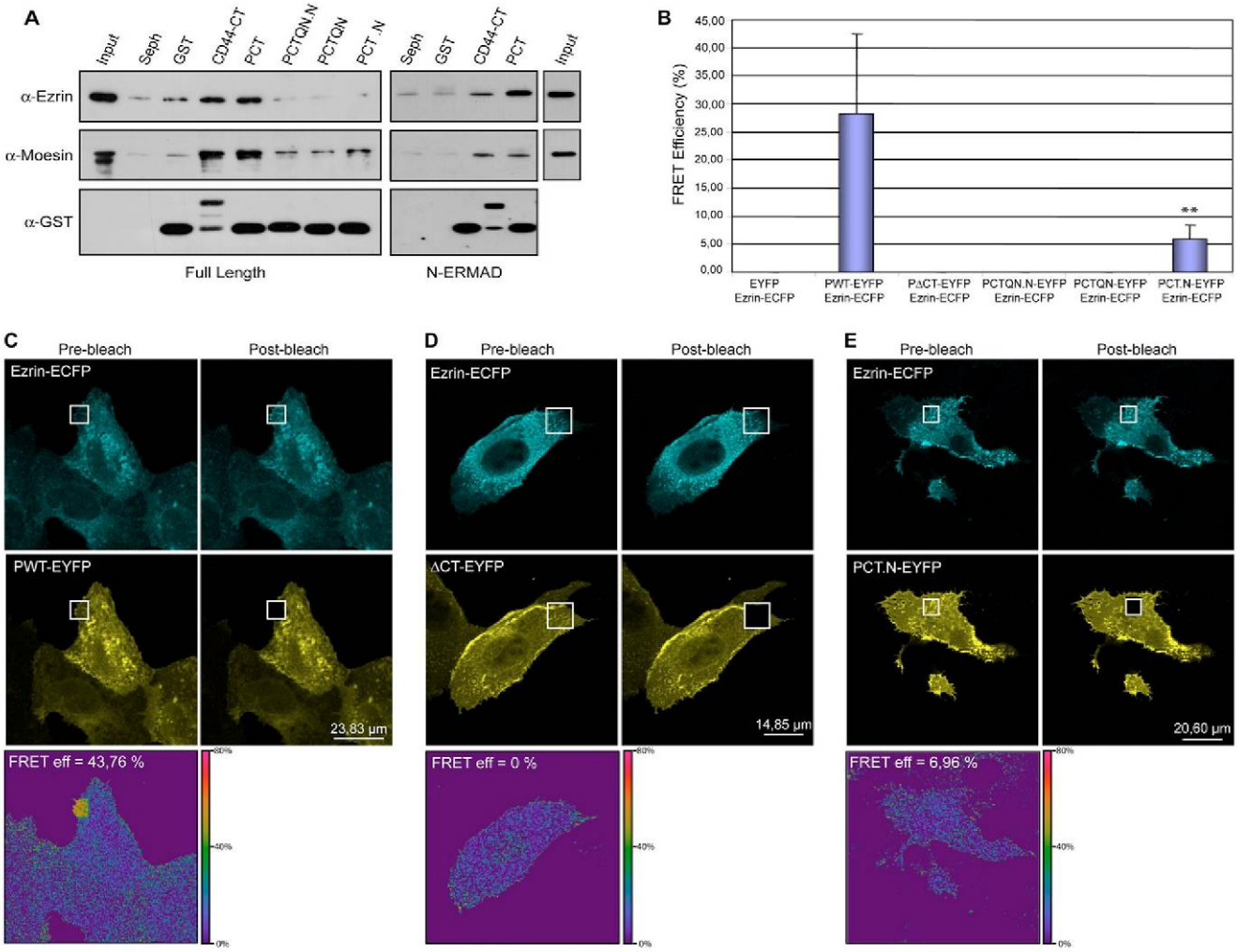

Fig. 2. Podoplanin binds to ERM proteins through a cluster of basic amino acids within its cytoplasmic tail. (A) Association of ezrin and moesin with podoplanin CT. GST and GST fusion proteins bound to Sepharose beads were incubated with purified recombinant full-length ezrin or moesin or their N-ERMADs. Proteins bound to the beads were fractionated by SDS-PAGE followed by western blotting using anti-ezrin or anti-moesin antibodies. CD44-CT was used as a positive control. (B) $FRET_{eff}$ values for cells coexpressing EYFP/Ezrin-ECFP (n=5), PWT-EYFP/Ezrin-ECFP (n=14), PΔCT-EYFP/Ezrin-ECFP (n=7), PCTQN.N-EYFP/Ezrin-ECFP (n=7), PCTQN-EYFP/Ezrin-ECFP (n=6) and PCT.N-EYFP/Ezrin-ECFP (n=10). Note the significant reduction (**P<0.01) of $FRET_{eff}$ in PCT.N with respect to PWT and the absence of FRET in PCTQN.N, PCTQN and PΔCT cell transfectants. (C-E) Confocal fluorescence images showing acceptor photobleaching FRET analysis in MDCK cell transfectants. Images of representative cells coexpressing Ezrin-ECFP with PWT-EYFP (C), PΔCT-EYFP (D) or PCT.N-EYFP (E) are shown. ECFP and EYFP emission signals were collected before (left panels) and after (right panels) EYFP photobleaching in the boxed regions. An increased ECFP fluorescence signal after photobleaching indicates FRET. The $FRET_{eff}$ is represented in the bottom panel on a pseudocolor cell map with scale shown on the right.

demonstrate that in vivo association of podoplanin with ezrin is mainly mediated by the juxtamembrane dipeptide RK. Mutation of the most C-terminal residue R159 significantly impaired but did not prevent this association.

Podoplanin induces an EMT in MDCK cells through the cytoplasmic domain

In a preliminary test in which the wild-type human podoplanin cDNA cloned into the pcDNA3 expression vector (Mart n-Villar et al., 2005) was stably expressed in MDCK type-II cells, we found a dramatic change from an epithelial to a fibroblast-like morphology (data not shown). Therefore, to investigate which region of the molecule is required to promote this morphological change, PWT and the mutant constructs fused to enhanced green fluorescent protein (EGFP), including one that lacked the ectodomain (PΔEC, see Fig. 1), were stably expressed in MDCK cells. All selected clones expressing PWT, PΔEC or PCT.N exhibited a clear fibroblastic morphological appearance. By contrast, cells expressing PΔCT, PCTQN.N and PCTQN maintained the epithelial morphology, as did control clones expressing EGFP alone (EGFP). Two clones of each construct were then selected for further studies. The total level of podoplanin expression and the size of the exogenous proteins were analyzed by western blotting (Fig. 3A). We also monitored the expression of differentiation protein markers. Fibroblastic clones induced by PWT and PΔEC had lost the expression of epithelial markers, such as E-cadherin. They also synthesized reduced levels of cytokeratin 8, β-catenin and

p120 catenin (ctn) isoform 3 (the main p120 ctn form expressed in epithelial MDCK cells) (Sarrio et al., 2004). Conversely, these cells had increased expression of N-cadherin, p120 ctn isoform 1 and fibronectin (Fig. 3A): all mesenchymal markers upregulated during EMT (Cavallaro and Christofori, 2004; Sarrio et al., 2004). Epithelial MDCK cells expressing PCTQN.N and PCTQN retained E-cadherin and cytokeratin levels and did not switch to expression of N-cadherin. Interestingly, clones expressing PCT.N, despite their fibroblastic morphology, retained expression of E-cadherin (although at a reduced level in clone 1), p120 ctn isoform 3 and cytokeratin 8, whereas expression of N-cadherin and p120 ctn isoform 1 was upregulated (Fig. 3A). These data indicated that MDCK cells expressing PCT.N have an intermediate phenotype between epithelial and mesenchymal (which we have termed fibroblastoid). No substantial change in the expression levels of mesenchymal vimentin was observed in the different clones regardless of their epithelial or fibroblastic morphology. Nevertheless, vimentin, which is already significantly expressed in MDCK cells (Peinado et al., 2003) (see also Fig. 3A), was better organized in a clear filament network in fibroblast-like cells induced by PWT and PΔEC in comparison to epithelial cell clones (Fig. S1 in supplementary material). As expected, PCT.N-MDCK cells were positively stained for E-cadherin, but the protein was relocated from cell-cell contacts to the cytoplasm, indicating a loss of E-cadherin function at cell-cell junctions (Fig. S1 in supplementary material). A summary of the phenotypic changes produced in MDCK cells by wild-type and mutant podoplanin proteins is presented in Table 1.

RT-PCR analysis showed that loss of E-cadherin expression in PWT and PΔEC cell transfectants occurred at the transcriptional level (Fig. 3B). Since several transcription repressors of E-cadherin, such as the zinc finger factors Snail and Slug, have been found to promote EMT (Cano et al., 2000; Batlle et al., 2000; Bol s et al., 2003), and Snail appears to be involved in the EMT induced by TGF-β_1 in MDCK cells (Peinado et al., 2003), we analyzed the mRNA levels of these transcription factors in the transfectants. No clear correlation could be established between the mRNA transcript levels and the level of E-cadherin expression or the phenotype of the different cell clones, suggesting that podoplanin-induced EMT did not involve upregulation of Snail or Slug transcription factors.

In summary, these results indicate that expression of wild-type podoplanin in MDCK cells induces a complete EMT associated with reprogramming of differentiation-related gene expression. The crucial region of the molecule involved in this transition appears to be the cluster of basic residues within the cytoplasmic tail responsible for binding to ERM proteins, particularly the juxtamembrane dipeptide RK.

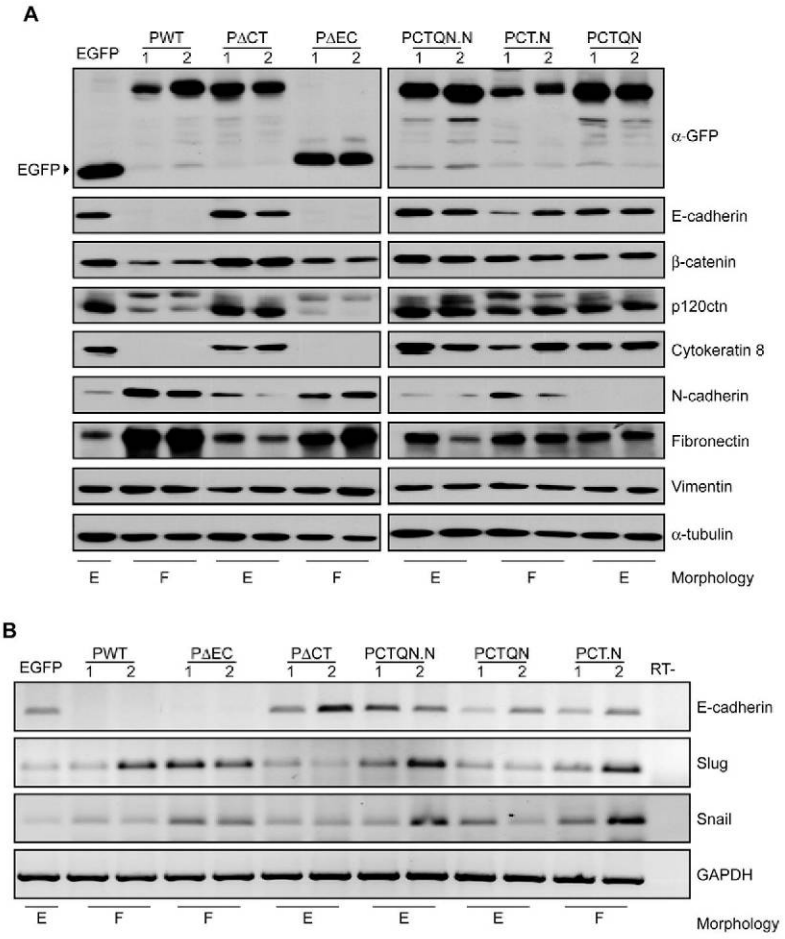

Fig. 3. MDCK cells expressing podoplanin undergo an EMT that depends on the cytoplasmic domain. (A) Western blot analysis of podoplanin proteins and of differentiation-related markers in MDCK-derived cell clones expressing EGFP (control) and PWT, PΔCT, PΔEC, PCTQN.N, PCTQN or PCT.N fusion proteins. (B) Expression of E-cadherin, Snail and Slug mRNA transcripts by RT-PCR. *GAPDH* was amplified as a control for the amount of cDNA present in each sample. The RT- lane shows the results of amplification in the absence of cDNA. The morphology of the cell transfectants is indicated below (E, epithelial; F, fibroblastic).

Localization of podoplanin at cell-surface protrusions does not require the cytoplasmic tail or the ectodomain

The subcellular localization of wild-type and mutant podoplanin proteins was analyzed by confocal microscopy. To determine the fraction of the exogenous protein that was specifically directed to the cell surface, we performed a comparison between the fluorescence signal due to EGFP and the signal obtained after in vivo pre-embedding staining (at 4°C) using either a specific antibody recognizing the podoplanin ectodomain (Mart n-Villar et al., 2005) or an anti-EGFP antibody (for detection of PΔEC). As shown in Fig. 4, PWT was distributed all along the plasma membrane concentrated at cell-surface protrusions (microvilli, filopodia and ruffles), as previously reported (Scholl et al., 1999; Mart n-Villar et al., 2005). Patchy staining was also seen in the cytoplasm, indicating the presence of podoplanin at internal membrane structures (see below). Deletion of the ectodomain did not alter this pattern of expression, although the amount of PΔEC directed to the cell surface was substantially

Table 1. Summary of the phenotypic changes induced by podoplanin constructs in MDCK cells

Construct	Morphology	E-CD	N-CD	p120 ctn i.3	p120 ctn i.1	K8	Fn	Cell migration (wound healing)	Invasiveness (Matrigel)	RhoA activity (cell lysates)
Control (EGFP)	Epithelial	+	+/–	++	–	+	+	Collective/Slow	–	–
PWT	Fibroblastic (well spread)	–	++	+/–	+	–	++	Individual/Fast	++	+
PΔEC	Fibroblastic (elongated)	–	++	+/–	+	–	++	Individual/Fast	++	+
PΔCT	Epithelial	+	+/–	++	–	+	+	Mixed/Intermediate	+	–
PCTQN.N	Epithelial	+	+/–	++	–	+	+	Collective/Slow	–	–
PCTQN	Epithelial	+	–	++	–	+	+	Collective/Slow	–	–
PCT.N clone 1	Fibroblastic (elongated)	+/–	++	+	+	+	+	Individual/Fast	++	+
PCT.N clone 2	Fibroblastic (elongated)	+	+	+	+	+	+	Individual/Fast	++	+/–

CD, cadherin; ctn, catenin; Fn, fibronectin; K, cytokeratin.

reduced with respect to PWT, because a significant fraction of the truncated molecule had a perinuclear location, probably concentrated at the Golgi apparatus. Interestingly, neither deletion of the cytoplasmic tail nor mutation of the ERM-binding sites prevented localization of the mutant proteins at cell-surface protrusions: PΔCT, PCTQN.N and PCTQN proteins localized on the apical and lateral surfaces of polarized epithelial MDCK cells, concentrated at microvilli and cell-cell junctions (Fig. 4). On the other hand, the subcellular distribution of mutant PCT.N did not differ significantly from that of PWT. These results suggest that neither the ectodomain nor the association of podoplanin with the cytoskeleton through the cytoplasmic tail is required for localization of podoplanin at cell-surface protrusions.

We also studied the organization of the actin cytoskeleton in the cell transfectants (Fig. S2 in supplementary material). Epithelial MDCK cells transfected with mutant PΔCT, PCTQN.N and PCTQN showed strong cortical actin bundles and short thin stress fibers: the same pattern exhibited by the parental cell line and control clones. These cells also showed small vinculin-containing focal contacts. In cells expressing PWT, PΔEC or PCT.N, however, a reorganization of the actin cytoskeleton concomitantly with the induced morphological changes was observed. Thus, cortical actin bundles disappeared in these fibroblast-like cells,

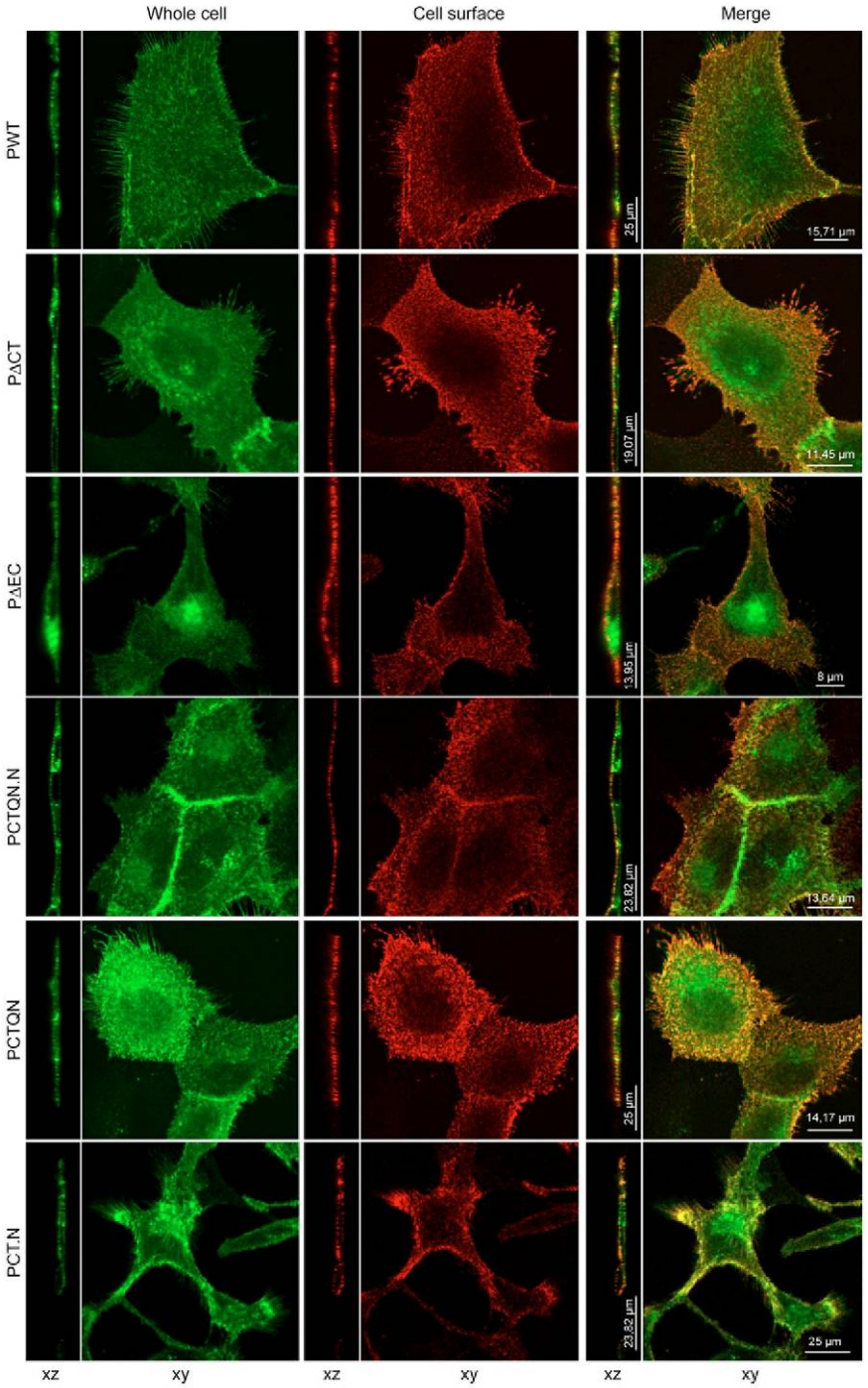

Fig. 4. Subcellular localization of wild-type and mutant podoplanin proteins. Confocal images of horizontal (*x*-*y*) and vertical (*x*-*z*) sections of MDCK cells expressing the indicated podoplanin proteins fused to EGFP are shown. The exogenous proteins specifically expressed at the cell surface were detected by in vivo pre-embedding staining using antibodies either recognizing the podoplanin EC domain or EGFP (for detection of PΔEC).

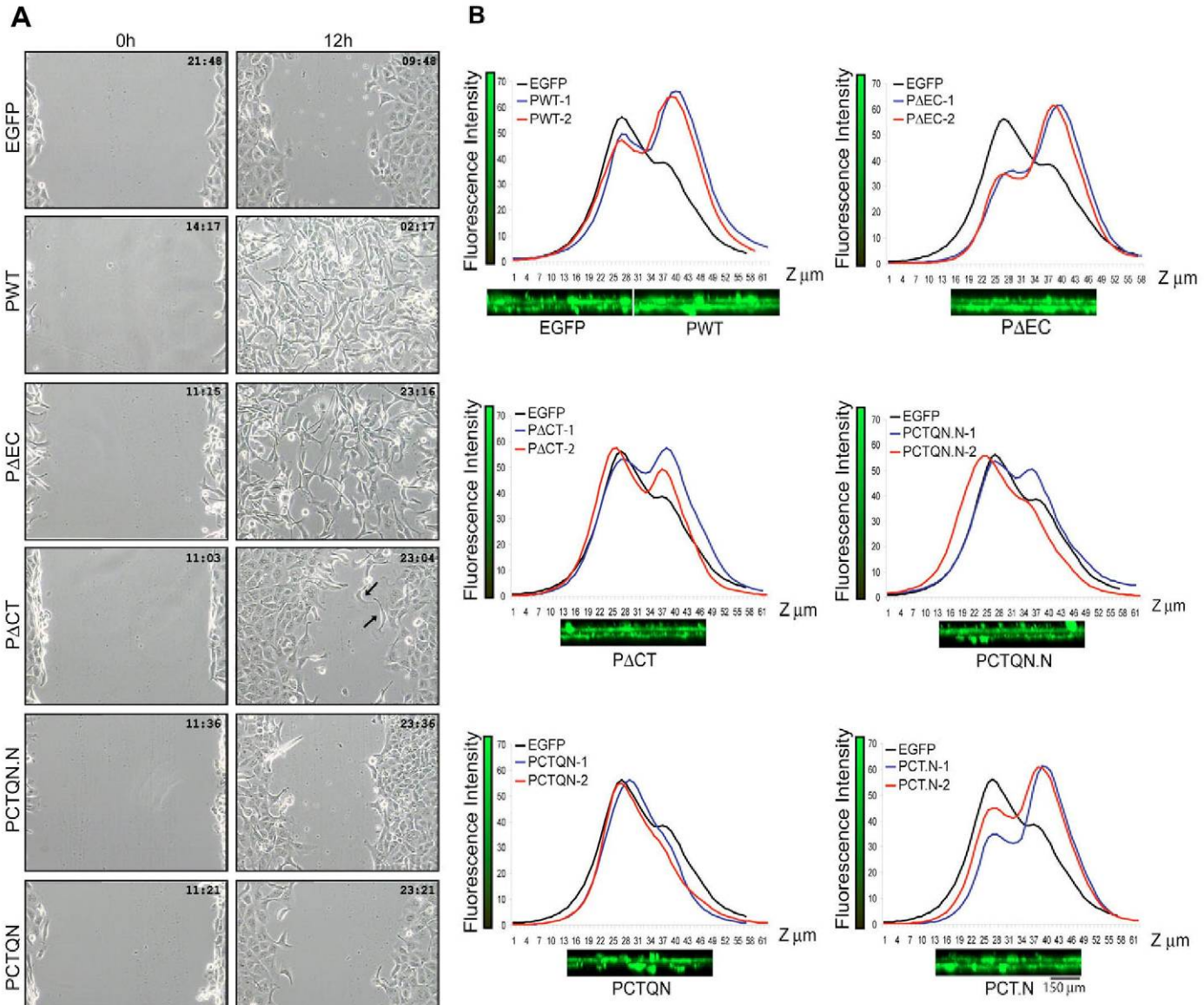

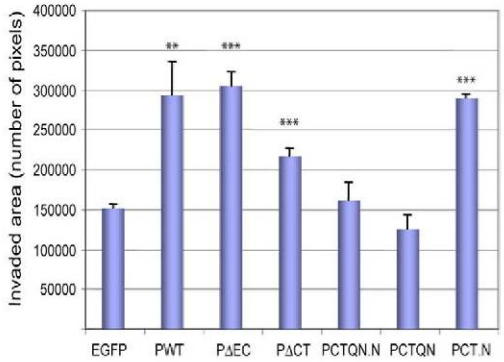

Fig. 5. Podoplanin-induced EMT is associated with increased migratory and invasive abilities. (A) In vitro wound-healing assay. Confluent cell cultures were scratched with a pipette tip to produce a wound and analyzed by time-lapse video microscopy. Images of the wounded area immediately (0 hours) and 12 hours after the incision was made are shown. Arrows in PΔCT indicate individual cells moving into the wound as fibroblasts. An animated sequence of these data is shown in supplementary material Movie 1. In the bottom panel a graph shows quantification of cell migration from three independent experiments. $^{**}P<0.01$; $^{***}P<0.001$ vs control (EGFP) cells. (B) Matrigel invasion assay. Cell transfectants expressing EGFP-tagged wild-type and mutant podoplanin proteins were seeded on a 24-well Matrigel invasion chamber. FBS (5%) was used as a chemoattractant. Fluorescent cells that invaded the Matrigel-coated filter after 24 hours were detected by confocal microscopy. Images were acquired each 2 μm along the *z*-axis and quantified by fluorescence intensity profiles. Vertical (*x*-*z*) sections of the filter are shown below. Results are representative of two experiments.

whereas F-actin accumulated at lamellipodia and ruffles. Nevertheless, well-spread PWT-MDCK fibroblasts showed more-pronounced focal contacts and longer and thicker stress fibers than elongated MDCK cells expressing PΔEC or PCT.N (Fig. S2 in supplementary material).

Dynamics of migration in MDCK cells expressing wild-type and mutant podoplanin proteins

To examine whether the observed phenotypic changes in MDCK cell transfectants were associated with increased motility, we performed an in vitro wound-healing assay. PWT- and PΔEC-MDCK cells were able to repopulate a wound made 12 hours earlier in a confluent culture, whereas closure of the wounds made in MDCK or control cell cultures was less than 50% (Fig. 5A). PCT.N-MDCK cells also had high migratory abilities, comparable with those of cells expressing PWT and PΔEC. Time-lapse video observations showed that fibroblast-like PWT-, PΔEC- and PCT.N-MDCK cells migrated individually, extending and retracting protrusions and continually changing their orientations and shapes (Fig. 5A and Movie 1 in supplementary material). By contrast, epithelial cells expressing PCTQN.N and PCTQN migrated collectively, maintaining cell-cell contacts (Fig. 5A and Movie 1 in supplementary material) following the principles reported for migration of parental MDCK cells (Matsubayashi et al., 2004; Faroqui and Fenteany, 2005). Surprisingly, epithelial PΔCT-MDCK cells exhibited an intermediate behavior, in which migration was significantly reduced when compared with fibroblast-like cell lines, but those cells migrated faster than the other epithelial cell transfectants. The dynamics of cell migration in PΔCT-MDCK wounds were similar to those described for control cells, although in this case the speed of movement was higher and contacts between marginal cells and their following neighbours became weaker, resulting in numerous individual cells moving as fibroblasts into the wound (arrows in Fig. 5A and Movie 1 in supplementary material).

We also studied the ability of the cell transfectants to invade into a reconstituted basement membrane (Matrigel). Invasiveness was highly enhanced in fibroblast-like PWT-, PΔEC- and PCT.N-MDCK cells with respect to epithelial cells expressing PCTQN.N, PCTQN and control clones (Fig. 5B). As in the in vitro wound-healing assay, PΔCT-MDCK cells showed an intermediate behavior between those two groups of transfectants.

Fluorescence time-lapse confocal microscopy on isolated MDCK cells expressing wild-type or mutant podoplanin proteins fused to EGFP allowed us to visualize the dynamics of the subcellular distribution of podoplanin during cell locomotion (Fig. 6 and Movies 3-5 in supplementary material). PWT was present at the edge of lamellipodial extensions, but it disappeared from attached lamellipodia (asterisk) whereas it remained on the top of ruffles moving centripetally across the cell surface. In addition, podoplanin clustered at the cell tail (arrowhead) before the rearmost adhesions to the substratum

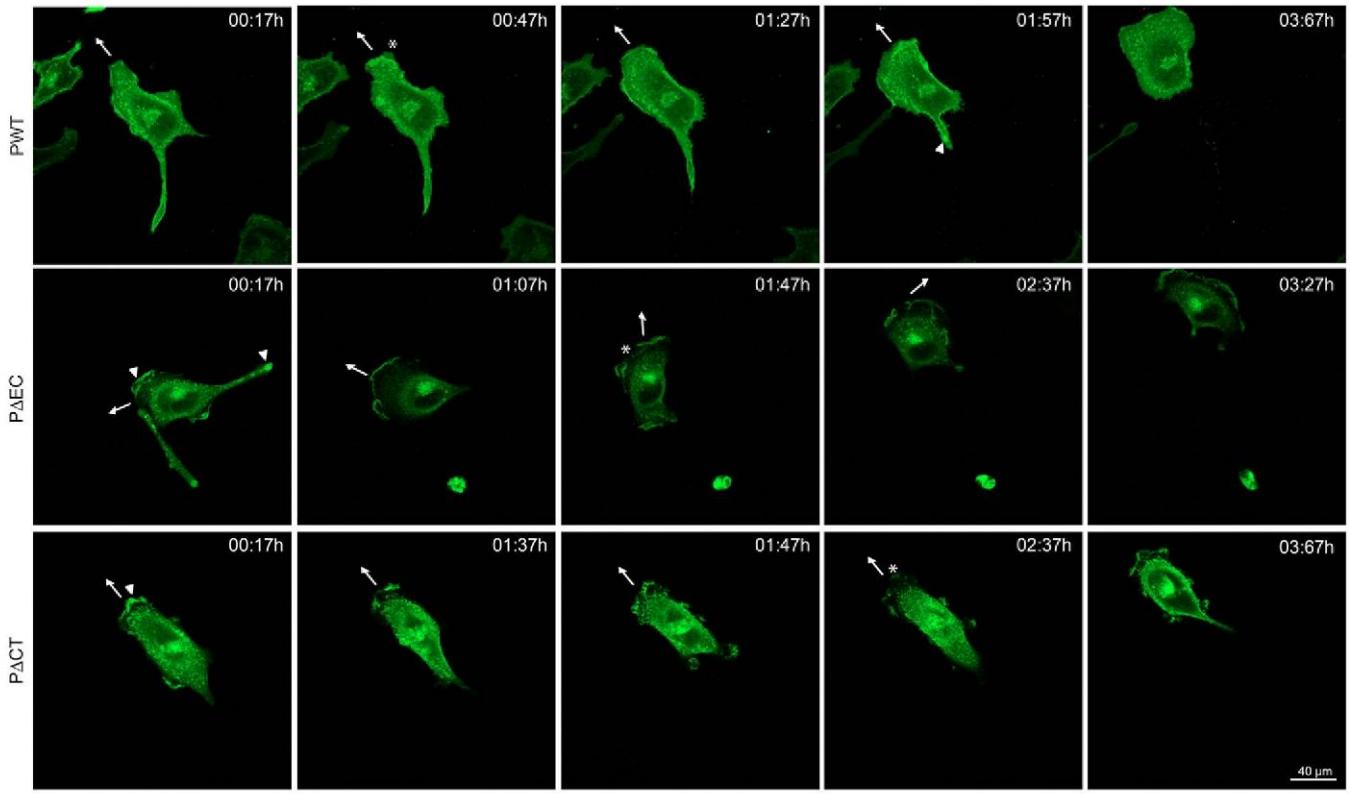

Fig. 6. Dynamics of podoplanin subcellular localization during cell locomotion. Isolated MDCK cells expressing EGFP-tagged PWT, PΔEC and PΔCT proteins were imaged by capturing sections of 0.5 μm every 10 minutes for 4 hours. Images in all panels correspond to 3D reconstructions. Arrowheads indicate podoplanin fluorescence signal concentrated at the leading edge of lamellipodial extensions and on the retracting tail, whereas asterisks indicate loss of fluorescence signal on lamellipodial extensions attached to the substratum. The direction of cell migration is indicated by arrows. Animated sequences of these data are shown in supplementary material Movies 3-5.

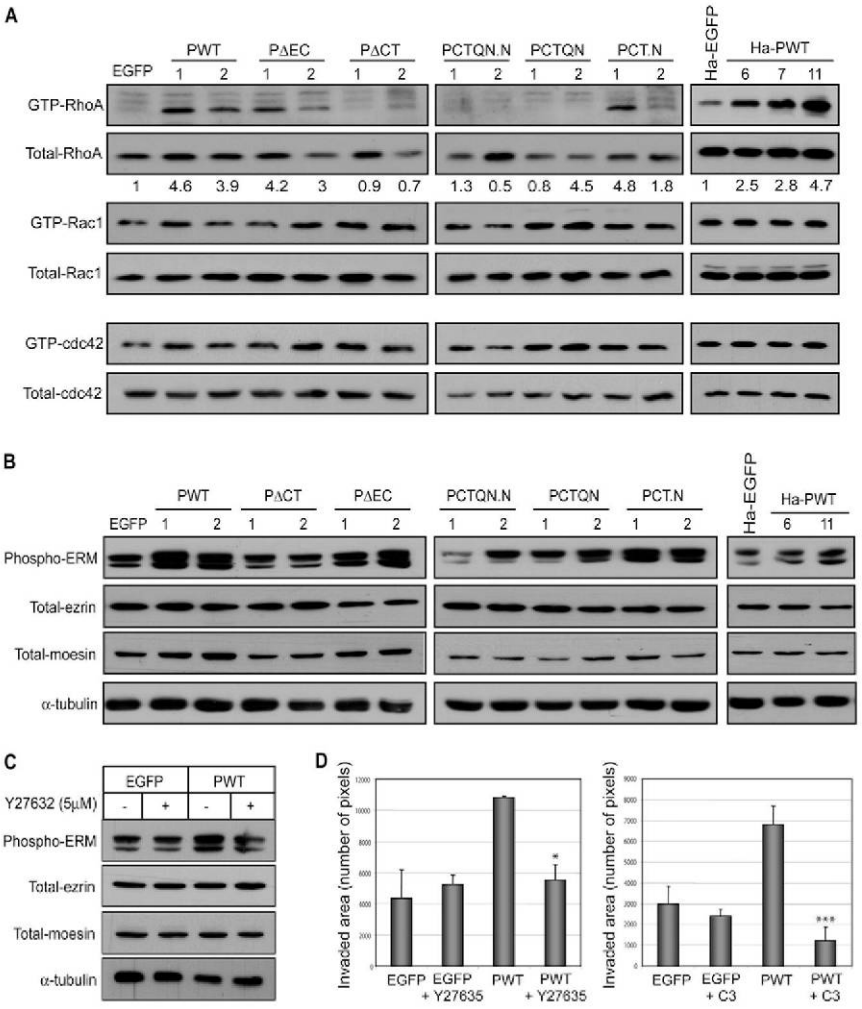

Fig. 7. Podoplanin-induced EMT is associated with upregulation of RhoA activity. (A) Rho, Rac and Cdc42 bound to GTP affinity pull-down assays were used to determine the levels of active Rho GTPases. Levels of active RhoA, Rac1 and Cdc42 in MDCK and HaCaT cell clones transfected with the empty vector (EGFP) and with wild-type and mutant podoplanin constructs fused to EGFP. Quantification of RhoA-GTP expression level relative to total RhoA level was performed by densitometric analysis. Values below blots are relative to control (EGFP) cells, to which an arbitrary value of 1 was given. Results are representative of two experiments. (B) Western blot analysis of ERM phosphorylation relative to the total expression levels of ezrin and moesin. The levels of α-tubulin were determined as a control for protein loading. (C) Western blot analysis of phospho-ERM levels relative to the total expression levels of ezrin and moesin in MDCK cells transfected with the empty vector (EGFP) and PWT before and after treatment with the Rock inhibitor Y27632. (D) Inhibition of RhoA signaling blocks podoplanin-stimulated cell migration. In vitro wound-healing assays of control (EGFP) and PWT-MDCK cells were performed (as in Fig. 5A) in the absence or presence of either Y27632 (which inhibits Rock) or soluble C3 transferase (which inhibits RhoA, RhoB and RhoC). Y27632 and C3 transferase reduced PWT-MDCK cell migration to basal and below basal levels, respectively. *P<0.05; ***P<0.001 vs PWT-MDCK cells.

disassembled and the tail retracted. These observations suggest that podoplanin might be involved in ruffling activity as well as in retractive processes. A substantial amount of podoplanin was also seen associated with internal membranous structures (probably the Golgi system) and on the surface of vesicles located close to the plasma membrane or surrounding the Golgi apparatus (see Movie 2 in supplementary material). The importance of this latter observation remains to be investigated. No significant change was observed in the distribution of mutant PΔEC (or PCT.N) with respect to PWT during cell locomotion, although migration of PΔEC-MDCK cells was rather erratic compared with directional movement of PWT-MDCK cells (Fig. 6; Movies 3 and 5 in supplementary material). On the other hand, mutant PΔCT (as well as PCTQN.N and PCTQN) concentrated at ruffles and microvilli, although ruffling activity was less intense in these epithelial cell transfectants (Movie 4 in supplementary material) compared with fibroblast-like cells expressing PWT, PΔEC or PCT.N.

Podoplanin-induced EMT involves increased RhoA activity

Rho GTPases have been found to mediate cytoskeletal rearrangements and have been implicated in cell migration and invasiveness (Ridley, 2001; Sahai and Marshall, 2002a). To ascertain whether podoplanin-induced EMT involved regulation of Rho GTPases activity, we used biochemical pull-down assays to analyze the activation state of RhoA, Rac1 and Cdc42 in the cell transfectants. While in parental MDCK cells or control clones the overall level of active RhoA (RhoA-GTP) was almost undetectable (Zondag et al., 2000), the activity of RhoA was dramatically increased in fibroblastic clones expressing PWT and PΔEC (Fig. 7A). Enhanced activation of RhoA was also found in fibroblastoid PCT.N-MDCK cells, although in this case the level of active RhoA varied between the two different clones (clone 1 showed higher RhoA-GTP levels than clone 2). Lysates from epithelial cells transfected with PΔCT, PCTQN.N and PCTQN did not show significant changes in RhoA activation over basal levels (Fig. 7A and Table 1). In all cases, there was little change in the total level of expression of RhoA in each of the transfectants after correcting for protein levels with α-tubulin (data not shown), indicating that activation of RhoA was not due to an increase in its expression levels. In contrast to RhoA, the levels of active Rac1 and Cdc42 did not vary substantially in any of the transfectants with respect to control cells. PWT alone (without EGFP) was also able to activate RhoA specifically without changing the levels of active Rac1 and Cdc42 (data not shown), indicating that this effect is not due to EGFP modification. On the other hand, we confirmed that the ability of podoplanin to activate RhoA specifically is not dependent on a particular cell line, because immortalized HaCaT keratinocytes

expressing PWT also showed increased RhoA-GTP levels whereas the levels of Rac1 and Cdc42 bound to GTP remained unchanged (Fig. 7A). Double immunofluorescence confocal microscopy analysis revealed that both RhoA and Rac1, but not Cdc42, colocalized with podoplanin at cell-surface protrusions in fibroblast-like MDCK cells expressing PWT, PΔEC, and PCT.N (Fig. S3 in supplementary material and data not shown). These results might indicate local activation of both RhoA and Rac1 at podoplanin-induced filopodia and ruffles even though no change in the activity of Rac1 was observed in whole-cell lysates.

Since RhoA-associated kinase (Rock), a downstream effector of RhoA, has been shown to phosphorylate and activate ERM proteins (Matsui et al., 1998), we analyzed the status of ERM phosphorylation in the cell transfectants (Fig. 7B). Increased levels of phospho-ERM proteins were found in fibroblastic and fibroblastoid clones with respect to control cells and epithelial cell transfectants. MDCK cells transfected with PWT alone (without EGFP) and HaCaT keratinocytes expressing PWT also showed enhanced phospho-ERM levels (Fig. 7B). Treatment of PWT-MDCK cells with the Rock inhibitor Y27632 reduced ERM phosphorylation to basal levels, whereas the inhibitor did not affect ERM phosphorylation in control cells (Fig. 7C). These results confirm that podoplanin stimulation of ERM phosphorylation is mediated by RhoA-dependent activation of Rock. Moreover, inhibition of either Rock with Y27632 or RhoA with the exoenzyme C3 transferase blocked podoplanin-stimulated cell migration (Fig. 7D).

Taken together, these results suggest that to activate RhoA, podoplanin needs to recruit ERM proteins through its ERM-binding site. Upregulation of RhoA activity leads to Rock-mediated ERM phosphorylation and stabilization of ERM proteins in an open, active conformation (Matsui et al., 1998), which further strengthens the anchorage of podoplanin to the cytoskeleton, allowing EMT and enhanced cell migration and invasion. Therefore, we reasoned that podoplanin-induced EMT should be prevented by inhibiting the function of either ezrin or RhoA.

Blocking ezrin or RhoA prevents podoplanin-induced EMT

In order to analyze the effects of the functional loss of ezrin or RhoA in podoplanin-mediated EMT, MDCK cells were cotransfected with PWT and a construct encoding a dominant-negative form of either ezrin or RhoA. The N-terminal domain of ezrin (N-ezrin) tagged with vesicular stomatitis virus glycoprotein G (VSVG) (Crepaldi et al., 1997) and a hemagglutinin (HA)-tagged N19RhoA mutant form were used to suppress ezrin and RhoA functions, respectively. The results of these experiments are shown in Fig. 8. When coexpressed together with one of these dominant-negative forms, podoplanin was unable to upregulate RhoA activity (Fig. 8C) and to promote EMT (Fig. 8A,B). Loss of function of ezrin or RhoA also suppressed podoplanin stimulation of phospho-ERM levels (Fig. 8C). These results demonstrated that ezrin and RhoA play crucial roles in podoplanin-mediated EMT.

Discussion

We show in this work that expression of human podoplanin in epithelial MDCK cells promotes a complete EMT linked to downregulation of epithelial genes (E-cadherin, p120 ctn isoform 3 and cytokeratin 8) and upregulation of mesenchymal markers (N-cadherin, p120 ctn isoform 1 and fibronectin). This conversion allowed MDCK cells to acquire migratory features, including a switch from a relatively slow collective pattern of cell migration to a faster, individualized cell locomotion pattern during wound healing, and increased invasiveness through Matrigel. In several human cancer types, downregulation of E-cadherin expression is accompanied by upregulation of mesenchymal N-cadherin, and this cadherin switch also occurs during EMTs in embryonic development. N-cadherin appears to exert the opposite effect to that of E-cadherin, because it promotes cell migration or invasion instead of cell-cell cohesion (reviewed by Cavallaro and Christofori, 2004). Interestingly, in podoplanin-induced EMT the E- to N-cadherin switch correlates with a change in the expression of p120 ctn isoforms from isoform 3 to isoform 1. Although this p120 ctn switch was previously observed in EMTs induced in MDCK cells by the E-cadherin transcriptional repressors Snail and Slug (Sarrio et al., 2004), no correlation was found between the levels of these transcription factors and the expression of p120 ctn isoform 1 in podoplanin-induced EMT, indicating that changes from p120 ctn isoform 3 to isoform 1 and from E- to N-cadherin do not necessarily involve upregulation of Snail or Slug.

As also shown in this study, podoplanin induces upregulation of RhoA activity in MDCK and HaCaT cells. Since podoplanin promoted cell scattering, but not a complete EMT in HaCaT keratinocytes (Martín-Villar et al., 2005), these results indicate that podoplanin-induced RhoA activation in epithelial cells precedes EMT rather than being a consequence of it. Several reports have implicated RhoA in epithelial tumor progression in vivo and in vitro (reviewed by Sahai and Marshall, 2002a; Lozano et al., 2003). Thus, elevation of RhoA activity has been found to result in disruption of adherens junctions and EMT in colon carcinoma cells (Sahai and Marshall, 2002b), TGF-β_1-stimulated mammary epithelial cells (Bhowmick et al., 2001) and Rac1-activated epithelial-like NIH3T3 cells (Sander et al., 1999). Epithelial MDCK cells are characterized by high Rac1 and low RhoA activity, and downregulation of Rac1 activity by oncogenic Ras also leads to increased RhoA activity and EMT (Zondag et al., 2000). The fact that podoplanin is able to activate RhoA without affecting Rac1 or Cdc42 activity suggests a direct link between podoplanin expression and RhoA activation in MDCK cells, but does not exclude a role for Rac1 or Cdc42 in podoplanin-mediated cell motility. In fact, Rac1 colocalizes with podoplanin at cell-surface protrusions in podoplanin-induced MDCK fibroblastic cells. Whereas Rac1 and Cdc42 have been involved in the establishment and maintenance of epithelial intercellular adhesions and are respectively required for lamellipodium and filopodium extensions in migrating cells, RhoA is implicated in the generation of contractile force, and in moving the body and tail of the cell behind the leading edge (Ridley, 2001). As podoplanin clusters on the cell tail just before tail retraction is completed, it would have a direct role in retractive processes by activating RhoA on the trailing edge.

The crucial podoplanin structural motif involved in RhoA activation and EMT seems to reside in the endodomain, because its deletion (PΔCT) prevented upregulation of RhoA activity and halted conversion to a fibroblast-like phenotype, whereas deletion of the ectodomain (PΔEC) did not. The

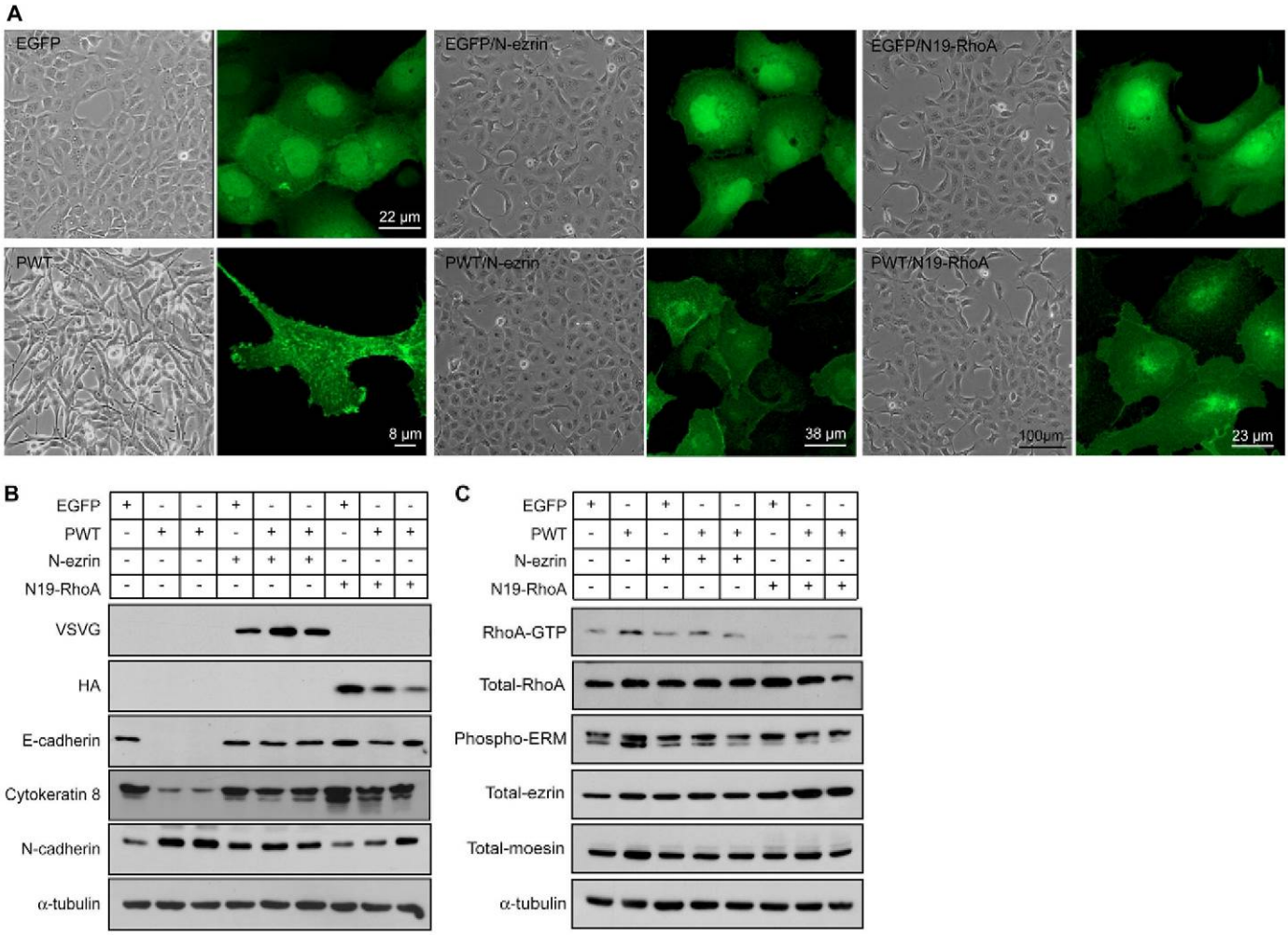

Fig. 8. Dominant-negative effects of N19RhoA and of N-terminal domain of ezrin (N-ezrin) in podoplanin-induced EMT. (A) Phase-contrast micrographs and confocal fluorescence detection of podoplanin in MDCK cells cotransfected with EGFP-tagged PWT and N-ezrin or N19RhoA. Control cells expressing EGFP alone, EGFP/N-ezrin and EGFP/N19RhoA are also shown. Confocal images are maximum projections of horizontal optical sections through the whole depth of the transfectants. (B) Western blot analysis of N-ezrin (VSVG), N19RhoA (HA) and differentiation-related proteins in MDCK cell transfectants. N-ezrin and N19RhoA expression was determined by using antibodies against their respective tags. (C) N-ezrin and N19RhoA inhibits podoplanin-mediated RhoA activation and ERM phosphorylation. The levels of RhoA-GTP relative to the levels of total RhoA and the levels of phospho-ERM relative to the total expression levels of ezrin and moesin are shown. The expression of α-tubulin was determined as a control for protein loading.

cytoplasmic tail of podoplanin (**RK**MSG**R**YSP) is extremely short and binds directly to ezrin and moesin through a cluster of three basic residues (bold). In vivo, the interaction of podoplanin with ezrin appears to be mainly mediated by the juxtamembrane dipeptide RK, because substitution of these two or all three basic residues by uncharged polar amino acids (PCTQN or PCTQN.N) had the same effect as deletion of the entire cytoplasmic tail (PΔCT) in blocking podoplanin association with ezrin. By contrast, mutation of the most C-terminal residue R159 (PCT.N) impaired, but did not prevent, podoplanin-ezrin interaction. PΔCT, PCTQN and PCTQN.N were unable to induce RhoA activation and EMT, whereas PCT.N pushed MDCK cells to an intermediate phenotype (the so-called fibroblastoid phenotype) characterized by mixed expression of epithelial (i.e. E-cadherin) and mesenchymal (i.e. N-cadherin) protein markers and by a fibroblast-like morphology and migratory behavior. Overall, these results suggested that podoplanin needs to recruit ERM proteins through the endodomain in order to activate RhoA and promote EMT, and this hypothesis was confirmed by loss-of-function experiments. Suppression of the function of either ezrin or RhoA by the introduction in MDCK cells of a dominant-negative form of any of these proteins blocked podoplanin-induced RhoA activation and EMT. An intriguing question is how podoplanin expression in MDCK cells leads to RhoA activation. We speculate that this could occur by a similar mechanism to that exhibited by the hyaluronan receptor CD44. Hirao and coworkers found that Rho-GDP dissociation inhibitor (Rho-GDI), which sequesters Rho GTPases bound to GDP in the cytoplasm, could be coimmunoprecipitated together with CD44-ERM complexes (Hirao et al., 1996). The binding of Rho-GDI to the exposed N-ERMAD domain of ERM proteins releases RhoA-GDP from the inhibitor, allowing its activation by a GDP-GTP exchange factor (Takahashi et al.,

1997; Takahashi et al., 1998). Thus, podoplanin recruitment of ezrin and/or moesin to the membrane not only would mediate its anchorage to the actin cytoskeleton but also would activate RhoA facilitating EMT. In this regard, it has been shown that ezrin influences the metastatic potential of tumor cell lines, at least in part, through activation of RhoA (Yu et al., 2004). Once activated, RhoA can contribute to stabilize ERM proteins further in an active conformation either by Rock-dependent phosphorylation of a T residue in the C-terminal domain, as shown in this work, or by RhoA-dependent production of PIP_2 (Tsukita and Yonemura, 1999; Ivetic and Ridley, 2004).

A recent report (Wicki et al., 2006) has described podoplanin stimulation of collective cell migration and invasion (in the absence of EMT) in MCF7 breast carcinoma cells. This effect was mediated by the induction of filopodia-like structures in the migrating front, and, surprisingly, involved combined inactivation of RhoA, Rac1 and Cdc42, although only inhibition of RhoA signaling appeared to mediate filopodia formation. These results suggest a direct role of podoplanin in stimulating epithelial cell migration independently of promoting EMT, and are in line with our previous observations suggesting that the extent of podoplanin-mediated phenotypic changes is dependent on the cell type or the state of cellular differentiation. Thus, podoplanin induces filopodia formation in human immortalized HaCaT keratinocytes, but fails to downregulate E-cadherin expression and to promote a complete EMT (Mart n-Villar et al., 2005). This is in contrast to the profound phenotypic changes induced by podoplanin in MDCK, a highly sensitive cell line, which undergoes EMT in the presence of different inducers (Gotzman et al., 2004). A major discrepancy with the results of Wicki and co-workers is the fact that, in our hands, podoplanin activates RhoA without affecting Rac1 and Cdc42 activities in both MDCK and HaCaT cells. In MCF7 cells, stimulation of cell migration is associated with RhoA inhibition, whereas the opposite is true in MCDK cells. It is well established that RhoA activation can either inhibit or promote cell migration in distinct cell types (see Ridley, 2004; Lozano et al., 2005). This fact probably reflects a particular organization of the cellular cytoskeleton (microfilaments, microtubules and intermediate filaments) and of adhesion components, as well as a different way for Rho GTPases to coordinately regulate cell migration. As a matter of fact, while the basal level of active RhoA is relatively high in MCF7 cells (Wicki et al., 2006), it is low in MDCK and HaCaT cells compared with the levels of active Rac and Cdc42 (Zondag et al., 2000) (this paper). After all, both situations, i.e. podoplanin stimulation of in vitro cell migration or invasion with and without EMT, are compatible with the in vivo data. In many human carcinomas, podoplanin is coexpressed together with E-cadherin in the invasive front of the tumors (Wicki et al., 2006), but we also found that the presence of podoplanin coincides with the loss of E-cadherin expression in the invasive front of some oral squamous cell carcinomas (Martin-Villar et al., 2005).

Interestingly, epithelial MDCK cells expressing mutant PΔCT consistently showed loose cell-cell contacts and enhanced migratory and invasive abilities in comparison with control cells or cells expressing PCTQN.N and PCTQN. These results suggest that the podoplanin CT domain might contain residues that positively affect the stability of adherens junctions. These residues should be other than those involved in ERM binding or should become functional when the ERM-binding sites are inactivated. This hypothesis is supported by the fact that PCTQN.N, PCTQN and PΔCT mutant proteins are expressed at cell-cell contacts in epithelial MDCK cells. In this regard, Wicki and co-workers observed that the majority of pancreatic carcinomas in a transgenic mouse model (Rip1Podo;Rip1Tag2) with targeted expression of podoplanin in β cells of islets of Langerhans retained E-cadherin expression whereas it was lost in most carcinomas of control mice (Wicki et al., 2006). Yet, at present, we do not have a rational explanation for the unexpected phenotype of PΔCT-MDCK cell transfectants. Other observations related to the phenotypes of MDCK cells expressing PCT.N and PΔEC suggest that podoplanin can influence cell spreading. Both types of fibroblast-like cell transfectants showed smaller focal contacts and fewer stress fibers when compared with well-spread MDCK cells expressing PWT. Since podoplanin appears to be absent from focal contacts and does not associate with stress fibers (Scholl et al., 1999), these observations suggest that the ectodomain, and possibly its interaction with extracellular components could affect the dynamics of cell to substratum adhesion. It has been found that podoplanin induces platelet aggregation through the EC domain (Kato et al., 2003; Kaneko et al., 2006). In addition, we have obtained experimental evidence indicating that podoplanin interacts with extracellular matrix components (unpublished results). These data suggest an adhesive role for this glycoprotein. The interaction of podoplanin with extracellular components might be mechanically transmitted to the actin cytoskeleton through the cytoplasmic tail, as occurs with most, if not all, membrane adhesion receptors (Brunton et al., 2004). Thus, the inability of podoplanin to bind to extracellular components (PΔEC) or the diminished or inappropriate interaction of podoplanin with intracellular molecules involved in actin dynamics (PCT.N) could affect the dynamics of focal adhesions.

A final point brought to the discussion is the fact that although podoplanin-induced EMT is dependent on the interaction of the cytoplasmic tail with ERM proteins and then with the cytoskeleton, the localization of podoplanin at cell-surface protrusions requires neither the endodomain nor the ectodomain, pointing to the transmembrane domain as the structural element responsible for the presence of podoplanin within this particular membrane region. This might be mediated by the association of the podoplanin TM domain with lipid rafts, as occurs with CD44 (Perschl et al., 1995). It has been proposed that protrusive motility at the cell surface might be regulated through the local accumulation of raft domains enriched in PIP_2 (Yin and Janmey, 2003; Golub and Caroni, 2005). The implication of the podoplanin TM domain in the localization of this glycoprotein at cell-surface protrusions and its possible interaction with lipid rafts is currently being investigated.

Materials and Methods

Constructs

Constructs for GST fusion proteins of the podoplanin CT were generated by synthesizing each cDNA carrying *Eco*RI and *Xho*I restriction sites to facilitate subcloning into the pGEX-4T1 vector (Amersham Biosciences). cDNAs for the CT of CD44 and full-length ezrin or its N-ERMAD region (residues 1-310) were obtained by PCR amplification from HT1080 and HeLa cells, respectively. Constructs for GST-full-length moesin and its N-ERMAD region were a gift from Francisco S nchez-Madrid (Hospital de la Princesa, Madrid, Spain) and constructs for tagged dominant-negative forms of ezrin (N-ezrin) and RhoA (N19RhoA) were

kindly provided by Paul Mangeat (University of Montpellier, France) and Piero Crespo (Instituto de Investigaciones Biom dicas, Madrid, Spain), respectively. Ezrin tagged with ECFP at the C-terminus, EYFP- and EGFP-tagged podoplanin constructs were obtained by PCR amplification using primers that carry both the desired mutation (in the case of podoplanin mutant constructs) and a convenient restriction site to facilitate subcloning into pECFP-N1, pEYFP-N1, pEGFP-N1 and pEGFP-C1 vectors. Oligonucleotides used for amplification of all these constructs are described in Table S1 in supplementary material. All PCR-derived constructs were sequenced in an ABI Prism 377 system (Perkin Elmer) to confirm that nucleotide sequences were correct.

RT-PCR analysis

RT-PCR analysis was carried out as described previously (Mart n-Villar et al., 2005). Canine PCR products were obtained after 30-35 cycles of amplification with an annealing temperature of 60-65°C. Primer sequences for canine E-cadherin (*CDH1*), *Snail* and glyceraldehyde-3-phosphate dehydrogenase (*GAPDH*) have been described elsewhere (Peinado et al., 2003). For canine *Slug* the following oligonucleotides were used: 5′-AGTGATTATTTCCCCATATCTCTATGA-3′ and 5′-GTAGTCTTTCCTCTTCATCACTAATGG-3′ (amplifies a fragment of 300 bp).

Cell culture conditions and cDNA transfections

Cell culture conditions and transfection procedures were as previously described (Mart n-Villar et al., 2005). MDCK cell transfectants were selected in 0.5 mg/ml of G418 (Promega) for 2 weeks. Individual clones were isolated with cloning rings. For FRET experiments, MDCK cells at 60-70% confluence were cotransfected with Ezrin-ECFP and EYFP-tagged podoplanin constructs. Cells selected in 0.5 mg/ml of G418 for 10 days were plated onto coverslips, fixed with 3.7% formaldehyde and mounted on Mowiol. The Rock inhibitor Y27632 (Calbiochem) and the cell permeable recombinant C3 transferase (Cytoskeleton) were added to the cell cultures at 5 μM and 2 μg/ml, respectively. For treatments with C3 transferase, a 0.1% concentration of serum was used in the cultures.

In vitro binding assay between ERM and GST fusion proteins

GST and GST fusion proteins were produced in *E. coli* BL21 cells as described (Sander et al., 1998). Pure dialyzed GST and GST fusion proteins were bound to CNBr-activated Sepharose (Amersham Pharmacia Biotech) according to the manufacturer's instructions. Approximately 1 nmol of pure dialyzed full-length ezrin or moesin and their respective N-ERMADs were mixed with 500 pmol of fusion proteins bound to Sepharose in a final volume of 500 μl of binding buffer (50 mM Tris-HCl pH 7.5, 1 mM $MgCl_2$, 100 mM NaCl, 0.4% Triton X-100), in the presence or absence of 50 μg/ml PIP2 (Sigma-Aldrich), and incubated for 30 minutes at room temperature. Beads were then washed six times in binding buffer, boiled in Laemmli buffer, and bound ERMs analyzed by western blotting.

Western blot analysis and antibodies

Cell lysates were obtained in RIPA buffer (0.1% SDS, 0.5% sodium deoxycholate, 1% NP-40, 150 mM NaCl, 50 mM Tris-HCl pH 7.5 and a cocktail of protease inhibitors) and analyzed by western blotting. Polyclonal antibodies against ezrin and moesin were kindly provided by Paul Mangeat; anti-phospho-ERM antibody was from Cell Signaling Technology; antibodies for RhoA and HA were from Santa Cruz Biotechnology; antibodies for EGFP, fibronectin, VSVG and α-tubulin (mAb DM1A) were from Sigma-Aldrich; mAbs for p120ctn, β-catenin (C19220), Rac1 and Cdc42 were from BD Biosciences; and mAbs for N-cadherin, vimentin and cytokeratin 8 from Zymed Laboratories, Dako and Progen, respectively. Horseradish-peroxidase-conjugated sheep anti-mouse (Amersham Biosciences), goat anti-rat (Pierce) and goat anti-rabbit (Nordic) IgGs were used as secondary antibodies.

Immunofluorescence analysis and time-lapse confocal microscopy

Detection of E-cadherin and β-catenin was performed on confluent cells grown on glass coverslips and fixed in cold methanol using mAbs 4A2C7 (Zymed) and C19220 (BD Biosciences), respectively. Detection of vimentin, fibronectin, ezrin, vinculin, RhoA, Rac1 and F-actin was performed in cells fixed with 3.7% formaldehyde in PBS and permeabilized with 0.05% Triton X-100. The mAb 3C12 (Sigma-Aldrich) was used for detection of ezrin. For F-actin staining, phalloidin coupled to Alexa Fluor 594 (Molecular Probes) was used. Secondary antibodies were Alexa Fluor 594-labeled anti-rabbit or anti-mouse IgGs (Molecular Probes). Staining of nuclei was performed in a 1 μg/ml solution of 4′,6-diamino-2-phenilindole (DAPI; Sigma-Aldrich). Confocal laser-scanning microscopy was performed in a Leica TCS-SP2 microscope (Leica Microsystems, Heidelberg, Germany). Images were taken using a 63× (NA 1.32) oil-immersion objective and assembled using Leica Confocal Software 2.0.

For in vivo podoplanin pre-embedding staining, subconfluent cells grown on glass coverslips were incubated in DMEM containing 25 mM HEPES and 1% BSA (buffer D) for 15 minutes, and stained with rabbit anti-podoplanin (Mart n-Villar et al., 2005) or rabbit anti-EGFP A11122 (Molecular Probes) antibodies at 1:100 dilution in buffer D for 1 hour at 4°C. Alexa Fluor 594-labeled anti-rabbit IgG (Molecular Probes) was used as secondary antibody. Coverslips were then fixed with 3.7% paraformaldehyde in buffer D, mounted on Mowiol and examined in a Leica TCS-SP2 confocal scanning laser microscope.

For time-lapse confocal microscopy, cells grown at low confluence on glass-bottom dishes (Lab-Tek® II) were maintained at 37°C in a 5% CO_2 atmosphere using an incubation system. Confocal series of fluorescence images (22 slices of 0.5 μm) were simultaneously obtained with a 63×/1.32 oil immersion objective every 10 minutes intervals for 4 hours. Images were processed and assembled into movies using the Leica Confocal Software 2.0 and Adobe Premiere Pro 1.5 software.

FRET by acceptor photobleaching

FRET was examined by the acceptor photobleaching method with EYFP-tagged podoplanin and ECFP-tagged ezrin incorporated into MDCK cells. A Leica TCS-SP2 confocal scanning laser microscope equipped with a 63×/1.32 oil-immersion lens was used. Energy transfer was detected as an increase in donor fluorescence (CFP) after photobleaching of the acceptor molecules (EYFP). ECFP and EYFP emission signals were collected before and after EYFP photobleaching by using the 458 nm or 514 nm laser lines, respectively. Images were background corrected and the $FRET_{eff}$ was calculated for each pixel from the increase of the donor fluorescence: $FRET_{eff}=(D_{post}-D_{pre})/D_{post}$; for all $D_{post}>D_{pre}$, where D_{pre} and D_{post} are the donor fluorescence intensities before and after acceptor photobleaching, respectively.

Wound healing assay and time-lapse video microscopy

The migratory behavior of cell transfectants was analyzed in an in vitro wound-healing assay, as described previously (Scholl et al., 1999). Wounded cell cultures were maintained at 37°C in a 5% CO_2 atmosphere using an incubation system. Images of the wounds were acquired every 10 minutes for 12 hours using a Zeiss Axiovert 135 TV inverted microscope equipped with a Digital JVC video camera. Quantification of migrated cells was done by measuring the number of pixels in the wounded area at different times using Adobe® Photoshop®. Images and videos were assembled using Analysis® 3.2 (Soft Imaging System) and Adobe Premiere Pro 1.5 software.

In vitro invasion assay

Cells (2.5×10^4) were suspended in 500 μl DMEM and loaded onto the upper compartment of BD BioCoat™ Matrigel™ Invasion Chamber (BD Biosciences). 5% FBS was used as a chemoattractant in the lower compartment. Cell invasion was analyzed by detection of EGFP using a Leica TCS-SP2 confocal microscope equipped with a 20×/0.70 and 63×/1.32 oil immersion lens. Fluorescence intensity profiles were obtained by image analysis using Leica Confocal Software 2.0.

RhoA, Rac1 and Cdc42 activity assays

The level of active RhoA (RhoA-GTP) in cell lysates was measured using a GST fusion protein with the RhoA-binding domain of Rhotekin (GST-C21). For Rac1 and Cdc42 activities, a GST fusion protein of the binding domain of PAK (GST-PAK) was used. Assays were performed as described by Sander and co-workers (Sander et al., 1998).

Statistics

Data are presented as mean ± s.e.m. Significance was determined using the Student's *t*-test. All statistical analyses were performed using GraphPad Prism 4.0 software.

We thank Francisco S nchez-Madrid, Piero Crespo and Paul Mangeat for their useful gifts of antibodies or plasmids. We also thank David Sarrio for his help with p120 ctn expression studies, Paloma Ord ez for her help with dominant-negative RhoA studies and Jaime Renart for critical reading of the manuscript. This work was supported by grants: SAF2004-04902 from the Ministry of Education and Science (MEC), GR/SAL/0871/2004 from the Autonomous Community of Madrid (CAM) and RTICCC CO3/10 from the 'Instituto de Salud Carlos III' (FIS) of Spain. E.M.-V. and M.M.Y. were the recipients of a postgraduate I3P fellowship from the Spanish Research Council (CSIC) and an MEC predoctoral fellowship, respectively.

References

Batlle, E., Sancho, E., Franci, C., Dominguez, D., Monfar, M., Baulida, J. and Garcia De Herreros, A. (2000). The transcription factor snail is a repressor of E-cadherin gene expression in epithelial tumour cells. *Nat. Cell Biol.* **2**, 84-89.

Bhowmick, N. A., Ghiassi, M., Bakin, A., Aakre, M., Lundquist, C. A., Engel, M. E., Arteaga, C. L. and Moses, H. L. (2001). Transforming growth factor-beta1 mediates epithelial to mesenchymal transdifferentiation through a RhoA-dependent mechanism. *Mol. Biol. Cell* **12**, 27-36.

Bissell, M. J. and Radisky, D. (2001). Putting tumours in context. *Nat. Rev. Cancer* **1**, 46-54.

Bol s, V., Peinado, H., Perez-Moreno, M. A., Fraga, M. F., Esteller, M. and Cano, A. (2003). The transcription factor Slug represses E-cadherin expression and induces epithelial to mesenchymal transitions: a comparison with Snail and E47 repressors. *J. Cell Sci.* **116**, 499-511.

Breiteneder-Geleff, S., Matsui, K., Soleiman, A., Meraner, P., Poczewski, H., Kalt, R., Schaffner, G. and Kerjaschki, D. (1997). Podoplanin, novel 43-kd membrane protein of glomerular epithelial cells, is down-regulated in puromycin nephrosis. *Am. J. Pathol.* **151**, 1141-1152.

Breiteneder-Geleff, S., Soleiman, A., Kowalski, H., Horvat, R., Amann, G., Kriehuber, E., Diem, K., Weninger, W., Tschachler, E., Alitalo, K. et al. (1999). Angiosarcomas express mixed endothelial phenotypes of blood and lymphatic capillaries: podoplanin as a specific marker for lymphatic endothelium. *Am. J. Pathol.* **154**, 385-394.

Bretscher, A., Edwards, K. and Fehon, R. G. (2002). ERM proteins and merlin: integrators at the cell cortex. *Nat. Rev. Mol. Cell Biol.* **3**, 586-599.

Brunton, V. G., MacPherson, I. R. and Frame, M. C. (2004). Cell adhesion receptors, tyrosine kinases and actin modulators: a complex three-way circuitry. *Biochim. Biophys. Acta* **1692**, 121-144.

Cano, A., Perez-Moreno, M. A., Rodrigo, I., Locascio, A., Blanco, M. J., del Barrio, M. G., Portillo, F. and Nieto, M. A. (2000). The transcription factor snail controls epithelial-mesenchymal transitions by repressing E-cadherin expression. *Nat. Cell Biol.* **2**, 76-83.

Cavallaro, U. and Christofori, G. (2004). Multitasking in tumor progression: signaling functions of cell adhesion molecules. *Ann. N. Y. Acad. Sci.* **1014**, 58-66.

Chu, A. Y., Litzky, L. A., Pasha, T. L., Acs, G. and Zhang, P. J. (2005). Utility of D2-40, a novel mesothelial marker, in the diagnosis of malignant mesothelioma. *Mod. Pathol.* **18**, 105-110.

Crepaldi, T., Gautreau, A., Comoglio, P. M., Louvard, D. and Arpin, M. (1997). Ezrin is an effector of hepatocyte growth factor-mediated migration and morphogenesis in epithelial cells. *J. Cell Biol.* **138**, 423-434.

Farooqui, R. and Fenteany, G. (2005). Multiple rows of cells behind an epithelial wound edge extend cryptic lamellipodia to collectively drive cell-sheet movement. *J. Cell Sci.* **118**, 51-63.

Gandarillas, A., Scholl, F. G., Benito, N., Gamallo, C. and Quintanilla, M. (1997). Induction of PA2.26, a cell-surface antigen expressed by active fibroblasts, in mouse epidermal keratinocytes during carcinogenesis. *Mol. Carcinog.* **20**, 10-18.

Golub, T. and Caroni, P. (2005). PI(4,5)P2-dependent microdomain assemblies capture microtubules to promote and control leading edge motility. *J. Cell Biol.* **169**, 151-165.

Gotzmann, J., Mikula, M., Eger, A., Schulte-Hermann, R., Foisner, R., Beug, H. and Mikulits, W. (2004). Molecular aspects of epithelial cell plasticity: implications for local tumor invasion and metastasis. *Mutat. Res.* **566**, 9-20.

Hirao, M., Sato, N., Kondo, T., Yonemura, S., Monden, M., Sasaki, T., Takai, Y., Tsukita, S. and Tsukita, S. (1996). Regulation mechanism of ERM (ezrin/radixin/moesin) protein/plasma membrane association: possible involvement of phosphatidylinositol turnover and Rho-dependent signaling pathway. *J. Cell Biol.* **135**, 37-51.

Ivetic, A. and Ridley, A. J. (2004). Ezrin/radixin/moesin proteins and Rho GTPase signalling in leucocytes. *Immunology* **112**, 165-176.

Kaneko, M. K., Kato, Y., Kitano, T. and Osawa, M. (2006). Conservation of a platelet activating domain of Aggrus/podoplanin as a platelet aggregation-inducing factor. *Gene* **378**, 52-57.

Kato, Y., Fujita, N., Kunita, A., Sato, S., Kaneko, M., Osawa, M. and Tsuruo, T. (2003). Molecular identification of Aggrus/T1alpha as a platelet aggregation-inducing factor expressed in colorectal tumors. *J. Biol. Chem.* **278**, 51599-51605.

Kato, Y., Sasagawa, I., Kaneko, M., Osawa, M., Fujita, N. and Tsuruo, T. (2004). Aggrus: a diagnostic marker that distinguishes seminoma from embryonal carcinoma in testicular germ cell tumors. *Oncogene* **23**, 8552-8556.

Kato, Y., Kaneko, M., Sata, M., Fujita, N., Tsuruo, T. and Osawa, M. (2005). Enhanced expression of Aggrus (T1alpha/podoplanin), a platelet-aggregation-inducing factor in lung squamous cell carcinoma. *Tumour Biol.* **26**, 195-200.

Kotani, M., Tajima, Y., Osanai, T., Irie, A., Iwatsuki, K., Kanai-Azuma, M., Imada, M., Kato, H., Shitara, H., Kubo, H. et al. (2003). Complementary DNA cloning and characterization of RANDAM-2, a type I membrane molecule specifically expressed on glutamatergic neuronal cells in the mouse cerebrum. *J. Neurosci. Res.* **73**, 603-613.

Legg, J. W. and Isacke, C. M. (1998). Identification and functional analysis of the ezrin-binding site in the hyaluronan receptor, CD44. *Curr. Biol.* **8**, 705-708.

Lozano, E., Betson, M. and Braga, V. M. (2003). Tumor progression: small GTPases and loss of cell-cell adhesion. *BioEssays* **25**, 452-463.

Mart n-Villar, E., Scholl, F. G., Gamallo, C., Yurrita, M. M., Munoz-Guerra, M., Cruces, J. and Quintanilla, M. (2005). Characterization of human PA2.26 antigen (T1alpha-2, podoplanin), a small membrane mucin induced in oral squamous cell carcinomas. *Int. J. Cancer* **113**, 899-910.

Matsubayashi, Y., Ebisuya, M., Honjoh, S. and Nishida, E. (2004). ERK activation propagates in epithelial cell sheets and regulates their migration during wound healing. *Curr. Biol.* **14**, 731-735.

Matsui, T., Maeda, M., Doi, Y., Yonemura, S., Amano, M., Kaibuchi, K. and Tsukita, S. (1998). Rho-kinase phosphorylates COOH-terminal threonines of ezrin/radixin/moesin (ERM) proteins and regulates their head-to-tail association. *J. Cell Biol.* **140**, 647-657.

Peinado, H., Quintanilla, M. and Cano, A. (2003). Transforming growth factor beta-1 induces snail transcription factor in epithelial cell lines: mechanisms for epithelial mesenchymal transitions. *J. Biol. Chem.* **278**, 21113-21123.

Perschl, A., Lesley, J., English, N., Hyman, R. and Trowbridge, I. S. (1995). Transmembrane domain of CD44 is required for its detergent insolubility in fibroblasts. *J. Cell Sci.* **108**, 1033-1041.

Ramirez, M. I., Millien, G., Hinds, A., Cao, Y., Seldin, D. C. and Williams, M. C. (2003). T1alpha, a lung type I cell differentiation gene, is required for normal lung cell proliferation and alveolus formation at birth. *Dev. Biol.* **256**, 61-72.

Ridley, A. J. (2001). Rho GTPases and cell migration. *J. Cell Sci.* **114**, 2713-2722.

Rishi, A. K., Joyce-Brady, M., Fisher, J., Dobbs, L. G., Floros, J., VanderSpek, J., Brody, J. S. and Williams, M. C. (1995). Cloning, characterization, and development expression of a rat lung alveolar type I cell gene in embryonic endodermal and neural derivatives. *Dev. Biol.* **167**, 294-306.

Sahai, E. and Marshall, C. J. (2002a). RHO-GTPases and cancer. *Nat. Rev. Cancer* **2**, 133-142.

Sahai, E. and Marshall, C. J. (2002b). ROCK and Dia have opposing effects on adherens junctions downstream of Rho. *Nat. Cell Biol.* **4**, 408-415.

Sander, E. E., van Delft, S., ten Klooster, J. P., Reid, T., van der Kammen, R. A., Michiels, F. and Collard, J. G. (1998). Matrix-dependent Tiam1/Rac signaling in epithelial cells promotes either cell-cell adhesion or cell migration and is regulated by phosphatidylinositol 3-kinase. *J. Cell Biol.* **143**, 1385-1398.

Sander, E. E., ten Klooster, J. P., van Delft, S., van der Kammen, R. A. and Collard, J. G. (1999). Rac downregulates Rho activity: reciprocal balance between both GTPases determines cellular morphology and migratory behavior. *J. Cell Biol.* **147**, 1009-1022.

Sarrio, D., Perez-Mies, B., Hardisson, D., Moreno-Bueno, G., Suarez, A., Cano, A., Martin-Perez, J., Gamallo, C. and Palacios, J. (2004). Cytoplasmic localization of p120ctn and E-cadherin loss characterize lobular breast carcinoma from preinvasive to metastatic lesions. *Oncogene* **23**, 3272-3283.

Schacht, V., Ramirez, M. I., Hong, Y. K., Hirakawa, S., Feng, D., Harvey, N., Williams, M., Dvorak, A. M., Dvorak, H. F., Oliver, G. et al. (2003). T1alpha/podoplanin deficiency disrupts normal lymphatic vasculature formation and causes lymphedema. *EMBO J.* **22**, 3546-3556.

Schacht, V., Dadras, S. S., Johnson, L. A., Jackson, D. G., Hong, Y. K. and Detmar, M. (2005). Up-regulation of the lymphatic marker podoplanin, a mucin-type transmembrane glycoprotein, in human squamous cell carcinomas and germ cell tumors. *Am. J. Pathol.* **166**, 913-921.

Scholl, F. G., Gamallo, C., Vilar , S. and Quintanilla, M. (1999). Identification of PA2.26 antigen as a novel cell-surface mucin-type glycoprotein that induces plasma membrane extensions and increased motility in keratinocytes. *J. Cell Sci.* **112**, 4601-4613.

Scholl, F. G., Gamallo, C. and Quintanilla, M. (2000). Ectopic expression of PA2.26 antigen in epidermal keratinocytes leads to destabilization of adherens junctions and malignant progression. *Lab. Invest.* **80**, 1749-1759.

Takahashi, K., Sasaki, T., Mammoto, A., Takaishi, K., Kameyama, T., Tsukita, S. and Takai, Y. (1997). Direct interaction of the Rho GDP dissociation inhibitor with ezrin/radixin/moesin initiates the activation of the Rho small G protein. *J. Biol. Chem.* **272**, 23371-23375.

Takahashi, K., Sasaki, T., Mammoto, A., Hotta, I., Takaishi, K., Imamura, H., Nakano, K., Kodama, A. and Takai, Y. (1998). Interaction of radixin with Rho small G protein GDP/GTP exchange protein Dbl. *Oncogene* **16**, 3279-3284.

Thiery, J. P. (2002). Epithelial-mesenchymal transitions in tumour progression. *Nat. Rev. Cancer* **2**, 442-454.

Tsukita, S. and Yonemura, S. (1999). Cortical actin organization: lessons from ERM(ezrin/radixin/moesin) proteins. *J. Biol. Chem.* **274**, 34507-34510.

Wetterwald, A., Hoffstetter, W., Cecchini, M. G., Lanske, B., Wagner, C., Fleisch, H. and Atkinson, M. (1996). Characterization and cloning of the E11 antigen, a marker expressed by rat osteoblasts and osteocytes. *Bone* **18**, 125-132.

Wicki, A., Lehembre, F., Wick, N., Hanfusch, B., Kerjaschki, D. and Christofori, G. (2006). Tumor invasion in the absence of epithelial-mesenchymal transition: podoplanin-mediated remodelling of the actin cytoskeleton. *Cancer Cell* **9**, 261-272.

Williams, M. C., Cao, Y., Hinds, A., Rishi, A. K. and Wetterwald, A. (1996). T1 alpha protein is developmentally regulated and expressed by alveolar type I cells, choroid plexus, and ciliary epithelia of adult rats. *Am. J. Respir. Cell Mol. Biol.* **14**, 577-585.

Yin, H. L. and Janmey, P. A. (2003). Phosphoinositide regulation of the actin cytoskeleton. *Annu. Rev. Physiol.* **65**, 761-789.

Yonemura, S., Hirao, M., Doi, Y., Takahashi, N., Kondo, T., Tsukita, S. and Tsukita, S. (1998). Ezrin/radixin/moesin (ERM) proteins bind to a positively charged amino acid cluster in the juxta-membrane cytoplasmic domain of CD44, CD43, and ICAM-2. *J. Cell Biol.* **140**, 885-895.

Yu, Y., Khan, J., Khanna, C., Helman, L., Meltzer, P. S. and Merlino, G. (2004). Expression profiling identifies the cytoskeletal organizer ezrin and the developmental homeoprotein Six-1 as key metastatic regulators. *Nat. Med.* **10**, 175-181.

Zimmer, G., Oeffner, F., Von Messling, V., Tschernig, T., Groness, H. J., Klenk, H. D. and Herrler, G. (1999). Cloning and characterization of gp36, a human mucin-type glycoprotein preferentially expressed in vascular endothelium. *Biochem. J.* **341**, 277-284.

Zondag, G. C., Evers, E. E., ten Klooster, J. P., Janssen, L., van der Kammen, R. A. and Collard, J. G. (2000). Oncogenic Ras downregulates Rac activity, which leads to increased Rho activity and epithelial-mesenchymal transition. *J. Cell Biol.* **149**, 775-782.

nature cell biology

AMPK and PFKFB3 mediate glycolysis and survival in response to mitophagy during mitotic arrest

Elena Domènech[1], Carolina Maestre[1], Lorena Esteban-Martínez[2], David Partida[1], Rosa Pascual[3], Gonzalo Fernández-Miranda[3], Esther Seco[2], Ramón Campos-Olivas[4], Manuel Pérez[5], Diego Megias[5], Katherine Allen[6], Miguel López[7,8], Asish K. Saha[6], Guillermo Velasco[9], Eduardo Rial[10], Raúl Méndez[3], Patricia Boya[2], María Salazar-Roa[1,11] and Marcos Malumbres[1,11]

Blocking mitotic progression has been proposed as an attractive therapeutic strategy to impair proliferation of tumour cells. However, how cells survive during prolonged mitotic arrest is not well understood. We show here that survival during mitotic arrest is affected by the special energetic requirements of mitotic cells. Prolonged mitotic arrest results in mitophagy-dependent loss of mitochondria, accompanied by reduced ATP levels and the activation of AMPK. Oxidative respiration is replaced by glycolysis owing to AMPK-dependent phosphorylation of PFKFB3 and increased production of this protein as a consequence of mitotic-specific translational activation of its mRNA. Induction of autophagy or inhibition of AMPK or PFKFB3 results in enhanced cell death in mitosis and improves the anti-tumoral efficiency of microtubule poisons in breast cancer cells. Thus, survival of mitotic-arrested cells is limited by their metabolic requirements, a feature with potential implications in cancer therapies aimed to impair mitosis or metabolism in tumour cells.

Chromosome segregation requires a marked reorganization of cellular structures including centrosome duplication and generation of the microtubule spindle, disassembly of the Golgi apparatus, breakdown of the nuclear envelope and chromosome condensation. At this stage, transcription is strongly suppressed, translation is limited to a subset of messenger RNAs, and the absence of the nuclear envelope temporally maintains on hold multiple regulatory mechanisms that are based on the separation of the nuclear and cytoplasmic compartments[1]. Progression through mitosis is monitored by the spindle assembly checkpoint (SAC), a regulatory pathway that delays mitotic exit until all chromosomes are bipolarly attached to the spindle[2,3]. The target of the SAC is the anaphase-promoting complex/cyclosome (APC/C), an E3 ubiquitin ligase that, when activated by Cdc20, targets for degradation the separase inhibitor securin, and the Cdk1 activatory subunit cyclin B. Stable bipolar attachment of chromosomes satisfies the SAC releasing APC/C–Cdc20 inhibition and resulting in Cdk1 inhibition and activation of separase, thus leading to chromosome segregation and the reformation of two new nuclei[4,5].

Disruption of the mechanisms that regulate the proper attachment of chromosomes to the bipolar spindle results in mitotic arrest in a SAC-dependent manner. Thus, inhibition of mitotic kinases such as Aurora A or Plk1, or treatment of cells with microtubule poisons that disrupt the proper dynamics of the spindle, results in mitotic arrest, a feature that may be used to prevent tumour cell proliferation. Yet, the success of mitotic-targeted therapies is limited by the low mitotic index of human tumours, and mitotic slippage; that is, the ability of cells to exit from mitosis in the presence of mitotic blockers[6,7]. As mitotic slippage is APC/C–Cdc20-dependent[8], targeting the mitotic exit machinery has been proposed as an efficient method to prevent resistance to anti-mitotic drugs[8–11].

Although death in mitosis is at least partially mediated by apoptosis, the molecular pathways that control survival or death in mitosis are not well understood[12,13]. Here we show that death in mitosis is modulated by the energetic balance that counteracts the loss of mitochondrial mass during mitotic arrest. Using Cdc20-knockout cells or human cells treated with microtubule poisons, we describe here that

[1]Cell Division and Cancer Group, Spanish National Cancer Research Centre (CNIO), Madrid 28029, Spain. [2]Department of Cellular and Molecular Biology, Centro de Investigaciones Biológicas, CSIC, E-28040 Madrid, Spain. [3]ICREA and Institute for Research in Biomedicine (IRB), Barcelona 08028, Spain. [4]Spectroscopy and Nuclear Magnetic Resonance Unit, CNIO, Madrid 28029, Spain. [5]Confocal Microscopy Unit, CNIO, Madrid 28029, Spain. [6]Division of Endocrinology, Diabetes & Nutrition, Boston University School of Medicine, Boston, Massachusetts 02215, USA. [7]Department of Physiology, CIMUS, University of Santiago de Compostela-Instituto de Investigación Sanitaria, Santiago de Compostela 15782, Spain. [8]CIBER Fisiopatología de la Obesidad y Nutrición (CIBERobn), 15706, Spain. [9]Department of Biochemistry and Molecular Biology I, School of Biology, Complutense University, and Instituto de Investigaciones Sanitarias San Carlos (IdISSC), 28040 Madrid, Spain. [10]Department of Cellular and Molecular Medicine, Centro de Investigaciones Biológicas, CSIC, E-28040 Madrid, Spain.
[11]Correspondence should be addressed to M.S.-R. or M.M. (e-mail: msalazar@cnio.es or malumbres@cnio.es)

Received 8 August 2014; accepted 24 July 2015; published online 31 August 2015; DOI: 10.1038/ncb3231

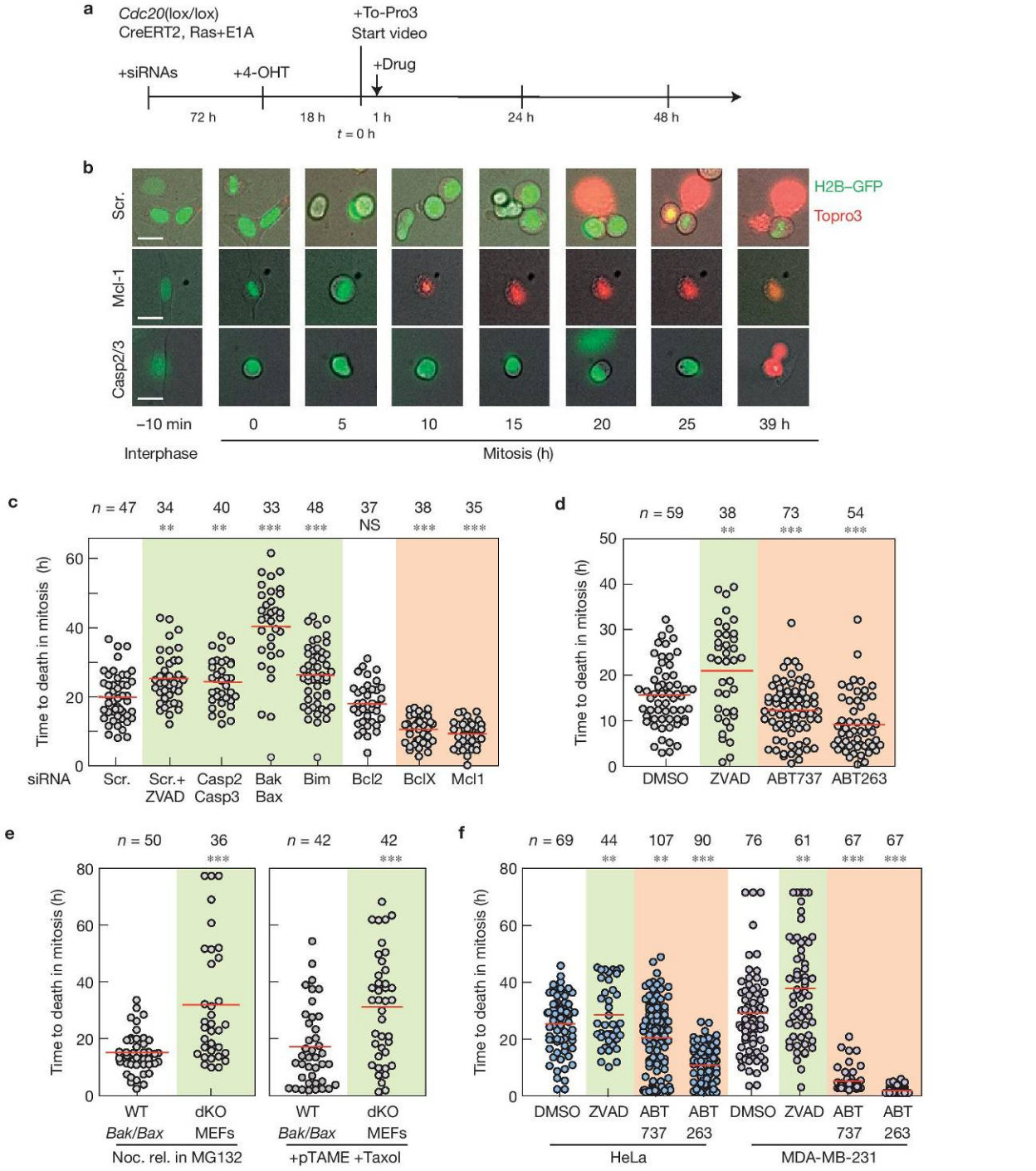

Figure 1 MCD is modulated by the intrinsic apoptotic pathway. (**a**) Protocol used for time-lapse microscopy in Cdc20-deficient cells. Ras/E1A-transformed *Cdc20*(lox/lox); CreERT2 cells were nucleofected with siRNAs, seeded at low density and treated with 4-OHT 18 h before starting the video in the presence of TO-PRO3 or other chemicals. (**b**) Representative micrographs of Cdc20-deficient (*Cdc20*(Δ/Δ)) cells after the indicated periods of mitotic arrest (h after chromosome condensation and cell rounding) in the presence of siRNAs against Mcl1 or caspase 2 and 3. Scale bars, 10 μm. (**c**) Plots representing the duration of mitosis (from mitotic entry until cell death) in Cdc20-null cells treated with the indicated siRNAs (Scr., scrambled sequences) or in the presence of the caspase inhibitor ZVAD. (**d**) Duration of mitosis (from metaphase until cell death) in Cdc20-null cells treated with caspase or Bcl-2 family inhibitors. (**e**) Duration of mitosis (from metaphase until cell death) in Bax/Bak-null and control MEFs. Cells were synchronized in prometaphase for 12 h with nocodazole, and released in the presence of the proteasome inhibitor MG132 (left panel); or synchronized in G_2 for 18 h with the Cdk1 inhibitor RO-3306 (5 μM) and released in the presence of Taxol (300 nM) and the APC/C inhibitor proTAME (10 μM; right panel). (**f**) Duration of mitosis in human cell lines cells treated with caspase inhibitors or the indicated Bcl-2 family inhibitors. In **c**–**f**, dots represent individual cells and the mean is indicated by red lines. The number of cells analysed (*n*) is indicated in each condition, and data in every panel represent 1 out of 6 independent experiments. Green or orange backgrounds indicate a significant delay or premature cell death in mitosis, respectively. NS, not significant. $^{**}P < 0.01$; $^{***}P < 0.001$ (Student's *t*-test). Source data can be found in Supplementary Table 4.

the presence of autophagy during mitotic arrest is accompanied by a gradual decline in the mitochondrial mass and oxidative respiration. This results in the activation of AMPK and the subsequent induction of glycolysis in a PFKFB3-dependent manner. Inhibition of these energetic pathways in breast cancer cells prevents mitotic slippage and results in accelerated death of mitotic cells, thus potentiating the therapeutic effect of microtubule poisons used at present in the clinic.

RESULTS

Mitotic death is modulated by the intrinsic apoptotic pathway

To analyse the molecular pathways modulating cell viability in mitosis we used Cdc20 conditional-knockout fibroblasts in which Cdc20 is excised on treatment with 4-hydroxytamoxifen (4-OHT; ref. 8). These cells exhibit normal mitotic entry but mitotic exit is prevented owing to the lack of cyclin B1 degradation. Mitotic cell death (MCD) can be observed in these cells by time-lapse microscopy using TO-PRO3, a dye that is internalized into the cells on the permeabilization of membranes that precedes cell death (Fig. 1a,b). *Cdc20*(Δ/Δ) cells exhibit a variable survival in mitosis (SiM, time since mitotic entry until cell death) of 22 ± 14 h (Fig. 1b,c). No *Cdc20*(Δ/Δ) cell was able to exit from the mitotic arrest suggesting that this APC/C cofactor is essential for mitotic slippage.

To test the relevance of apoptosis in MCD, we transfected these cells with small interfering (si)RNAs (Supplementary Fig. 1a) against several apoptotic regulators following the protocol depicted in Fig. 1a. Knockdown of Mcl1, an anti-apoptotic regulator of the Bcl2 family involved in the response to Taxol[14,15], or BclX resulted in earlier MCD whereas knockdown of caspases 2 and 3, as well as Bax and Bak, significantly delayed MCD (Fig. 1b,c). The involvement of the apoptotic machinery was also validated using the pan-caspase inhibitor ZVAD (Fig. 1c,d and Supplementary Fig. 1b,c) or two different inhibitors of the Bcl2 family (Fig. 1d). SiM was improved with ZVAD and significantly decreased with the two Bcl2 family inhibitors (Fig. 1d), being more pronounced in the case of ABT-263, perhaps as a consequence of the more potent effect of this compound against Mcl1 (ref. 16). We also used Bax/Bak double-knockout cells in which the intrinsic apoptotic pathway is totally inhibited[17]. To mimic the metaphase arrest caused by Cdc20 ablation, cells were released from a nocodazole-induced prometaphase arrest in the presence of the proteasome inhibitor MG132 or arrested in the presence of the APC/C inhibitor proTAME, which is known to prevent cyclin B degradation and mitotic exit in the presence of Taxol[18] (Fig. 1e). Yet, all cells died in mitosis in these conditions in the presence of necrotic figures (Supplementary Fig. 1d). Similar data were obtained in human cancer cells (HeLa or MDA-MB-231) when arrested with MG132 or proTAME+Taxol (Fig. 1f and Supplementary Fig. 1e).

Autophagy modulates survival during mitotic arrest

Although autophagy has been previously found to be inhibited during mitosis[19], we tested the changes in this process during prolonged mitotic arrest. Cdc20-null cells were first synchronized in G_2 using the Cdk1 inhibitor RO-3306 and mitotic entry and progression were monitored after release from this compound (Fig. 2a and Supplementary Fig. 2a). The autophagic flux was first scored by monitoring the accumulation of the lipidated and autophagosome-associated form of LC3 (LC3-II). This isoform was augmented in *Cdc20*(Δ/Δ) (Fig. 2b) and human cancer cells (Supplementary Fig. 2b) as early as 3 h after mitotic arrest. Incubation during mitotic arrest with E64d (a calpain and cathepsin B inhibitor) and pepstatin A (PA, an inhibitor of aspartic proteases), which block the last steps of autophagic degradation, enhanced accumulation of LC3-II, confirming the presence of a dynamic autophagy flux during mitosis. We also used a fluorescent-tagged LC3 sensor in which the pH sensitivity differences exhibited by GFP (green fluorescent protein) and mRFP (red fluorescent protein) can monitor progression from the autophagosome to autolysosome[20]. Whereas autophagosomes emit both mRFP and GFP signals (yellow in overlaid images), autolysosomes emit only an acid-stable mRFP signal in these acidic lysosomes. Autophagy was increased during prolonged mitotic arrest in comparison with normal mitosis in asynchronous cultures (Fig. 2c). Autophagy was significantly prevented in the presence of the class III PI(3)K inhibitor 3-methyladenine (3MA), and increased on treatment with the mTOR inhibitor PP242, confirming the dynamic autophagic flux in mitotic cells. The presence of double-membrane structures with the morphological features of autophagosomes was also verified using electron microscopy (Fig. 2d). About 10–20% of *Cdc20*(Δ/Δ) mitotic cells were positive for both apoptotic and autophagy signals, suggesting the coexistence of these pathways in the same cells (Supplementary Fig. 2c).

We then tested whether autophagy was able to modulate MCD on downregulation of several autophagy regulators (Supplementary Fig. 2d). Knockdown of Raptor, a member and positive regulator of the mTOR complex 1 that inhibits autophagy, resulted in earlier death in mitosis whereas downregulation of Ulk1, Vps34 or Beclin1 prevented MCD to a similar extent to the apoptosis inhibitor ZVAD (Fig. 2e). The requirements for autophagy in MCD were also validated during mitotic arrest in Atg5-null cells (Fig. 2f). Induction of autophagy by inhibitors of the PI(3)K–Akt–mTOR pathway resulted in premature MCD in Cdc20-null or mitotic human cells (Supplementary Fig. 2e–i), whereas 3MA delayed death in mitosis to a similar extent to ZVAD (Fig. 2g). Yet, concomitant inhibition of apoptosis and autophagy using a combination of ZVAD and 3MA did not further enhance SiM and all Cdc20-null cells eventually died in the presence of these two inhibitors (Fig. 2g). Similarly, inhibition of autophagy in Bax/Bak double mutant cells, or inhibition of apoptosis in Atg5-deficient cells resulted in significant delays in MCD but did not prevent cell death (Supplementary Fig. 2j). Finally, whereas caspase inhibition did not prevent LC3 lipidation, treatment of cells with E64d/PA inhibited poly(ADP-ribose) polymerase (PARP-1) cleavage (Supplementary Fig. 2k), suggesting a pro-apoptotic activity for autophagy in mitotic-arrested cells.

Mitophagy leads to loss of mitochondria during mitotic arrest

The cellular mitochondrial mass is tightly regulated by a balance between biosynthesis and the removal of old mitochondria by a specific autophagy process known as mitophagy[21,22]. As protein synthesis is limited during mitosis owing to the lack of proper transcription and translation, we next tested whether mitotic arrest was accompanied by mitochondrial loss. In fact, the cellular mitochondrial content started to decrease a few hours after mitotic arrest in Cdc20-null cells (Supplementary Fig. 3a), as detected by time-lapse microscopy (Fig. 3a) and flow cytometry (Fig. 3b), using a mitochondrial dye resistant to loss of membrane potential

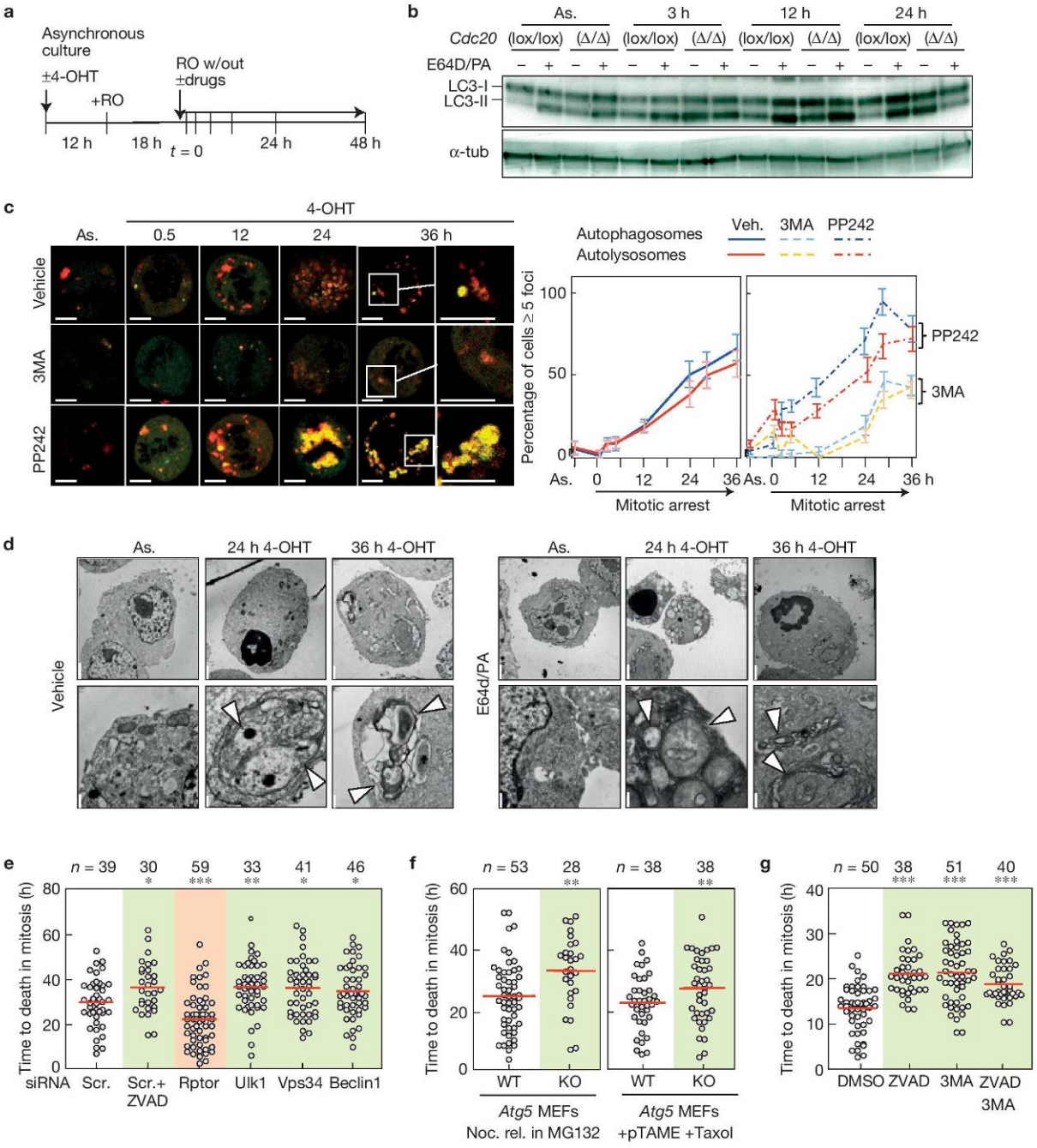

Figure 2 Autophagy modulates cell death during mitotic arrest. (**a**) Protocol for synchronized entry into mitosis in *Cdc20*(Δ/Δ) cells. *Cdc20*(lox/lox) cells were first treated with 4-OHT, Cdk1 was then inhibited with RO-3306 during 18 h for G_2 arrest, and cells were released for synchronous entry into mitosis (see also Supplementary Fig. 2). (**b**) Immunodetection of LC3-I and LC3-II (lipidated form) either in the absence or presence of the cathepsin inhibitors E64d and PA in *Cdc20*(lox/lox) and *Cdc20*(Δ/Δ) cells at different time points. As., asynchronous cultures. α-tubulin was used as a loading control. Unprocessed original scans of blots are shown in Supplementary Fig. 7. (**c**) Live confocal microscopy pictures of Cdc20-null cells transiently expressing the LC3 reporter system in the presence of an mTOR inhibitor (PP242) and the autophagy inhibitor 3MA. Quantification of the autophagic flux (at least 5 puncta per cell) in asynchronous (As.) cultures or at the indicated times after release from the G_2 arrest. Data are represented as mean ± s.e.m. ($n = 30$ cells per point). Scale bars, 5 μm. (**d**) Electron micrographs showing the presence of autophagosomes characterized by double membranes (arrowheads) in asynchronous cultures (As.) or mitotic Cdc20-null cells after release from G_2, either in the absence or presence of E64d/PA. Scale bars, 2 μm and 500 nm for low- and high-magnification images, respectively. (**e**) Duration of mitosis (from mitotic entry until cell death) in Cdc20-null cells transfected with the indicated interfering RNAs or in the presence of the caspase inhibitor ZVAD. (**f**) Duration of mitosis in Atg5-null and control MEFs synchronized following the protocols described in Fig. 1e. (**g**) Duration of mitosis in Cdc20-null cells treated with caspase and/or autophagy inhibitors. In **b**,**c**,**d** data represent 1 out of 3 independent experiments. In **e**–**g**, dots represent individual cells and the mean is indicated by red lines. The number of cells analysed (n) is indicated in each condition and data represent 1 out of 6 independent experiments. Green or orange backgrounds indicate a significant delay or premature cell death in mitosis. $^{*}P < 0.05$; $^{**}P < 0.01$; $^{***}P < 0.001$ (Student's t-test). Source data can be found in Supplementary Table 4.

(Mitotracker deep red FM). Exposure of mitotic cells to carbonyl cyanide *m*-chlorophenyl hydrazine (CCCP), a classical inducer of mitophagy, resulted in decreased mitochondrial signal during the first few hours after mitotic arrest (Fig. 3b,c). Immunodetection of the mitochondrial proteins Tom20, Tim23, Tom40 or Parkin1 corroborated the loss of mitochondrial mass during mitotic arrest in Cdc20-null cells and this effect was prevented when the lysosomal function was inhibited with E64d/PA (Fig. 3d).

The decrease in mitochondrial content was accompanied by a gradual co-localization of LC3 in the mitochondria suggesting the presence of mitophagy (Fig. 3e). In fact, the formation of autophagosomes affecting mitochondria was evident as early as 6 h after mitotic arrest and these organelles were frequently found within the autophagosomes at later stages (Fig. 3f). Prevention of mitophagy or lysosomal function with 3MA, or exposure to cyclosporin A (CsA), a blocker of the opening of mitochondrial permeability transition pores, significantly prevented loss of mitochondrial mass (Fig. 3g) and mitochondrial markers in mitotic cells (Supplementary Fig. 3b,c). In line with these observations, loss of mitochondrial function in Cdc20-null cells or cells arrested in mitosis with proTAME and Taxol was accompanied by increased reactive oxygen species, and the inhibition of this process resulted in a delayed cell death both in mouse and human cells (Supplementary Fig. 3d–f).

During mitosis, mitochondria are fragmented to facilitate segregation of this organelle to daughter cells[1]. Whereas elongated mitochondria are spared from autophagic degradation[23,24], fragmentation of this organelle facilitates the uptake by autophagosomes owing to their smaller size[25,26]. Mitochondrial fission is mediated by Cdk1-dependent phosphorylation and activation of the dynamin-like protein Drp1 (ref. 27). As depicted in Fig. 3h, knockdown of Drp1 by siRNAs in Cdc20-null cells prevented fragmentation of mitochondria and Drp1-siRNA-treated cells exhibited longer tubular organelles during mitosis. Knockdown of Drp1 also resulted in reduced co-localization of mitophagy markers in mitochondria (Fig. 3i), prevented loss of mitochondrial mass (Fig. 3j) and led to delayed MCD in Cdc20-deficient cells (Fig. 3k), in agreement with the relevance of maintaining the proper level of mitochondrial mass to prevent cell death in mitosis.

AMPK promotes glycolysis during mitotic arrest

We next investigated the functional relevance of mitochondrial loss during mitosis by studying the rates of mitochondrial respiration (oxygen consumption, OCR) and glycolysis (extracellular acid release; ECAR). *Cdc20*(Δ/Δ) cells were arrested in G_2 using RO-3306 for 18 h and released to arrest in mitosis (red) in a synchronized manner. G_2-synchronized (blue) or asynchronous (green) *Cdc20*(lox/lox) cells were used as controls (Fig. 4a). OCR quickly increased on mitotic entry in agreement with recent data indicating the activation of the oxidative respiration during the G_2/M transition in a Cdk1-dependent manner[28]. However, the respiratory capacity became extenuated after ~12 h in mitosis (Fig. 4b). ECAR levels gradually increased during mitosis but were further augmented during late mitotic arrest in parallel with the loss of oxidative respiration both in mouse (Fig. 4b) and human (Fig. 4c) cells.

In these cells, mitotic arrest was accompanied by a progressive activation of AMPK as detected by increased AMPK phosphorylation at its activation loop both in Cdc20-null (Fig. 4d) and human cells (Supplementary Fig. 4a,b). Time-lapse microscopy assays using an AMPK biosensor[29] (Supplementary Fig. 4c,d) showed that AMPK was gradually activated after ~8 h of mitotic arrest but not during a normal mitosis/G_1 transition in control cells (Fig. 4e). G_2-arrested cells exhibited increased phosphorylation of AMPK (Fig. 4d) in agreement with increased AMP/ATP levels (black versus green in Fig. 4f). This defect is possibly a consequence of Cdk1 inactivation by RO-3306 given the crucial role of Cdk1 in activating mitochondrial function during the G_2/M transition[28]. In *Cdc20*(Δ/Δ) cells, the AMP/ATP ratio exhibited a new gradual increase ~8 h after mitotic arrest (red in Fig. 4f) in agreement with the timing of AMPK activation (Fig. 4d).

Quantification of extracellular metabolites indicated that mitotic arrest resulted in a significantly higher consumption of glucose and generation of lactate (Fig. 4g, red), suggesting glycolytic flux, as compared with G_2-released, non-arrested cells (blue) or asynchronous cultures (green). Mitotic arrest in Cdc20-null cells was also accompanied by a significant consumption of multiple amino acids, whereas alanine, glutamic acid and glycine were released to the extracellular medium (Supplementary Fig. 5a–d). The AMPK-dependent increase in glucose uptake and generation of lactate was also observed in human cells treated with microtubule poisons and APC/C inhibitors to prevent mitotic exit (Supplementary Fig. 5e,f). These changes were reduced after knockdown of both AMPKα1 and AMPKα2 (Supplementary Fig. 4e and Fig. 4h), suggesting the involvement of AMPK in the glycolytic induction observed in mitotic cells. Silencing of both AMPK isoforms also partially rescued the decrease in OCR and the increase in ECAR (Supplementary Fig. 4f), as well as loss of mitochondrial mass (Supplementary Fig. 4g), in agreement with a role for this kinase in the regulation of these processes[30].

Glycolysis is a major determinant of survival in mitosis

The activation of AMPK and the subsequent glycolytic switch observed in mitotic cells raised the possibility of a dependence on energy pathways to survive in mitosis. Treatment of mitotic cells with the AMPK inhibitor Compound C resulted in reduced SiM in mitotic Cdc20-null cells (Fig. 5a) or human cell lines (Fig. 5b). Furthermore, addition of two different glycolytic poisons, 2-deoxy-D-glucose (2-DG; a glucose analogue that cannot be metabolized) or oxamate (an isosteric and isoelectronic inhibitory analogue of pyruvate), also resulted in premature MCD; whereas supplementation of media with glucose led to a significant increase in SiM (Fig. 5c).

The relevance of the glycolytic pathway was directly addressed by studying 6-phosphofructo-2-kinase/fructose-2,6-bisphosphatase 3 (PFKFB3), a key regulator of the glycolytic enzyme phosphofructokinase-1 (PFK1) that is frequently overexpressed in cancer cells. PFKFB3 is known to be regulated by AMPK and p38MAPK in a phosphorylation-dependent manner in cancer cells[31,32]. As depicted in Fig. 5d, serine-dependent phosphorylation of PFKFB3 was increased during mitosis in an AMPK-dependent manner because it was prevented by Compound C, but not by SB203580, an inhibitor of p38MAPK. Using mass spectrometry, we found a significant increase in the phosphorylation of PFKFB3 Ser 461 during mitosis. This phosphorylation was reduced in the presence of Compound C, suggesting an AMPK-dependent phosphorylation of

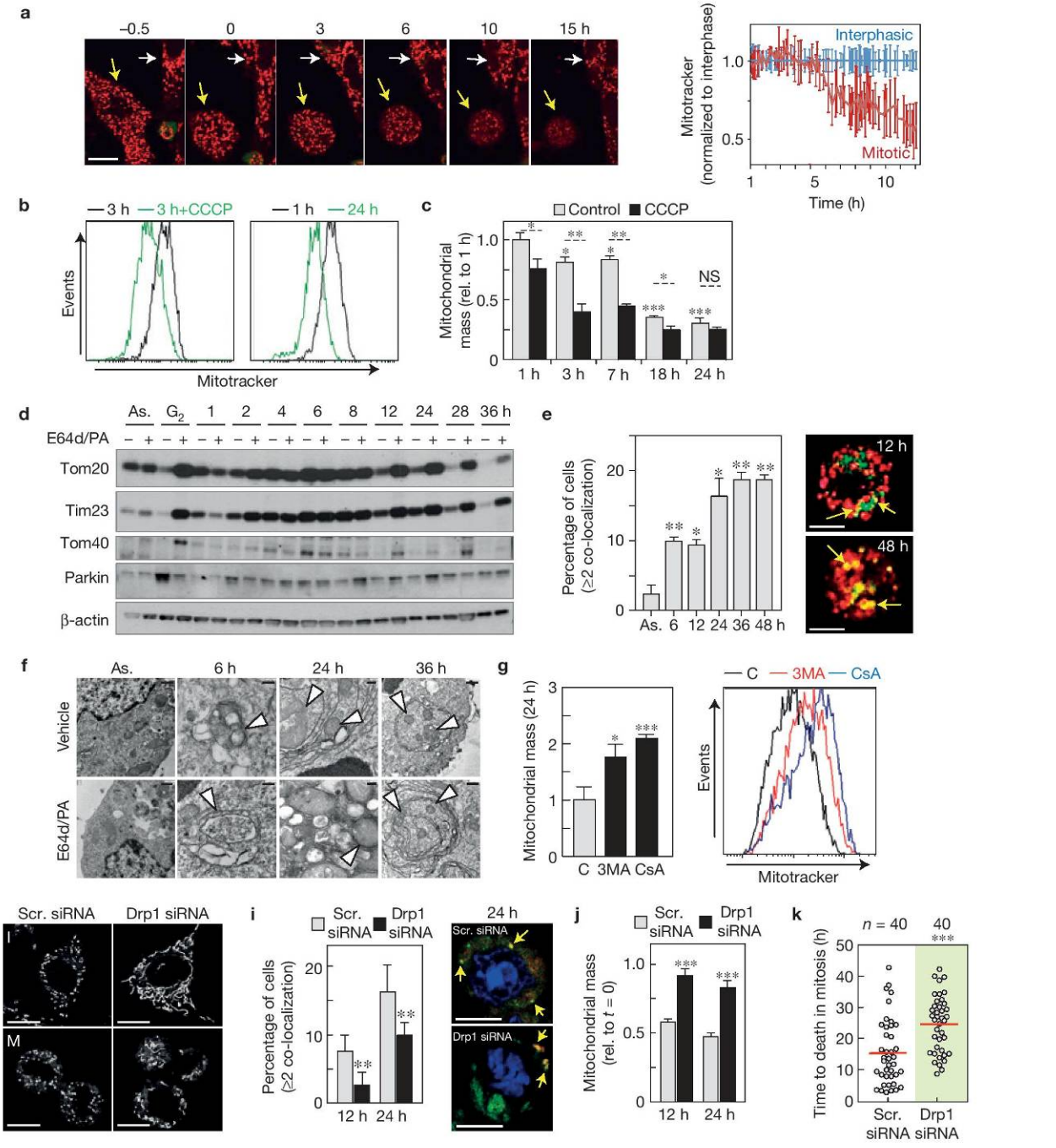

Figure 3 Reduced mitochondrial mass as a consequence of mitophagy during mitotic arrest. (**a**) Mitotracker signal (mean ± s.d.) detected by time-lapse microscopy in interphasic ($n = 12$ cells; white arrows) or mitotic ($n = 18$ cells, yellow) Cdc20-null cells. Scale bar, 10 μm. (**b**) Representative profiles of mitotic *Cdc20*(Δ/Δ) cells with or without CCCP (left panel), or after 1 h and 24 h in mitosis (right panel). (**c**) Quantification of Mitotracker intensity at the indicated time points of mitotic arrest (mean ± s.e.m.; $n = 7$ experiments). (**d**) Immunodetection of the indicated mitochondrial proteins in asynchronous (As.), G_2-arrested or mitotic Cdc20-null cells either in the absence or presence of E64d/PA. β-actin was used as a loading marker. Unprocessed original scans of blots are shown in Supplementary Fig. 7. (**e**) Percentage of cells (mean ± s.e.m.; $n = 30$ cells per condition) showing co-localization of LC3–GFP and Mitotracker (arrows) during mitotic arrest. Scale bar, 10 μm. (**f**) Representative electron micrographs showing the inclusion of mitochondria in autophagosomes (arrowheads) during mitotic arrest with or without E64d/PA. Scale bars, 200 nm (As.) and 500 nm (mitotic). (**g**) Mitotracker intensity in Cdc20-null cells after 24 h in mitosis treated with vehicle (C), 3MA or CsA (related to vehicle-treated cells; mean ± s.e.m.; $n = 3$ independent experiments). Right: profile of *Cdc20*(Δ/Δ) after 24 h in mitosis in the absence or presence of 3MA (red) or cyclosporin A (blue). (**h**) Mitotracker signal in Cdc20-null cells treated with siRNAs against Drp1 or scrambled sequences (Scr. siRNA). Scale bars, 10 μm. (**i**) Co-localization of LC3–GFP and Mitotracker (arrows) after mitotic arrest in Drp1 siRNA cells (mean ± s.e.m.; $n = 30$ cells per condition). Scale bars, 10 μm. (**j**) Mitotracker intensity after 12 and 24 h of mitotic arrest relative to 1 h of mitotic arrest in the presence (Scr. siRNA) or absence (Drp1 siRNA) of Drp1 (mean ± s.e.m.; $n = 3$ experiments). (**k**) Duration of mitosis in Cdc20-null cells treated with siRNAs against Drp1. The mean is indicated by red lines ($n = 40$ cells). In **c**,**e**,**g**,**i**–**k**, NS, not significant; $^{*}P < 0.05$; $^{**}P < 0.01$; $^{***}P < 0.001$, Student's *t*-test. In **a**,**d**,**e**,**g**–**k** data represent 1 out of 3 independent experiments. Source data can be found in Supplementary Table 4.

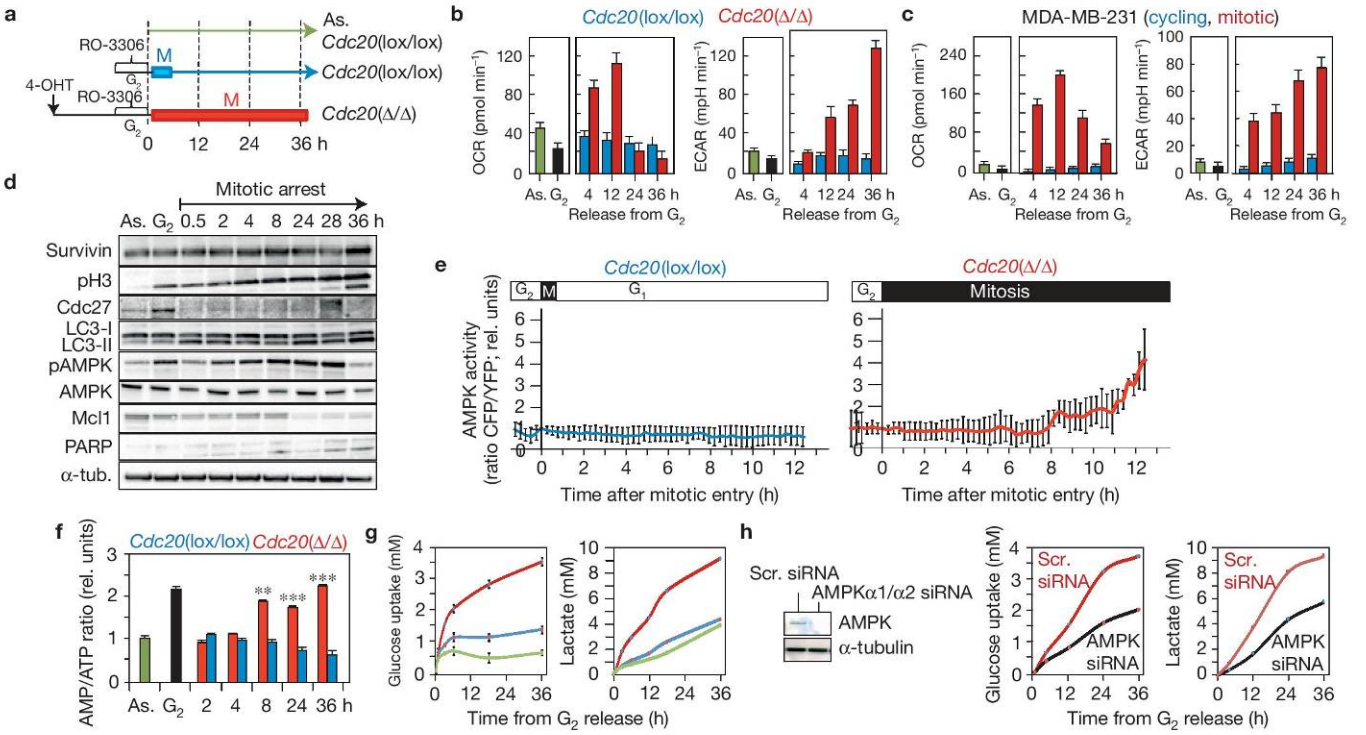

Figure 4 Metabolic switch from OXPHOS to glycolysis is mediated by AMPK. (**a**) Protocol used to synchronize entry into mitosis. Treatment of *Cdc20*(lox/lox) cells with 4-OHT results in mitotic arrest after release from RO-3306. Control cells include *Cdc20*(lox/lox) cells, which do not arrest (blue), or asynchronous cultures (As., green). Colour codes are maintained throughout the figure. (**b**) Respirometry profile of asynchronous (As.), G_2-arrested or mitotic-arrested *Cdc20*(Δ/Δ) cells after the release from G_2. (**c**) Respirometry profile in MDA-MB-231 human breast cancer cells synchronized in G_2 for 18 h by the addition of RO-3306 and released in the presence of 700 nM Taxol and the APC/C inhibitor proTAME (10 μM). (**d**) Immunodetection of the indicated antigens in asynchronous (As.) G_2-arrested or mitotic-arrested after the release from G_2. α-tubulin was used as a loading marker. Unprocessed original scans of blots are shown in Supplementary Fig. 7. (**e**) AMPK activity monitored by a FRET biosensor (mean ± s.d.; $n=12$ cells per genotype) in control *Cdc20*(lox/lox) (blue) or Cdc20-null (red) cells on mitotic entry at the single-cell level. Time 0 indicates mitotic entry and the length of the black bar represents duration of mitosis. (**f**) AMP/ATP ratio measured by HPLC in control *Cdc20*(lox/lox) and Cdc20-null cells. $^{**}P<0.01$; $^{***}P<0.001$, Student's *t*-test. (**g**) Glucose uptake and concentration of extracellular lactate (NMR analysis) in the presence of ^{13}C-labelled glucose. (**h**) Similar glucose uptake and concentration of extracellular lactate in Cdc20-null cells after knockdown of AMPKα1/α2 using specific siRNAs. Data in **g**,**h** represent 1 out of 3 independent experiments. In **b**,**c**,**e**–**h** data represent mean ± s.d. and in **g**,**h** a spline function is used to connect the sampled points. In **b**,**c**,**f** $n=3$ independent experiments. Data in **b**,**c** are not normalized for dead cells and the differences in mitotic-arrested cells are likely to be under-estimated. Source data can be found in Supplementary Table 4.

PFKFB3 (Fig. 5e). PFKFB3 was a critical component of the glycolytic switch during mitosis as silencing of this protein resulted in decreased consumption of glucose and release of lactate (Fig. 5f). In addition, increased levels of fructose-2,6-bisphosphate (F2,6P2, an allosteric activator of PFK-1 and the product of the reaction catalysed by PFKFB3) were detected in mitotic-arrested cells. The accumulation of F2,6P2 was prevented by Compound C or the PFKFB3 inhibitor 3-(3-pyridinyl)-1-(4-pyridinyl)-2-propen-1-one (3PO), supporting a role for AMPK in promoting the glycolytic switch observed in mitosis by modulating PFKFB3 enzymatic activity (Fig. 5g).

During these studies we observed that PFKFB3 (Fig. 6a), but not PFKFB1/4 (Supplementary Fig. 5g), levels accumulated during mitotic arrest. During mitotic arrest, transcription is impaired owing to hyper-compaction of chromatin. Translational initiation is also largely inhibited and only a specific subset of transcripts are specifically activated at this time[33,34]. These transcripts are characterized for a specific *cis*-acting element present in their 3′ UTR named cytoplasmic polyadenylation element (CPE). CPEs recruit the CPE-binding proteins (CPEB1–4) that in turn promote cytoplasmic polyadenylation and translational activation[34]. Interestingly, *Pfkfb3* mRNA contains a combinatorial arrangement of CPEs (Fig. 6b) predicted to promote translational activation during mitosis[35]. In agreement with this early activation being mostly supported by CPEB1 (ref. 34), RNA immunoprecipitation studies showed that *Pfkfb3* transcripts were associated with CPEB1, similarly to known mitotic CPEB targets such as cyclin B1 or Cdk1 (Fig. 6c). Both cordycepin, a known inhibitor of CPEB-dependent polyadenylation[36], and the general inhibitor of translation cycloheximide reduced the mitotic accumulation of PFKFB3 (Fig. 6d). Inhibition of polyadenylation or translation with cordycepin and cycloheximide (Fig. 6e) or downregulation of CPEB transcripts using siRNAs (Fig. 6f) resulted in precocious MCD. Silencing of PFKFB3 (Supplementary Fig. 5h) also reduced SiM (Fig. 6f), whereas knockdown of the related protein PFKFB1 had no effect (Supplementary Fig. 5h,i). Chemical inhibition of PFKFB3 with 3PO also resulted in a significant reduction in SiM both in mouse or human (Fig. 6g) cells. Importantly, overexpression of PFKFB3 rescued the deleterious effect of AMPK silencing in the survival of mitotic ells (Fig. 6h), suggesting the relevance of the AMPK–PFKFB3 axis in SiM.

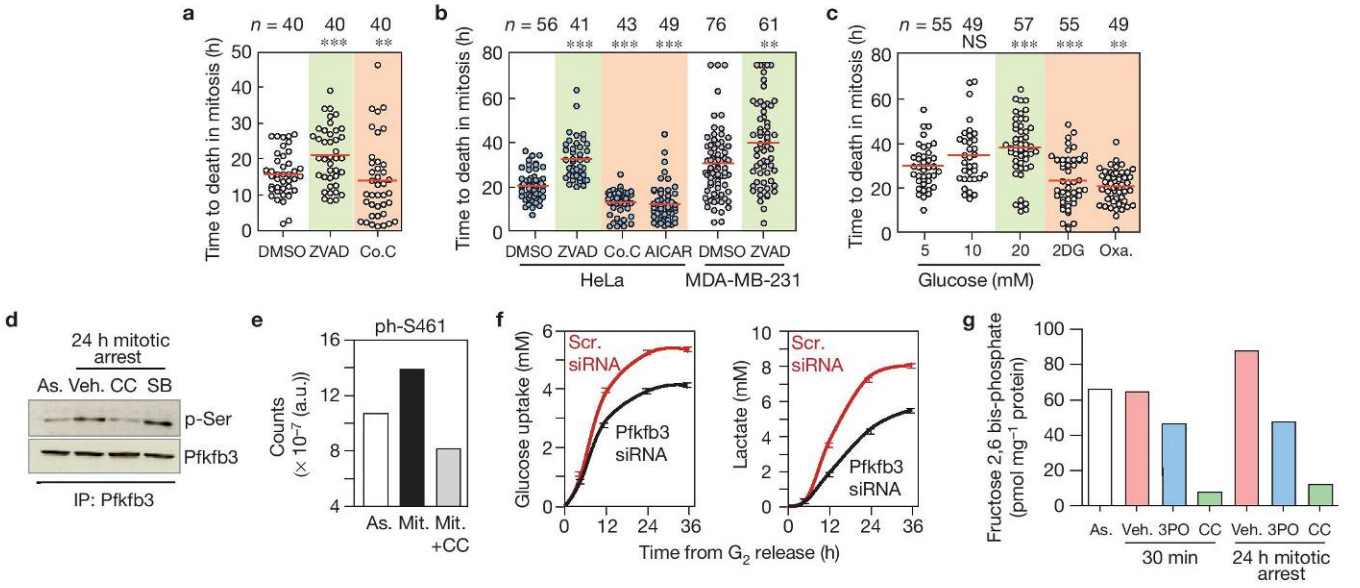

Figure 5 Glycolysis determines survival during mitotic arrest. (**a**) Duration of mitosis (from mitotic entry until cell death) in Cdc20-null cells treated with the caspase inhibitor ZVAD and the indicated AMPK modulators. (**b**) Similar studies in human cells after synchronization for 12 h with nocodazole and release in the presence of the proteasome inhibitor MG132 (and the indicated drugs) to induce mitotic arrest. (**c**) Duration of mitosis in Cdc20-null cells treated with the indicated inhibitors of glycolysis and on glucose addition at the indicated concentration. In **a–c**, dots represent individual cells and red lines indicate mean. The number of cells analysed (*n*) is indicated in each condition, and data are representative of six (**a**) or three (**b**,**c**) separate experiments. In these plots, green or orange backgrounds indicate a significant delay or premature cell death in mitosis, respectively. (**d**) Immunoprecipitation of endogenous PFKFB3 in asynchronous (As.) *Cdc20*(lox/lox) or Cdc20-null (after 24 h of mitotic arrest) cells treated either with vehicle, the AMPK inhibitor compound C (CC) or the p38 MAPK inhibitor SB203580 (SB). The immunoprecipitates were blotted against total phospho-Ser (p-Ser) and PFKFB3. These plots are representative of three independent experiments. Unprocessed original scans of blots are shown in Supplementary Fig. 7. (**e**) Phospho-proteomic analysis of exogenous rat GFP–PFKFB3 transfected in *Cdc20*(lox/lox) (As.) or Cdc20-null (after 24 h of mitotic arrest) cells. Mitotic-arrested cells were treated either with vehicle or the AMPK inhibitor Compound C (CC). Graph shows the mean counts identified for Ser 461 phosphorylation in one experiment with technical triplicates. (**f**) Glucose uptake (left panel) and concentration of extracellular lactate (right panel) measured by NMR in Cdc20-null cells nucleofected with Scramble or PFKFB3-directed siRNAs. Data represent mean ± s.d. and are representative of 3 independent experiments. (**g**) Fructose-2,6-bisphosphate levels (mean; $n = 2$ independent experiments) in asynchronous (As.) and mitotic-arrested (30 min and 24 h) Cdc20-null cells, either in the absence or presence of the inhibitors 3PO and Compound C. NS, not significant. $^{**}P < 0.01$; $^{***}P < 0.001$ (Student's *t*-test). Source data can be found in Supplementary Table 4.

Inhibition of glycolysis cooperates with microtubule poisons in MCD

We next tested the relevance of apoptosis, autophagy and energy production in the therapeutic effect of microtubule poisons. MBA-MD-231 breast cancer cells were treated with multiple agents against the referred pathways either in the presence or absence of Taxol. As indicated in Fig. 7a, several combinations were more efficient than the single agents in killing these breast cancer cells. The effect of ABT-263, PP242, 2DG and 3PO was also tested in additional breast cancer cell lines such as MDA-MD-468, EVSA-T or MCF7, as well as in non-transformed human cells (Supplementary Fig. 6). Treatment of MBA-MD-231 cells with ABT-263, PP242, 2DG or 3PO resulted in a variable efficiency in cell death ranging from 10 to 40% without affecting mitotic cells (Fig. 7b). Single treatment with Taxol also resulted in a significant percentage of dead cells (21%), of which only 12% died in mitosis. Notably, combination of Taxol with ABT-263, PP242 and 3PO resulted in efficient MCD (Fig. 7c,d) and the SiM was significantly reduced compared with the effect of Taxol alone (Fig. 7e).

Whereas the synergism between taxanes and Bcl2 and mTORC1 inhibitors in tumour growth has been explored in the past[37–39], the cooperation between Taxol and the inhibition of glycolysis has not been tested *in vivo*. Subcutaneous xenografts were generated with MBA-MD-231 cells, and Taxol (5 mg kg^{-1}) and 3PO (several doses from 0.05 to 50 mg kg^{-1}) were injected intraperitoneally when tumours reached 200 mm^3. Taxol was very inefficient at that dose whereas treatment with 3PO alone resulted in a significant reduction in tumour volume and weight (Fig. 8a,b). The combination of Taxol with 3PO further improved the effect when compared with single treatments and resulted in a significant increase in apoptotic cells in the tumours (Fig. 8c), suggesting the possible benefit of combining glycolytic inhibitors with mitotic-targeted therapies.

DISCUSSION

The arrest imposed by anti-mitotic drugs is frequently transient and cells exit from mitosis in an APC/C–Cdc20-dependent process[8] known as mitotic slippage[12,40]. Inhibiting the APC/C has been therefore proposed as a therapeutic option to prevent mitotic slippage, a possible mechanism of resistance to mitotic therapies in cancer cells[10,11,41,42]. Cdc20-knockout cells exhibit a permanent mitotic arrest until death[8], providing a clean genetic model to analyse molecular pathways that determine cell fate in mitosis. Among cell death pathways, multiple lines of evidence have established the involvement of intrinsic apoptosis in response to mitotic aberrations[10,12], whereas the extrinsic apoptotic pathway is thought to be inhibited at this stage

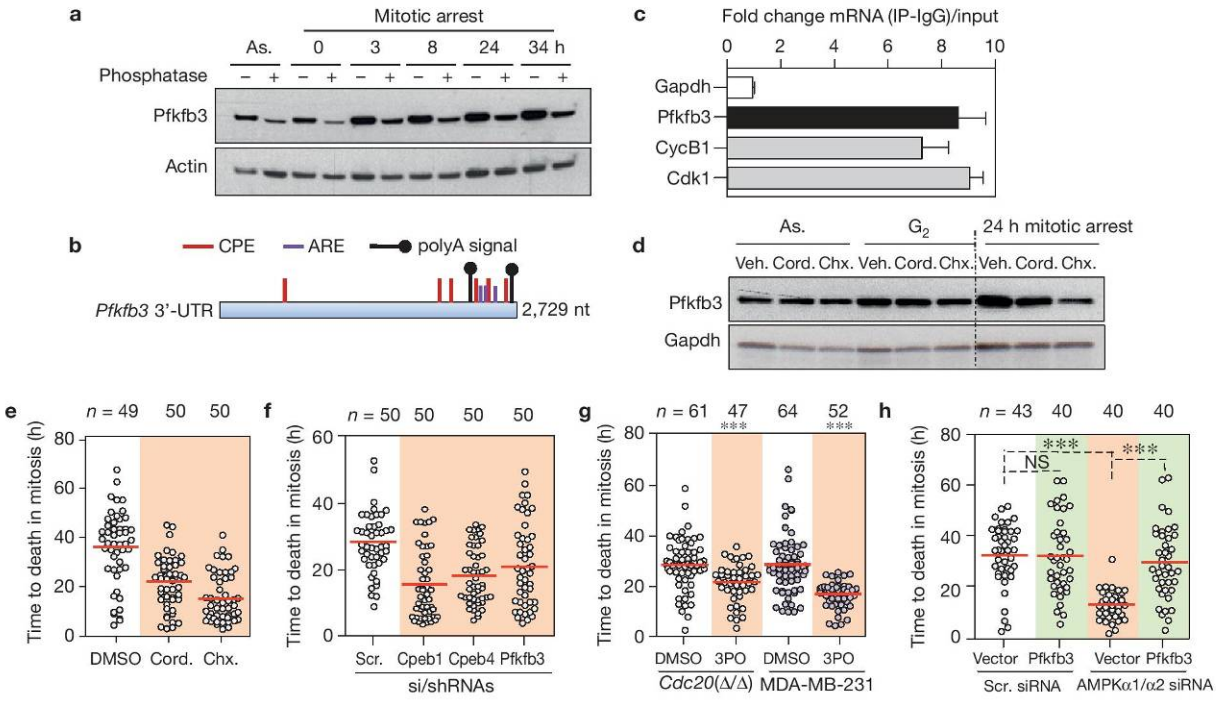

Figure 6 PFKFB3 regulation during mitotic arrest. (**a**) PFKFB3 protein levels in asynchronous cultures (As.) or during mitotic arrest in Cdc20-null cells. Actin was used as a loading control. Data represent 1 out of 2 independent experiments. (**b**) Schematic representation of the position of cytoplasmic polyadenylation elements (CPE), A/T-rich elements (ARE) and polyadenylation signals in the 3′-UTR of the murine *Pfkfb3* transcript. (**c**) RT–PCR detection of mRNA levels of the indicated proteins after immunoprecipitation of CPEB1 in RO-3306-arrested cells. Data are mean ± s.d. (one experiment with technical triplicates). (**d**) PFKFB3 protein levels in asynchronous (As.), G_2-arrested or mitotic Cdc20-deficient cells in the presence or absence or cordycepin (Cord.) or cycloheximide (Chx.). Samples were processed simultaneously and run in the same blot. GAPDH was used as a loading control. (**e**) Duration of mitosis (from mitotic entry until cell death) in Cdc20-null cells treated with cordycepin or cycloheximide. (**f**) Duration of mitosis (from mitotic entry until cell death) in Cdc20-null cells treated with siRNAs against CPEB1, CPEB4 or PFKFB3. (**g**) Duration of mitosis in Cdc20-null (left) or MDA-MB-231 cells arrested in mitosis by nocodazol synchronization and release in MG132 (right), treated with the PFKFB3 inhibitor 3PO. (**h**) Duration of mitosis in Cdc20-null cells treated with Scramble (Scr.) or AMPKα1/α2 siRNAs, and transfected with empty vector or plasmids overexpressing Pfkfb3. For **a**,**d**, unprocessed original scans of blots are shown in Supplementary Fig. 7. In **e**–**h**, dots represent individual cells and red lines indicate mean. The number of cells analysed (*n*) is indicated in each condition, and data are representative of one (**e**,**f**) or three (**g**,**h**) separate experiments. In these plots, green or orange backgrounds indicate a significant delay or premature cell death in mitosis, respectively. NS, not significant. $^{***}P < 0.001$ (Student's *t*-test). Source data for panels **c**,**e**–**h** can be found in Supplementary Table 4.

of the cell cycle[43]. Our results confirm previous results suggesting the relevance of the Bcl2 family in response to mitotic defects[10,12,14,15,44]. It has also been recently described that Cdc20 can suppress apoptosis targeting the pro-apoptotic factor Bim (ref. 45), suggesting that mitotically arrested cells in which Cdc20 is inhibited as a consequence of SAC activity are sensitive to this form of death.

It has been assumed that mitochondria are particularly active during the energy-expensive process driving spindle formation and chromosome segregation[46]. Cdk1 activity is necessary to phosphorylate and activate several components of the mitochondrial complex I thus enhancing mitochondrial respiration during the G_2/M transition[28]. Inhibition of Cdk1 results in decreased mitochondrial activity[28], impaired respiratory capacity (Fig. 4b,c), and reduced ATP levels (Fig. 4f). Thus, Cdk1 activity provides cells with the bioenergy required for a normal mitosis by enhancing mitochondrial respiration. However, on mitotic arrest, the mitochondrial mass declines after a few hours, presumably as a result of deficient renovation of organelles. This process occurs in the presence of mitophagy (Fig. 3), a critical autophagic process responsible for the clearance of damaged mitochondria in cells[26,47]. Although it was originally argued that autophagy was shut down during the later phases of the cell cycle[19,48,49], it has been more recently shown that autophagy can persist during mitosis[46]. Thus, the reduced biogenesis resulting from impaired transcription and reduced translation in mitotic cells possibly perpetuates mitochondrial dysfunction (Fig. 3) and reduced ATP levels (Fig. 4) during mitotic arrest. The involvement of Drp1 in mitotic mitochondria fragmentation and mitophagy susceptibility may explain the finding of this protein as a hit in a recent screen for molecules whose silencing improves the adaptation to mitotic arrest[50].

The increase in the AMP/ATP ratio during mitotic arrest is likely to contribute to the activation of AMPK, a major homeostatic regulator of cellular ATP levels[51]. Whereas the activation of AMPK has been shown to be predominantly cytoplasmic[29], mitotic cells may become more sensitive to AMPK owing to the absence of the nuclear envelope. AMPK activation can acutely increase glucose uptake and glycolysis, although in the long term it promotes the more energy-efficient oxidative metabolism by upregulating mitochondrial biogenesis and expression of oxidative enzymes. However, the latter process is thought to be transcription-dependent[52] and therefore inefficient in mitotic-arrested cells. Among other activities, AMPK forms stable

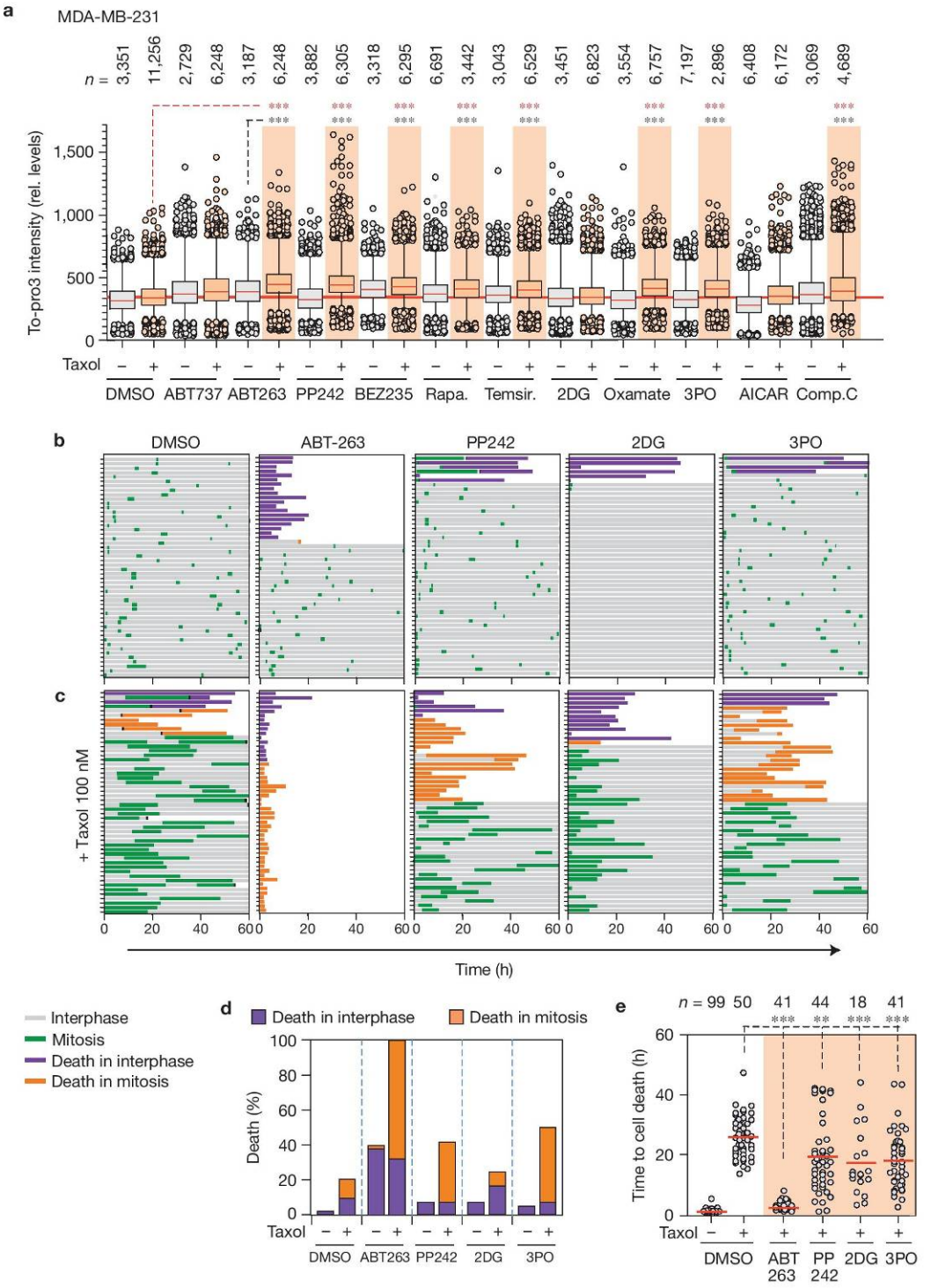

Figure 7 Taxol cooperates with different inhibitors of survival pathways to promote MCD. (**a**) Cell death in MDA-MB-231 as determined by To-Pro3 levels, measured using high-throughput microscopy, after the addition of the indicated compounds in the presence or absence of Taxol. Orange columns indicate significant synergistic combinations when compared with single inhibitors (black dashed comparisons) or Taxol (red dashed comparisons). The number of cells analysed (n) is indicated in each condition. Data are mean ± s.e.m. $^{***}P<0.001$; Student's t-test. ($n=3$ independent experiments). (**b**) Duration of interphase (grey) or mitosis (green) of MDA-MB-231 cells treated with the indicated inhibitors. Each lane represents one cell ($n=50$ cells per condition). Cell death observed in interphase is represented in violet, and cell death detected during mitosis is shown in orange. (**c**) Cell fate of single MDA-MB-231 cells treated with the indicated inhibitors in combination with Taxol, which was added to the cells 4 h before the above indicated drugs ($n=50$ cells per condition). (**d**) Quantification of the percentage of cells dying in interphase (violet) or in mitosis (orange) after the indicated treatments ($n=50$ cells per condition). (**e**) Duration of mitosis (mean ± s.e.m.; from mitotic entry until cell death) in MDA-MB-231 cells treated with the indicated drugs, alone or in combination with Taxol. The number of cells analysed (n) is indicated in each condition, and data are representative of six separate experiments. $^{**}P<0.01$; $^{***}P<0.001$ (Student's t-test). Source data can be found in Supplementary Table 4.

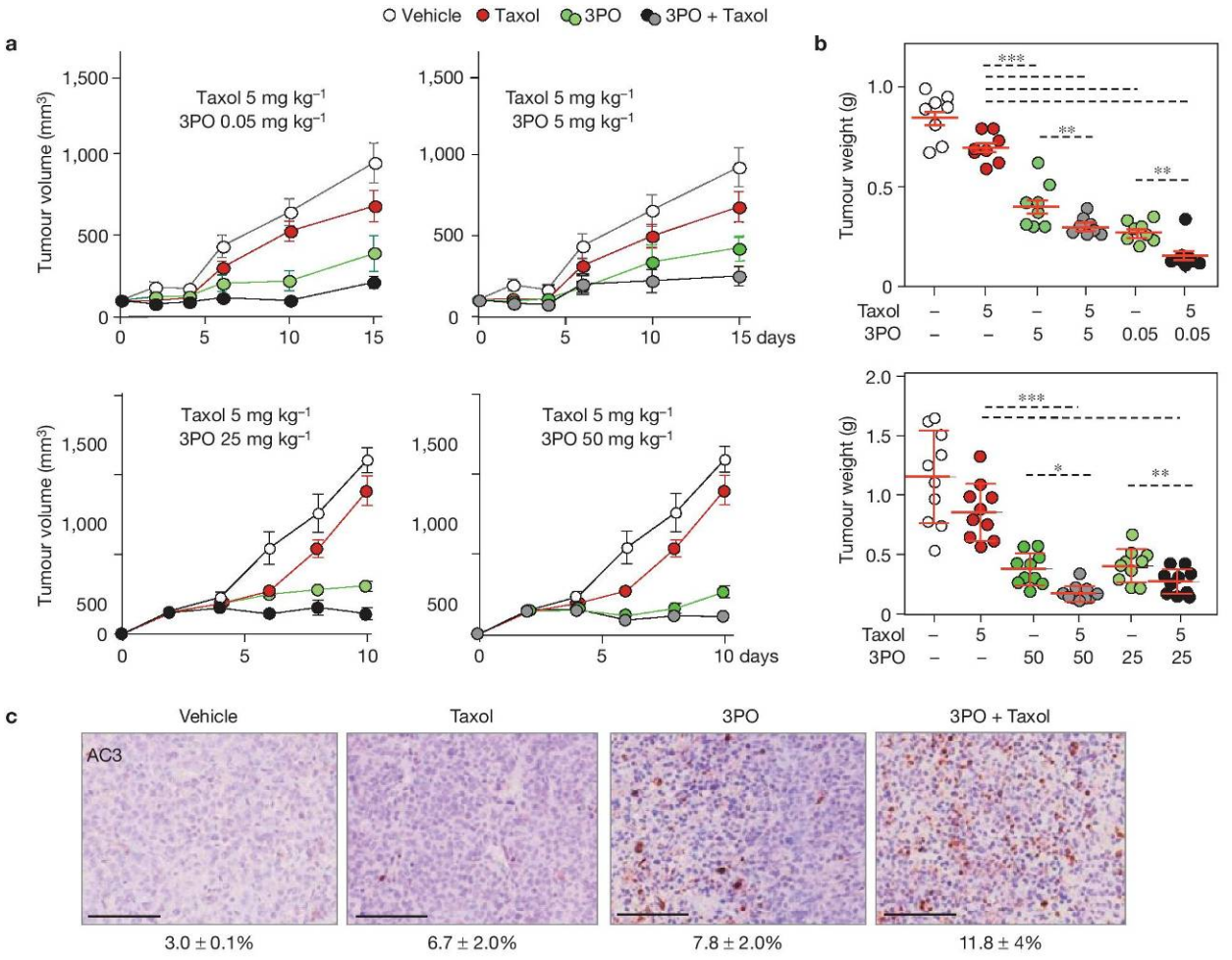

Figure 8 Anti-tumoral cooperation between microtubule poisons and PFKFB3 inhibitors *in vivo*. (**a**) Effect of the combination of Taxol (5 mg kg^{-1}) and 3PO (0.05 to 50 mg kg^{-1}) on the growth of tumour xenografts generated by subcutaneous injection of MDA-MB-231 cells in nude mice. See Methods for detailed information about animal procedures. Data are mean ± s.d. ($n = 8$ tumours (top panels) or 10 tumours (bottom panels), respectively from 2 tumours per animal). (**b**) Tumour weight at the final time point of the experiment ($n = 8$ tumours (top panels), 10 tumours (bottom panels) from 2 tumours per animal). Red lines indicate mean ± s.d. $^{**}P < 0.01$; $^{***}P < 0.001$ (Student's *t*-test). (**c**) Active caspase 3 (AC3) immunostaining in MDA-MB-231-derived tumour xenografts treated with either vehicle, Taxol (5 mg kg^{-1}), 3PO (0.05 mg kg^{-1}) or the combination of both treatments. The numbers indicate the percentage of active caspase-3-positive area (mean ± s.d.; $n = 6$ sections for each of two dissected tumours per condition. Scale bars, 100 μm. Source data can be found in Supplementary Table 4.

complexes with Ulk1 and Ulk2 and directly phosphorylates Ulk1, triggering autophagy[30,53]. Thus, in the presence of mitochondrial dysfunction, AMPK is likely to trigger glycolysis and can further promote autophagy during prolonged mitotic arrest (Fig. 4). It has been proposed that AMPK is active during mitosis and it is required for the completion of mitosis by phosphorylating components of the APC/C (APC1 and CDC27) and PP1 regulatory subunits[54]. In these studies, it was not obvious why a kinase activated by energy stress should be required for passage through mitosis[52]. However, it is important to note that nocodazole-arrested cells were used in these studies as a paradigm of mitotic cells[54], raising the possibility that some of these conclusions may not apply to a normal, short (<1 h) mitosis. AMPK activity is also pro-apoptotic, and necessary and sufficient for the activation of pro-apoptotic proteins such as Bim or Bmf and cell death during bioenergetics stress[55–57]. Thus, AMPK may have a dual role during mitotic arrest. On one hand, it senses loss of ATP and enhances glycolysis protecting from death. Also, it may enhance autophagy and apoptosis through the modulation of Ulk1 and Bim/Bmf activities[30,53,56,57].

The glycolytic activity of AMPK is thought to be determined by the phosphorylation and activation of PFKFB3 (refs 31,58). PFKFB3 is commonly overexpressed in human cancer[31] contributing to the Warburg effect, a switch away from oxidative metabolism and towards rapid glucose uptake, glycolysis and lactate output that is characteristic of many tumour cells[59]. Our data suggest that AMPK-dependent phosphorylation of PFKFB3 may also contribute to enhancing glycolysis during mitosis. In addition, PFKFB3 levels are maintained high during mitosis owing to CPEB-dependent translation (Fig. 6), a process known to be crucial for multiple aspects of mitosis[34]. Interestingly, PFKFB3 is regulated in a cell cycle-dependent manner through ubiquitin-dependent targeting by APC/C–Cdh1 complexes[60]. As APC/C–Cdh1 is activated only

downstream of APC/C–Cdc20 after mitotic exit, the combination of mitotic-specific translation and lack of degradation is likely to contribute to maintain high levels of PFKFB3 and active glycolysis during mitosis. Whereas the combination between microtubule poisons and apoptotic inducers has been extensively studied[12,14,15,61], our data suggest that promoting autophagy or inhibiting glycolysis may also enhance MCD before cancer cells exit from mitosis, thus providing the cellular basis for new combinatory therapies targeting cell cycle and metabolic pathways in cancer. □

METHODS

Methods and any associated references are available in the online version of the paper.

Note: Supplementary Information is available in the online version of the paper

ACKNOWLEDGEMENTS

We thank M. Soengas (Spanish National Cancer Research Centre, Spain), J. P. Bolaños (Institute of Functional Biology and Genomics, Spain) and N. Mizushima (The University of Tokyo, Japan) for reagents. We also thank S. Velasco for help with the Seahorse apparatus, J. Muñoz and M. P. Ximénez for their support in phospho-proteomics experiments, and F. Escobar and B. Pou for help with electron microscopy. E.D., C.M. and M.S.-R. were supported by the Spanish Fondo de Investigaciones Sanitarias (Madrid), MINECO (Juan de la Cierva programme) and Asociación Española contra el Cáncer (AECC), respectively. L.E.-M. is a recipient of a JAE predoctoral fellowship from the CSIC. A.K.S. was supported by USPHS grants RO1DK19514, RO1DK67509. G.V. was supported by grants from the Spanish Ministry of Economy and Competitiveness (MINECO) and Fondo Europeo de Desarrollo Regional (FEDER) (PI12/02248), Fundació La Marató de TV3 (m12 20134031), and Fundación Mutua Madrileña (AP101042012). M.L. was supported by the European Community's Seventh Framework Programme under grant agreement no. 281854—the ObERStress (European Research Council project). E.R. was financially supported by a MINECO grant (SAF 2010-20256). Work in the R.M. laboratory was supported by the Fundación Botín, Banco Santander and MINECO (BFU2011-30121, BFU2014-52125-REDT and Consolider RNAREG CSD2009-00080). Work in the P.B. laboratory is supported by a grant from the Spanish Ministry for Economy and Competitiveness (MINECO; SAF2012-36079). Work in the M.M. laboratory was supported by grants from the MINECO (SAF2012-38215), Consolider-Ingenio 2010 Programme (SAF2014-57791-REDC), Excellence Network CellSYS (BFU2014-52125-REDT), the OncoCycle Programme (S2010/BMD-2470) from the Comunidad de Madrid, Worldwide Cancer Research (WCR no. 15-0278), and the European Union Seventh Framework Programme (MitoSys project; HEALTH-F5-2010-241548).

AUTHOR CONTRIBUTIONS

E.D. and M.S.-R. performed most of the cellular and biochemical assays with the help of C.M. and D.P. L.E.-M., E.S. and P.B. collaborated in the analysis of mitophagy, and G.F.-M., R.P. and R.M. collaborated in the analysis of translation. R.C.-O. generated the NMR data. M.P. and D.M. helped with microscopy analysis. A.K.S. performed the AMP/ATP measurements and M.L. contributed to the analysis of AMPK. E.R. helped with metabolic measurements. E.D., C.M., G.V., E.R., P.B., M.S.-R. and M.M. analysed the data. M.M. conceived the project, M.S.R. and M.M., supervised the experiments, and M.M. wrote the manuscript with the help of all co-authors.

COMPETING FINANCIAL INTERESTS

The authors declare no competing financial interests.

Published online at http://dx.doi.org/10.1038/ncb3231
Reprints and permissions information is available online at www.nature.com/reprints

1. Alvarez-Fernandez, M. & Malumbres, M. Preparing a cell for nuclear envelope breakdown: spatio-temporal control of phosphorylation during mitotic entry. *Bioessays* **36,** 757–767 (2014).
2. Musacchio, A. & Salmon, E. D. The spindle-assembly checkpoint in space and time. *Nat. Rev. Mol. Cell Biol.* **8,** 379–393 (2007).
3. Foley, E. A. & Kapoor, T. M. Microtubule attachment and spindle assembly checkpoint signalling at the kinetochore. *Nat. Rev. Mol. Cell Biol.* **14,** 25–37 (2013).
4. Peters, J. M. The anaphase promoting complex/cyclosome: a machine designed to destroy. *Nat. Rev. Mol. Cell Biol.* **7,** 644–656 (2006).
5. Jia, L., Kim, S. & Yu, H. Tracking spindle checkpoint signals from kinetochores to APC/C. *Trends Biochem. Sci.* **38,** 302–311 (2013).
6. Komlodi-Pasztor, E., Sackett, D. L. & Fojo, A. T. Inhibitors targeting mitosis: tales of how great drugs against a promising target were brought down by a flawed rationale. *Clin. Cancer Res.* **18,** 51–63 (2012).
7. Mitchison, T. J. The proliferation rate paradox in antimitotic chemotherapy. *Mol. Biol. Cell* **23,** 1–6 (2012).
8. Manchado, E. *et al.* Targeting mitotic exit leads to tumor regression *in vivo*: modulation by Cdk1, Mastl, and the PP2A/B55α,δ phosphatase. *Cancer Cell* **18,** 641–654 (2010).
9. Gascoigne, K. E. & Taylor, S. S. Cancer cells display profound intra- and interline variation following prolonged exposure to antimitotic drugs. *Cancer Cell* **14,** 111–122 (2008).
10. Huang, H. C., Shi, J., Orth, J. D. & Mitchison, T. J. Evidence that mitotic exit is a better cancer therapeutic target than spindle assembly. *Cancer Cell* **16,** 347–358 (2009).
11. Rieder, C. L. & Medema, R. H. No way out for tumor cells. *Cancer Cell* **16,** 274–275 (2009).
12. Topham, C. H. & Taylor, S. S. Mitosis and apoptosis: how is the balance set? *Curr. Opin. Cell Biol.* **25,** 780–785 (2013).
13. Vitale, I., Galluzzi, L., Castedo, M. & Kroemer, G. Mitotic catastrophe: a mechanism for avoiding genomic instability. *Nat. Rev. Mol. Cell Biol.* **12,** 385–392 (2011).
14. Wertz, I. E. *et al.* Sensitivity to antitubulin chemotherapeutics is regulated by MCL1 and FBW7. *Nature* **471,** 110–114 (2011).
15. Inuzuka, H. *et al.* SCF(FBW7) regulates cellular apoptosis by targeting MCL1 for ubiquitylation and destruction. *Nature* **471,** 104–109 (2011).
16. Tse, C. *et al.* ABT-263: a potent and orally bioavailable Bcl-2 family inhibitor. *Cancer Res.* **68,** 3421–3428 (2008).
17. Wei, M. C. *et al.* Proapoptotic BAX and BAK: a requisite gateway to mitochondrial dysfunction and death. *Science* **292,** 727–730 (2001).
18. Zeng, X. *et al.* Pharmacologic inhibition of the anaphase-promoting complex induces a spindle checkpoint-dependent mitotic arrest in the absence of spindle damage. *Cancer Cell* **18,** 382–395 (2010).
19. Eskelinen, E. L. *et al.* Inhibition of autophagy in mitotic animal cells. *Traffic* **3,** 878–893 (2002).
20. Kimura, S., Noda, T. & Yoshimori, T. Dissection of the autophagosome maturation process by a novel reporter protein, tandem fluorescent-tagged LC3. *Autophagy* **3,** 452–460 (2007).
21. Ashrafi, G. & Schwarz, T. L. The pathways of mitophagy for quality control and clearance of mitochondria. *Cell Death Differ.* **20,** 31–42 (2013).
22. Galluzzi, L., Bravo-San Pedro, J. M. & Kroemer, G. Organelle-specific initiation of cell death. *Nat. Cell Biol.* **16,** 728–736 (2014).
23. Gomes, L. C., Di Benedetto, G. & Scorrano, L. During autophagy mitochondria elongate, are spared from degradation and sustain cell viability. *Nat. Cell Biol.* **13,** 589–598 (2011).
24. Rambold, A. S., Kostelecky, B., Elia, N. & Lippincott-Schwartz, J. Tubular network formation protects mitochondria from autophagosomal degradation during nutrient starvation. *Proc. Natl Acad. Sci. USA* **108,** 10190–10195 (2011).
25. Gomes, L. C. & Scorrano, L. High levels of Fis1, a pro-fission mitochondrial protein, trigger autophagy. *Biochim. Biophys. Acta* **1777,** 860–866 (2008).
26. Youle, R. J. & Narendra, D. P. Mechanisms of mitophagy. *Nat. Rev. Mol. Cell Biol.* **12,** 9–14 (2011).
27. Taguchi, N., Ishihara, N., Jofuku, A., Oka, T. & Mihara, K. Mitotic phosphorylation of dynamin-related GTPase Drp1 participates in mitochondrial fission. *J. Biol. Chem.* **282,** 11521–11529 (2007).
28. Wang, Z. *et al.* Cyclin B1/Cdk1 coordinates mitochondrial respiration for cell-cycle G2/M progression. *Dev. Cell* **29,** 217–232 (2014).
29. Tsou, P., Zheng, B., Hsu, C. H., Sasaki, A. T. & Cantley, L. C. A fluorescent reporter of AMPK activity and cellular energy stress. *Cell Metab.* **13,** 476–486 (2011).
30. Egan, D. F. *et al.* Phosphorylation of ULK1 (hATG1) by AMP-activated protein kinase connects energy sensing to mitophagy. *Science* **331,** 456–461 (2011).
31. Bando, H. *et al.* Phosphorylation of the 6-phosphofructo-2-kinase/fructose 2,6-bisphosphatase/PFKFB3 family of glycolytic regulators in human cancer. *Clin. Cancer Res.* **11,** 5784–5792 (2005).
32. Novellasdemunt, L. *et al.* PFKFB3 activation in cancer cells by the p38/MK2 pathway in response to stress stimuli. *Biochem. J.* **452,** 531–543 (2013).
33. Pyronnet, S., Pradayrol, L. & Sonenberg, N. A cell cycle-dependent internal ribosome entry site. *Mol. Cell* **5,** 607–616 (2000).
34. Novoa, I., Gallego, J., Ferreira, P. G. & Mendez, R. Mitotic cell-cycle progression is regulated by CPEB1 and CPEB4-dependent translational control. *Nat. Cell Biol.* **12,** 447–456 (2010).
35. Pique, M., Lopez, J. M., Foissac, S., Guigo, R. & Mendez, R. A combinatorial code for CPE-mediated translational control. *Cell* **132,** 434–448 (2008).
36. Rose, K. M., Bell, L. E. & Jacob, S. T. Specific inhibition of chromatin-associated poly(A) synthesis *in vitro* by cordycepin 5′-triphosphate. *Nature* **267,** 178–180 (1977).
37. Lieber, J. *et al.* The BH3 mimetic ABT-737 increases treatment efficiency of paclitaxel against hepatoblastoma. *BMC Cancer* **11,** 362 (2011).
38. Campone, M. *et al.* Safety and pharmacokinetics of paclitaxel and the oral mTOR inhibitor everolimus in advanced solid tumours. *British J. Cancer* **100,** 315–321 (2009).
39. Meier, F. *et al.* Significant response after treatment with the mTOR inhibitor sirolimus in combination with carboplatin and paclitaxel in metastatic melanoma patients. *J. Am. Acad. Dermatol.* **60,** 863–868 (2009).

40. Brito, D. A. & Rieder, C. L. Mitotic checkpoint slippage in humans occurs via cyclin B destruction in the presence of an active checkpoint. *Curr. Biol.* **16,** 1194–1200 (2006).
41. Manchado, E., Guillamot, M. & Malumbres, M. Killing cells by targeting mitosis. *Cell Death Differ.* **19,** 369–377 (2012).
42. Domenech, E. & Malumbres, M. Mitosis-targeting therapies: a troubleshooting guide. *Curr. Opin. Pharmacol.* **13,** 519–528 (2013).
43. Matthess, Y., Raab, M., Sanhaji, M., Lavrik, I. N. & Strebhardt, K. Cdk1/cyclin B1 controls Fas-mediated apoptosis by regulating caspase-8 activity. *Mol. Cell Biol.* **30,** 5726–5740 (2010).
44. Wang, P. *et al.* Phosphorylation of the proapoptotic BH3-only protein bid primes mitochondria for apoptosis during mitotic arrest. *Cell Rep.* **7,** 661–671 (2014).
45. Wan, L. *et al.* APC(Cdc20) suppresses apoptosis through targeting bim for ubiquitination and destruction. *Dev. Cell* **29,** 377–391 (2014).
46. Liu, L., Xie, R., Nguyen, S., Ye, M. & McKeehan, W. L. Robust autophagy/mitophagy persists during mitosis. *Cell Cycle* **8,** 1616–1620 (2009).
47. Okamoto, K. Organellophagy: eliminating cellular building blocks via selective autophagy. *J. Cell Biol.* **205,** 435–445 (2014).
48. Tasdemir, E. *et al.* Cell cycle-dependent induction of autophagy, mitophagy and reticulophagy. *Cell Cycle* **6,** 2263–2267 (2007).
49. Tasdemir, E. *et al.* p53 represses autophagy in a cell cycle-dependent fashion. *Cell Cycle* **7,** 3006–3011 (2008).
50. Diaz-Martinez, L. A. *et al.* Genome-wide siRNA screen reveals coupling between mitotic apoptosis and adaptation. *EMBO J.* **33,** 1960–1976 (2014).
51. Hardie, D. G., Ross, F. A. & Hawley, S. A. AMP-activated protein kinase: a target for drugs both ancient and modern. *Chem. Biol.* **19,** 1222–1236 (2012).
52. Hardie, D. G., Ross, F. A. & Hawley, S. A. AMPK: a nutrient and energy sensor that maintains energy homeostasis. *Nat. Rev. Mol. Cell Biol.* **13,** 251–262 (2012).
53. Kim, J., Kundu, M., Viollet, B. & Guan, K. L. AMPK and mTOR regulate autophagy through direct phosphorylation of Ulk1. *Nat. Cell Biol.* **13,** 132–141 (2011).
54. Banko, M. R. *et al.* Chemical genetic screen for AMPKα2 substrates uncovers a network of proteins involved in mitosis. *Mol. Cell* **44,** 878–892 (2011).
55. Davila, D. *et al.* Two-step activation of FOXO3 by AMPK generates a coherent feed-forward loop determining excitotoxic cell fate. *Cell Death Differ.* **19,** 1677–1688 (2012).
56. Concannon, C. G. *et al.* AMP kinase-mediated activation of the BH3-only protein Bim couples energy depletion to stress-induced apoptosis. *J. Cell Biol.* **189,** 83–94 (2010).
57. Kilbride, S. M. *et al.* AMP-activated protein kinase mediates apoptosis in response to bioenergetic stress through activation of the pro-apoptotic Bcl-2 homology domain-3-only protein BMF. *J. Biol. Chem.* **285,** 36199–36206 (2010).
58. Marsin, A. S. *et al.* Phosphorylation and activation of heart PFK-2 by AMPK has a role in the stimulation of glycolysis during ischaemia. *Curr. Biol.* **10,** 1247–1255 (2000).
59. Vander Heiden, M. G., Cantley, L. C. & Thompson, C. B. Understanding the Warburg effect: the metabolic requirements of cell proliferation. *Science* **324,** 1029–1033 (2009).
60. Herrero-Mendez, A. *et al.* The bioenergetic and antioxidant status of neurons is controlled by continuous degradation of a key glycolytic enzyme by APC/C-Cdh1. *Nat. Cell Biol.* **11,** 747–752 (2009).
61. Oltersdorf, T. *et al.* An inhibitor of Bcl-2 family proteins induces regression of solid tumours. *Nature* **435,** 677–681 (2005).

METHODS

Cell culture and synchronization. The Cdc20 conditional allele and its deletion by 4-OHT-inducible forms of Cre (RERT) were reported previously[8]. Atg5 and Bax/Bak mutant MEFs were described previously[62–64]. MEFs and human cell lines were grown in Dulbecco's modified Eagle's medium (DMEM) or RPMI (Sigma) complemented with fetal bovine serum (FBS) and gentamycin at 37 °C and 5% CO_2. For synchronization in G_2, cells were treated with RO-3306 (Calbiochem; 5 μM) for 18 h and released in DMEM with or without 4-OHT (Sigma; 1 μM), Taxol (Sigma; 700 nM) or proTAME (Boston Biochem.; 10 μM). For mitotic synchronization of Cdc20-proficient mouse or human cultures, cells were treated for 12 h with 200 nM nocodazole (Sigma) and released in fresh media containing 10 μM MG132. Cells were treated with small-molecule inhibitors as indicated in Supplementary Table 1. One micromolar TO-PRO-3 iodide (642/661; Invitrogen T3605) or APC Annexin V (BD Pharmigen) and DAPI at 1 μg ml^{-1} were used to monitor cell death by FACs.

MEFs and human cells lines were transfected with Lipofectamine 2000 (Invitrogen) or Amaxa nucleofector MEF 2 Kit (using Dharmacon siRNA smart pools) in accordance with the manufacturer's recommendations. For quantitative RT–PCR studies, total RNA was isolated by using the Qiagen RNeasy kit, according to the manufacturer's instructions. cDNA was synthesized with a Superscript III reverse transcriptase (Invitrogen) and PCR amplification was performed using SYBR Green PCR Master mix (Applied Biosystems) with specific primers (Supplementary Table 2). RNA immunoprecipitation was performed essentially as reported previously[65]. The cell lines used throughout this work were obtained from the ATCC and have not been authenticated. All of the cells used in this study were negative in mycoplasma tests.

Cytometry. Cell cycle profiles were monitored by adding 0.2 μg ml^{-1} DAPI (Sigma) to the samples before their analysis on the LSR Fortessa. All data were analysed using FlowJo v9.6.4 (Treestar). For quantifying mitochondrial mass, adherent cells were trypsinized for 5 min at 37 °C and resuspended in complete medium with 10 nM Mitotracker deep red (MTDR, M22426, Invitrogen) and 1 μm l^{-1} propidium iodide (P4864, Sigma) and then incubated for 15 min at 37 °C. Using an FC500 flow cytometer (Beckman Coulter), 10,000 cells were acquired in the FL3 and FL4 channels. Mean fluorescence in the FL4 channel in the viable cell (PI-negative) population was plotted and normalized against that of untreated cells. Additional protocols for quantifying autophagy have been reported previously[66,67].

Biochemical analysis and phospho-proteomics. For western blotting, cells were lysed in RIPA or a buffer containing 50 mM Tris HCl, pH 7.5, 1 mM phenylmethylsulphonyl fluoride, 50 mM NaF, 5 mM sodium pyrophosphate, 1 mM sodium orthovanadate, 0.1% Triton X-100, 1 μg ml^{-1} leupeptin, 1 mM EDTA, 1 mM EGTA and 10 mM sodium glycerophosphate[62]. Thirty micrograms of total protein was separated by SDS–PAGE and probed with antibodies as indicated in Supplementary Table 3.

For immunoprecipitation of endogenous PFKFB3, Cdc20-null cells were lysed in ELB buffer (Hepes 40 mM, pH 7.5; NaCl 150 mM, EDTA, NP40 1%, phosphatase inhibitors). Lysates (5 mg) were precleared by incubating with 5–20 μl of protein G–Sepharose conjugated to pre-immune IgG. PFKFB3 was immunoprecipitated from Cdc20-null cells using monoclonal anti-PFKFB3 antibody (Cell Signaling) immobilized on Dynabeads Protein A (Invitrogen). After overnight incubation at 4 °C on a rotatory wheel, the immunoprecipitates were washed 4 times with ELB buffer. The immunoprecipitates were then resuspended in 30 μl of sample buffer (not containing 2-mercaptoethanol) and filtered through a 0.22-μm Spin-X filter (to discard Dynabeads conjugated to the antibody), and 2-mercaptoethanol was added to a concentration of 1% (vol/vol). Samples were then subjected to electrophoresis and immunoblot analysis.

To study specific phospho-residues, Cdc20-null cells were transfected with a vector expressing GFP fused to the rat PFKFB3 (kindly provided by J. P. Bolaños) 24 h before the synchronization of cells. The immunoprecipitation was performed using monoclonal antibodies against GFP (Roche) immobilized on Dynabeads Protein A (Invitrogen). Protein eluates from the immunoprecipitated samples were separated by SDS–PAGE. The bands corresponding to PFKFB3 were excised and in-gel digested with trypsin. The resulting peptides were analysed by LC–MS/MS using an LTQ Orbitrap Velos mass spectrometer (Thermo Scientific). Raw files were searched against a TrEMBL mouse database (43539 entries) using Sequest-HT as the search engine through the Proteome Discoverer 1.4 (Thermo Scientific) software. Peptide identifications were filtered by Percolator at 1% FDR using the target–decoy strategy. Label-free quantification was performed with MaxQuant and extracted ion chromatograms for PFKFB3 phosphopeptides were manually validated in Xcalibur 2.2 (Thermo).

Immunofluorescence and microscopy. Cells were fixed in 4% buffered paraformaldehyde for 10 min at room temperature, permeabilized in 0.15% Triton X-100 for 5–10 min at room temperature and stained with 4′,6-diaminophenylindole (DAPI; Prolong Gold antifade, Invitrogen) to visualize nuclei. Images were captured using a laser scanning confocal microscope TCS-SP5 (AOBS) Leica or a Leica DMI 6000B microscope and quantified with ImageJ. The tandem fluorescent-tagged LC3 reporter[20] and the AMPK biosensor[29] were described previously.

For videomicroscopy human cell lines at 60–70% confluency were infected with lentiviruses containing H2B–GFP. Cells were plated on eight-well glass-bottom dishes (Ibidi) and imaged with a DeltaVision RT imaging system (Applied Precision, LLC; IX70/71; Olympus) equipped with a Pl APO 20X/1.42 NA objective lens, maintained at 37 °C in a humidified CO_2 chamber. One micromolar TO-PRO-3 iodide (642/661; Invitrogen T3605) or 10 nM Mitotracker (Life Technologies) was added before recording. Images were acquired every 15 min, and processed and analysed using ImageJ software.

For high-throughput microscopy (HTM) cells were grown on μCLEAR bottom 96-well plates (Greiner Bio-One). After specific treatments, 1 μM TO-PRO-3 iodide (642/661; Invitrogen T3605) and 5 μg ml^{-1} Hoechst 33342 (Invitrogen H3570) were added. After 30 min at 37 °C, images were automatically acquired from each well by an Opera High-Content Screening System (Perkin Elmer). A ×20 magnification lens was used and pictures were taken at non-saturating conditions. Images were segmented using the Hoechst 33342 staining to generate masks matching cell nuclei from which the mean TO-PRO-3 signal was calculated. To monitor reactive oxygen species (ROS), cells were treated with specific drugs and incubated for 30 min at 37 °C as indicated in the OxiSelect Intracellular ROS assay kit, Cell Biolabs and 5 μg ml^{-1} Hoechst 33342 (Invitrogen H3570). Data were acquired by FACS or an Opera High-Content Screening System (Perkin Elmer) as indicated above.

For FRET analysis[29], cells were plated on eight-well flow chambers (Ibidi) and imaged with a Leica AF6000W equipped with fast external filter wheels, a Hamamatsu CCD Camera, an HCX PL APO 40X/oil 1.25 NA objective lens and an AFC hardware autofocus system, maintained at 37 °C in a humidified CO_2 chamber. Images were acquired every 1 or 10 min. Images were processed and analysed using ImageJ software.

AMP/ATP levels, metabolic studies and NMR. Respirometry (OCR) and the extracellular acidification rate (ECAR) of cells were measured with an XF96 Extracellular Flux Analyzer (Seahorse Bioscience). In brief, cells were plated at 1.5–2 × 10^4 cells per well in buffered DMEM containing 25 mM glucose and 2 mM glutamine. Cells were incubated in a CO_2-free incubator at 37 °C for 1 h to allow for temperature and pH equilibration before loading into the XF96 apparatus. Assays consisted of sequential mix (2 min), pause (2 min), mix (0.33 min) and measurement (4 min) cycles, allowing for determination of OCR/ECAR every 8.33 min. Mitotic cells were obtained after shake off and plated in BD Cell-TaK-coated plates. Concentration of ATP was determined spectrophotometrically as described previously[68,69].

For NMR analysis of cell media metabolites[70], 0.5 × 10^6 MEFs were plated in DMEM containing ^{13}C-labelled glucose and synchronized as described above. Five hundred microlitres of supernatant was recovered for every time point, centrifuged at 10,000*g* for 10 min and filtered in 10 kDa Spin Columns (BioVision). Before measurements by NMR, samples were dissolved 1:3 in buffer (0.3 mM TMSP, PBS 3×, 70% deuterated water and 0.09% azide). High-resolution NMR spectra were registered on a Bruker Avance spectrometer operating at 16.4 T and integration regions were then manually defined using the AMIX3.8 software.

For determination of fructose-2,6-bisphosphate (F2,6P2), cell extracts were lysed in 0.1 M NaOH and centrifuged (20,000*g* for 20 min). An aliquot of the homogenate was used for protein determination and the remaining sample was heated at 80 °C (5 min), centrifuged (20,000*g* for 20 min) and the resulting supernatant was used for determination of F2,6P2 concentrations, following the protocols described previously[71].

Transmission electron microscopy. Cells were fixed for 4 h at 4 °C in 4% paraformaldehyde (w/v) and 2.5% glutaraldehyde (v/v) in 0.4 M HEPES buffer pH 7.4, washed and fixed again in aqueous 1% (w/v) osmium tetroxide, and embedded in Epon. Electron microscopy was performed with a JEOL 1230 transmission electron microscope, at 80 kV, on ultrathin sections of 60 nm.

***In vivo* studies.** Athymic nude mice (7-week-old females provided by Harlan Laboratories) were injected subcutaneously in the right and left flanks with 3 × 10^6 MDA-MB-231 cells in 0.1 ml of PBS + 0.5% BSA. Twenty days after cell injection, tumours had grown to an average volume of 150–200 mm^3. Mice were then randomly divided into different experimental groups of 5 animals each (no statistical method was used to predetermine sample size), which received the following treatments as intraperitoneal injections: saline (control), Taxol (5 mg kg^{-1}), 3PO (0.05, 5, 25 or 50 mg kg^{-1}) or a combination of these treatments. The injection was repeated every two days and treatment was continued for 20 days. Tumour volumes were monitored using calliper measurements and were calculated by the formula: $(4p/3) \times (w/2)2 \times (l/2)$. Eight or ten tumours per condition (2 tumours per mice)

DOI: 10.1038/ncb3231

were included in the final analysis as indicated in the corresponding figure legend. The investigators were not blinded to allocation during experiments and outcome assessment. Mouse protocols were approved by the Instituto de Salud Carlos III and Comunidad de Madrid ethical committees following the Spanish Legislation (RD 1201/2005) and the Directive 2010/63/EU of the European Parliament and the Council of the Protection of Animals used for Scientific Purposes.

Statistics. Statistical analysis was carried out using Prism 5 (GraphPad). All statistical tests were performed using two-sided, unpaired Student's *t*-tests, or the Fisher's exact test. Data with $P < 0.05$ were considered statistically significant ($^{*}, P < 0.05$; $^{**}, P < 0.01$; $^{***}, P < 0.001$). When statistical evaluation is not shown in the figures, data or images represent one out of several independent experiments, with no issues of repeatability, as indicated in the figure legends. Source data for all figures can be found in Supplementary Table 4.

62. Salazar, M. *et al.* Cannabinoid action induces autophagy-mediated cell death through stimulation of ER stress in human glioma cells. *J. Clin. Invest.* **119,** 1359–1372 (2009).
63. Tsukamoto, S. *et al.* Autophagy is essential for preimplantation development of mouse embryos. *Science* **321,** 117–120 (2008).
64. Buytaert, E., Callewaert, G., Vandenheede, J. R. & Agostinis, P. Deficiency in apoptotic effectors Bax and Bak reveals an autophagic cell death pathway initiated by photodamage to the endoplasmic reticulum. *Autophagy* **2,** 238–240 (2006).
65. Ortiz-Zapater, E. *et al.* Key contribution of CPEB4-mediated translational control to cancer progression. *Nat. Med.* **18,** 83–90 (2012).
66. Esteban-Martinez, L. & Boya, P. Autophagic flux determination *in vivo* and *ex vivo*. *Methods* **75C,** 79–86 (2015).
67. Mauro-Lizano, M. *et al.* New method to assess mitophagy flux by flow cytometry. *Autophagy* **11,** 833–843 (2015).
68. Saha, A. K. *et al.* Pioglitazone treatment activates AMP-activated protein kinase in rat liver and adipose tissue *in vivo*. *Biochem. Biophys. Res. Commun.* **314,** 580–585 (2004).
69. Maizels, E. Z., Ruderman, N. B., Goodman, M. N. & Lau, D. Effect of acetoacetate on glucose metabolism in the soleus and extensor digitorum longus muscles of the rat. *Biochem. J.* **162,** 557–568 (1977).
70. Bradley, S. A. *et al.* Fermentanomics: monitoring mammalian cell cultures with NMR spectroscopy. *J. Am. Chem. Soc.* **132,** 9531–9533 (2010).
71. Van Schaftingen, E., Lederer, B., Bartrons, R. & Hers, H. G. A kinetic study of pyrophosphate: fructose-6-phosphate phosphotransferase from potato tubers. Application to a microassay of fructose 2,6-bisphosphate. *Eur. J. Biochem.* **129,** 191–195 (1982).

Correction notice

Nature Cell Biology **17,** 1304–1316 (2015)

AMPK and PFKFB3 mediate glycolysis and survival in response to mitophagy during mitotic arrest

Elena Doménech, Carolina Maestre, Lorena Esteban-Martínez, David Partida, Rosa Pascual, Gonzalo Fernández-Miranda, Esther Seco, Ramón Campos-Olivas, Manuel Pérez, Diego Megias, Katherine Allen, Miguel López, Asish K. Saha, Guillermo Velasco, Eduardo Rial, Raúl Méndez, Patricia Boya, María Salazar-Roa and Marcos Malumbres

In the original version of this file posted online, detail was mistakenly omitted from Supplementary Figs 2, 3 and 6. These errors were corrected on 29 September 2015.

nature cell biology

DOI: 10.1038/ncb3231

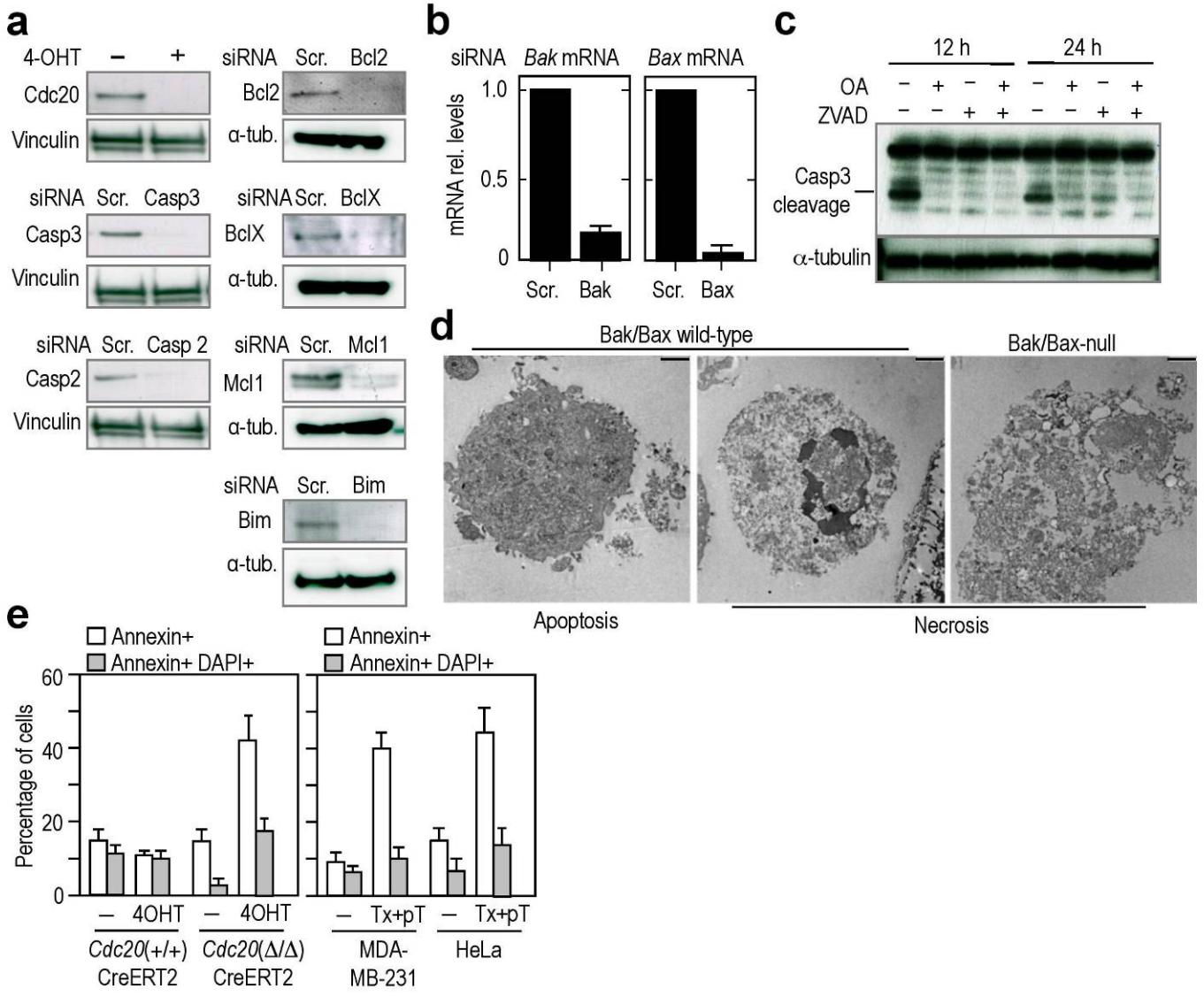

Supplementary Figure 1 Analysis of apoptosis, necrosis and necroptosis. **a**) Depletion of Cdc20 after treatment of *Cdc20*(lox/lox); CreERT2 cells with 4-hydroxytamoxifen (4-OHT) (left top panel). Immunodetection of the indicated proteins after treatment with the indicated siRNAs (rest of panels). Vinculin or α-tubulin were used as a loading control. **b**) Efficiency of the indicated siRNAs by quantification of mRNA levels 48 h after siRNA nucleofection. Data were normalized against the levels of β-actin transcripts. Data are mean ± SD and represent one out of at three independent experiments. **c**) Immunodetection of caspase 3 cleavage in Cdc20-null cells treated with either ZVAD, Okadaic Acid (OA) or both, at the time points indicated. α-tubulin was used as loading control. **d**) Representative electron microscopy images of Bak/Bax-null and wild-type cells arrested in mitosis by the nocodazole-MG132 treatment. Scale bars, 2 μm. **e**) Percentage of cells positive for Annexin V or DAPI in the indicated cultures. The left panel represents Cdc20-null or control cells expressing CreERT2 in the presence of 4-hydroxytamoxifen (4OHT). Right panel represents human cells arrested in mitosis with Taxol and proTAME (Tx+pT). Values are represented as mean ± SD (n=3 independent experiments). For (a,c) uncropped scans of the blots can be found in Supplementary Figure 7. Source data can be found in Supplementary Table 4.

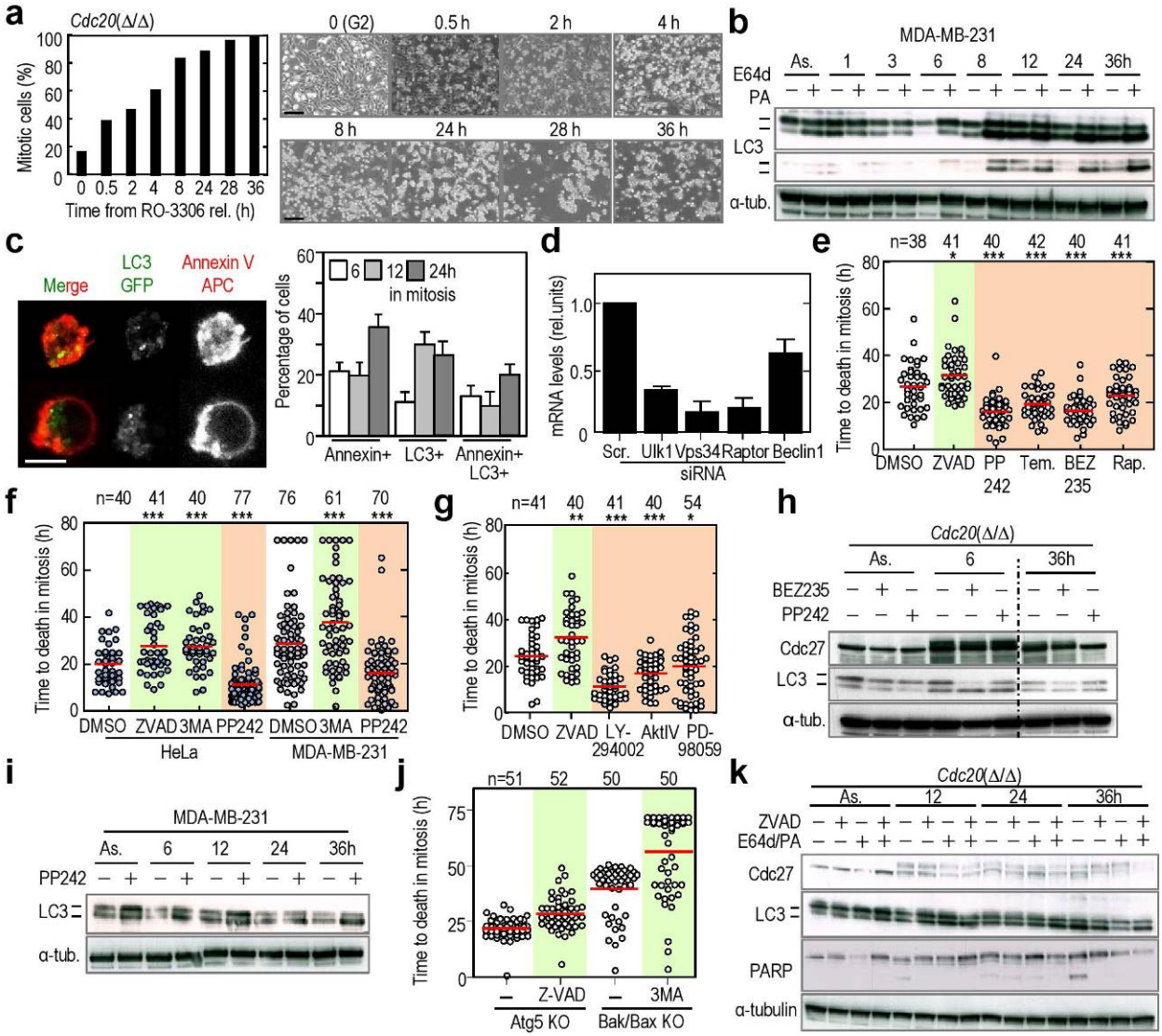

Supplementary Figure 2 Induction of autophagy during mitotic arrest. **a)** Mitotic entry in Cdc20-null cells after release from RO-3306. *Cdc20*(lox/lox) cells were treated with 4-OHT to eliminate Cdc20 12 h prior to the addition of the Cdk1 inhibitor RO-3306 to trigger G2 arrest. This compound was washed-out 18 h later allowing the accumulation of mitotic cells over time (left panel). Representative images are shown in the right panel. Scale bars, 50 μm. **b**) LC3 lipidation was analyzed in MDA-MB 231 cells arrested by treatment with taxol+pro-TAME, in the presence or absence of E64D/PA. Two different time exposures for LC3 are shown. **c**) Colocalization of LC3 and Annexin V (mean ± SD; n= 3 independent experiments) in Cdc20-null cells at the time points of mitotic arrest indicated in the graph. Images are representative for the double staining at 24 h. Scale bar, 10 μm. **d**) mRNA levels (mean ± SD; n=3 independent experiments) of the indicated transcripts 48 h after siRNA nucleofection. Data were normalized against the levels of β-actin transcripts. **e**) Duration of mitosis (from metaphase until cell death) in Cdc20-null cells treated with ZVAD, the indicated inducers of autophagy (mTOR inhibitors PP242, temsirolimus, BEZ235), or transfected with siRNAs against Raptor (Rap.). **f**) Duration of mitosis in Hela and MDA-MB 231 cells synchronized by the taxol+pro-TAME protocol and treated with the indicated inhibitors. **g**) Duration of mitosis in Cdc20-null cells treated with the indicated PI3K/Akt inhibitors. **h**) Immunoblot of LC3 after mTOR inhibition with PP242 or BEZ235 in Cdc20-null cells. Cdc27 band-shift (indicating phosphorylation) was used to confirm mitotic arrest. The samples were processed simultaneously and run in the same blot. **i**) Immunoblot of LC3 after mTOR inhibition with PP242 in MDA-MB-231 cells synchronized by the taxol + pro-TAME protocol. **j**) Duration of mitosis in Atg5-null cells treated or not with the caspase inhibitor ZVAD (left) and Bax/Bak double mutant cells treated or not with the autophagy inhibitor 3MA (right), in both cases using the taxol+pro-TAME protocol. **k**) LC3 lipidation and PARP cleavage after treatment with caspase (ZVAD) and autophagy (E64d/PA) inhibitors in Cdc20-null cells. Cdc27 phosphorylation (retarded motility) indicates mitotic cells. In (b,h,i,k), α-tubulin is included as a loading control. In (e-g; j) dots represent individual cells and the mean are indicated by red lines. The number of cells analyzed (n) is indicated in each condition, and data are representative of three (e), two (f), six (g) or one (j) separate experiments. Green or red backgrounds indicate a significant delay or premature cell death in mitosis, respectively. *, $p<0.05$; **, $p<0.01$; ***, $p<0.001$; Student's t-test. For (b, h, i, k) uncropped scans of the blots can be found in Supplementary Figure 7, and α-tubulin is included as a loading control. Source data can be found in Supplementary Table 4.

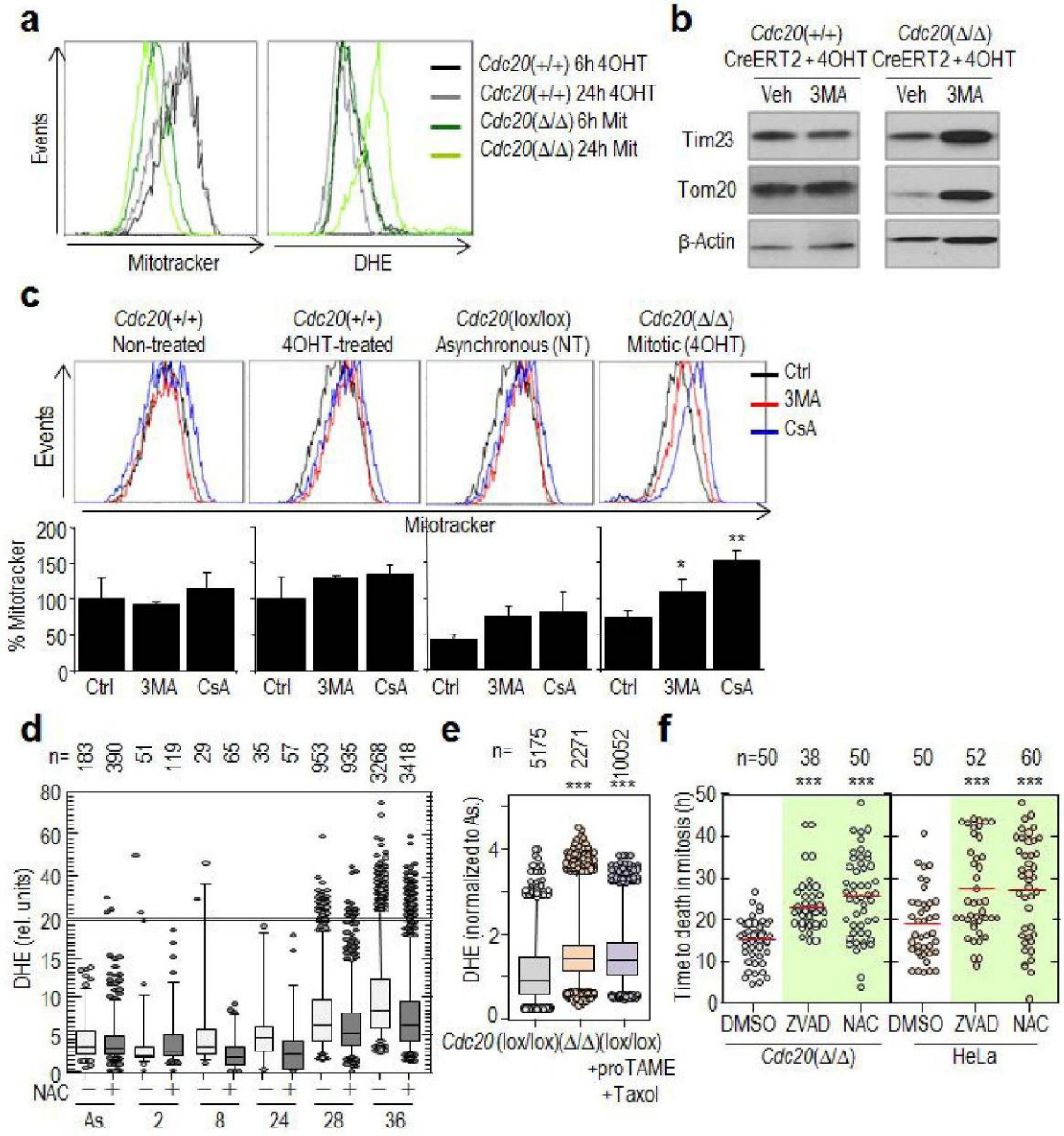

Supplementary Figure 3 Autophagosomes and ROS accumulate during mitotic arrest. **a**) Representative profiles of mitotracker (left) and Dihydroethidium (DHE; right) in Cdc20-null (green) or control (grey) cells expressing CreERT, at the indicated time points after the release from RO-3306 (all the cells were previously treated 18 hours with 4OHT). **b**) Immunodetection of the indicated mitochondrial proteins at 24 h after the release from RO-3306 (all the cells were previously treated 18 hours with 4OHT) in control-CreERT2 (left) and Cdc20-null cells treated with vehicle or the autophagy inhibitor 3MA. Uncropped scans of the blots can be found in Supplementary Figure 7. β-actin was used as a loading control. **c**) Effect of 3MA and Cyclosporin A (CsA) on mitotracker levels in control-CreERT2 (left panels) and Cdc20-null cells 24 h after the release from RO-3306 (all the cells were previously treated 18 hours with vehicle or 4OHT). Representative FACS profiles are shown and quantification of mitotracker signal is represented in the bottom graphs. Data are mean ± SEM (n=3 independent experiments). **d**) Quantification of ROS (mean ± SEM; n=3 independent experiments) in Cdc20-null cells as determined by the OxiSelect TM Intracellular ROS assay kit. The effect of NAC treatment in the accumulation of ROS (mean ± SEM; n=3 independent experiments) is also shown at the indicated times. **e**) Quantification of ROS (mean ± SEM; n=3 independent experiments) in Cdc20-null cells or *Cdc20*(lox/lox) cells arrested in mitosis after 24 h with taxol and pro-TAME, as determined by the OxiSelect TM Intracellular ROS assay kit. **f**) Duration of mitosis until cell death in Cdc20-null and HeLa cells treated with the antioxidant NAC or the caspase inhibitor ZVAD after synchronization with nocodazole and release in MG132. The mean is indicated by red bars and data represent two separate experiments.. In (d,e,f) the number of cells analyzed (n) is indicated in each condition. *, p<0.05; **, p<0.01; ***, p<0.001 (Student's t-test). Source data can be found in Supplementary Table 4.

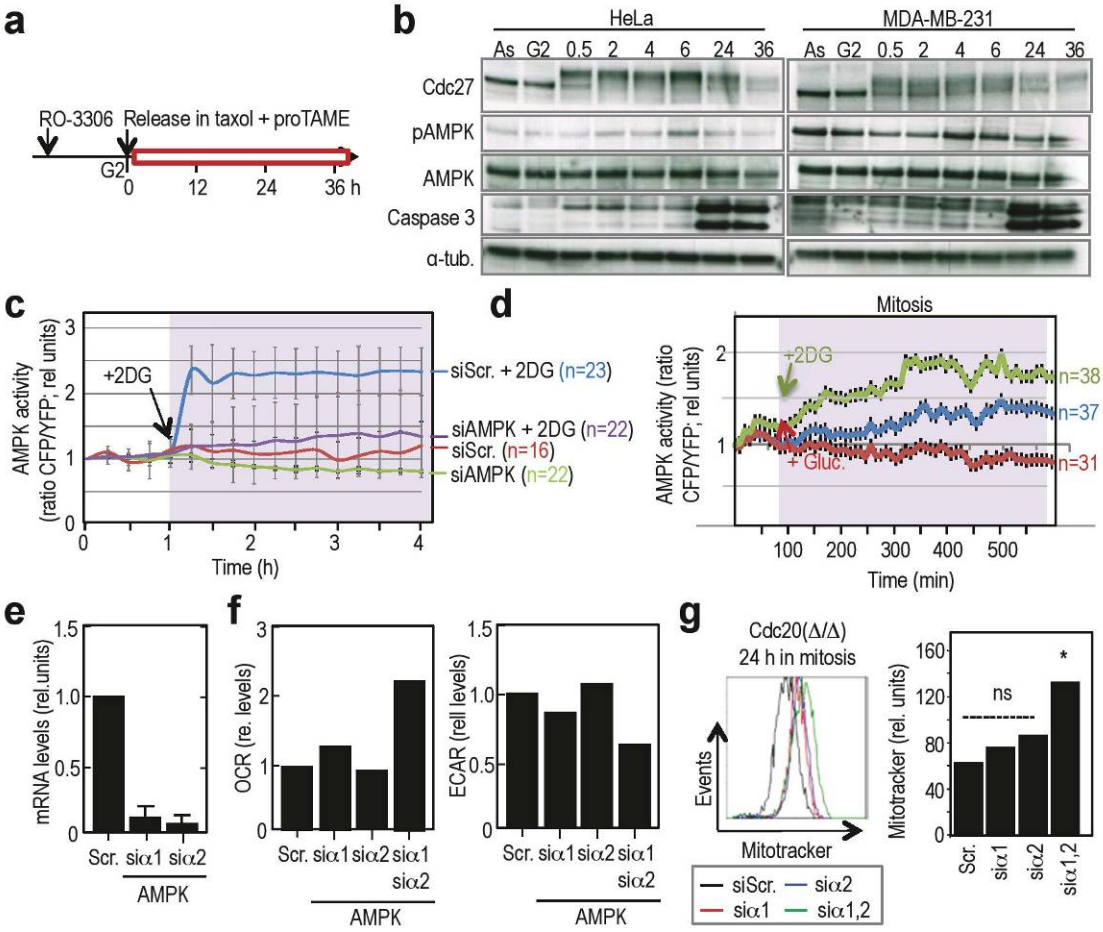

Supplementary Figure 4 AMPK is reactivated during mitotic arrest. **a**) Schematic representation of the protocol followed for synchronization in human cells. Cells were treated with RO-3306 and this compound was washed-out 18 h later allowing mitotic entry in the presence of taxol and pro-TAME (an APC/C inhibitor) which mimic the arrest in metaphase imposed by Cdc20 ablation. **b**) The levels of the indicated antigens were analyzed by immunoblot in HeLa or MDA-MB-231 cells. α-tubulin was included as a loading control and uncropped scans of the blots can be found in Supplementary Figure 7. **c**) Changes in AMPK activity were monitored by using a FRET biosensor in *Cdc20*(lox/lox) cells in the absence of 4-OHT. Upon treatment of these control cells with 2-DG, a glucose analog, AMPK is activated giving an increase of about 2-fold in biosensor signal (indicated in red in the images after 2DG addition; bottom panel). This increase is not observed in cells treated with siRNAs against AMPK**.** Data are mean ± SD (n=4 independent experiments). **d**) AMPK activity was also monitored by the FRET biosensor in mitotic cells treated with vehicle (blue), 2DG (green) or Glucose (red). Data are represented as mean ± SD (n=3 independent experiments) after scoring the indicated number of mitotic cells in each condition. **e**) mRNA levels of APMKα1 and AMPKα2 48 h after nucleofection of specific siRNAs. Data are mean ± SD (n=3 independent experiments) normalized against β-actin mRNA levels. **f**) Levels of OCR (left) and ECAR (right) in Cdc20-null cells arrested in mitosis for 24 h and transfected with siRNAs against siAMPKα1 (siα1), siAMPKα2 (siα2) or the combination of both relative to Scrambled (Scr.) sequences. Data are mean ± SD (one experiment with 12 replicates). **g**) Effect of siRNAs against AMPKα1 and/or AMPKα2 on mitotracker levels in Cdc20-null cells 24 h after the release from RO-3306. Representative FACS profiles are shown on the left, and the quantification of mitotracker signal mean ± SEM (n=3 independent experiments) is represented in the histogram. In (g), ns, no significant; *, p<0.05 (Student's t-test). Source data for all the figures can be found in Supplementary Table 4.

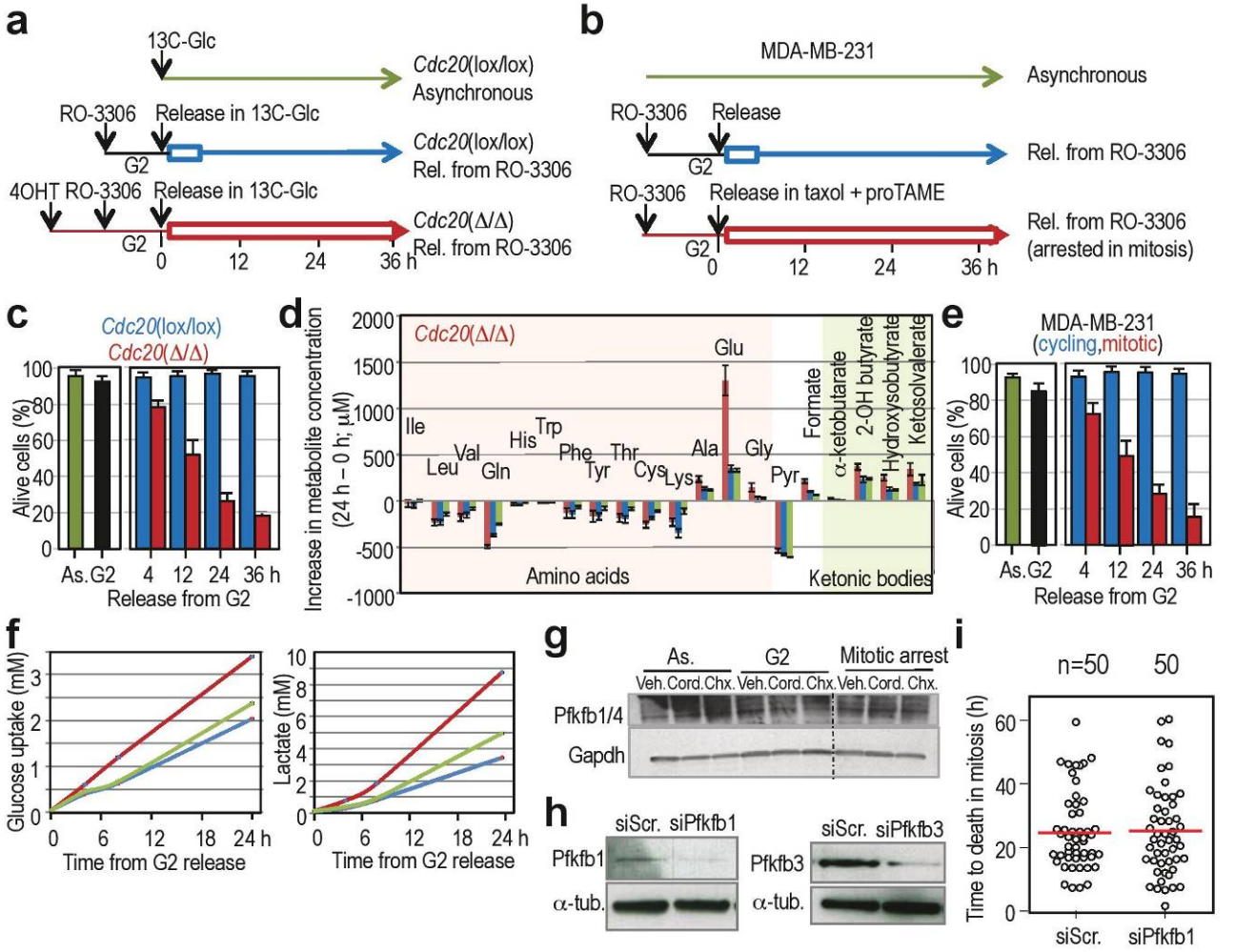

Supplementary Figure 5 Metabolic profile of mitotic arrested cells. **a**) Protocol for synchronized mitotic entry. *Cdc20* (lox/lox) cells were untreated or treated with 4-OHT to eliminate Cdc20 expression, 12 h prior the addition of the Cdk1 inhibitor RO-3306 to trigger G2 arrest. This compound was washed-out 18 h later, allowing cells to progress through the cell cycle (*Cdc20*(lox/lox); blue) or arrest in mitosis in the absence of Cdc20 (*Cdc20*(Δ/Δ); red). Green lines indicate asynchronous cultures and these color codes are maintained throughout the figure to indicate the three different cell cultures. **b**) Similar protocol followed for synchronization in human MDA-MB-231 cells. **c**) Cell viability (TO-PRO3 staining) assessed by flow cytometry in the different cultures represented in (a). **d**) Differential extracellular concentration of the indicated metabolites after 24 h of adding new medium, as monitored by NMR. 34 metabolites were analyzed and only those exhibiting significant differences are represented (23 in this figure + glucose and lactate). No differences were found in carnosine, adenine, glyoxylate, cholesterol, EtOH, niacinamide, acetate, asparagine and aspartic acid. **e**) Cell viability (TO-PRO3 staining) assessed by flow cytometry in the cultures represented in (b). **f**) Glucose uptake and concentration of extracellular lactate in asynchronous (green), normally release from G2 arrest (blue) or mitotic arrested (red) MDA-MB-231 cells, in the presence of ^{13}C-labelled glucose. Data in d) and f) are not normalized for death cells and the differences in mitotic-arrested cells are likely under-estimated. **g**) PFKFB1/4 protein levels in asynchronous (As.), G2-arrested or mitotic Cdc20-deficient cells in the presence or absence or cordycepin (Cord.) or cycloheximide (Chx.). GAPDH was used as a loading control. Images are representative of 2 independent experiments. **h**) Immunodetection of PFKFB1 and PFKFB3 48 hours after transfection. α-tubulin was included as a loading control. For panels (g,h), uncropped scans of the blots can be found in Supplementary Figure 7. **i**) Duration of mitosis (from mitotic entry until cell death) in Cdc20-null cells transfected with siRNAs against PFKFB1 or Scrambled sequences. Each dot indicates a single cells and red lines indicate mean (n=50 cells per condition; one independent experiment). ns, not significant differences. In (c,-f) data are mean ± SD (n=3 independent experiments. Source data can be found in Supplementary Table 4.

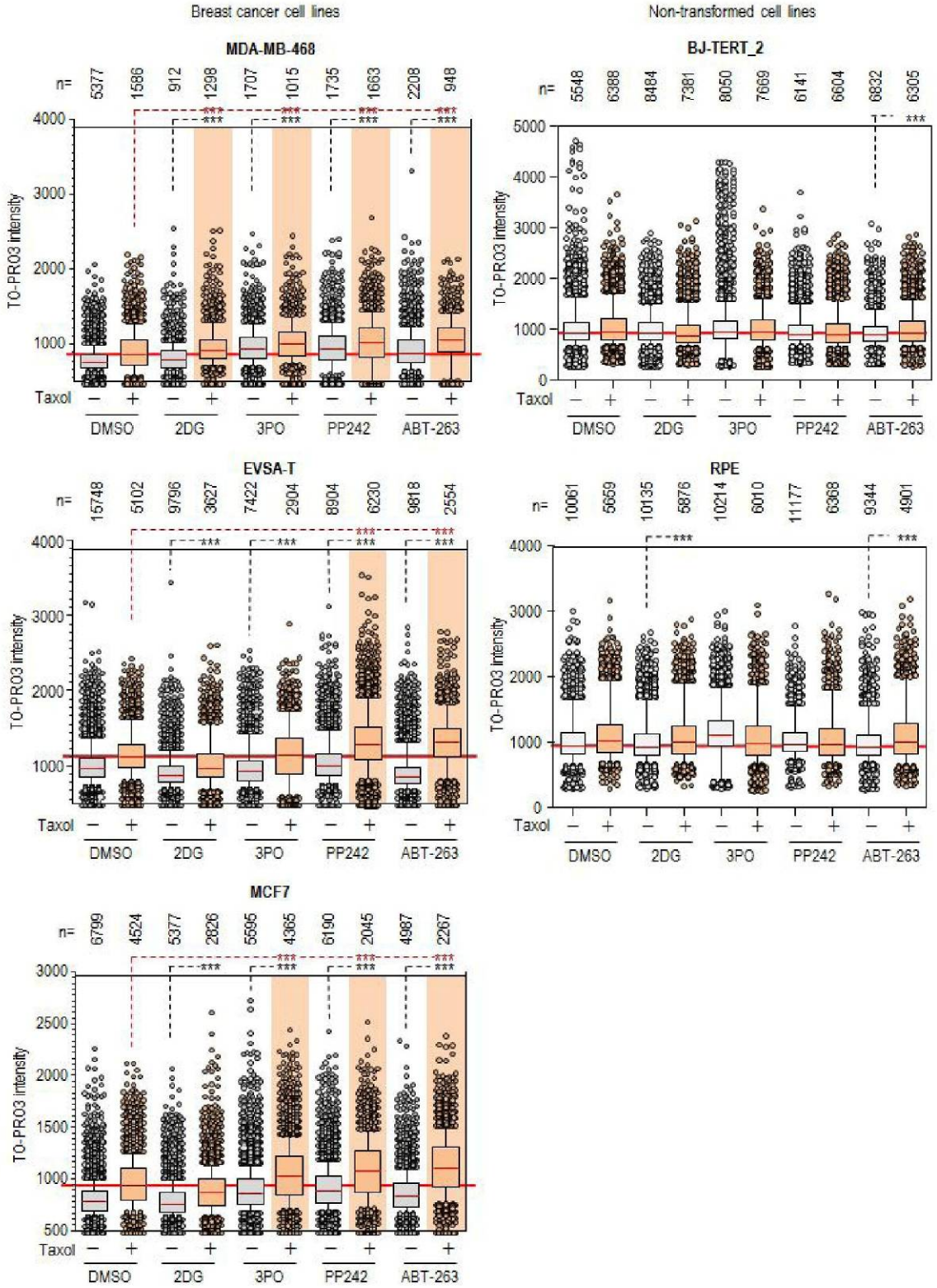

Supplementary Figure 6 Cooperation between taxol and inhibitors of mitotic survival pathways. Cell death was quantified by scoring To-Pro3 levels by high-throughput microscopy after the addition of the indicated compounds in the presence or absence of taxol in MDA-MB-468, EVSA-T or MCF7 breast cancer cells (left panels) or BJ-TERT-2 and RPE non-transformed cells (right panels). Pink columns indicate significant cooperation when compared to both single inhibitors (black dotted comparisons) and taxol (red dotted comparisons). The number of cells analyzed (n) is indicated in each condition. Data are mean ± SEM (n=6 independent experiments). ***, $p<0.001$; Student's t-test, and represent one out of 6 independent experiments. Source data can be found in Supplementary Table 4.

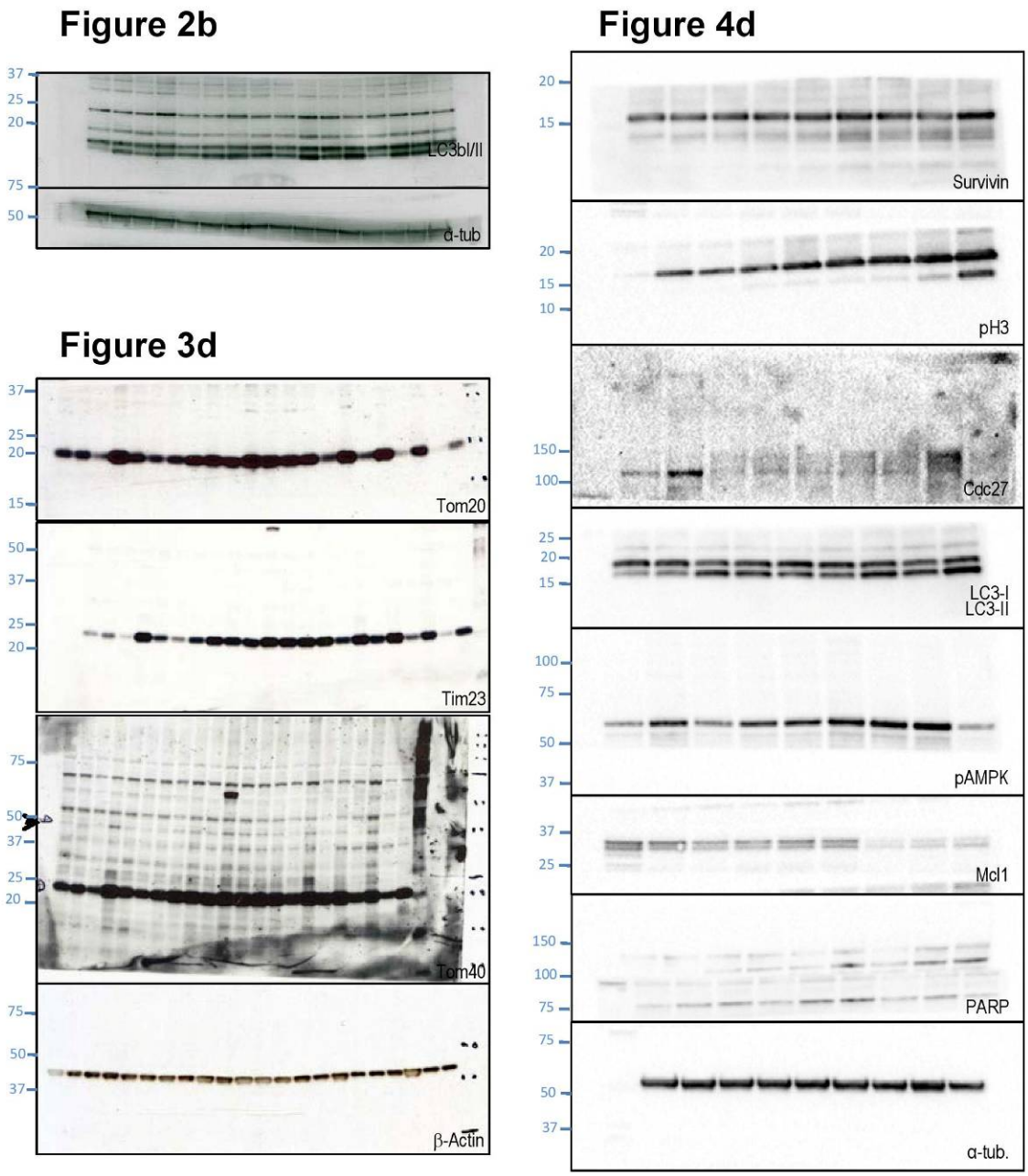

Supplementary Figure 7 Uncropped images of immunoblots.

Figure 5d

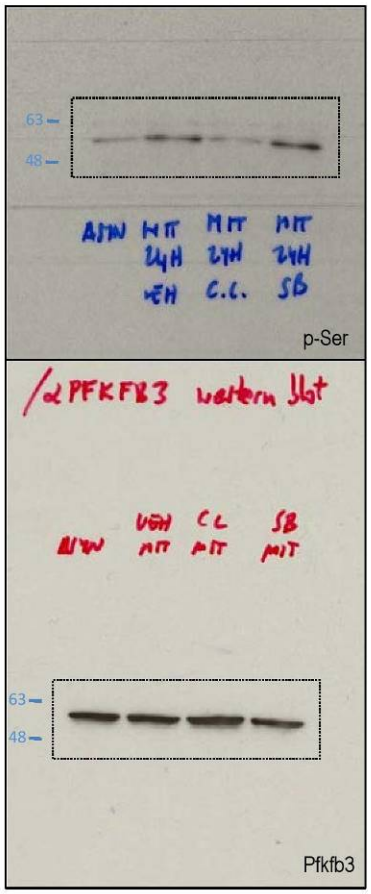

Figure 6a

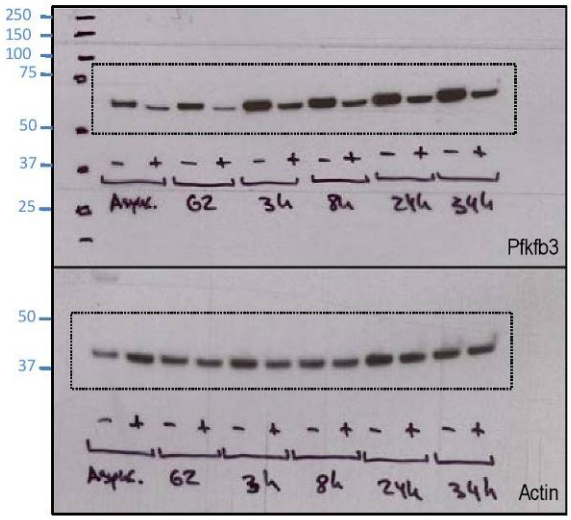

Figure 6d

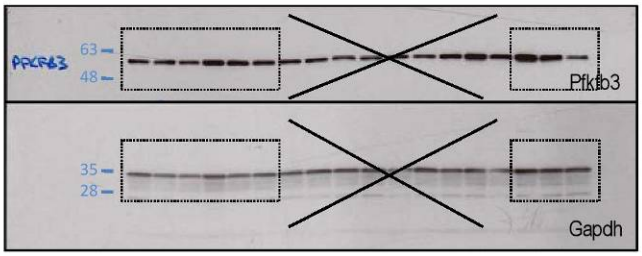

Figure S1a

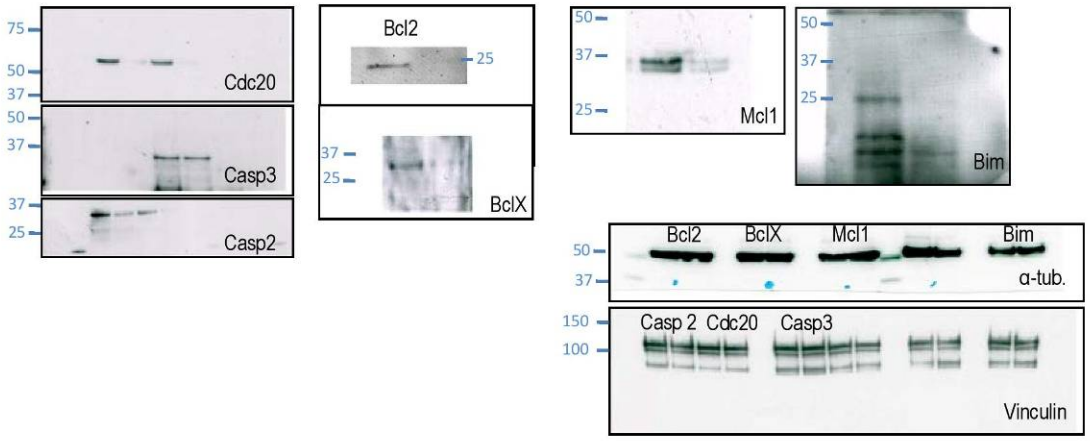

Supplementary Figure 7 continued

Figure S1c

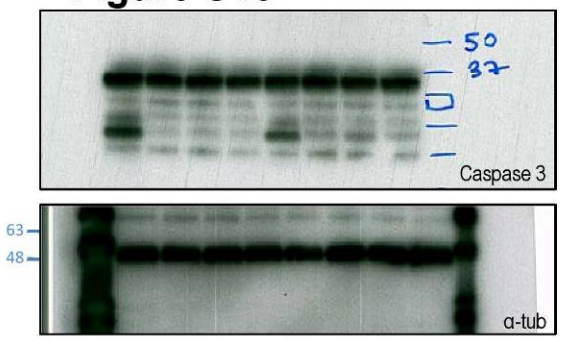

Figure S2k

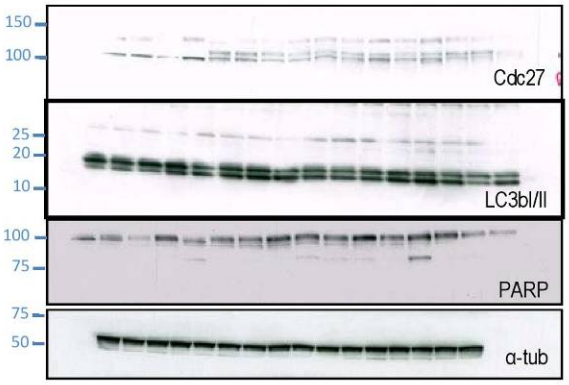

Figure S2b

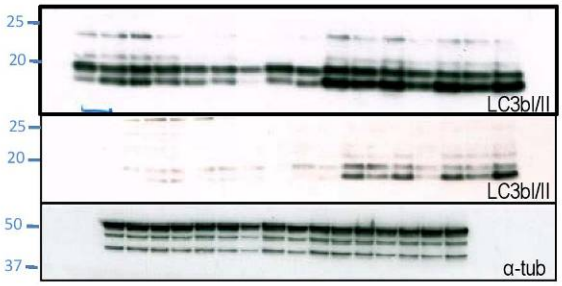

Figure S3b

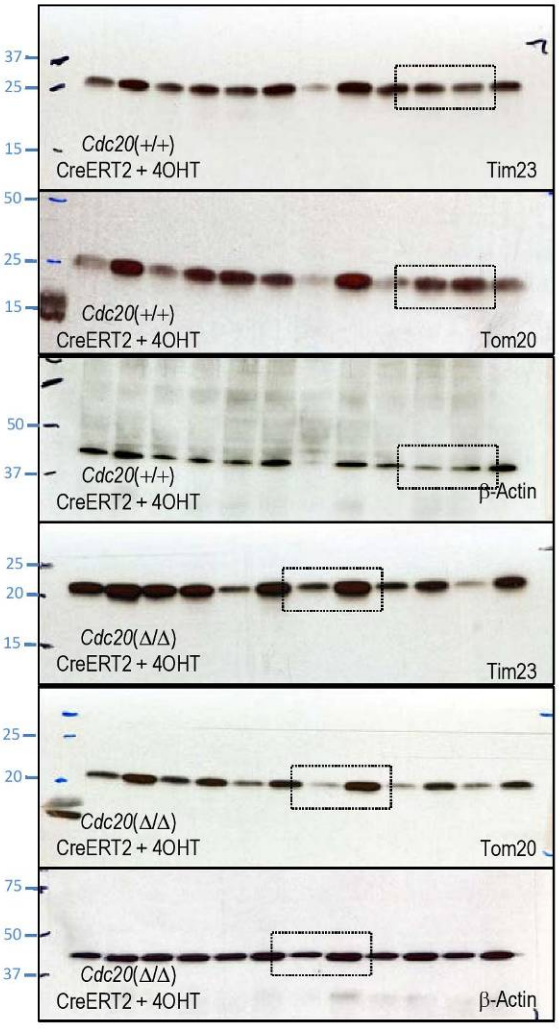

Figure S2h

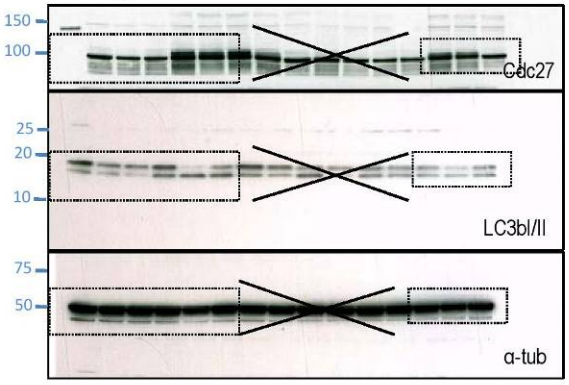

Figure S2i

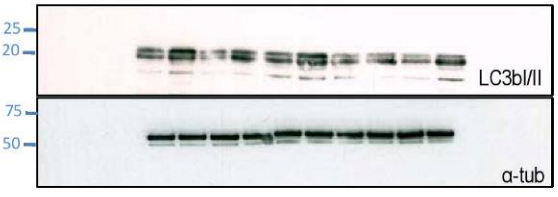

Supplementary Figure 7 continued

Figure S4b

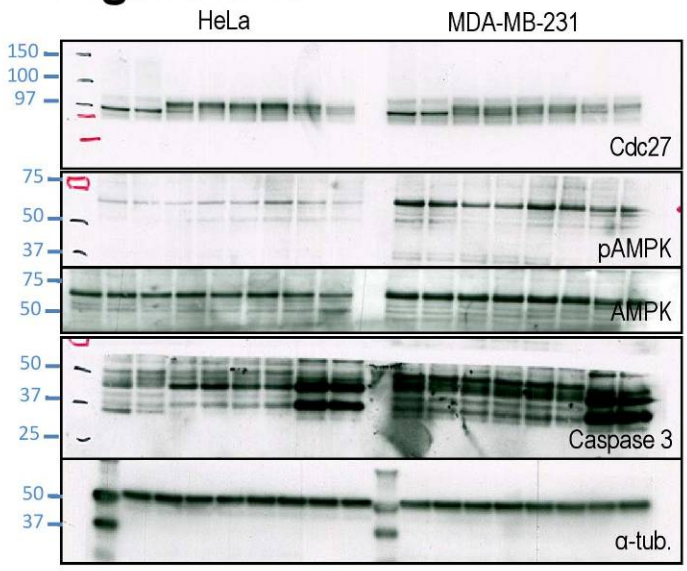

Figure S5g

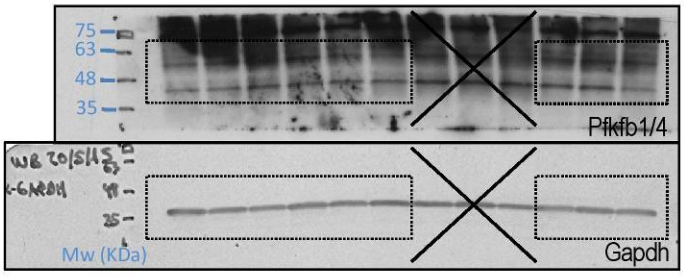

Figure S5h

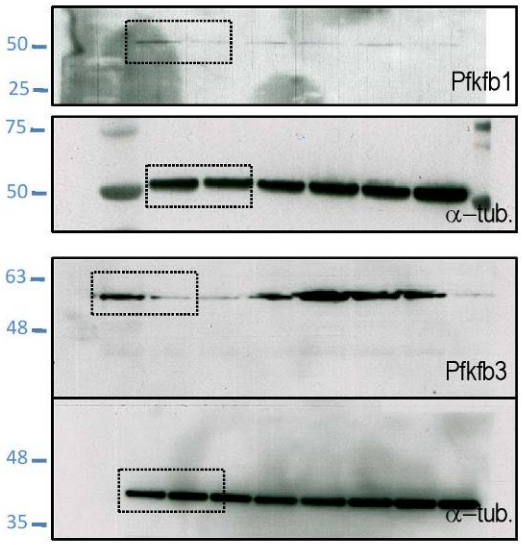

Supplementary Figure 7 continued

Inhibitor	Target	Concentration	Source
2-DG	Hexokinase	5-20 mM	Sigma
3MA	Vps34 (PI3KCIII)	5 mM	Sigma
3PO	PFKFB3	1-100 μM	Millipore
ABT-263	Bcl-2 family + Mcl-1	100 nM	ActiveBiochem
ABT-737	Bcl-2 family	100 nM	Selleckbio
AKTIV	Akt	2 μM	Calbiochem
Actinomycin A	mitochondrial electron transport	1 μM	Sigma
BEZ235	mTORC1 and PI3K	20 nM	Selleck
CCCP	H+ ionophore	10 μM	Sigma
Compound C	AMPK	10 μM	Calbiochem
Cordycepin	Polyadenylation	2 μg/mL	Sigma
Cycloheximide	Protein synthesis	10 μg/mL	Sigma
Cyclosporin A	Cyclophilin	5 μM	Sigma
E64d	Cystein proteases	10 μg/mL	Sigma
LY294002	PI3K	20 μM	Calbiochem
MG132	Proteasome inhibitor	10 μM	Sigma
Necrostatine-1	RIPK1	20 μM	Enzo
Nocodazol	Microtubules	200 nM	Sigma
Oligomycin A	F0 part of the H+-ATP-synthase	2-10 μM	Sigma
Oxamate	LDHA	1 mM	Sigma
PD98059	MEK1 and MEK2	20 μM	Calbiochem
Pepstatin A	Aspartyl proteases	5 μg/mL	Sigma
proTAME	APC/cyclosome	10 μM	Boston Biochem
PP242	mTORC1	10 nM	Sigma
Rapamycin	mTORC1	500 nM	Sigma
RO-3306	Cdk1	1-10 μM	Sigma
Roscovitine	Cdk1	100 μM	Sigma
SB203580	pP38MAPK	20 μM	Enzo
Taxol	Microtubules	20-700 nM	Sigma
Temsirolimus	mTORC1	100 nM	Sigma
Z-VAD-fmk	Pan caspase inhibitor	20 μM	Calbiochem

Supplementary Table 1 Small-molecule inhibitors and other chemicals used in this work.

Gene	Orientation	Sequence
Bak	Forward	CATCTTGGGTCAGGTGGGTC
	Reverse	TGGAACTCTGTGTCGTAGCG
Bax	Forward	TCTCCGGCGAATTGGAGATG
	Reverse	CGTGTCCACGTCAGCAATCA
Beclin1(BECN1)	Forward	TTGAAACTCGCCAGGATGGT
	Reverse	ATCAGATGCCTCCCCGATCA
Drp1	Forward	TCAGAAATGCTACTGGCCCC
	Reverse	TCACGGGCAACCTTTTACGA
PFKFB3	Forward	CCGCGTACCATCTACCTGTG
	Reverse	CAGAGCACTGGCAAACTTCTTG
Raptor	Forward	CTGCTCGTGGCAAGTTTGTT
	Reverse	CTGCTTACTGGGGTGCAGTT
RIPK1	Forward	ACATCAATGCAAAGCCCACG
	Reverse	TGCAGATCACGAACTGCTCA
RIPK3	Forward	GTACGTTCGAAAGAGCCGGG
	Reverse	ATCTTGTCACCAGAGCCTGC
ULK1	Forward	CCTGACTTCCTACAGCGGAG
	Reverse	CTAGCCAACAGGGTCAGCAA
Vps34 (PI3KCIII)	Forward	AGACTTCAGGCCTTGCTTGG
	Reverse	CTTGACGCAAGTCGTCTCCA

Supplementary Table 2 Oligonucleotides used in this work.

Antigen	Catalogue number	Clone number	Source Ig	Dilution	Source
α-tubulin	T9026	DM1A	Mouse	5000	Sigma
AMPK	2532S		Rabbit	1000	Cell Signalling
b-actin	A5441		Mouse	1000	Sigma
Bcl-2	3498		Rabbit	1000	Cell Signalling
Bcl-X	551022	2H12	Mouse	1000	BD Pharmigen
Bim	15184		Rabbit	1000	Abcam
Caspase 2	2251		Rabbit	1000	Abcam
Caspase 3	9662		Rabbit	1000	Cell Signalling
Caspase 3, Active	MAB835		Rabbit	1000	RYD Systems
Cdc20	8358		Rabbit	500	Santa Cruz
Cdc27	10538	35	Mouse	1000	Abcam
CEPB1	13274-1-AP		Rabbit	250	ProteinTech
CEPB4	83009		Rabbit	1000	Abcam
LC3b	L7543		Rabbit	1000	Sigma
Mcl-1	600-401-394		Rabbit	1000	Rockland
Parkin1	15954		Rabbit	1000	Abcam
PARP	9542		Rabbit	1000	Cell Signalling
PFKFB1/4	10096	E-16	Goat	500	Santa Cruz
PFKFB3	131238		Rabbit	1000	Cell Signalling
Phospho-AMPK(Thr172)	2531		Rabbit	1000	Cell Signalling
Phospho-Histone 3 (ser10)	06-570		Rabbit	1000	Millipore
Phospho-Ser	05-1000	4A4	Rabbit	1000	Millipore
Survivin	500-201		Rabbit	1000	Novus Biological
Tim23	611223		Rabbit	1000	BD Bioscience
Tom20	11415		Rabbit	1000	Santa Cruz
Tom40	11414		Rabbit	1000	Santa Cruz
Vinculin	V9131	hVIN-1	Mouse	1000	Sigma

Supplementary Table 3 Antibodies used in this work for immunodetection of proteins.

Supplementary Table 4 Source data used for statistical analysis.

Molecular Biology of the Cell
Vol. 21, 4387–4399, December 15, 2010

Podoplanin Associates with CD44 to Promote Directional Cell Migration

Ester Mart n-Villar,* Beatriz Fernández-Muñoz,†‡ Maddy Parsons,* Maria M. Yurrita,† Diego Meg as,§ Eduardo Pérez-Gómez,† Gareth E. Jones,* and Miguel Quintanilla†

*Randall Division of Cell and Molecular Biophysics, King's College London, Guy's Campus, SE1UL, UK; †Instituto de Investigaciones Biomédicas Alberto Sols, Consejo Superior de Investigaciones Cient ficas (CSIC)-Universidad Autónoma de Madrid (UAM) and §Centro Nacional de Investigaciones Oncológicas, 28029 Madrid, Spain

Submitted June 7, 2010; Revised September 27, 2010; Accepted October 12, 2010
Monitoring Editor: Jonathan Chernoff

Podoplanin is a transmembrane glycoprotein up-regulated in different human tumors, especially those derived from squamous stratified epithelia (SCCs). Its expression in tumor cells is linked to increased cell migration and invasiveness; however, the mechanisms underlying this process remain poorly understood. Here we report that CD44, the major hyaluronan (HA) receptor, is a novel partner for podoplanin. Expression of the CD44 standard isoform (CD44s) is coordinately up-regulated together with that of podoplanin during progression to highly aggressive SCCs in a mouse skin model of carcinogenesis, and during epithelial-mesenchymal transition (EMT). In carcinoma cells, CD44 and podoplanin colocalize at cell surface protrusions. Moreover, CD44 recruitment promoted by HA-coated beads or cross-linking with a specific CD44 antibody induced corecruitment of podoplanin. Podoplanin–CD44s interaction was demonstrated both by coimmunoprecipitation experiments and, in vivo, by fluorescence resonance energy transfer/fluorescence lifetime imaging microscopy (FRET/FLIM), the later confirming its association on the plasma membrane of cells with a migratory phenotype. Importantly, we also show that podoplanin promotes directional persistence of motility in epithelial cells, a feature that requires CD44, and that both molecules cooperate to promote directional migration in SCC cells. Our results support a role for CD44-podoplanin interaction in driving tumor cell migration during malignancy.

INTRODUCTION

Podoplanin (PA2.26 antigen, Aggrus, or T1α) is a type I transmembrane sialomucin up-regulated in different types of cancer, such as squamous cell carcinomas (SCCs) and testicular germ cell tumors (see Wicki and Christofori, 2007 for a review). Several reports support the involvement of podoplanin in malignant progression. First, it has been shown that podoplanin/Aggrus induces platelet aggregation facilitating tumor-platelet aggregate formation and metastasis (Kunita *et al.*, 2007). Second, we found that podoplanin/PA2.26 antigen promotes either cell scattering or a full epithelial–mesenchymal transition (EMT) associated with cell migration, invasion, and metastasis (Scholl *et al.*, 1999; Scholl *et al.*, 2000; Martin-Villar *et al.*, 2005; Martin-Villar *et al.*, 2006). Third, Wicki and colleagues reported that podoplanin can promote collective tumor cell migration and invasion in a pancreatic cancer mouse model (Wicki *et al.*, 2006). Because podoplanin lacks any obvious enzymatic motif within its structure, all these activities have to be mediated by protein–protein interactions, hence the need to identify its binding partners. Thus, the binding of podoplanin ectodomain to C-type lectin-like receptor 2 (CLEC-2) is involved in podoplanin-induced platelet aggregation (Kato *et al.*, 2008), a process which is attenuated by the interaction of podoplanin with CD9 tetraspanin (Nakazawa *et al.*, 2008). In addition, podoplanin-induced EMT is linked to RhoA activation and requires the association of the podoplanin cytoplasmic tail with ezrin and/or moesin, members of the ERM (ezrin, radixin, moesin) protein family of membrane-cytoskeleton linkers (Martin-Villar *et al.*, 2006).

In this report, we identify the standard isoform of CD44 (CD44s) as a novel partner for podoplanin. CD44 is a widely distributed and highly polymorphic type I transmembrane glycoprotein. Although it is encoded by a single gene, the region comprising the extracellular domain includes 10 vari-

This article was published online ahead of print in *MBoC in Press* (http://www.molbiolcell.org/cgi/doi/10.1091/mbc.E10–06–0489) on October 20, 2010.

‡ Present address for B.F.-M.: Centro de Biologia Molecular Severo Ochoa, UAM, Cantoblanco, 28049 Madrid, Spain.

Address correspondence to: Ester Mart n-Villar (ester.martin@kcl.ac.uk) or Miguel Quintanilla (mquintanilla@iib.uam.es).

Abbreviations used: CD44s, CD44 standard isoform; CD44v, CD44 variant isoform; eGFP, enhanced green fluorescent protein; EMT, epithelial to mesenchymal transition; ERM, ezrin, radixin, moesin; FRET-FLIM, fluorescence resonance energy transfer–fluorescence lifetime imaging microscopy; HA, hyaluronan; SCC, squamous cell carcinomas.

able exons (v1–10; CD44v) that can be alternatively spliced, generating multiple isoforms (Screaton *et al.*, 1992). CD44s lacks all the variable exons and has a widespread tissue distribution. An additional source of variation for all the CD44 isoforms is glycosylation, which differ depending on the type and activation state of the cell (Hathcock *et al.*, 1993; Skelton *et al.*, 1998). CD44 functions as the major hyaluronan (HA) receptor and mediates cell adhesion and migration in a variety of pathophysiological processes, including tumor metastasis, wound healing, and inflammation (Isacke and Yarwood, 2002; Marhaba and Zoller, 2004). CD44 can also act as a coreceptor modulating signal transduction through cell-surface tyrosine kinase receptors. Interestingly, this function depends on the ability of CD44 to bind ERM proteins through its cytoplasmic tail (Ponta *et al.*, 2003). The podoplanin–CD44s interaction described here provides a new mechanism by which both of these glycoproteins cooperate to promote cell migration and tumor progression.

MATERIALS AND METHODS

Cell Culture

Epidermal cell lines (Supplemental Table S1) were grown as described before (Quintanilla *et al.*, 2003). MDCK- and MCA3D-podoplanin cell transfectants have been described previously (Scholl *et al.*, 1999; Scholl *et al.*, 2000; Martin-Villar *et al.*, 2006). HEK293T, HT1080, and MDCK-Snail1, -Snail2, and -E47 cells were a generous gift from Dr. Amparo Cano (Instituto de Investigaciones Biomedicas Alberto Sols, Madrid, Spain). HN5 cells were kindly provided by Dr. Marcella Flinterman (Oral Pathology Department, King's College London, London, UK). HaCaT, HEK293T, HT1080, HN5, and MDCK cells were grown in Dulbecco's Modified Eagle Medium (DMEM) supplemented with 10% fetal calf serum, (Biosera, Sussex UK) 1% Pen-Strep (Sigma, Dorset, UK) and L-glutamine (PAA Laboratories GmbH, Germany).

cDNA Constructs and RNA Interference

Full-length wild-type human podoplanin and mutant constructs subcloned into the pcDNA3 and pEGFP vectors have been described elsewhere (Martin-Villar *et al.*, 2006). Human podoplanin and CD44s tagged with Hae and Flag at the C terminus and mRFP-tagged CD44s constructs were obtained by PCR amplification using primers that carry convenient restriction sites to facilitate subcloning into pcDNA3-Hae/Flag and pmRFP-N1 vectors. Oligonucleotides used for amplification of all these constructs are described in Table S2 in the Supplemental material.

Short-hairpin RNAs (shRNAs) targeting human podoplanin mRNA were cloned into pLKO.1 vector (Addgene, Cambridge, UK). Lentiviral supernatants were produced in HEK293T cells by cotransfection of pCMV-d8.9 (packaging plasmid), pMD2G (envelope plasmid), and pLKO.1 including targeting sequences and collected after 24 and 48 h. HN5 cells were grown at (~70%) confluence and infected with lentiviral supernatants. After 48 h, infected HN5 cells were selected by addition of 1.4 μg/ml puromycin (Sigma). Both podoplanin target sequences, 5′AAGACCGTTCACCAGACTTGG3′ (podo sh1) and 5′AACACTGGACCATTGGATCGA3′ (podo sh2), successfully knocked-down expression of the target gene. For control experiments, cells were infected with viral vectors containing scrambled shRNA (Addgene; ID 1864).

For CD44 down-regulation in MDCK cells following small interfering (siRNA) oligonucleotides were used: 5′ GACCACGACUCAUCGGUUC dT dT3′ and GAACCGAUGAGUCGUGGUC dT dT3′. siRNA against Firefly luciferase GL3 was used as negative control (Elbashir *et al.*, 2001).

For human CD44 knockdown the following siRNAs were used: 5′GUAUGACACAAUAUUGCUUC dT dT3′ and 5′GAAGCAAUAUGUGUCAUAC dT dT3′ (Roscic-Mrkic *et al.*, 2003). Control oligonucleotides where purchased from Ambion (Warrington, UK; Silencer Negative control #1, AM4611). Annealed siRNA oligonucleotides were transfected with 100 μM oligofectamine (Invitrogen, Paisley, UK) in Opti-MEM reduced-serum medium (Invitrogen). Cells were incubated at 37oC for 6 h before the addition of FBS to 10%. All the assays were conducted at 48–72 h after transfection.

Mouse Skin Carcinogenesis

The two-stage mouse skin carcinogenesis (a single DMBA application followed by twice weekly applications of TPA for 16 wk) was performed following standard protocols (Perez-Gomez *et al.*, 2007). Tumors were collected at different time periods after initiation (papillomas at 30 wk and SCCs at 43 wk) and processed for Western blotting. Tumors were histologically typed by H&E staining of paraffin sections and characterized by the expression of the following differentiation/progression markers: keratins K1 and K10, which are lost in SCCs; the extracellular matrix component SPARC, which is induced during progression from papillomas to SCCs; as well as the E-cadherin transcriptional repressor Snail1 and the enzyme lysyl oxidase-like 2, which accumulate in poorly differentiated SCCs, as previously described (Perez-Gomez *et al.*, 2007).

RT-PCR

Reverse transcription was performed as previously described (Martin-Villar *et al.*, 2006). For CD44 analyses specific primers were designed to amplify both human and canine genes: 5′-TATTGCTTCAATGCTTCAGCTCCA-3′ and 5′-AGGTTGTGTTTGCTCCACCTTCTTGAC-3′. PCR products were obtained after 35 cycles of amplification with an annealing temperature of 60°C.

Western Blot and Coimmunoprecipitation Experiments

For detection of podoplanin and CD44 in Western blots, cells or tissues were lysed in buffer RIPA (0.1% SDS, 0.5% sodium deoxycholate, 1% Nonidet P-40, 150 mM NaCl, 50 mM Tris-HCl pH 8.0) and a cocktail of protease inhibitors (1 mM phenylmethylsulfonyl fluoride, 2 μg/ml aprotinin and 2 μg/ml leupeptin). Samples containing the same amount of protein (10–30 μg) were run on 10% SDS-PAGE and transferred to Immobilon P membranes (Millipore, Bedford, MA). Filters were then immunoblotted with the following Abs: anti mouse podoplanin (PA2.26 mAb; previously described in Gandarillas *et al.*, 1997), anti human podoplanin (NZ1 mAb purchased from Acris Antibodies, Herford, Germany), rat mAb IM7 against CD44 ectodomain (generously provided by Dr Helen Yarwood; The Institute of Cancer Research, London, UK), rabbit polyclonal Ab raised to the COOH terminal region of CD44 (CD44cyto, Abcam, Cambridge, UK), and mouse mAbs against α-tubulin, β-actin (Sigma) and GAPDH (Roche Diagnostics, Welwyn Garden City, UK).

For coimmunoprecipitation experiments HEK293T cells were transiently cotransfected with expression vectors using Effectene (Qiagen, Crawley, UK), as indicated by the manufacturer. After 24 h, cells were lysed in IP buffer (50 mM Tris-HCl pH 8.0, 100 mM NaCl, EDTA 5 mM, 0.5% Triton X-100, 10% glycerol) containing Complete Protease Inhibitors Cocktail Tablets (Roche Diagnostics). Tagged CD44s-Hae or podoplanin-Flag proteins were immunoprecipitated using anti-Hae (Roche Diagnostics) or anti-Flag (Sigma) mAbs linked to protein A/G resin (Alpha Diagnostic, TX), respectively. After incubation with 500–750 μg of cell lysates for 2h at 4°C, the resin was then washed five times with lysis buffer, and the coimmunoprecipitates were eluted in 1× Laemmli Buffer. Immunoprecipitation of endogenous podoplain in CarC cells was performed using the PA2.26 mAb for mouse podoplanin and the coimmunoprecipitated products were detected by using the rat mAb IM7 against the CD44 ectodomain.

Coimmunoprecipitation assays of podoplanin-eGFP tagged constructs were performed using an anti-GFP antibody-conjugated resin. The resin was made by cross-linking a GFP polyclonal antibody (MBL International, Woburn, MA) to the protein G beads using a Seize X protein G immunoprecipitation kit purchased from Pierce Biotechnology (Leicestershire, UK). Coimmunoprecipitation was done following the protocol provided by the manufacturer.

Bead and Antibody-Mediated Clustering Assays

Bead coating and incubation were performed as previously described (del Pozo *et al.*, 2004). Briefly, 5-μm polystyrene beads (Duke Scientific Corporation, Palo Alto, California) were washed in PBS and incubated with 5 mg/ml BSA or 1 mg/ml high molecular mass HA (Sigma, H7630). Beads were left overnight at 4°C to allow even protein binding, washed three times, and resuspended in PBS to form a 50% slurry final concentration. Coating efficiency of beads with HA was also tested by incubating the beads with fluorescently labeled HA (FITC-HA). Cells plated onto coverslips were incubated with 5 μl/ml coated-beads in growth media and incubated at 37°C for 15–30 min. Cells were then washed three times in medium and fixed for immunofluorescence analysis.

Antibody-mediated clustering assays were performed as described previously (Clark *et al.*, 2005). HN5 cells were platted on glass coverslips in DMEM. To cluster CD44, CD44 mAb HP2/9 (generously provided by Dr. Francisco Sánchez-Madrid; Centro Nacional de Investigaciones Cardiovasculares, Madrid, Spain) was incubated with cells in serum-free medium at a concentration of 1 μg/ml for 1 h at 37°C. After three washes with warm PBS to remove all nonbound Ab, a Cy3-labeled secondary Fc-specific Ab (2 μg/ml), was added for 1 h. Under these conditions the secondary Ab induces the cross-linking of the primary Ab through its Fc-tail. This results in clustering the protein of interest. After washing the samples three times with warm PBS, cells were fixed and processed for immunofluorescence as described below.

FRET-FLIM Microscopy

FLIM was used to measure FRET between podoplanin eGFP constructs and CD44s-mRFP in MDCK cotransfected cells. Podoplanin-eGFP and CD44-mRFP constructs (at a Podoplanin-eGFP to CD44s-mRFP ratio of 1:3) or with Podoplanin-eGFP alone were cotransfected using FuGene6 (Roche) according to the manufacturer's instructions. Cells were left to express the constructs for 48 h and then fixed with 4% paraformaldehyde in PBS for 20 min, permeabilized with 0.01% Triton X-100/PBS for 10 min, and incubated with 1 mg/ml fresh Sodium Borohydride/PBS for 10 min at room temperature.

FLIM measurements were performed on a multiphoton microscope via time-correlated single-photon counting (for details see Parsons *et al.*, 2008). FLIM analysis to calculate eGFP lifetime and FRET efficiency was performed using TRI2 software (developed by Paul Barber, Gray Cancer Institute, London, UK).

Confocal Microscopy and Morphological Analysis

Cells on coverslips were fixed with 3.7% formaldehyde for 30 min and permeabilized with 0.05% Triton-X100/PBS for 10 min. Podoplanin and CD44 staining was carried out using the anti-human podoplanin mAb (NZ-1) and the anti-CD44 HP2/9 mAb. Confocal images were acquired on a Leica TCS-SP2 microscope for Figure 2A or on a NIKON A1 confocal laser-scanning microscope for Figure 2, B and C and Figure 7. Images were assembled using Leica confocal software 2.0 or NIS-Elements AR 3.0.

For morphological analyses cells were allowed to spread for 24 h and then processed for immunofluorescence. The actin cytoskeleton was visualized by staining with Alexa Fluor 568-labeled phalloidin (Invitrogen). Tubulin was detected using a specific mouse anti–α-tubulin Ab (Sigma). Cell area was quantified using the public domain program NIH ImageJ (developed at the US National Institutes of Health).

Cell Migration Assays and Time-Lapse Microscopy

The migratory behavior of the cells was analyzed by using 8-μm pore transwell chambers (Corning, Amsterdam, NE) and in vitro scratch assays. For transwell assays MDCK cells were cotransfected with podoplanin-eGFP or eGFP and CD44 or control siRNA. 2.5×10^4 cells per well were seeded 48 h after transfection in DMEM containing 0.1% FBS and allowed to transmigrate to 10% FBS medium for 12 h at 37°C. Cells on the upper side of the transwell were then removed, and those on the underside were fixed and stained with crystal violet. Cell migration was quantified by counting the number of cells that migrated through the inserts (three different fields per well were counted under a NIKON Eclipse TS100 inverted light microscope, using a ×10 objective).

Random migration analysis in MDCK cells was performed by time-lapse fluorescence microscopy. Cells were sparsely plated, grown in the absence of serum, and imaged overnight. Pictures were taken every 5 min with the ×10 objective of a Leica DMI6000B inverted fluorescence microscope. Migration was analyzed by Imaris 6.4.2 software to obtain cell trajectories and calculate path length, displacement from origin, and average speed (total path length/time). Persistence of migration (directionality) was defined as displacement from origin/total cell path.

For wound healing assays podoplanin- and/or CD44-depleted HN5 cells were plated onto collagen I (BD Biosciences, Oxford, UK)-coated 12-well plates and left for 24 h to form a monolayer. Confluent monolayers were scratched with a tip and cells were imaged in an atmosphere of 5% CO2 at 37°C with a ×5 phase objective and an inverted microscope (Axiovert 100, Carl Zeiss MicroImaging,) equipped with a charge-coupled device camera (Sensicam;PCO) and motorized stage (Ludl). Images of the wounds were collected every 10-min intervals for a period of 18 h. Image acquisition was controlled by ANDOR IQ software. Sequences of images were quantitatively analyzed using ImageJ software. Cell outlines were drawn along the wound edge at time 0 h and 18 h. Migration was quantified by calculating the area between the two outlines. Kinetics of migrating cells along the wound edge were analyzed using the manual tracking tool in Image J and Mathematica 7.0 workbooks (Allen *et al.*, 1998). Images and videos were assembled using Image J and Adobe Premiere Pro1.5 software.

Statistics

All experiments were performed at least three times. Data are presented as mean ± SEM. Significance was determined using one-way analysis of variance (ANOVA) followed by Bonferroni's post test or two-tailed Student's *t* test. $p < 0.05$ was considered statistically significant. All statistical analyses were performed using GraphPad Prism 4.0 software.

RESULTS

The Coordinate Expression of Podoplanin and CD44s Correlates with Malignant Progression and EMT

We have previously shown that ectopic expression of podoplanin in epithelial MDCK cells promoted a dramatic change from an epithelial to a fibroblastic-like morphology linked to down-regulation of epithelial genes, such as E-cadherin, and up-regulation of mesenchymal markers, such as fibronectin (Figure S1 in supplementary material; Martin-Villar *et al.*, 2006). When the levels of CD44 mRNA and protein were analyzed in MDCK cells expressing podoplanin (MDCK-Podo), a switch in the expression from CD44v isoforms to CD44s was associated with the acquisition of a fibroblastic phenotype (Figure 1A). As shown in Figure 1B, this CD44 isoform switch was also seen in EMTs induced by the overexpression of the E-cadherin repressors Snail 1, Snail 2, and E47 in MDCK cells (Peinado *et al.*, 2007).

EMT in mouse skin chemical carcinogenesis is associated with progression from well-differentiated tumors to highly aggressive undifferentiated or spindle cell carcinomas (Akhurst and Balmain, 1999). Because podoplanin was identified as a cell-surface protein induced in keratinocytes during mouse skin carcinogenesis (Gandarillas *et al.*, 1997), we analyzed CD44 and podoplanin expression in cell lines and tumors corresponding to different stages of carcinogenesis (Figure 1, C and D). In both cases, the coordinated up-regulation of podoplanin and CD44s was associated with the undifferentiated phenotype. CD44s was barely detected in the normal epidermis and in benign papillomas, but it was clearly induced in SCCs and further increased in poorly differentiated tumors (Figure 1C). We, therefore, observed an overall increase in CD44 expression that correlated with malignant progression during carcinogenesis in vivo. Furthermore, epithelial premalignant (MCA3D and PB) and weakly metastatic carcinoma (PDV and B9) cell lines expressed low or null amounts of CD44s (Figure 1D); however, its expression was significantly enhanced in highly invasive carcinoma cell lines exhibiting a fibroblastic or spindle phenotype (HaCa4, A5, CarC, and CarB), and this increase occurred concomitantly to down-regulation of CD44v. For a summary of characteristics of the epidermal cell lines used in this study, see Table S1 in supplemental material. Interestingly, podoplanin expression followed a pattern roughly similar to that of CD44s in tumors and cell lines (Figure 1, C and D). The pair of cell lines B9 and A5 representing a homogeneous model for malignant progression is illuminating in this respect. Both cell lines were derived from the same carcinoma, B9 from the squamous component and A5 from the anaplastic spindle region (Burns *et al.*, 1991). While B9 neither expressed CD44s nor podoplanin, both glycoproteins were present in A5 cells (Figure 1D). Furthermore, the ectopic expression of mouse podoplanin in pre-malignant MCA3D keratinocytes promoted an EMT associated with the acquisition of highly invasive and metastatic properties (Scholl *et al.*, 1999; Scholl *et al.*, 2000) and the induction of CD44s expression (Figure 1D). Both podoplanin and CD44s protein levels were also increased in LN11 cells derived from a lymph node metastasis produced by podoplanin-expressing MCA3D cells (Figure 1D and Table S1).

Podoplanin Interacts with CD44s

The subcellular localization of CD44 in podoplanin-expressing cells was analyzed by confocal microscopy. Images revealed that CD44 was distributed along the plasma membrane, concentrated at cell surface protrusions where it colocalized with podoplanin. This was the case for MDCK cells expressing exogenous podoplanin tagged with eGFP (P_{WT} eGFP) and oral carcinoma HN5 cells expressing endogenous podoplanin (Figure 2A). To determine whether the binding of HA to CD44 affected the membrane localization of podoplanin, P_{WT} eGFP cells plated onto coverslips were incubated with 5-μm beads coated with HA. As shown in Figure 2B, podoplanin was recruited by HA-coated beads together with CD44. Binding was specific, as control BSA-coated beads did not trigger recruitment of CD44 or podoplanin. To analyze the possibility of a physical association between podoplanin and CD44, we performed coclustering experiments in P_{WT} eGFP-expressing HN5 cells. These cells were treated in vivo with an antibody raised to the CD44 ectodomain (HP2/9), and then the antibody was clustered with a secondary antibody. This resulted in the formation of

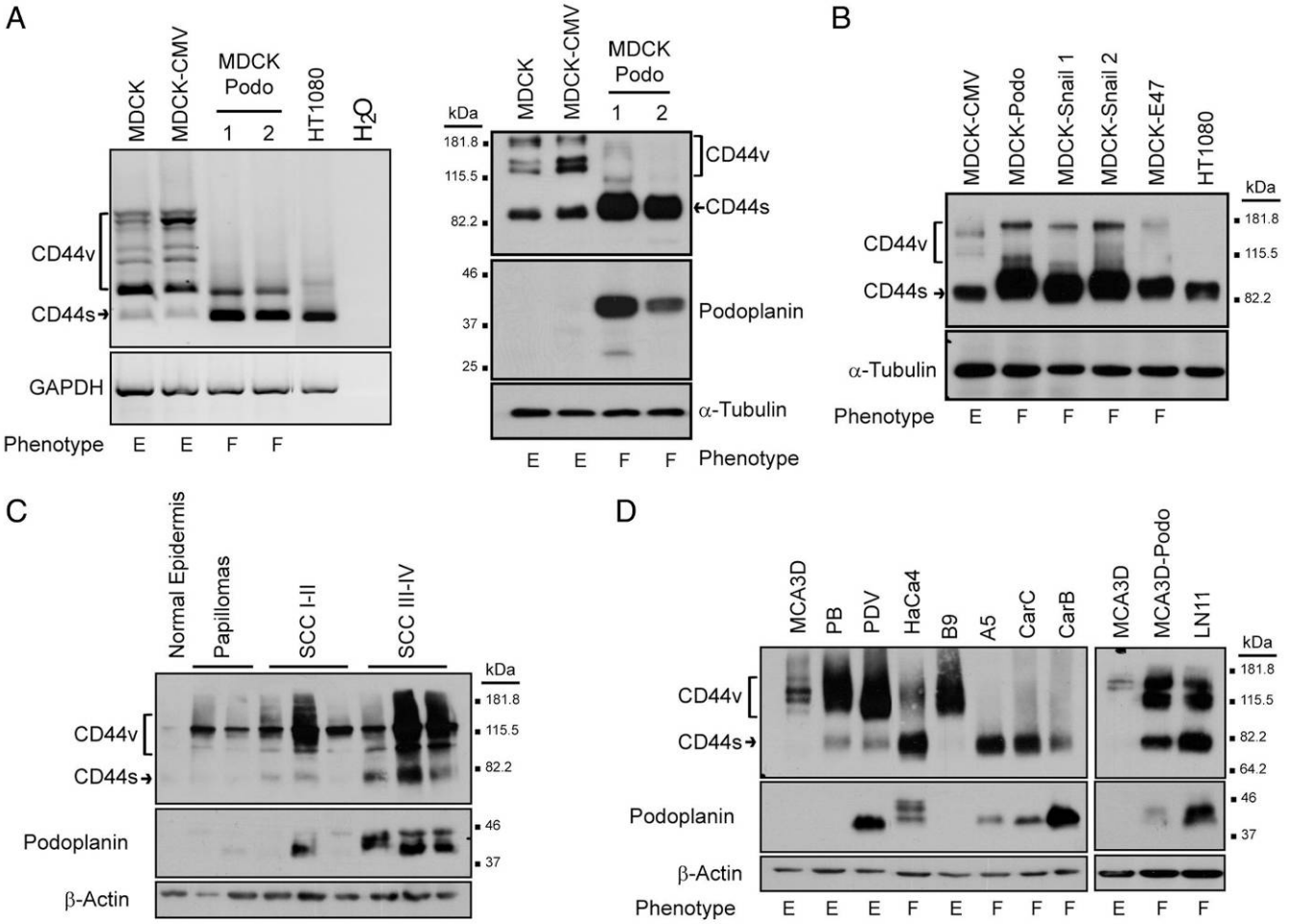

Figure 1. Podoplanin and CD44 expression during EMT and mouse skin carcinogenesis. (A) Podoplanin-promoted EMT in MDCK cells is associated with induction of CD44s expression. The phenotype of the cell lines is indicated: E, epithelial; F, fibroblastic. The morphology and characterization of these cells is shown in Supplemental Figure S1 and in Martin-Villar *et al.* (2006). The fibrosarcoma HT1080 cell line was used as a positive control for CD44s expression. Left and right panels show, respectively, the expression of CD44 transcripts (RT-PCR) and proteins (Western blot). (B) CD44 protein expression in MDCK cells that underwent EMT by transfection of E-cadherin repressors Snail 1, 2, and E47. (C) CD44 and podoplanin protein expression in mouse normal epidermis and skin tumors induced by two-stage carcinogenesis. All squamous cell carcinomas (SCCs) were excised at 43 wk post-initiation. SCCI-II, well to moderately differentiated; SCCIII-IV, poorly differentiated. (D) CD44 and podoplanin protein expression in mouse epidermal cell lines (see table S1 for further information of the cells lines). MCA3D keratinocytes forced to express podoplanin (MCA3D-Podo) undergo EMT. CD44s, CD44 standard isoform; CD44v, variant CD44 isoforms. GAPDH and α-tubulin/β-actin were used as loading controls for RNA and protein, respectively.

CD44 fluorescent spots on the cell surface and in cell–cell contacts (Figure 2C). Interestingly, CD44 clustering induced corecruitment of P_{WT}eGFP suggesting that both proteins are associated either directly or indirectly within the plasma membrane. Reciprocally, clustering of podoplanin also induced corecruitment of CD44 (Figure S2).

We next studied the interaction of these proteins by coimmunoprecipitation analysis. To this end, HEK293T cells were cotransfected with constructs encoding podoplanin and CD44s tagged with Flag and hemagglutinin (Hae) epitopes at the COOH-terminal end, respectively (see in Figure 5A a schematic representation of these constructs). Expression of both molecules resulted to be heterogeneous in their apparent molecular masses as several bands were detected in the immunoblots (Figure 3 and Supplemental Figure S3). We have previously shown that podoplanin heterogeneity in SDS-PAGE arises from the presence of O-linked carbohydrates in its ectodomain (Scholl *et al.*, 1999; Martin-Villar *et al.*, 2005). Similarly, molecular mass variability of CD44s has been commonly attributed to glycosylation changes, in particular N-linked oligosaccharides (Camp *et al.*, 1991; Skelton *et al.*, 1998). Indeed, removal of N-linked sugars in the CD44s protein confirmed that extracellular modifications were largely responsible for CD44s molecular mass heterogeneity (Supplemental Figure S3, C and D). Immunoprecipitation experiments confirmed that CD44 and podoplanin coprecipitated with each other (Figure 3A). Interestingly, coprecipitated CD44s and podoplanin had a lower molecular mass (45–65 kDa for CD44s, and ~30 kDa for podoplanin; Figure 3A and Supplemental Figure S3) than that of the corresponding mature fully glycosylated forms, indicating that the interaction between podoplanin and CD44s could be dependent on the carbohydrate structure present in the extracellular domain of both molecules. To confirm these results in a different cellular system, we also performed immunoprecipitation assays using the SCC cell line CarC, because it expresses high levels of podoplanin and CD44s (Figure 1D). The occurrence of endogenous partially glycosylated forms of both podoplanin (~30 kDa) and CD44s (~70 kDa) was confirmed in CarC lysates (Figure 3B).

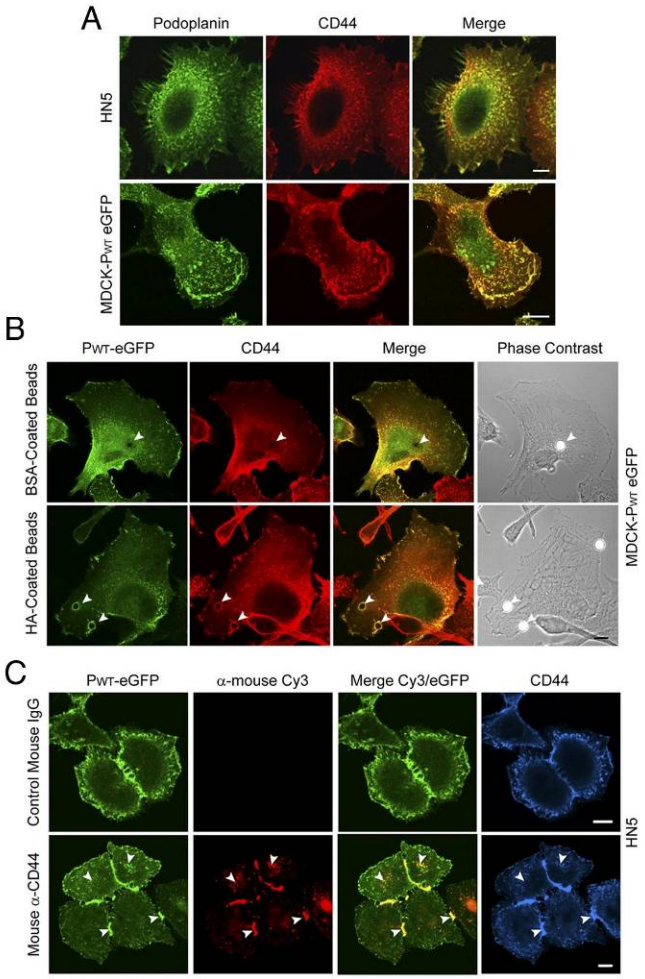

Figure 2. Podoplanin and CD44 colocalize at cell-surface protrusions. (A) Confocal microscopy showing localization of endogenous podoplanin and CD44 in HN5 oral carcinoma cells, and in MDCK cells stably transfected with podoplanin-eGFP (P_{WT} eGFP). (B) Recruitment of both podoplanin and CD44 by HA-coated beads (arrowheads). MDCK-P_{WT} eGFP cells plated onto coverslips were incubated with 5-μm beads coated with BSA or HA for 15 min. Cells were then processed for immunofluorescence to detect CD44. (C) Ab-induced clustering of CD44 (HP2/9 mAb, red) induced corecruitment of P_{WT} GFP (green) to CD44 patches (arrowheads) in HN5 cells. CD44 staining (blue) was performed using a different CD44 mAb (IM7) to visualize total distribution of CD44. Mouse IgGs were used as a negative control. Bars, 10 μm.

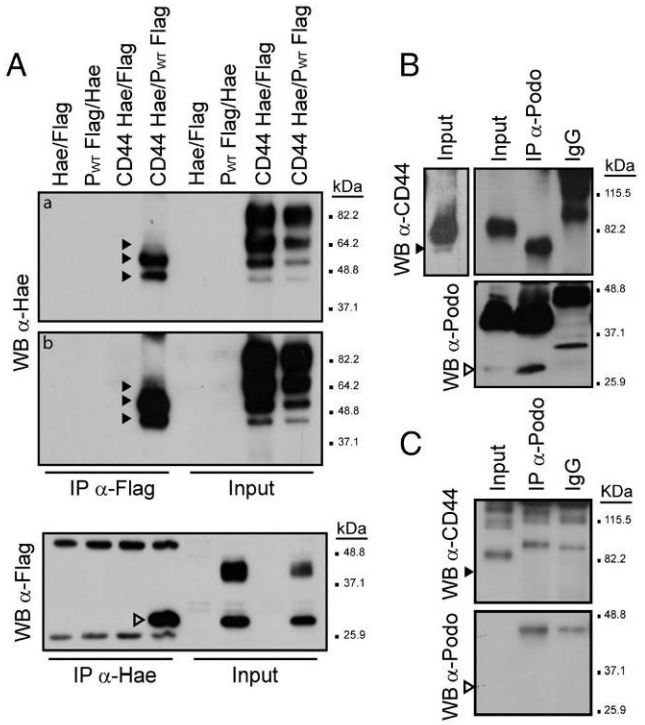

Figure 3. Podoplanin coimmunoprecipitates with CD44s. (A) HEK293T were transiently cotransfected with Flag-tagged human podoplanin or Hae-tagged human CD44s, as indicated. After 24 h of transfection, total lysates were immunoprecipitated with anti-Hae or anti-Flag Abs. Immunoprecipitates were electrophoresed by 10% SDS-PAGE and immunoblotted with anti-Flag or anti-Hae Abs, respectively. Panels a and b represent different exposure times of the same immunoblot. (B) Coimmunoprecipitation of endogenous CD44 and podoplanin in the mouse carcinoma cell line CarC. Lysates were immunoprecipitated with either a mAb specific for mouse podoplanin (PA2.26) or rat IgG as a control. The presence of podoplanin and CD44s in the precipitate was determined with anti-podoplanin PA2.26 and anti-CD44 IM7 mAbs, respectively. A longer exposure time of the input showing the occurrence of a ~70 kDa CD44s form in CarC lysates is shown in the left panel. (C) Coimmunoprecipitation assay in HaCaT keratinocytes. Note that HaCaT cells do not express podoplanin and were used as negative control for the coimmunoprecipitation assays depicted in panel B. Arrowheads indicate incompletely glycosylated forms of CD44s (black arrowheads) and podoplanin (open arrowheads).

Interestingly, endogenous ~70 kDa CD44s was coprecipitaed with a specific Ab recognizing murine podoplanin (PA2.26 mAb). These results demonstrate that podoplanin interacts with CD44s in SCC cells.

Podoplanin Binds CD44s at Cell-Surface Protrusions

The interaction of podoplanin with CD44s on the plasma membrane of MDCK cells was also confirmed in vivo by fluorescence resonance energy transfer (FRET) monitored by the acceptor photobleaching method. The mean FRET efficiency value (n = 8) between eYFP-tagged podoplanin (acceptor) and eCFP-tagged CD44s (donor) was 16% (Figure S4). To further analyze the spatial relationship between podoplanin and CD44s in vivo we used fluorescence lifetime imaging microscopy (FLIM) to monitor FRET. This technique enables visualization and quantification of protein–protein interactions by analysis of the donor lifetime decay kinetics (Parsons *et al.*, 2008). Interaction of P_{WT} eGFP (donor) and CD44s-mRFP (acceptor) was observed in single polarized cells, as measured by decreases in eGFP donor fluorescence lifetime relative to its lifetime in control cells expressing P_{WT} eGFP alone (Figure 4B, compare with panel A). FRET was localized at the trailing edge during rear retraction, and on small foci that were distributed throughout the apical surface of the cell across the lamellae. Interestingly, FRET efficiency was significantly decreased in cells in contact. Although specific interaction in the free lamellas at the outer edge of the colonies was sometimes detected, no interaction was observed at cell junctions, despite the presence of high levels of both molecules (Figure 4, B and C). Moreover, stimulation of MDCK cell migration/scattering with EGF or HGF increased the number of cells in which podoplanin–CD44s complexes were present (data not shown).

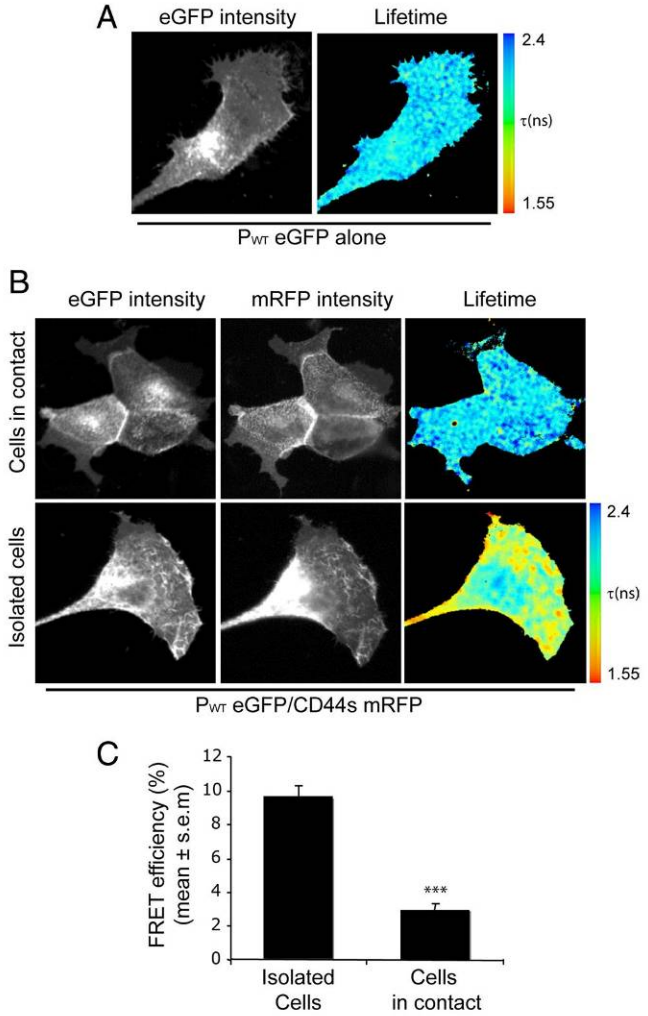

Figure 4. Podoplanin–CD44s complexes at the plasma membrane are up-regulated in cells with a migratory phenotype. (A–C) Multiphoton FLIM was used to image FRET between P_{WT} eGFP (donor) and CD44s-mRFP (acceptor) in MDCK cells. The images show the eGFP multiphoton intensity image and (where appropriate) the corresponding wide-field CCD camera image of mRFP expression. Lifetime images mapping spatial FRET across the cells are depicted using a pseudocolor scale (blue, normal eGFP lifetime; red, FRET). (A) Control MDCK cells expressing P_{WT} eGFP alone demonstrated a normal GFP lifetime (τ in ns) in the absence of acceptor. (B) Cells coexpressing P_{WT} eGFP and CD44s-mRFP display a localized shortening of the eGFP fluorescence lifetime, which is demonstrated by red in the pseudocolor scale. Note that although colocalization between P_{WT} eGFP and CD44s–mRFP was always detected, FRET was recorded mainly in isolated cells (i.e., those that had detached from their neighbors). (C) Bar graph representing average FRET efficiency of 14 cells for each condition over three independent experiments. The Student's *t* test was used to evaluate statistical significance between different populations of data. ***$p < 0.0005$.

These results strongly suggest that podoplanin–CD44s interaction may contribute to a motile phenotype.

Podoplanin Binding to CD44s Is not Mediated by ERM Proteins

The fact that podoplanin–CD44s interaction could be monitored by FRET suggested that the molecules may interact directly. However, because both CD44 and podoplanin bind to ERM proteins through their cytoplasmic (CT) tails, we also investigated the possibility that their interaction could be mediated by ERM proteins. To analyze this, podoplanin mutant constructs lacking the CT tail ($P_{\Delta CT}$) or the ERM binding site (P_{QNN}) were used for FRET/FLIM experiments (Figure 5A). As depicted in Figure 5B-C, preventing the binding of ezrin/moesin to podoplanin (Martín-Villar *et al.*, 2006) did not impair CD44s–podoplanin interaction, indicating that it is not mediated by ERM proteins. To further analyze which regions of the podoplanin molecule are important for podoplanin–CD44s binding we carried out coimmunoprecipitation experiments in HEK293T cells. These experiments were performed coexpressing CD44s-Hae and several podoplanin mutant constructs fused to eGFP, including $P_{\Delta CT}$, P_{QNN} and a mutant construct lacking the extracellular domain ($P_{\Delta EC}$). All these mutant proteins have been previously characterized (Martín-Villar *et al.*, 2006). The ability of $P_{\Delta EC}$ mutant to interact with CD44s in vivo could not be tested in FRET/FLIM experiments due to the fact that the eGFP tag in this construct is located at the NH_2-terminal end of the fusion protein (Figure 5A). However, coimmunoprecipitation assays showed that only the deletion of the podoplanin extracellular domain prevented its interaction with CD44s (Figure 5D) confirming that ERM proteins are not required for podoplanin–CD44s (figure 5D) association. Likewise, these results indicate that the podoplanin ectodomain is a crucial region for its binding to CD44.

Podoplanin-Induced Cell Migration and Directionality Requires CD44

To analyze the contribution of CD44 to podoplanin-induced cell migration, we performed transwell assays using MDCK cells transiently cotransfected with podoplanin cDNA and a small interfering (si)RNA to mediate down-regulation of CD44. Confirming our previous findings (Martín-Villar *et al.*, 2006), P_{WT} eGFP expression increased MDCK cell migration ~1.7-fold (Figure 6). The knockdown of CD44 (~70% reduction) did not significantly change the migratory behavior of MDCK-eGFP cells. However, CD44 down-regulation prevented podoplanin-enhanced migration, demonstrating that podoplanin requires CD44 to promote cell migration in MDCK cells (Figure 6, A and B).

Our previous observations suggested that podoplanin promotes intrinsic directional motility in MDCK cells (Martín-Villar *et al.*, 2006). To further investigate this, MDCK cells were imaged by fluorescence time-lapse microscopy allowing measurement of the total distance traveled, the displacement from origin, and calculation of mean speed and directional persistence (Figure 6, C and D). The migration pattern of control MDCK cells was erratic, with cells often changing direction, while P_{WT} eGFP-expressing cells frequently continued migrating in the same direction without turning. Comparison of the migration tracks of a representative number of cells for each condition showed that the directionality ratio was significantly increased in podoplanin-expressing cells, and that this was prevented when CD44 was knocked-down. Neither podoplanin expression nor CD44 down-regulation affected the migration speed of MDCK cells (Figure 6, C and D). Altogether, these results demonstrate that CD44 plays a crucial role in podoplanin-mediated migration.

Podoplanin and CD44 Depletion Alters Lamellipodia Extension/Stabilization and Cell Spreading

To further analyze the role of the podoplanin–CD44 complex in the migration of tumor cells, we down-regulated the

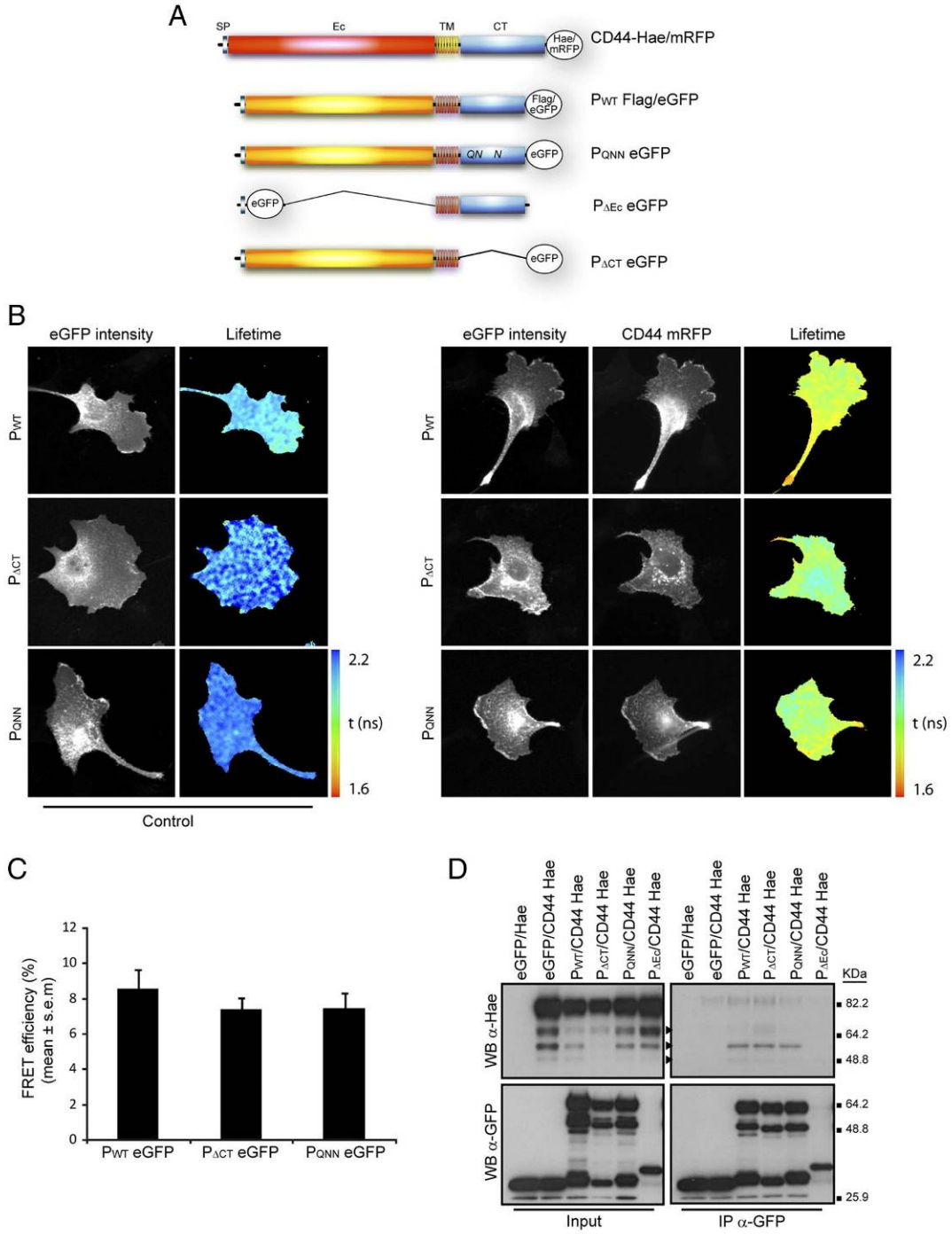

Figure 5. Podoplanin–CD44s interaction is not mediated by ERM proteins. (A) Schematic representation of podoplanin and CD44s fusion constructs used for coimmunoprecipitation and FRET/FLIM assays. SP, signal peptide; Ec, ectodomain; TM, transmembrane domain; CT, cytoplasmic tail; QN N, positive charged residues (RK.R) in podoplanin juxtamembrane domain were substituted by uncharged polar amino acids (QN.N) in order to impair podoplanin binding to ERM proteins (Martin-Villar *et al.*, 2006). (B) MDCK cells were cotransfected with CD44s mRFP and podoplanin eGFP mutant constructs, and cells were then imaged by FLIM to detect FRET as depicted in Figure 4. Images show the eGFP multiphoton intensity image and (where appropriate) the corresponding wide-field CCD camera image of the mRFP expression. Control MDCK cells expressing P_{WT}, $P_{\Delta CT}$, or P_{QNN} eGFP alone showed a normal GFP lifetime (τ in ns) in the absence of acceptor (CD44s mRFP), while cells coexpressing CD44s mRFP and podoplanin mutant constructs displayed a localized shortening of the eGFP fluorescence lifetime. (C) The bar graph represents average FRET efficiency of 15 cells over three independent experiments. (D) Coimmunoprecipitation assays performed in HEK293T cells coexpressing CD44s Hae and podoplanin eGFP mutant constructs. Total cell lysates were immunoprecipitated with an anti-GFP Ab-conjugated resin as described in Materials and Methods. The coimmunoprecipitated products were detected with an anti-Hae Ab.

expression of both molecules in the SCC cell line HN5, which expresses high levels of endogenous podoplanin and CD44. We used a vector-based small hairpin (sh)RNA approach to deplete podoplanin, in combination with an al-

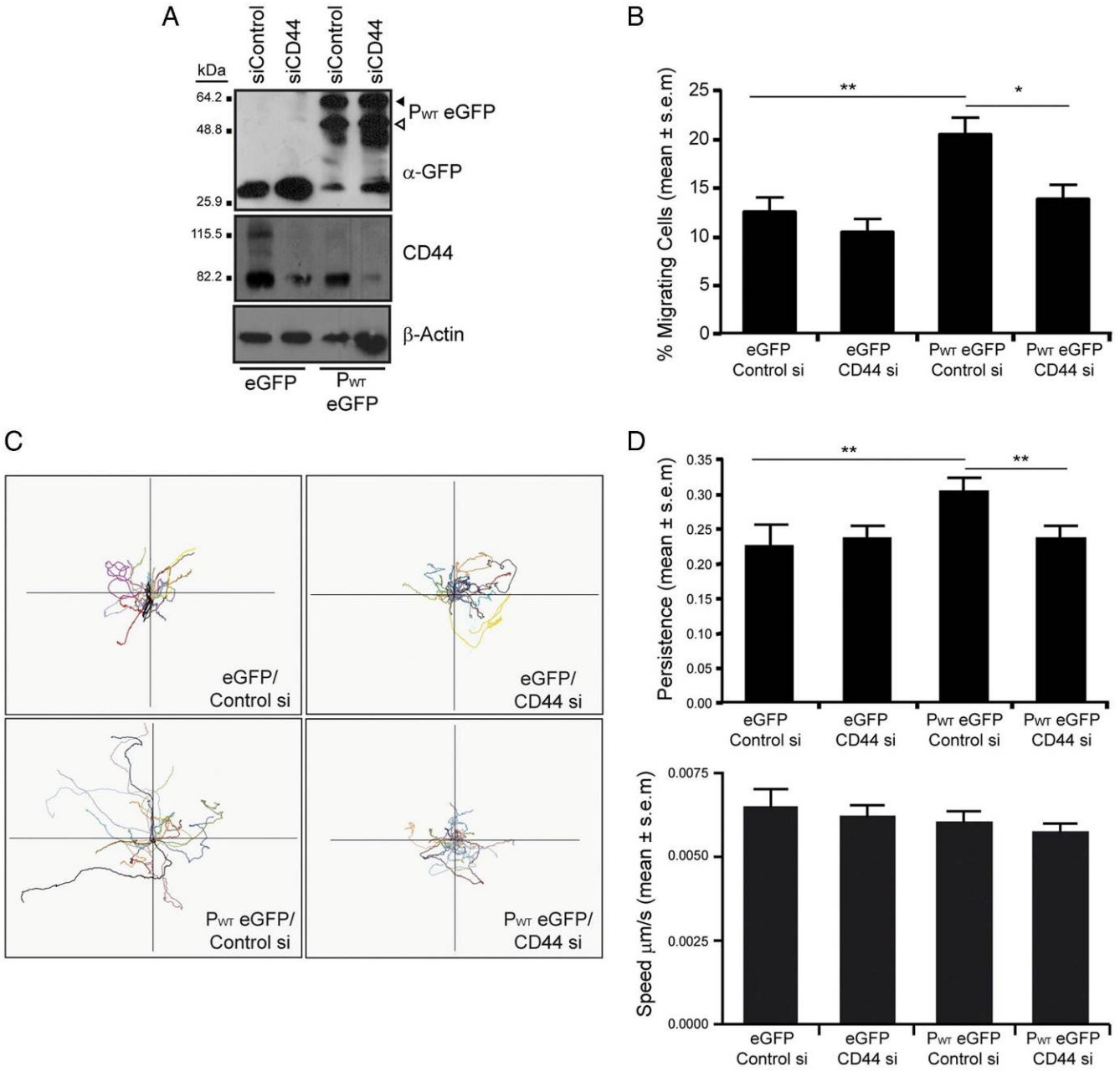

Figure 6. Podoplanin-induced migration and directionality in MDCK cells requires CD44. (A) Expression levels of podoplanin (P_{WT} eGFP) and CD44 after P_{WT} eGFP and CD44 siRNA coexpression. β-actin was used as a loading control. Arrowheads indicate fully (black arrowheads) and incompletely glycosylated (open arrowheads) forms of PWT eGFP. (B) Transwell migration assay. Bar graph representing percentage of migrating cells per total number of cells. Results are representative of three independent experiments performed in duplicates. (C) Representative migration tracks of MDCK cells expressing P_{WT} eGFP in the presence or absence of CD44 (n = 30). (D) Average persistence and speed of migration derived from the tracks depicted in C. n = 40–85 cells per bar. Asterisks indicate significant differences in a Student's t test. $^{**}p < 0.005$, $^{*}p < 0.05$.

ready established siRNA to mediate the knockdown CD44 in human cells (Tzircotis *et al.*, 2005). As depicted in Figure 7A, CD44 expression was efficiently down-regulated (~70%), and similarly, podoplanin protein levels were almost completely suppressed (~90% reduction) by using two different shRNAs (podo-sh1 and -sh2). A significant siRNA-mediated reduction of CD44 levels (~80%) was also achieved in podoplanin-depleted cells. siRNA mediated down-regulation of CD44 seemed not to affect podoplanin expression and vice versa.

Control cells usually displayed a characteristic highly organized leading edge with well-extended lamellipodia extensions, and the microtubule network often aligned parallel to, but localized at a considerable distance from, the leading edge. Interestingly, the single knockdown of CD44 enhanced cell spreading whereas the opposite was found to occur by silencing podoplanin expression alone (Figure 7, B and C). CD44si cells extended wide lamella with clear marginal F-actin ruffles. These cells also showed a well organized microtubule network (Figure 7B). Podoplanin-deficient cells,

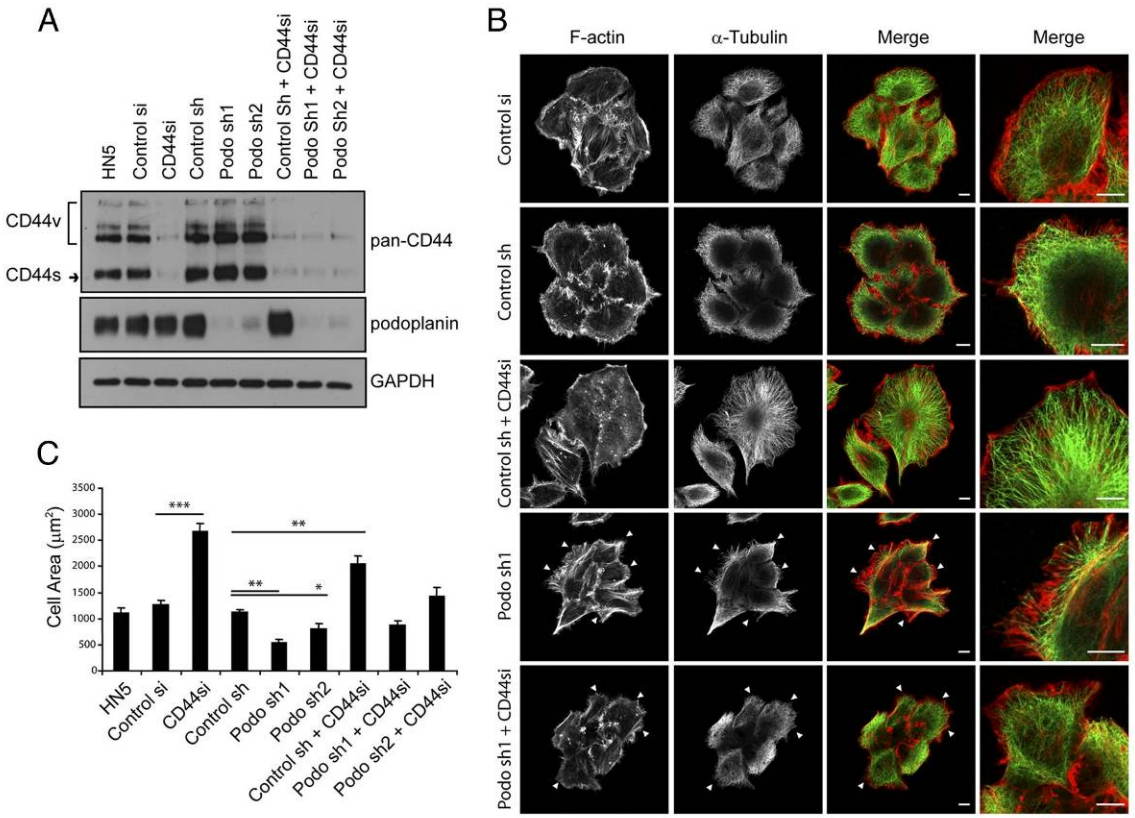

Figure 7. Knockdown of CD44 and podoplanin in oral carcinoma HN5 cells affects cell spreading. (A) Expression levels of CD44 and podoplanin in single and double knockdown cells by Western blot analysis. The expression of GAPDH was used as a loading control. (B) Immunofluorescence detection of F-actin and microtubules in single and double knockdown cells. Cells were double stained for F-actin (red) with phalloidin and microtubules (green) with a specific anti-tubulin mAb. Note the extremely disorganized leading edge of podoplanin-deficient cells and double knockdown cells (arrowheads) compared with control cells. (C) Graphical representation of the cell spread areas quantified using Image J software as described in Materials and Methods (n = 40–50 cells per bar). P values were obtained using a one-way analysis of variance (ANOVA). *$p < 0.05$; **$p < 0.005$; ***$p < 0.0005$. Bars, 10 μm.

however, had an extremely disorganized leading edge. These cells were unable to extend typical broad lamellipodia, exhibiting narrower (filopodia-like) protrusions instead, and the microtubules penetrated into the leading edge area (Figure 7B). RNAi-mediated knockdown of endogenous CD44 in podoplanin-deficient cells did not significantly change the cell shape of these cells (Figure 7, B and C). These results point to a role of the podoplanin–CD44 complex in regulating lamellipodia extension/stabilization during cell spreading and migration.

Podoplanin and CD44 Cooperate to Promote Directional Cell Motility during Wound Healing

To assess whether the observed morphological changes in single and double knockdown HN5 cells were coupled with defects in cell motility, we performed an in vitro wound healing assay. Time-lapse video microscopy was used to monitor wound closure. All the control cell lines showed ~95% wound closure 18 h after wounding. Podo-sh1 and sh2 cells covered ~40 and 60% of the control area, respectively, and CD44si cells covered 20–30% in the same period of time. Interestingly, wound closure delay became significantly more evident in double knockdown cells, as only 2–10% of the wound area was covered (Figure 8B and Movie 1 in supplemental material). Subsequently, we analyzed the migration pattern of a representative number of cells at the wound edges for a time period of 6 h. When the migration tracks were graphed to show directionality, it was evident that down-regulation of either podoplanin or CD44 alone resulted in a more random, less directional movement of cells positioned along the wound edge (Figure 8, A and C and Movie 2 in supplemental material). Moreover, by silencing both molecules the migration of HN5 cells toward the wound was almost suppressed. Altogether, these results strongly indicate that podoplanin and CD44 collaborate to promote directional motility.

DISCUSSION

Podoplanin and CD44 are type I membrane glycoproteins that are anchored to the actin cytoskeleton through association with ERM proteins (Legg and Isacke, 1998; Yonemura *et al.*, 1998; Scholl *et al.*, 1999; Martin-Villar *et al.*, 2006), and both are involved in cell adhesion, motility, and signal transduction despite lacking intrinsic kinase activity (reviewed in Ponta *et al.*, 2003; Wicki and Christofori, 2007). In this study, we report CD44 as a novel binding partner for podoplanin and describe a close relationship between CD44s and podoplanin expression associated with EMT and advanced stages of tumor progression in an experimental model of carcinogenesis. Although studies regarding expression of CD44 isoforms in human cancer are contradictory (Marhaba and Zoller, 2004), it has been proposed that a switch from CD44v to CD44s expression is a feature of poorly differentiated

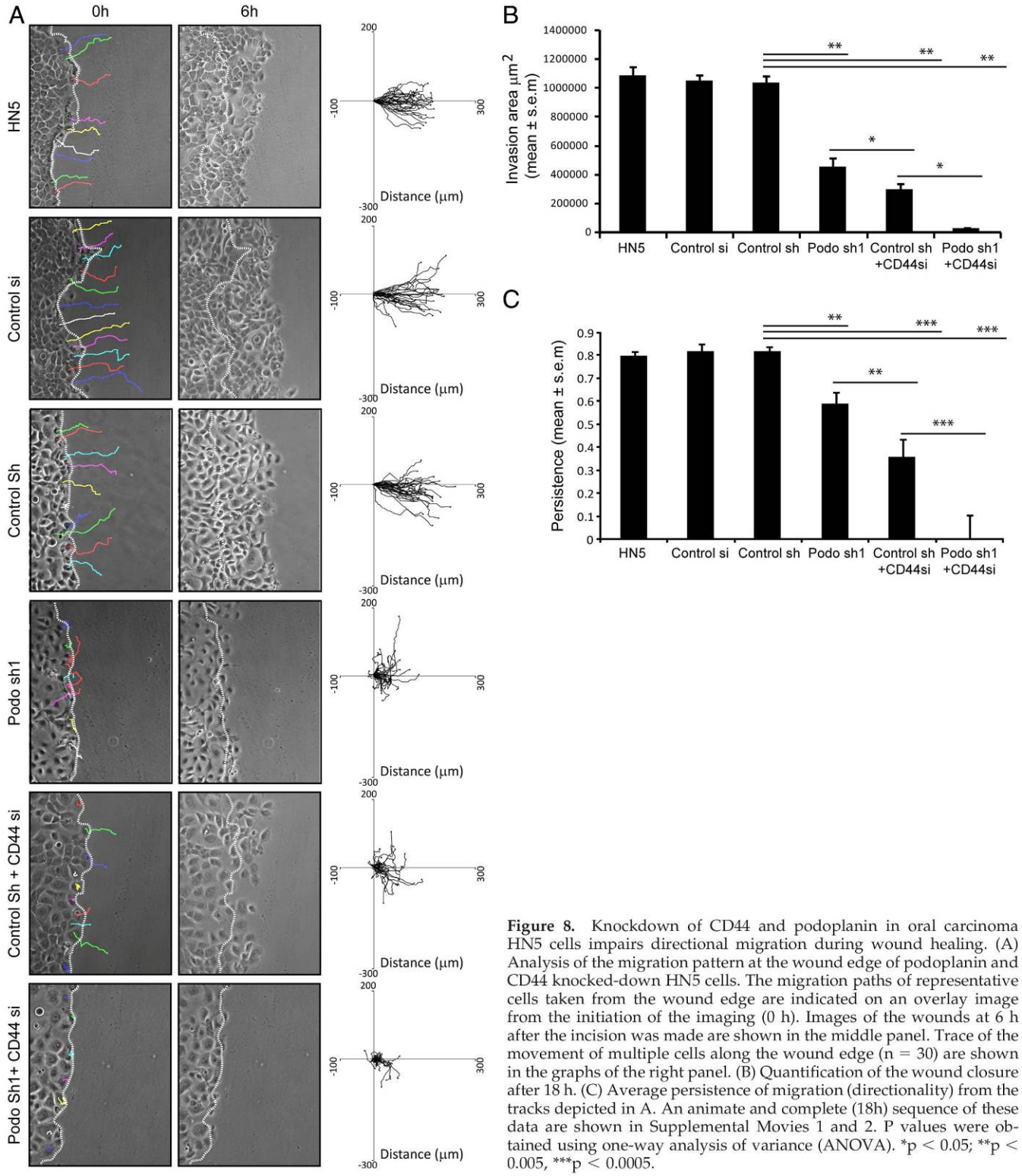

Figure 8. Knockdown of CD44 and podoplanin in oral carcinoma HN5 cells impairs directional migration during wound healing. (A) Analysis of the migration pattern at the wound edge of podoplanin and CD44 knocked-down HN5 cells. The migration paths of representative cells taken from the wound edge are indicated on an overlay image from the initiation of the imaging (0 h). Images of the wounds at 6 h after the incision was made are shown in the middle panel. Trace of the movement of multiple cells along the wound edge (n = 30) are shown in the graphs of the right panel. (B) Quantification of the wound closure after 18 h. (C) Average persistence of migration (directionality) from the tracks depicted in A. An animate and complete (18h) sequence of these data are shown in Supplemental Movies 1 and 2. P values were obtained using one-way analysis of variance (ANOVA). *$p < 0.05$; **$p < 0.005$, ***$p < 0.0005$.

SCCs (Hudson *et al.*, 1996; Stoll *et al.*, 1999). Accordingly, our conclusion from the analysis of both tumors and cell lines derived from the mouse skin carcinogenesis model is that despite the high heterogeneity of CD44 expression in vivo, a clear CD44s (and podoplanin) up-regulation is observed associated with the loss of differentiation in skin carcinomas. Similarly, increased expression of podoplanin has been associated with poor clinical outcome and metastasis in human SCCs (Yuan *et al.*, 2006; Chuang *et al.*, 2009). Interestingly, a recent study has found that podoplanin and CD44 were coexpressed in cells localized at the periphery of tumor nests in a high proportion of SCCs of the lung, although the distribution of CD44 was broader than that of podoplanin (Shimada *et al.*, 2009). Moreover, CD44 is a common cell-

surface marker for cancer stem cells in solid tumors (Visvader and Lindeman, 2008), and podoplanin has recently been postulated as a novel candidate marker of SCC stem cells, where it was coexpressed with CD44 (Atsumi *et al.*, 2008). These data suggest that there is a subpopulation of carcinoma cells with stem-like properties that coexpress podoplanin and CD44. While the biological significance of the presence of both proteins in cancer stem cells is still uncertain, it is tempting to speculate that coexpression of podoplanin and CD44s identify a cancer stem cell subpopulation with a high potential to disseminate and metastasize because of its association with EMT and the undifferentiated state of SCCs (Polyak and Weinberg, 2009).

Interestingly, we also found that podoplanin and CD44s interact to form a dynamic complex at the plasma membrane of migratory cells. This interaction seems to be direct, as it is not mediated by their common partners ezrin/moesin, and might be dependent on extracellular modifications of both glycoproteins. Supporting this hypothesis is the finding that the extracellular domain of podoplanin appears to be crucial for its association with CD44s. Accordingly, podoplanin interactions with other proteins such as CLEC-2 (Kato *et al.*, 2008) or galectin-8 (Cueni and Detmar, 2009) have been found to be dependent on the carbohydrate moieties present in their ectodomains. Moreover, it has been recently reported that recombinant soluble forms of the podoplanin ectodomain with different degrees of glycosylation can decrease cell adhesion and migration of lymphatic endothelial cells. Interestingly, in this study, the less glycosylated forms were more effective than the more extensively glycosylated proteins (Cueni *et al.*, 2010). CD44 is known to undergo sequential proteolytic cleavages that have an important role in cell migration (reviewed in Nagano and Saya, 2004). For this reason, one could argue that the CD44 forms (~45–70 kDa) coprecipitating with podoplanin might be fragments of the molecule rather than less glycosylated proteins. However, these forms were recognized either by antibodies raised to the CD44 NH_2-terminal end (IM7: Figure 3B) or to its CT tail (anti-CD44cyto Ab or anti-Hae Ab; Figure 3A and Supplemental Figure S3), indicating that these forms are not processing products of 80-kDa CD44s. Moreover, inhibition of CD44 proteolysis did not alter the pattern of CD44s coprecipitating forms (Supplemental Figure S3). On the other hand, removal of N-linked oligosaccharides in the CD44s molecule gave rise to protein forms of ~45–70 kDa with similar apparent molecular masses as the ones precipitated together with podoplanin. Glycosylation has been implicated in the regulation of CD44-mediated cell binding to HA, as well as in CD44 association with the actin cytoskeleton (Thorne *et al.*, 2004). The fact that podoplanin–CD44s interaction preferentially occurs when both molecules are not heavily glycosylated allows us to speculate that this association could be regulated by the glycosylation status of both molecules. Further investigations to address the mechanisms that regulate podoplanin–CD44s complex formation and its dependence on differential glycosylation are currently in progress.

Podoplanin–CD44s interaction appears to occur mainly on the trailing edge and on discrete foci on the lamella. Because both proteins can activate RhoA GTPase through binding to ERM proteins (Hirao *et al.*, 1996; Martin-Villar *et al.*, 2006), and RhoA-ROCK activity is required for actomyosin-based cortical contractility leading to detachment of the trailing edge (Ridley, 2001), podoplanin–CD44s interaction might be associated with tail retraction during mesenchymal-type of tumor cell movement (Friedl and Wolf, 2003). However, it is not clear yet how binding of these molecules to ERM proteins affects podoplanin–CD44s association and whether podoplanin–CD44s interaction influences signal transduction pathways mediated by any of these two molecules. On the other hand, knockdown of CD44 in HN5 oral SCC cells resulted in increased spreading and formation of extended lamella, while the opposite effect was observed upon silencing podoplanin expression. Moreover, knockdown of CD44 in podoplanin-deficient cells did not change significantly the shrunken shape characteristic of these cells. These results also suggest an involvement of podoplanin in lamellipodial extension/stabilization and spreading that is regulated by CD44. What strongly emerges from our gain- and loss-of-function experiments is the notion that podoplanin and CD44 cooperate to stimulate directional motility. Thus, podoplanin enhances the intrinsic directional motility of MDCK cells migrating either randomly or in a chemotactic transwell assay, and this effect is abolished by knocking-down CD44. Likewise, single knockdown of either CD44 or podoplanin inhibited the migratory potential of HN5 carcinoma cells in an in vitro wound healing assay, and depletion of both molecules almost suppressed the migration of HN5 cells toward the wound. Both CD44 and podoplanin appear to be required for cells to maintain direction during movement, as the knockdown of any of them resulted in less directional migration. Previous studies have found an important role for CD44 in mediating directional migration of different cell types, including cancer cells (Miletti-Gonzalez *et al.*, 2005; Tzircotis *et al.*, 2005; Colone *et al.*, 2008). Interestingly, in neutrophils and fibroblasts, CD44 is characteristically localized at the trailing edge of polarized cells (Jacobson *et al.*, 1984; Seveau *et al.*, 2001). It has been found that the binding of CD44 to ezrin is crucial for CD44-dependent directional motility (Legg *et al.*, 2002). Also, podoplanin mutant proteins unable to bind ezrin/moesin confer less motile phenotypes than wild-type podoplanin when expressed in MDCK cells (Martin-Villar *et al.*, 2006). However, it remains to be investigated whether podoplanin association with ERM proteins controls podoplanin-dependent directional motility as occurs with CD44.

Interest in podoplanin has considerably increased over the years because of its up-regulation in different human tumors, especially those derived from squamous stratified epithelia. However, many aspects of the biology and function of this glycoprotein still remain elusive. The lack of any obvious functional domains in the podoplanin molecule highlights the need to identify its binding partners. Similarly, the precise mechanisms controlling the structural and signaling events associated to CD44 have yet to be elucidated. In summary, the data presented here demonstrate that podoplanin associates with CD44s and that this interaction is important for driving directional cell migration in epithelial and tumor cells. Determining how this interaction is regulated could help to clarify many open questions in the biology of both molecules.

ACKNOWLEDGMENTS

We thank Drs. Amparo Cano, Francisco Sánchez-Madrid, and Helen Yarwood for their generous gifts of cell lines and antibodies and Patricia Carrasco for her help with Western blots. We also thank Dr. Véronique Orian-Rousseau and Helmut Ponta for their technical advice. This work was supported by grant SAF2007-63821 from the Spanish Ministry of Science and Innovation (to M.Q.), the Royal Society University Research Fellowship (to M.P.), Medical Research Council (to G.E.J.) EU FP7 T3Net Consortium (GEJ), and Cancer Research UK (to G.E.J. and E.M.V.).

REFERENCES

Akhurst, R. J., and Balmain, A. (1999). Genetic events and the role of TGF beta in epithelial tumour progression. J. Pathol. *187*, 82–90.

Allen, W. E., Zicha, D., Ridley, A. J., and Jones, G. E. (1998). A role for Cdc42 in macrophage chemotaxis. J. Cell Biol. *141*, 1147–1157.

Atsumi, N., Ishii, G., Kojima, M., Sanada, M., Fujii, S., and Ochiai, A. (2008). Podoplanin, a novel marker of tumor-initiating cells in human squamous cell carcinoma A431. Biochem. Biophys. Res. Commun. *373*, 36–41.

Burns, P. A., Kemp, C. J., Gannon, J. V., Lane, D. P., Bremner, R., and Balmain, A. (1991). Loss of heterozygosity and mutational alterations of the p53 gene in skin tumours of interspecific hybrid mice. Oncogene *6*, 2363–2369.

Camp, R. L., Kraus, T. A., and Pure, E. (1991). Variations in the cytoskeletal interaction and posttranslational modification of the CD44 homing receptor in macrophages. J. Cell Biol. *115*, 1283–1292.

Chuang, W. Y., Yeh, C. J., Wu, Y. C., Chao, Y. K., Liu, Y. H., Tseng, C. K., Chang, H. K., Liu, H. P., and Hsueh, C. (2009). Tumor cell expression of podoplanin correlates with nodal metastasis in esophageal squamous cell carcinoma. Histol. Histopathol. *24*, 1021–1027.

Clark, K., Pankov, R., Travis, M. A., Askari, J. A., Mould, A. P., Craig, S. E., Newham, P., Yamada, K. M., and Humphries, M. J. (2005). A specific alpha5beta1-integrin conformation promotes directional integrin translocation and fibronectin matrix formation. J. Cell Sci. *118*, 291–300.

Colone, M., Calcabrini, A., Toccacieli, L., Bozzuto, G., Stringaro, A., Gentile, M., Cianfriglia, M., Ciervo, A., Caraglia, M., Budillon, A., Meo, G., Arancia, G., and Molinari, A. (2008). The multidrug transporter P-glycoprotein: a mediator of melanoma invasion? J. Invest. Dermatol. *128*, 957–971.

Cueni, L.N., Chen, L., Zhang, H., Marino, D., Huggenberger, R., Alitalo, A., Bianchi, R., and Detmar, M. (2010). Podoplanin-Fc reduces lymphatic vessel formation in vitro and in vivo and causes disseminated intravascular coagulation when transgenically expressed in the skin. Blood. In press.

Cueni, L. N., and Detmar, M. (2009). Galectin-8 interacts with podoplanin and modulates lymphatic endothelial cell functions. Exp. Cell Res. *315*, 1715–1723.

del Pozo, M. A., Alderson, N. B., Kiosses, W. B., Chiang, H. H., Anderson, R. G., and Schwartz, M. A. (2004). Integrins regulate Rac targeting by internalization of membrane domains. Science *303*, 839–842.

Elbashir, S. M., Harborth, J., Lendeckel, W., Yalcin, A., Weber, K., and Tuschl, T. (2001). Duplexes of 21-nucleotide RNAs mediate RNA interference in cultured mammalian cells. Nature *411*, 494–498.

Friedl, P., and Wolf, K. (2003). Tumour-cell invasion and migration: diversity and escape mechanisms. Nat. Rev. Cancer *3*, 362–374.

Gandarillas, A., Scholl, F. G., Benito, N., Gamallo, C., and Quintanilla, M. (1997). Induction of PA2.26, a cell-surface antigen expressed by active fibroblasts, in mouse epidermal keratinocytes during carcinogenesis. Mol. Carcinog. *20*, 10–18.

Hathcock, K. S., Hirano, H., Murakami, S., and Hodes, R. J. (1993). CD44 expression on activated B cells. Differential capacity for CD44-dependent binding to hyaluronic acid. J. Immunol. *151*, 6712–6722.

Hirao, M., Sato, N., Kondo, T., Yonemura, S., Monden, M., Sasaki, T., Takai, Y., and Tsukita, S. (1996). Regulation mechanism of ERM (ezrin/radixin/moesin) protein/plasma membrane association: possible involvement of phosphatidylinositol turnover and Rho-dependent signaling pathway. J. Cell Biol. *135*, 37–51.

Hudson, D. L., Speight, P. M., and Watt, F. M. (1996). Altered expression of CD44 isoforms in squamous-cell carcinomas and cell lines derived from them. Int. J. Cancer *66*, 457–463.

Isacke, C. M., and Yarwood, H. (2002). The hyaluronan receptor, CD44. Int. J. Biochem. Cell Biol. *34*, 718–721.

Jacobson, K., O'Dell, D., Holifield, B., Murphy, T. L., and August, J. T. (1984). Redistribution of a major cell surface glycoprotein during cell movement. J. Cell Biol. *99*, 1613–1623.

Kato, Y., Kaneko, M. K., Kunita, A., Ito, H., Kameyama, A., Ogasawara, S., Matsuura, N., Hasegawa, Y., Suzuki-Inoue, K., Inoue, O., Ozaki, Y., and Narimatsu, H. (2008). Molecular analysis of the pathophysiological binding of the platelet aggregation-inducing factor podoplanin to the C-type lectin-like receptor CLEC-2. Cancer Sci. *99*, 54–61.

Kunita, A., Kashima, T. G., Morishita, Y., Fukayama, M., Kato, Y., Tsuruo, T., and Fujita, N. (2007). The platelet aggregation-inducing factor aggrus/podoplanin promotes pulmonary metastasis. Am. J. Pathol. *170*, 1337–1347.

Legg, J. W., and Isacke, C. M. (1998). Identification and functional analysis of the ezrin-binding site in the hyaluronan receptor, CD44. Curr. Biol. *8*, 705–708.

Legg, J. W., Lewis, C. A., Parsons, M., Ng, T., and Isacke, C. M. (2002). A novel PKC-regulated mechanism controls CD44 ezrin association and directional cell motility. Nat. Cell Biol. *4*, 399–407.

Marhaba, R., and Zoller, M. (2004). CD44 in cancer progression: adhesion, migration and growth regulation. J. Mol. Histol. *35*, 211–231.

Martin-Villar, E., Megias, D., Castel, S., Yurrita, M. M., Vilaro, S., and Quintanilla, M. (2006). Podoplanin binds ERM proteins to activate RhoA and promote epithelial-mesenchymal transition. J. Cell Sci. *119*, 4541–4553.

Martin-Villar, E., Scholl, F. G., Gamallo, C., Yurrita, M. M., Munoz-Guerra, M., Cruces, J., and Quintanilla, M. (2005). Characterization of human PA2.26 antigen (T1alpha-2, podoplanin), a small membrane mucin induced in oral squamous cell carcinomas. Int. J. Cancer *113*, 899–910.

Miletti-Gonzalez, K. E., Chen, S., Muthukumaran, N., Saglimbeni, G. N., Wu, X., Yang, J., Apolito, K., Shih, W. J., Hait, W. N., and Rodriguez-Rodriguez, L. (2005). The CD44 receptor interacts with P-glycoprotein to promote cell migration and invasion in cancer. Cancer Res. *65*, 6660–6667.

Nagano, O., and Saya, H. (2004). Mechanism and biological significance of CD44 cleavage. Cancer Sci. *95*, 930–935.

Nakazawa, Y., Sato, S., Naito, M., Kato, Y., Mishima, K., Arai, H., Tsuruo, T., and Fujita, N. (2008). Tetraspanin family member CD9 inhibits Aggrus/podoplanin-induced platelet aggregation and suppresses pulmonary metastasis. Blood *112*, 1730–1739.

Parsons, M., Messent, A. J., Humphries, J. D., Deakin, N. O., and Humphries, M. J. (2008). Quantification of integrin receptor agonism by fluorescence lifetime imaging. J. Cell Sci. *121*, 265–271.

Peinado, H., Olmeda, D., and Cano, A. (2007). Snail, Zeb and bHLH factors in tumour progression: an alliance against the epithelial phenotype? Nat. Rev. Cancer *7*, 415–428.

Perez-Gomez, E., Villa-Morales, M., Santos, J., Fernandez-Piqueras, J., Gamallo, C., Dotor, J., Bernabeu, C., and Quintanilla, M. (2007). A role for endoglin as a suppressor of malignancy during mouse skin carcinogenesis. Cancer Res. *67*, 10268–10277.

Polyak, K., and Weinberg, R. A. (2009). Transitions between epithelial and mesenchymal states: acquisition of malignant and stem cell traits. Nat. Rev. Cancer *9*, 265–273.

Ponta, H., Sherman, L., and Herrlich, P. A. (2003). CD *44*, from adhesion molecules to signalling regulators. Nat. Rev. Mol. Cell Biol. *4*, 33–45.

Quintanilla, M., Ramirez, J. R., Perez-Gomez, E., Romero, D., Velasco, B., Letarte, M., Lopez-Novoa, J. M., and Bernabeu, C. (2003). Expression of the TGF-beta coreceptor endoglin in epidermal keratinocytes and its dual role in multistage mouse skin carcinogenesis. Oncogene *22*, 5976–5985.

Ridley, A. J. (2001). Rho GTPases and cell migration. J. Cell Sci. *114*, 2713–2722.

Roscic-Mrkic, B., Fischer, M., Leemann, C., Manrique, A., Gordon, C. J., Moore, J. P., Proudfoot, A. E., and Trkola, A. (2003). RANTES (CCL5) uses the proteoglycan CD44 as an auxiliary receptor to mediate cellular activation signals and HIV-1 enhancement. Blood *102*, 1169–1177.

Scholl, F. G., Gamallo, C., and Quintanilla, M. (2000). Ectopic expression of PA2.26 antigen in epidermal keratinocytes leads to destabilization of adherens junctions and malignant progression. Lab. Invest. *80*, 1749–1759.

Scholl, F.G., Gamallo, C., Vilaro, S., and Quintanilla, M. (1999). Identification of PA2.26 antigen as a novel cell-surface mucin-type glycoprotein that induces plasma membrane extensions and increased motility in keratinocytes. J. Cell Sci. *112 (Pt* 24), 4601–4613.

Screaton, G. R., Bell, M. V., Jackson, D. G., Cornelis, F. B., Gerth, U., and Bell, J. I. (1992). Genomic structure of DNA encoding the lymphocyte homing receptor CD44 reveals at least 12 alternatively spliced exons. Proc. Natl. Acad. Sci. USA *89*, 12160–12164.

Seveau, S., Eddy, R. J., Maxfield, F. R., and Pierini, L. M. (2001). Cytoskeleton-dependent membrane domain segregation during neutrophil polarization. Mol. Biol. Cell *12*, 3550–3562.

Shimada, Y., Ishii, G., Nagai, K., Atsumi, N., Fujii, S., Yamada, A., Yamane, Y., Hishida, T., Nishimura, M., Yoshida, J., Ikeda, N., and Ochiai, A. (2009). Expression of podoplanin, CD44, and p63 in squamous cell carcinoma of the lung. Cancer Sci. *100*, 2054–2059.

Skelton, T. P., Zeng, C., Nocks, A., and Stamenkovic, I. (1998). Glycosylation provides both stimulatory and inhibitory effects on cell surface and soluble CD44 binding to hyaluronan. J. Cell Biol. *140*, 431–446.

Stoll, C., Baretton, G., Soost, F., Terpe, H. J., Domide, P., and Lohrs, U. (1999). Prognostic importance of the expression of CD44 splice variants in oral squamous cell carcinomas. Oral Oncol. *35*, 484–489.

Thorne, R. F., Legg, J. W., and Isacke, C. M. (2004). The role of the CD44 transmembrane and cytoplasmic domains in co-ordinating adhesive and signalling events. J. Cell Sci. *117*, 373–380.

Tzircotis, G., Thorne, R. F., and Isacke, C. M. (2005). Chemotaxis towards hyaluronan is dependent on CD44 expression and modulated by cell type variation in CD44-hyaluronan binding. J. Cell Sci. *118*, 5119–5128.

Visvader, J. E., and Lindeman, G. J. (2008). Cancer stem cells in solid tumours: accumulating evidence and unresolved questions. Nat. Rev. Cancer *8*, 755–768.

Wicki, A., and Christofori, G. (2007). The potential role of podoplanin in tumour invasion. Br. J. Cancer *96*, 1–5.

Wicki, A., Lehembre, F., Wick, N., Hantusch, B., Kerjaschki, D., and Christofori, G. (2006). Tumor invasion in the absence of epithelial-mesenchymal transition: podoplanin-mediated remodeling of the actin cytoskeleton. Cancer Cell *9*, 261–272.

Yonemura, S., Hirao, M., Doi, Y., Takahashi, N., Kondo, T., and Tsukita, S. (1998). Ezrin/radixin/moesin (ERM) proteins bind to a positively charged amino acid cluster in the juxta-membrane cytoplasmic domain of CD44, CD43, and ICAM-2. J. Cell Biol. *140*, 885–895.

Yuan, P., Temam, S., El-Naggar, A., Zhou, X., Liu, D. D., Lee, J. J., and Mao, L. (2006). Overexpression of podoplanin in oral cancer and its association with poor clinical outcome. Cancer *107*, 563–569.